

Rapid Approximate 3D Inversion of Transient Electromagnetic Data

by

Ralf Schaa, MSc., University of Cologne, Germany, 2005

SUBMITTED IN FULFILMENT OF THE REQUIREMENTS FOR THE
DEGREE OF DOCTOR OF PHILOSOPHY (GEOPHYSICS)

ARC Centre of Excellence in Ore Deposits

University of Tasmania

February 2010

Science
Thesis
SCHAA
PhD
2010



ii _____

A 7002 2412646B

955697

Statement of Originality

I hereby declare that this submission is my own work and to the best of my knowledge it contains no materials previously published or written by another person, or substantial proportions of material which have been accepted for the award of any other degree or diploma at the University of Tasmania or any other educational institution, except where due acknowledgement is made in the thesis. Any contribution made to the research by others, with whom I have worked at the University of Tasmania or elsewhere, is explicitly acknowledged in the thesis. I also declare that the intellectual content of this thesis is the product of my own work, except to the extent that assistance from others in the project's design and conception or in style, presentation and linguistic expression is acknowledged.

Ralf Schaa: Ralf Schaa Date: 17.02.'10

Authority of Access

This thesis may be made available for loan. Copying of any part of this thesis is prohibited for two years from the date this statement was signed; after that time limited copying is permitted in accordance with the *Copyright Act 1968*.

Ralf Schaa: Ralf Schaa Date: 17.02.'10

Statement of Co-authorship

Chapter 4 has been partly published as a scientific manuscript in co-authorship with supervisors Dr. Peter K. Fullagar and Dr. James E. Reid. The candidate had the primary responsibility for program development, modelling, data analysis and presentation. The supervisors contributed to data analysis and interpretation of results and manuscript preparation. Except for Chapter 4 all seven chapters presented in this thesis are primarily the candidate's work. Supervisors Dr. Peter K. Fullagar and Dr. James E. Reid identified the initial project, sponsors, and collaborators. The candidate developed and planned the thesis outline and was responsible for writing the full thesis. Dr Peter K. Fullagar provided editorial assistance on all chapters and technical input as clearly referenced in Chapters 2 and 5.

Acknowledgements

First and foremost, I would like to thank my supervisor Peter Fullagar without whom this thesis could not have been written. At all stages during my project he provided invaluable insight, inspiration and encouragement. I am grateful to James Reid who made it possible for me to undertake my PhD far away from home and who took care of me when I started the project. Many thanks to Michael Roach and Anya Reading for their numerous suggestions to improve my manuscript. I am furthermore indebted to Jeff Foster for moral and financial support. Thanks to Mike Webb for giving me the exciting opportunity to join his exploration team in the Australian outback. I would like to extend my appreciation to Glenn Pears and Tim Chalke who never got tired for helping me out with Gocad.

This research was funded by the ARC Centre of Excellence in Ore Deposits (CODES), with industry support from Fullagar Geophysics Pty. Ltd. and Geophysical Resources and Services Pty Ltd. I am grateful to Anglo American Geoscience Resource Group (South Africa) for financial support and to Anglo American Exploration (South Africa and Australia) for providing TEM data and for enabling me to participate on a TEM field survey. The University of Toronto provided the source code for program SPHERE. Mira Geoscience Asia Pacific Pty Ltd supplied the geological model of Gamsberg.

Abstract

Three-dimensional geophysical inversion of EM data aims to give an idealised estimate of the 3D geoelectrical structure of the subsurface which can meaningfully describe a set of observations. Rigorous 3D inversion of time-domain electromagnetic data is an onerous computational challenge, often taking several hours or even days. Motivated by the demand for a rapid and reliable 3D inversion method for TEM data, a fast, approximate 3D inversion scheme of transient electromagnetic data has been developed. The new scheme combines the TEM moments concept and geologically constrained 3D inversion methodology. The TEM moment inversion scheme builds on the pre-existing VPmg potential field modelling and inversion framework which has been extended and modified so as to accommodate approximate 3D TEM inversion. The method has potential for fast, constrained 3D inversion of large airborne TEM data sets.

The moment transform of TEM data is a time-weighted integral of the impulse response which accentuates late-time features. Due to the time integration, a TEM decay is effectively reduced to a single value. Depth resolution is lost due to the time integration, which, in effect, converts the nonlinear 3D TEM inversion problem into a linear 3D magnetic inversion problem.

Using TEM moments, EM interaction may tolerably be ignored, therefore justifying linear superposition of TEM responses. 3D TEM forward modelling is realised as a linear combination of a discretised 3D target response and a continuous background response. Superposition of the TEM moment responses of magnetic dipoles, distributed on a cubic mesh, gives the target response whereas the TEM moment response of a half space serves as the background response. Computations are based on analytical formulae. For the approximate scheme, a reduction in accuracy is accepted as a trade-off for much improved speed of calculation.

For the 3D inversion, a starting model (or a set of weights) generated from conductivity-depth imaging (CDI) is used to inject depth resolution. The CDIs are based on total magnetic field data which facilitates derivation of unambiguous apparent conductivities for fixed-loop TEM. Depth resolution is also recovered by means of geological constraints and depth weighting. The underlying model is both geological and petrophysical, so that the inversion can be focused on selected units. A fast steepest descent method is employed, so that computationally slow matrix inversion is not required. Typically, for ground-TEM, the fast approximate 3D inversion completes in minutes, thus facilitating exploration of non-uniqueness. The inversion scheme was successfully tested on synthetic fixed-loop TEM examples and on fixed-loop TEM field data from South Africa.

x

List of Figures

1.1	Typical ranges of resistivities of earth materials.	4
1.2	Schematic illustration of inductive TEM exploration.	8
1.3	Schematic of principal field layouts for ground-TEM survey types. . .	9
1.4	Square bipolar transmitter waveform and recorded transients. . .	11
1.5	TEM decay responses for a homogeneous half space excited by a vertical magnetic dipole.	12
1.6	Current diffusion and equivalent current filament concept.	13
1.7	Inductive and galvanic coupling for a plate example.	16
2.1	Conducting sphere excited by a transient magnetic pole source. . .	31
2.2	Coordinate system for secondary magnetic fields for a conductive sphere in a dipolar field.	34
2.3	Z-component of 1 st TEM moment synthetic towed bird AEM profile. .	43
2.4	Synthetic fixed transmitter TEM profile for a conducting sphere as compared with program SPHERE.	44
2.5	0-th TEM moment for a sphere in a uniform and dipolar field. . .	45
2.6	1-st – 4-th TEM moment for a sphere in a uniform and dipolar field. .	46
2.7	1-st order vertical TEM moment of a half space with rectangular loop source.	49
2.8	1-st order horizontal TEM moment of a half space with rectangular loop source.	54
2.9	Schematic of Head and Tail contribution to TEM moment response. .	55
3.1	Local subcell and adjacent cells in 3D mesh.	60
3.2	TEM moment response of a subcelled sphere in free-space energised by a fixed transmitter loop.	64
3.3	Primary magnetic field at the location of a thin plate.	65
3.4	TEM moment response of a subcelled thin plate in free-space energised by a fixed transmitter loop.	67
3.5	Superposition of point conductor responses for a sphere in different depths.	69
3.6	Exact and approximate Z-component TEM moments for a small shallow sphere for various transmitter loop sizes.	70
3.7	Schematic of a coincident loop system traversing a buried sphere. .	72

3.8	Surface-plot of normalised TEM response of a buried sphere in a conducting host recorded directly above the sphere.	74
3.9	Surface of normalised TEM response of a buried sphere in a conducting host recorded at 150 East.	75
3.10	Normalised incomplete TEM moment for a range of host conductivities specifying negligence of EM interaction.	76
3.11	Example of horizontal slab model in a resistive host for comparison with fully 3D EM modelling schemes.	78
3.12	Time constant decay curve of horizontal slab model at zero Easting .	79
3.13	TEM moment response curves for horizontal slab model.	80
3.14	Vertical dyke model (top) and time constant analysis (bottom). .	82
3.15	'Full' Z-component TEM moment response profiles at a range of Northings over vertical dyke model.	83
3.16	'Stripped' Z-component TEM moment response profiles at a range of Northings over vertical dyke model.	84
4.1	Total-field fixed-loop TEM decay curves over a homogeneous half space.	90
4.2	Apparent conductivities for two-layered earth models	95
4.3	Apparent conductivities for three-layered earth models	96
4.4	Conductivity-depth pseudo sections for two-and for three-layered earth.	98
4.5	χ^2 -misfit images of total magnetic field apparent conductivities for two- and three-layered earth models.	100
4.6	χ^2 -misfit images of single-component and quasi- $ \mathbf{B} $ apparent conductivities for two-layered earth model.	101
4.7	Vertical prism model for a synthetic fixed-loop survey.	103
4.8	Stacked profiles of Z- and X-component TEM step response over a vertical prism.	104
4.9	CDIs of vertical prisms in a moderately conducting host. . . .	105
4.10	Horizontal slab model for a synthetic fixed-loop survey.	106
4.11	Total-field CDIs of horizontal slab.	107
4.12	Dipping plate model for a synthetic fixed-loop survey.	108
4.13	Z-component TEM decay of dipping plate underneath transmitter loop.	108
4.14	Total-field CDIs of dipping plate model.	109
4.15	Stacked profiles for field data fixed loop TEM.	111
4.16	Measured field data and plate model together with total-field CDIs for measured and modelled data.	112
5.1	Schematic illustration of parametrisation of rock property for the litho-categorical model of VPem3D.	118
5.2	VPem3D depth weighting curves.	129
5.3	Horizontal slab model with a conductivity of 1 S/m in burial depth of 400 m depth.	131

5.4	TEM moments of horizontal slab with 5% random Gaussian noise added.	132
5.5	Conductivity-depth sections for horizontal slab model.	133
5.6	Recovered time constant model after inversion of the horizontal slab TEM moments based on the unconstrained starting model. .	135
5.7	Recovered TEM moment responses based on unconstrained starting model.	136
5.8	Recovered time constant model based on CDI starting model. . .	137
5.9	Recovered TEM moment responses based on CDI starting model. .	138
5.10	Conductivity weights and recovered time constant model after inversion for zero starting model.	139
5.11	Recovered TEM moment responses based on zero starting model with conductivity weights.	140
5.12	Horizontal slab depth weighing scheme for zero starting model. .	141
5.13	Recovered time constant models for a thick horizontal slab based on a zero starting model conditioned with two different depth weighting schemes.	142
5.14	Recovered TEM moment responses based on zero starting model with depth weights.	143
5.15	Section and plan of vertical dyke model.	145
5.16	Total-field conductivity-depth section of vertical dyke model. . .	146
5.17	'Full' TEM moment responses of vertical dyke model.	148
5.18	'Stripped' TEM moment responses of vertical dyke model. . . .	149
5.19	Recovered time constant model based on CDI starting model of vertical dyke.	151
5.20	TEM moment responses of recovered time constant model based on CDI starting model of vertical dyke.	152
5.21	Conductivity weights for vertical dyke model.	153
5.22	Recovered time constant model of vertical dyke model based on zero starting model with conductivity weights.	154
5.23	TEM moment responses of recovered time constant model based on zero starting model with conductivity weights for vertical dyke.	155
5.24	Depth weighting scheme for vertical dyke model.	156
5.25	Recovered time constants for the vertical dyke model based on a zero starting model conditioned with depth weights and fixed background.	157
5.26	Recovered time constants for the vertical dyke model based on a zero starting model conditioned with depth weights and variable background.	158
5.27	TEM moment responses of recovered time constant model based on zero starting model conditioned depth weights.	159
6.1	Aerial view and geological map of the Gamsberg prospect.	168
6.2	3D geological model of Gamsberg-East	169
6.3	SQUID magnetometer and helium dewar in field operation.	170
6.4	Transmitter and receiver during field operations.	170

6.5	Fixed-loop TEM survey layout at Gamsberg-East.	172
6.6	Stacked Bz-profiles at Gamsberg-East.	173
6.7	Stacked Bx-profiles at Gamsberg-East.	174
6.8	Time constant maps from Gamsberg z-component TEM decays. .	175
6.9	Plan view of geological model with drill markers at increasing depth superimposed.	176
6.10	Example of Savitzky-Golay filter for z-component at early, inter- mediate and late time.	177
6.11	Gamsberg-East conductivity-depth-images from B -field amplitudes.	178
6.12	1st order TEM moments from BZ-decays at Gamsberg-East. . .	179
6.13	TEM moments from recovered time constant model of Gamsberg- East, based on unconstrained inversion.	183
6.14	Recovered time constant model of Gamsberg-East after uncon- strained inversion.	184
6.15	Recovered time constant model of Gamsberg-East after standard inversion based on a CDI-starting model.	186
6.16	Recovered time constant model of Gamsberg-East after inversion with bound-cancellation, based on a CDI-starting model.	187
6.17	TEM moment profiles for recovered time constant model of Gamsberg- East after inversion based on a CDI-starting model.	188
6.18	Cross-section through recovered time constant model after in- version of the Gamsberg-East TEM data using a zero starting model.	190
6.19	Iso-surface of recovered time constant model after inversion of the Gamsberg-East TEM data using a zero starting model	191
6.20	TEM moment profiles for recovered time constant model using a zero starting model of Gamsberg-East conditioned with depth weights.	192
6.21	Recovered time constant distribution of the Gams Formation unit after inversion.	193
6.22	Recovered time constant model after geologically-constrained in- version of Gamsberg-East TEM moments.	194
6.23	Eastwest and northsouth section of recovered time constant model after inversion of geological constrained model for Gamsberg-East.	195
6.24	Map of the amplitude of the normalised vertical component pri- mary field intersecting the Gams Formation unit.	196
6.25	TEM moments from recovered time constant model of Gamsberg- East after geologically constrained inversion.	197
6.26	Maxwell Plates model for the Gamsberg-East data set.	198
6.27	Gamsberg-East CDI section with plate model superimposed . . .	199
6.28	Plate model and recovered time constant model of Gamsberg-East for geologically constrained inversion.	200
6.29	Observed TEM data and plate model responses of Gamsberg-East for three lines.	201

Contents

1	Introduction	1
1.1	Scope and objectives	1
1.2	Synopsis of inductive TEM exploration	3
1.2.1	Governing equations	3
1.2.2	Concept of the TEM exploration method	8
1.2.3	Brief review of transient electromagnetics	17
1.3	Approximate 3D inversion of TEM moments	24
1.4	Thesis structure	25
2	Methodology of the TEM moments approach	27
2.1	The TEM moment transformation	28
2.1.1	Moment transform definition	28
2.1.2	Moments for the magnetic field and its derivative	29
2.1.3	Inductive and resistive limit as TEM moments	29
2.2	Quasi-static time domain EM response of a sphere	30
2.2.1	Scalar magnetic potential of a pole source	30
2.2.2	Secondary magnetic potential	32
2.2.3	Impulse response solution	32
2.2.4	The field solutions	33
2.2.5	Evaluation of associated Legendre polynomials	36
2.3	TEM response of a sphere in a uniform field	37
2.4	TEM moments of a sphere	38
2.4.1	Evaluation of sum of Bessel zeros	39
2.5	Point conductor TEM moments	39
2.5.1	Primary field	41
2.6	Comparison with magnetostatic solution	42
2.6.1	Program implementation	43
2.7	The TEM moment of a half space for a rectangular loop source	46
2.7.1	The vertical-component half space TEM moment	47
2.7.2	The horizontal-component half space TEM moment	49
2.8	TEM moments of measured data	55

3	Approximate 3D modelling of TEM moments	57
3.1	Background response	58
3.2	Discrete target response	59
3.2.1	Calculating the target response	59
3.2.2	Effect of primary field and conductivity gradient	60
3.2.3	3D grid time constants	61
3.3	Linear superposition of point conductors	63
3.3.1	Subcelled sphere in free space	63
3.3.2	Subcelled plate in free space	65
3.3.3	Proximity of transmitter source	68
3.4	Effect of host-rock	71
3.5	Comparison with fully 3D electromagnetic modelling schemes	77
3.5.1	Horizontal slab in resistive host	78
3.5.2	Vertical dyke in conductive host	80
3.6	Concluding remarks	85
4	1D imaging of TEM data	87
4.1	Apparent conductivity	89
4.2	Unambiguous apparent conductivity from magnetic field amplitudes	89
4.2.1	Derivatives of magnetic field amplitude	91
4.3	Time-depth transformation	93
4.4	Total B-field CDI processing for layered earth models	94
4.4.1	Unambiguous total magnetic field apparent conductivity	99
4.4.2	Comparison with quasi $ \mathbf{B} $ -field amplitudes and single component data	102
4.5	CDIs of 3D structures	102
4.5.1	Vertical prism in a moderately conducting host	103
4.5.2	Horizontal slab in conductive host	106
4.5.3	Dipping plate in a conductive host	107
4.6	Field data example	110
4.7	Concluding remarks	113
5	3D Inversion of TEM moments	115
5.1	Overview of the inversion algorithm	117
5.1.1	Rock property constraints	119
5.1.2	Discrete target and continuous background response	120
5.1.3	The starting model	121
5.2	The inverse problem	121
5.2.1	Objective function	123
5.2.2	The method of steepest descent	124
5.2.3	Under-determined case ($K > N$)	125
5.2.4	Over-determined case ($N > K$)	126
5.2.5	Background optimisation	126
5.2.6	Implementation of rock property constraints	127
5.3	3D Inversion example Horizontal Slab	130
5.3.1	Unconstrained starting model	135

5.3.2	CDI starting model	137
5.3.3	Zero starting model with conductivity weights	139
5.3.4	Zero starting model with depth weights	141
5.3.5	Review of inversion results for horizontal slab model	144
5.4	3D Inversion example Vertical Dyke	145
5.4.1	CDI starting model	150
5.4.2	Zero starting model with conductivity weights	153
5.4.3	Zero starting model with depth weights	156
5.4.4	Review of inversion results for vertical dyke model	160
5.5	Concluding remarks	161
6	Application of approximate 3D TEM inversion to field data.	163
6.1	Geological context	165
6.1.1	Exploration history	165
6.1.2	Lithology and stratigraphy	165
6.2	Gamsberg-East geological model	167
6.3	EM equipment and data acquisition	170
6.4	The field data	171
6.5	Time constant analysis	176
6.6	Conductivity-depth imaging	177
6.7	Transformation of field data to TEM moments	180
6.8	Inversion of Gamsberg TEM moments	181
6.8.1	Unconstrained inversion	182
6.8.2	Inversion with CDI starting model	185
6.8.3	Inversion with Zero starting model	189
6.8.4	Geologically constrained inversion	193
6.9	Conventional forward modelling employing plate conductors	198
6.10	Discussion of inversion results	202
6.11	Concluding remarks	204
7	Conclusions	205
7.1	Summary and discussion of research	205
7.1.1	Approximate forward modelling	206
7.1.2	Robust 1D imaging	208
7.1.3	3D inversion of TEM moments	208
A	Future work	213
	Bibliography	219

meinem Vater

Chapter 1

Introduction

1.1 Scope and objectives

Rigorous three-dimensional (3D) inverse modelling of time-domain electromagnetic (TEM) data is complex and time-consuming. In the mineral exploration industry, however, there is often a perceived requirement to interpret the data quickly. Simplified approximate 3D solutions therefore facilitate, fast and flexible data interpretation of large TEM data sets acquired over 3D geology. The focus of the present work is on rapid 3D inversion of TEM data as an aid in exploration for deep conductive targets.

The transition from pre-dominantly shallow mineral exploration to deep exploration is inevitable as it becomes increasingly less likely to discover large outcropping bodies (McMonnies and Gerrie, 2007; Williams, 2008). However, as exploration depth increases, interpretation of a limited set of isolated geophysical observations will progressively become more ambiguous. Therefore, an approach of integrated interpretation of all information available is needed to reduce uncertainty (Knox-Robinson and Wyborn, 1997; Paterson, 2003).

The current thesis accommodates integration of geological information for constrained inversion of TEM data in order to resolve the geoelectrical subsurface structure of concealed mineralisation. The presented methodology is a novel and innovative approach to tackle the 3D inverse TEM problem in an approximate and rapid fashion. The presented 3D interpretation scheme is complementary to existing 1D interpretation schemes and aims to help build confidence in the geological interpretation of the subsurface.

1D approaches are fast, but artifact-prone. The aim of the project therefore is to, in effect, generalise conductivity-depth-imaging (CDI) processing to 3D. 1D interpretation of TEM data in form of CDI and 1D inversion can serve as preparatory steps for 3D constrained inversion. However, 1D interpretation schemes may contain artifacts when applied to data arising from 3D geology which therefore may lead to spurious features in the 3D inversion. Therefore, a novel CDI scheme, based on multi-component TEM data, was developed in order to minimise the impact of 3D geology on CDIs.

Fast, approximate EM modelling employs the TEM moment transform which is a weighted time-integration of the TEM earth response (Smith and Lee, 2002b). Because the TEM moment transform puts emphasis on 'late-time', EM interaction is tolerably disregarded. For this thesis the first order TEM moment is exclusively used which is equivalent to the resistive limit response. Smith and Lee (2002b) note that TEM moments may enhance deep and conductive features which may otherwise be difficult to detect. Complicated non-linear expressions for the time-domain response of simple bodies simplify in the moment domain.

Geophysical inversion has achieved widespread acceptance as a valid interpretation tool and major progress has been made by integrating geological models as constraints (Fullagar and Pears, 2007; Oldenburg and Pratt, 2007). Potential field inversion techniques have progressed from representations using simple 3D models to integrated interpretation using Common Earth Models, which specifies a litho-structural model based on quality geology, structural interpretation, petrophysical and geophysical data, defining a coherent model for the formation of the 3D geology (McGaughey, 2006; Oldenburg and Pratt, 2007).

The TEM moment transformation of transient EM data to TEM moments transposes the inversion problem from the non-linear time-domain to the linear, potential field-like, moment domain. The inversion employs the potential field inversion framework of the program VPmg (Fullagar et al., 2000, 2004; Fullagar and Pears, 2007; Fullagar et al., 2008). VPmg is modified so as to accommodate the TEM moments methodology; the new program is referred to as VPem3D.

The significance and innovation of the presented thesis is the fast integrated 3D interpretation of TEM data, based on parametrised approximate TEM solutions, for arbitrarily shaped anomalous volumes in terms of time constants utilising geological constraints and potential field inversion devices. In short, the objectives of the thesis can be summarised as

- the development of an approximate, fast 3D-TEM forward modelling program using analytical parametrised TEM solutions as a combination of a discrete target response and a continuous background response.
- the derivation of an unambiguous apparent conductivity based on \mathbf{B} -field amplitudes for fixed-loop TEM which serves as a preparatory process of 3D inversion.
- the realisation of a true 3D inversion scheme for TEM data using the approximate forward modelling solution.
- the presentation of a fast and efficient 3D integrated interpretation technique utilising geological constraints for TEM data as a supplement to fast 1D interpretation schemes

The remainder of this introductory chapter provides a synopsis of the transient electromagnetic prospecting method. First the governing equations and the TEM methodology are presented, followed by a brief literature review of EM modelling and inversion. The chapter concludes with an introduction to the TEM moments modelling and inversion method and an overview of following chapters.

1.2 Synopsis of inductive TEM exploration

The aim of electromagnetic (EM) prospecting is to resolve the subsurface geoelectrical structure. Inductive EM methods in applied geophysics are used to determine the distribution of electrical conductivity in the subsurface. Because the employed frequencies are low, dielectric properties can be neglected. EM methods measure the decaying earth response due to an electromagnetic excitation. For this study the designated method of surveying is the inductively coupled transient electromagnetic (TEM) method which satisfies the electromagnetic diffusion equation which therefore inevitably results in the relatively low resolution of geoelectrical imaging techniques. The method is sensitive to electrical conductivity 'averaged' over the volume of the ground in which induced currents are caused to flow. The theoretical expositions of the TEM exploration method may be found for example in Grant and West (1965); Kaufman and Keller (1983) and Ward and Hohmann (1988). The application and practise of the method is dealt with in depth in Nabighian and Macnae (1991) and West and Macnae (1991).

The work presented here is focused primarily on mineral exploration for detection of deep and strong conductive targets (e.g. Palacky, 1983; Nabighian and Asten, 2002; Nabighian and Macnae, 2005). The transient electromagnetic method is widely-used in Australia for exploration for electrically-conductive base-metal mineralisation. The method uses the time-varying magnetic field produced by abruptly terminating a steady current in a large, square or rectangular transmitter loop to induce the flow of eddy currents in buried conductors. The decaying secondary magnetic fields associated with the eddy currents are detected at a coil receiver or magnetometer, and can be used to determine the depth, size, shape and conductivity of concealed mineralisation. Typical ranges of the conductivity of earth materials are shown in Figure 1.1

Measurement configurations in mineral prospecting for ground TEM surveys customarily employ a square or rectangular transmitter loop in conjunction with a coil receiver or magnetometer. The receiver can be placed in the centre of the loop, termed central-loop or in-loop, or the receiver can be placed outside the transmitter which results in an offset-loop or shingram configuration. During measurements, the transmitter loop can either stay in a fixed position and only the receiver locations vary (fixed-loop) or both the transmitter and receiver move simultaneously (moving-loop). The details in field setup and technique can however vary considerably (e.g. Nabighian and Macnae, 1991, p.453), dependent on the objectives of the measurements.

1.2.1 Governing equations

EM phenomena are governed by Maxwell's equations and by the constitutive relations which link the interaction of electric and magnetic fields and fluxes with the physical properties of the earth. Diffusive EM methods are described by a parabolic partial differential equation, the diffusion equation, describing the variation in space and time of diffusive EM fields. The diffusion equation follows from the EM wave equation in the quasi-static approximation. The governing equations are presented in the following followed by a synopsis of the TEM prospecting method.

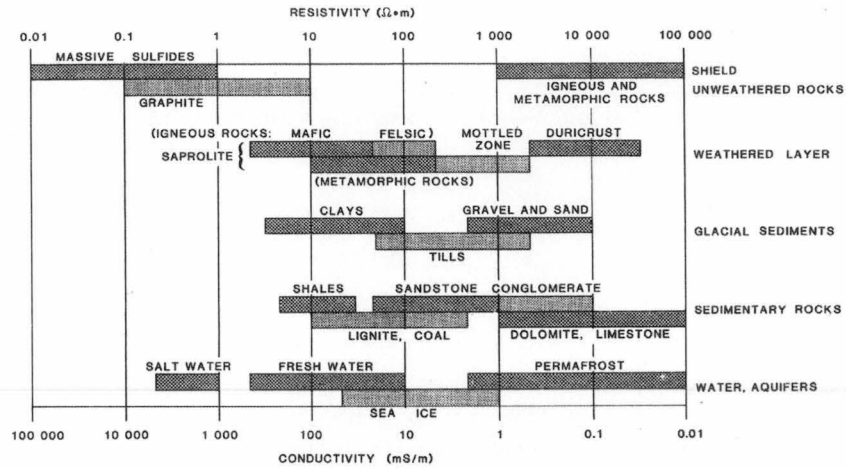


Figure 1.1 – Typical ranges of resistivities of earth materials after Palacky (1988, Fig.2).

Maxwell equations

The conception of the electromagnetic induction exploration method is based on the Maxwell equations. For time-varying fields, the differential form of these equations are given by:

$$\nabla \cdot \mathbf{D} = q \quad \text{Gauss's law} \quad (1.1)$$

$$\nabla \times \mathbf{E} = -\partial_t \mathbf{B} \quad \text{Faraday's law} \quad (1.2)$$

$$\nabla \cdot \mathbf{B} = 0 \quad \text{Magnetic flux} \quad (1.3)$$

$$\nabla \times \mathbf{H} = \partial_t \mathbf{D} + \mathbf{J} \quad \text{Ampère's law} \quad (1.4)$$

Gauss's law in differential form states that the electric flux density (or dielectric displacement) \mathbf{D} diverges from any distribution of charge q . Faraday's law of electric induction relates the change of the magnetic flux density (or magnetic induction) \mathbf{B} to the vorticity of the electric field intensity \mathbf{E} . Unlike Gauss's law, which gives evidence of electric charges, the equation for magnetic flux gives reference that there are no magnetic charges but only magnetic moments and that the field lines of the magnetic flux density \mathbf{B} are closed curves. Ampère's law describes the induction of the magnetic field intensity \mathbf{H} by changes in the dielectric displacement and/or by moving charges as denoted by the electric current density \mathbf{J} . \mathbf{D} and \mathbf{H} involve macroscopic properties of the material. All quantities and units are described in Table 1.1.

Symbol	Meaning	SI Unit where applicable	Abbreviation
E	Electric field intensity	Volt / metre	V/m
B	Magnetic flux density	Tesla	T
D	Electric flux density	Coulomb / metre ²	C/m ²
H	Magnetic field intensity	Ampere / metre	A/m
J	Electric current density	Ampere / metre ²	A/m ²
σ	Electric conductivity	Siemens / metre	S/m
μ	Magnetic permeability	Henry / metre	H/m
ϵ	Dielectric permittivity	Farad / metre	F/m
q	Electric charge density	Volt / metre ³	V/m ³
L	Inductance	Henry	H
R	Resistance	Ohm	Ω
τ	Time constant	second	s
μ_0	Vacuum permeability	$4\pi \cdot 10^{-7}$ H/m	
ϵ_0	Vacuum permittivity	$1/36\pi \cdot 10^{-9}$ F/m	
∂_t, ∂_t^2	Time differential operators	$\partial/\partial t, \partial/\partial t^2$	

Table 1.1 – Definition of symbols and units.

Constitutive relations

Maxwell’s equations are completed by the constitutive relations, connecting the vectors **D** and **B** to the field intensities **E** and **H** together with Ohm’s law, relating the electric current density **J** in a material medium as the result of the electric field intensity **E**. Generally, the constitutive relationships have tensorial character where the tensors ϵ , μ and σ depend on position, time, the microscopic structure of the material, as well as bulk properties like density and temperature (Ward and Hohmann, 1988, p.133). The constitutive equations in these linearised forms are valid in substances other than ferroelectrics or ferromagnets and for weak enough fields:

$$\mathbf{D} = \epsilon \mathbf{E} \quad (1.5)$$

$$\mathbf{B} = \mu \mathbf{H} \quad (1.6)$$

$$\mathbf{J} = \sigma \mathbf{E} \quad (1.7)$$

where the scalars ϵ , μ and σ denote the (dielectric) permittivity, the (magnetic) permeability and the (electrical) conductivity respectively. For the purpose of TEM exploration it is usually assumed that earth materials are isotropic, linear and homogeneous media with electrical properties independent of time, temperature and pressure. Also, for the purpose of this study, it is always assumed that the magnetic permeability is to be that of free space with $\mu = \mu_0$.

Free charges in conducting media

All substances exhibit conductivity to some degree and the range of observed values is of many orders in magnitude. The maximum possible range is from pure sulphur (10^{-16} S/m) to native silver (1.6×10^8 S/m) (Telford et al., 1985, p.289). Within regions of non-vanishing conductivity there remains no permanent distribution of external charges. From the divergence of Ampère's law (Equation 1.4) the continuity equation, which expresses the conservation of charge by current flux, may be derived. Specifically

$$\nabla \cdot \mathbf{J} = -\partial_t q \quad (1.8)$$

A relationship for the relaxation time for decaying currents in a uniform conducting media is found via Equations (1.7) and (1.5):

$$\partial_t q + \frac{\sigma}{\epsilon} q = 0 \quad (1.9)$$

with solution

$$q = q_0 e^{-(\sigma/\epsilon)t} \quad (1.10)$$

The equation gives the density of charge at any instance of time where q_0 is equal to the charge density at time $t = 0$. The initial charge distribution decays exponentially and independent of the applied field. The relaxation time, defined by ϵ/σ , required for the charge at any point to decay to $1/e$ of its original value, is for homogeneous earth materials of conductivity 10^{-4} S/m less than 10^{-6} s (Stratton, 1941, p.15). Unless frequencies occur with $\omega \geq \sigma/\epsilon$, i.e. frequencies far in excess of optical frequencies, free charges in homogeneous media may be neglected. Hence

$$\begin{aligned} \nabla \cdot \mathbf{J} &= 0 \\ \nabla \cdot \mathbf{D} &= 0 \end{aligned} \quad (1.11)$$

Wave equations

Maxwell's equations are partial, linear, coupled differential equations of the first order. They may be decoupled by making use of vector identities together with the simplified constitutive equations for neutral media, resulting in the wave equations. The wave equations are decoupled differential equations of the second kind for the electric and magnetic field. The wave equations follow by first taking the curl of Faraday's law and Ampère's law, and substituting each into the other. By making use of $\nabla \times \nabla \times \mathbf{V} = -\nabla^2 \mathbf{V}$ in a Cartesian coordinate system, where \mathbf{V} denotes one of the vector fields \mathbf{E} or \mathbf{H} , one obtains the time-domain wave equations, according to

$$\nabla^2 \mathbf{E} = \mu\sigma \partial_t \mathbf{E} + \mu\epsilon \partial_t^2 \mathbf{E} \quad (1.12)$$

$$\nabla^2 \mathbf{H} = \mu\sigma \partial_t \mathbf{H} + \mu\epsilon \partial_t^2 \mathbf{H} \quad (1.13)$$

Quasi-static approximation

For earth materials at frequencies less than 10^5 Hz, displacement currents can be neglected and the electromagnetic fields are assumed to be quasi-static (Ward and Hohmann, 1988, p.136). That is for distances which are small in relation to the wavelength of radiation from an antenna, the fields are everywhere almost in phase with the antenna circuit, this close-in region is identified as the quasi-static zone (Grant and West, 1965, p.470). Quasi-static therefore refers to the regime for which the finite speed of light can be neglected and fields are treated as if they propagate instantaneously. Inductively coupled TEM recordings generally take place in the quasi-static zone. Since charge does not disappear, Equations (1.11) hold for the interior, but not for the surface where σ and q are discontinuous and charges may accumulate.

Diffusion equations

Permittivity ϵ , permeability μ , conductivity σ and time determine the behaviour of the wave equation. With the exception of water, permittivities seldom vary more than an order of magnitude (Grant and West, 1965, p.469). The permeability is considered to be that of free air. The conductivity, however, varies over many orders of magnitude. Diffusive EM takes place in the quasi-static zone, so that displacement currents are much smaller than conduction currents. Hence, the wave equation (1.12) simplify to the Laplace equation in insulators and to the diffusion equation in conductors:

$$\nabla^2 \mathbf{E} = \mu\sigma \partial_t \mathbf{E} \quad (1.14)$$

$$\nabla^2 \mathbf{H} = \mu\sigma \partial_t \mathbf{H} \quad (1.15)$$

The diffusion equations imply that the resolution of EM methods will decrease with increasing distance from the source. The signals are highly dispersive and strongly attenuated in conductive media. Finding solutions for the diffusion equations is the fundamental objective for 3D transient electromagnetic modelling.

1.2.2 Concept of the TEM exploration method

The excitation for geophysical inductive EM methods is a time-varying primary magnetic field, which, according to the Maxwell equations, induces electrical currents in conductive surroundings (Figure 1.2a). The induced electrical and magnetic fields, recorded at receiver stations, are termed the secondary fields. In routine applications of the transient electromagnetic exploration technique, the ground is energised by means of a sharp turn-off of steady-state current in an insulated transmitter loop. During and after current turn-off, a time varying magnetic field is generated which in turn induces an electromotive force in the conducting surroundings according to Faraday's law. In a conductive earth, these electric fields generate currents as specified by Ohm's law (Figure 1.2b). These currents successively generate a secondary magnetic field as described by Ampère's law (Figure 1.2c). The transient secondary EM fields are subsequently recorded at a series of measurement times at designated recording stations. Recordings are obtained via coil receivers which measure the rate of change of the magnetic flux density cutting the coil ($\partial_t \mathbf{B}$), or via magnetometers which measure the magnetic flux directly (\mathbf{B}).

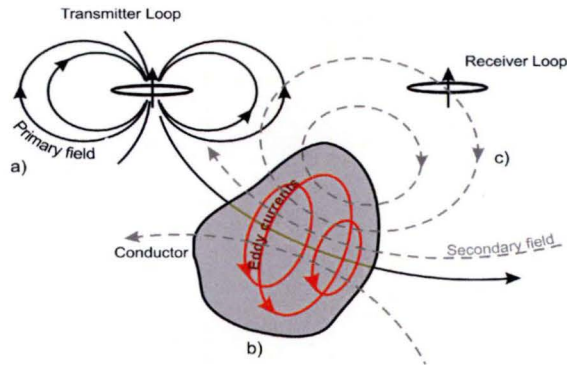


Figure 1.2 – Schematic illustration of inductive TEM exploration after Grant and West (1965, p.445).

Immediately after current shut-off in the transmitter loop, the inductive limit is encountered. In the inductive limit, the induced current is confined to the surface underneath the transmitter and is governed purely by geometry defined by transmitter, receiver and target. The ground responds (instantaneously) like a perfect conductor. At early times the induced current system in the subsurface primarily reflects the conductivity of the top layers. At later decay times the current has diffused deeper into the ground, and the measured signal then contains information about the conductivity of the deeper layers. Recordings of the secondary EM fields will therefore give information about the conductivity as a function of depth. As time passes by, the currents in the host propagate away and resistance in the subsurface weakens the induced currents, and eventually the current density dissipates due to these Ohmic losses.

Configuration principles

Ground TEM data acquisition employs either the moving-loop or fixed-loop survey geometry. In the fixed-loop geometry, a large transmitter loop is laid out on the surface of the earth, and remains in position for the duration of the TEM survey. For each transmitter setup, TEM measurements are made sequentially at a series of receiver positions along a survey line, usually oriented perpendicular to the loop. Loop sizes vary from several hundreds of meters to up a few kilometres and are positioned for maximum magnetic field coupling with prospective targets. Typically, rectangular transmitter loops are employed, with the long side oriented parallel to the expected strike of the target conductors. Although the moment-based modelling and inversion is not restricted to fixed-loop, for the course of this study all model calculations and field data examples are for the fixed-loop configuration. The fixed-loop configuration is shown in Figure 1.3a.

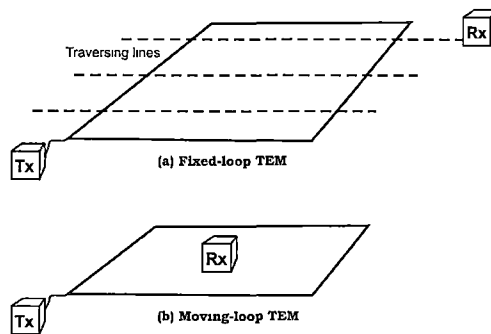


Figure 1.3 – Schematic of principal field layouts for ground-TEM survey types. The TEM source (Tx) consists of a fast turn-off, high current transmitter driving a large loop placed on the ground, where the transmitter loop dimension is dependent on the desired depth of investigation. Recordings are obtained at designated receiver stations (Rx) where measurements are obtained during the transmitter turn-off time. Two basic TEM configurations are illustrated: (a) Fixed-loop configuration where the receiver is moving along lines perpendicular to the long side of the loop. (b) Moving in-loop configuration where both, transmitter and receiver move together. In case of in-loop the receiver is centred in the transmitter loop.

Because the transmitter is stationary during the survey, appropriate placement of the loop is essential in order to ensure electromagnetic coupling between the primary magnetic field of the transmitter and buried conductors. Therefore, a good understanding of the prospective target is needed as for example acquired from other geophysical measurements. Large transmitter loops induce strong eddy currents in conductive near-surface weathered material, and interpretation of fixed-loop data from a single transmitter loop can be ambiguous in areas of irregular conductive overburden (Spies and Parker, 1984). Furthermore, good conductors located close to the transmitter loop can strongly suppress

the response of more distant targets. For these reasons, fixed-loop survey lines are typically remeasured using two transmitter positions; this ensures adequate energising of buried targets by the primary field of the transmitter, but increases the logistical cost of the technique.

In the moving-loop geometry, transmitter and receiver are moved simultaneously along a survey line, and a single TEM measurement is made for each transmitter setup. The logistical difficulties involved with moving large transmitters mean that loop sizes for the moving-loop method are typically restricted to 100-200 m. This limits the depth of investigation, and moving-loop surveys are generally used for reconnaissance. Because the transmitter is moved regularly during the survey, electromagnetic coupling with buried conductors is guaranteed, regardless of their orientation. A drawback of the moving-loop technique is that spatial sampling of the anomalous response is typically much less dense than for the fixed-loop method; this may result in some ambiguity in interpretation. The moving in-loop configuration is shown in Figure 1.3b.

Ground TEM transmitter systems customarily employ approximate square bipolar transmitter waveforms as illustrated in Figure 1.4. In case of $\partial_t \mathbf{B}$ measurements the earth's impulse response is recorded, and in case of \mathbf{B} measurements, the earth's step response is recorded. Formally, the impulse response $\mathbf{I}(t)$ can be posed as the time derivative of the step response $\mathbf{S}(t)$ with

$$\mathbf{I}(t) = \frac{\partial}{\partial t} \mathbf{S}(t) = -(\delta(t) \mathbf{H}(t) + u(t) \frac{\partial}{\partial t} \mathbf{H}(t)) \quad (1.16)$$

where the sign is conveniently chosen. $\delta(t)$ is the Dirac delta function with units $1/s$, $u(t)$ is the dimensionless Heaviside function and $\mathbf{H}(t)$ is the magnetic field decay associated with the decay of the induced current systems in the ground with units A/m . Limiting values are $\mathbf{H}(0)$, which corresponds to the inductive limit, and $\mathbf{H}(\infty) = 0$. The magnetic flux density \mathbf{B} is related to \mathbf{H} via the constitutive relation, Equation (1.6).

The use of a repetitive transmitter waveform allows readings to be stacked, with a resulting improvement in signal-to-noise ratio. The data sets are recorded in decay-time windows which are arranged with a logarithmically increasing width to improve the signal-to-noise ratio particularly at late-times. The transmitter and hence the primary magnetic field alternates for each single current step-off and a typical sounding consists of several hundreds repeated transients. Stacking reduces the noise proportional to $1/\sqrt{N}$ where N is the number of measurements in the stack.

Typical time delays monitored on the decay waveform vary from tens of microseconds to hundreds of milliseconds for mining applications and for shallow engineering applications time windows can vary from fraction of microseconds to about ten milliseconds. All synthetic and field data examples in the present work are for channel delay times consistent with the SMARTEM-V receiver (Duncan et al., 1998). The SMARTEM-V channel centre times for 42 channels range from 0.1 ms to 710.31 ms and are displayed in Table 1.2. The transmitter parameters such as ramp turn-on and turn-off for ground-based systems vary widely.

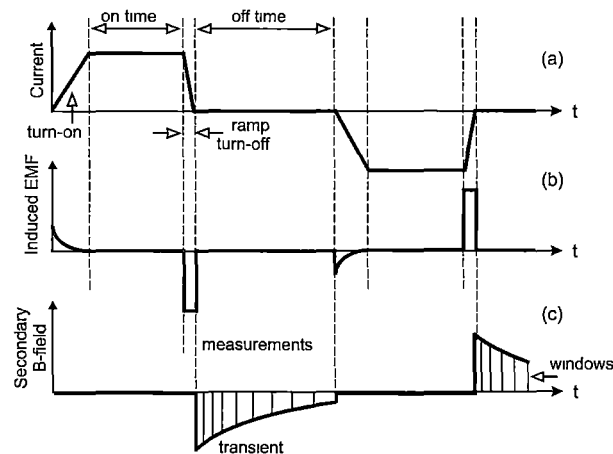


Figure 1.4 – Typical approximate square bipolar transmitter waveform and transients recorded at the centre of the transmitter loop. Panel (a) shows the current in the transmitter loop; the induced electromotive force is depicted in panel (b) and the generated secondary magnetic field transient in the off-time is shown in panel (c).

Channel	Delay	Width	Channel	Delay	Width
1	0.100	0.020	22	9.390	2.340
2	0.125	0.030	23	11.660	2.920
3	0.150	0.040	24	14.470	3.620
4	0.195	0.050	25	17.965	4.490
5	0.240	0.060	26	22.310	5.580
6	0.295	0.070	27	27.695	6.930
7	0.365	0.090	28	34.380	8.600
8	0.455	0.110	29	42.685	10.670
9	0.560	0.140	30	52.990	13.240
10	0.700	0.180	31	65.785	16.450
11	0.870	0.220	32	81.670	20.420
12	1.075	0.270	33	101.395	25.350
13	1.340	0.340	34	125.875	31.470
14	1.665	0.410	35	156.275	39.070
15	2.065	0.510	36	194.010	48.500
16	2.565	0.650	37	240.855	60.210
17	3.185	0.790	38	299.015	74.750
18	3.955	0.990	39	371.220	92.800
19	4.905	1.230	40	460.860	115.220
20	6.090	1.520	41	572.150	143.040
21	7.565	1.890	42	710.310	177.580

Table 1.2 – Channel delay times for the SMARTEM-V instrument for 42 channels from 0.1 ms to 710.31.

TEM response over a conducting half space

The solutions for a vertical magnetic dipole source on a homogeneous half space provides an understanding of the basic principles of TEM soundings. A vertical magnetic dipole transmitter is realised by a small horizontal loop source carrying a dipole moment m . After instantaneous step-current shut-off of the dipole source, azimuthal induction currents are induced which circulate around the dipole axis.

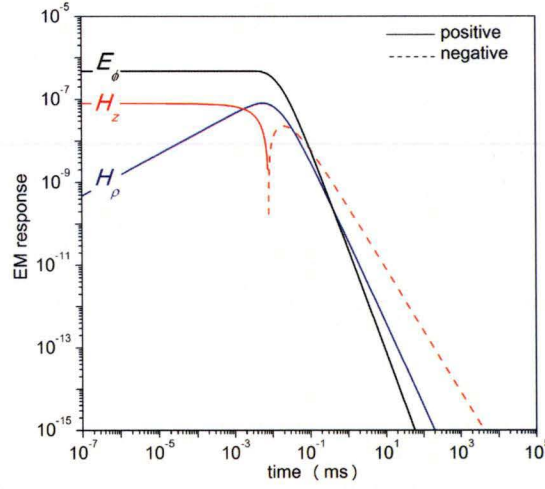


Figure 1.5 – TEM decay responses for a homogeneous half space excited by a vertical magnetic dipole placed on the ground. The half space has a conductivity of 0.01 S/m and recordings are obtained for $r = 100$. Because of the logarithmic scale, the sign change in the vertical component H_z will manifest as a jump in the data. Shown are the decays for E_ϕ in V/m, H_z and H_ρ in A/m as calculated using Equations (1.17), (1.18) and (1.19) with unit source dipole moment.

Mathematically, the secondary electric field on the ground surface is (Ward and Hohmann, 1988, p.214):

$$E_\phi(t, r) = -\frac{m}{2\pi\sigma r^4} \left(3\operatorname{erf}(\gamma r) - \frac{2}{\sqrt{\pi}}\gamma r (3 + 2\gamma^2 r^2) e^{-\gamma^2 r^2} \right) \quad (1.17)$$

where

$$\gamma = \sqrt{\frac{\mu\sigma}{4t}} \quad \text{with units } 1/m \text{ and for times } t > 0$$

The vertical component of the secondary magnetic field on the surface is given by (Ward and Hohmann, 1988, p.215):

$$H_z(t, r) = \frac{m}{4\pi r^3} \left(\left(\frac{9}{2\gamma^2 r^2} - 1 \right) \operatorname{erf}(\gamma r) - \frac{e^{-\gamma^2 r^2}}{\sqrt{\pi}} \left(\frac{9}{\gamma r} + 4\gamma r \right) \right) \quad (1.18)$$

The accompanying horizontal component is (Ward and Hohmann, 1988, p.216):

$$H_{\rho}(t, r) = -\frac{m}{4\pi r^3} \left(I_1 \left(\frac{\gamma^2 r^2}{2} \right) - I_2 \left(\frac{\gamma^2 r^2}{2} \right) \right) e^{-\gamma^2 r^2/2} \quad (1.19)$$

where t denotes the time, r the horizontal transmitter-receiver distance, where $\text{erf}(\cdot)$ denotes the Error function, $I_1(\cdot)$, $I_2(\cdot)$ are modified Bessel functions of the first kind of order 1 and 2 respectively.

Figure 1.5 shows the decay response profiles for each component as calculated with Equations (1.17), (1.18) and (1.19) for a unit source dipole moment. Upon transmitter shut-off, a circular current is induced below the transmitter source, which, according to Lenz's law, is distributed in such a way as to maintain the magnetic field at the value that existed before shut-off. The initial current distribution then starts to diffuse and decays into the subsurface. As the (physical) current system diffuses and decays it moves outward and downward which has been described by Nabighian (1979) as a system of 'smoke rings' blown by the transmitter loop (Figure 1.6).

Nabighian (1979) showed that the transient EM field observed over a conducting half space can be represented by a simple current filament of the same shape as the transmitter loop, moving downward and outward with a decreasing velocity and diminishing amplitude. The current filament is a mathematical abstraction which replicates the magnetic field on the surface. When the 'smoke ring' passes below the observation point, the vertical magnetic field changes sign and the horizontal field is maximal. Neither the electric field, nor the horizontal component changes sign. The zero-crossover of the vertical component migrates outward with time.

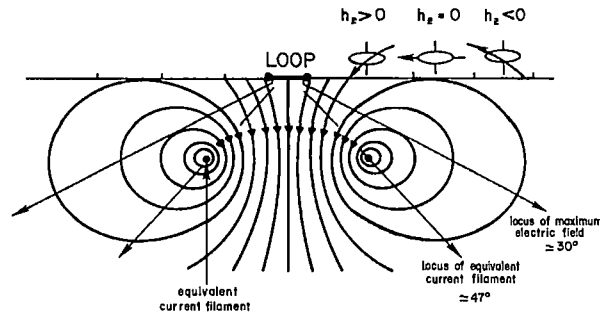


Figure 1.6 – Current diffusion and equivalent current filament concept from Nabighian and Macnae (1991, p.435). This diagram traces field lines of magnetic flux, thus the current filament is associated with maximum magnetic field (located at the $|B|_{max}$ depth). The depth of the maximum physical current, $|E|_{max}$, is shallower. The vertical magnetic field changes sign near the time that the current maximum passes beneath the observation point. The magnetic field can be represented approximately as due to an expanding circular line of current. The downward movement of the current filament occurs at about 47° , whereas the actual induced currents maximum moves with about 30° .

1D imaging concepts of TEM data based on the current diffusion in a homogeneous half space can utilise the equivalent current filament or the physical current system. The physical current maximum, $|\mathbf{E}|_{max}$, travels down into a half space along a straight line path at an angle of approximately 30° , whereas the image current filament travels in a similar manner but more steeply at about 47° . This is so because the equivalent current filament which has an infinite current density must always be deeper than the maximum of the actual distributed current system (Fullagar, 2008b). The consequence of this is that depth conversion methods based on image currents will inherently overestimate penetration depths. The depth conversion method used in this thesis (Chapter 4) pertains to physical currents.

The decay curves in Figure 1.5 show that at late times the vertical magnetic field component decays more slowly than the horizontal magnetic field component. During the late stage the TEM response decay follows a power-law and is characterised by a relatively high sensitivity to changes in conductivity of the medium. The late-time asymptotic forms for the field components are given by (Kaufman and Keller, 1983, p.334):

$$E_\phi \approx -\frac{m r \mu_0}{40} \left(\frac{\mu_0 \sigma}{\pi}\right)^{3/2} \frac{1}{t^{5/2}} \quad (1.20)$$

$$H_z \approx \frac{m}{30} \left(\frac{\mu_0 \sigma}{\pi}\right)^{3/2} \frac{1}{t^{3/2}} \quad (1.21)$$

$$H_\rho \approx -\frac{m r}{128\pi} (\mu_0 \sigma)^2 \frac{1}{t^2} \quad (1.22)$$

The vertical magnetic field component at the late stage of the response is independent of source-receiver separation. The late-time asymptotes plot as a straight line on log-log decay plots as in Figure 1.5.

TEM response of confined conductors in free space

The time-domain response of a simple loop-circuit can be expressed as an exponential function (e.g. Nabighian and Macnae, 1991, p.429). Correspondingly, the step response of any confined conductor can be expressed as a sum of exponentials where each term in the sum corresponds to the response of a simple loop-circuit inside the conductor (Kaufman, 1978):

$$H^s(t) = \sum_{k=1}^{\infty} G_k e^{-t/\tau_k} \quad (1.23)$$

where G_k contains the geometrical relationship between the k -th loop and the receiver. Each term of the sum in Equation (1.23) corresponds to a non-interacting 'eigencurrent' with a geometrical coupling factor G_k and a time constant τ_k (West and Macnae, 1991, p.929). The term 'eigencurrent' refers

to the solution of the homogeneous differential equations for the fields in a given conductivity distribution. Each 'eigencurrent' independently satisfies the differential equations (Dyck, 1991, p.929). The time constant is defined as the rise time, characterising the conductor's response and is related to the conductivity and the size of the conductor. At the late stage of the decay of the currents, the behaviour of the field is described only by one exponent and one time constant.

Inductive and galvanic coupling

The previous section considered inductive coupling for confined conductors in free-space. However, for a confined conductor buried in a conductive host, time-varying electromagnetic excitation gives rise to two modes of current flow. Inductive vortex currents flow in the target according to Faraday's law (Figure 1.7a) whereas, when currents induced in the conductive host are diverted into the conductive target, the current is deemed 'galvanic' (Figure 1.7b). Inductive currents will be distributed in such a manner as to cancel the primary magnetic field. Likewise, galvanic currents tend to cancel most of the primary electrical field inside the conducting target (McNeill et al., 1984; Nabighian and Macnae, 1991, p 443). Galvanic currents result from charge accumulations which arise on the surface of a target conductor embedded in a conductive host medium. The decay of those accumulations is a galvanic current flow.

The continuity equation in a source free medium, together with Gauss's Law (Equation 1.1) and the constitutive relations (Equations 1.5 and 1.7), provide insight into the phenomena, viz.:

$$\begin{aligned}\nabla \cdot \mathbf{J} = 0 &\Rightarrow \nabla \cdot (\sigma \mathbf{E}) = 0 \\ \nabla \cdot \mathbf{D} = q &\Rightarrow \nabla \cdot \mathbf{E} = \frac{q}{\epsilon}\end{aligned}$$

The above equations are valid if $\nabla \epsilon = 0$. Applying the product rule of differentiation to $\nabla \cdot (\sigma \mathbf{E})$ and combining the resulting equations, yields (Nabighian and Macnae, 1991, p.442)

$$q = -\epsilon \mathbf{E} \cdot \nabla (\log \sigma) \quad (1.24)$$

According to this result, electrical charges appear whenever there is a non-vanishing gradient of conductivity and the electric field has a component parallel to it. The strength of the galvanic currents is governed predominantly by the host conductivity at the target's location. However, conductivity-contrast with respect to host, the location of the transmitter with respect to the conductor and conductor dimensions are all effects which contribute to galvanic coupling (Spies and Parker, 1984).

Reid and Macnae (2000) investigated galvanic current flow in the case for airborne EM. Two cases where galvanic currents can dominate the inductive vortex currents are identified:

- at early delay times for all transmitter offsets, and
- at late delay times when the transmitter is distant from the target.

Early time galvanic current flow is most pronounced for targets of large strike extent and low conductance. Walker and West (1992) identify these targets as galvanically undersaturated enabling them to channel all the host current flowing close to the target. Additionally, the low conductance of such targets implies that they are unable to support a strong vortex current system, and their response is thus due almost entirely to current channelling.

Moderate to strong conductors, however, give rise to a strong vortex response at late times, even when they are embedded in quite conductive host rocks (Reid and Macnae, 2000). With a focus on late-time and deep conductive targets, galvanic coupling is considered of minor importance for the TEM moments modelling approach in most practical cases. Throughout this study galvanic currents will be disregarded.

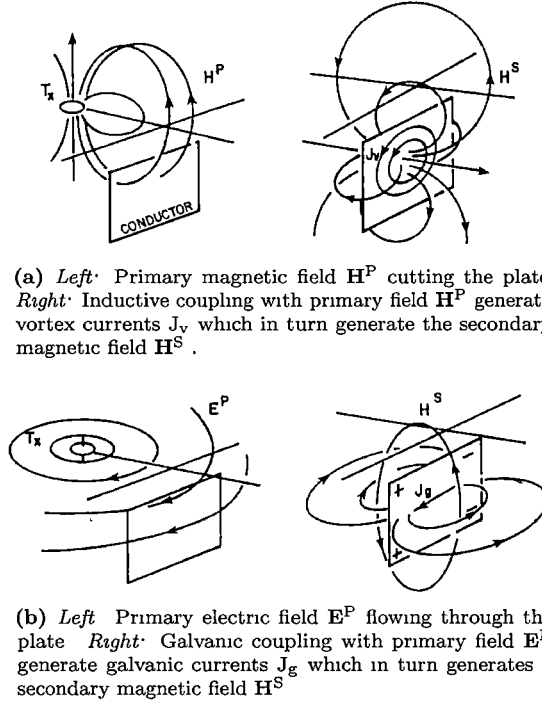


Figure 1.7 – Inductive and galvanic coupling for a plate example (from Nabighian and Macnae, 1991, p.445). The upper panel (a) shows inductive coupling with the primary magnetic field generated by the transmitter, whereas the lower panel shows galvanic coupling with the primary electric field of the transmitter.

Inductive and resistive limit

Generally, an EM response is circumscribed by two limiting extremes referred to as inductive and resistive limit. The limiting extreme for very early times is known as the inductive limit, and the resistive limit is encountered at late times. From a physical point of view, the inductive limit reflects the state of the magnetic field during the transmitter on-time. After turn-off, the magnetic field decays as a consequence of the attenuation of secondary currents which will initially be distributed in such a manner as to maintain the magnetic field everywhere at the value that existed before turn-off. At the inductive limit, the response is independent of ground conductivity and is a function of geometry only (King and Macnae, 2001).

The resistive limit of a confined conductor characterises the magnetic field of the steady state current, flowing in the conductor after the secondary currents have fully penetrated the body. In the resistive limit, the rate of change of the electromagnetic field is sufficiently slow that eddy current self-interaction is negligible. The electromagnetic response varies linearly with conductivity and is additive for bodies that are not in contact (Macnae et al., 1999). Conductive bodies in contact with each other are not additive in the resistive limit, due to charge accumulations at the conductor interfaces, giving rise to galvanic current flow (Reid and Macnae, 2002).

Based on the results of Kaufman (1978), Stolz and Macnae (1997) use the limiting values of the sum of exponentials (Equation 1.23) to model the approximate response of 3D conductors. The limiting values of the inductive limit (IL) and the resistive limit (RL) for confined conductors, evaluate as (King, 1997, p.27):

$$IL = \sum_k G_k \quad (1.25)$$

$$RL = \sum_k G_k \tau_k \quad (1.26)$$

where equation (1.25) corresponds to the inductive limit which is independent of the time constant of the conductor. Equation (1.26) defines the resistive limit which is linearly related to the time constant of the conductor and bears resemblance to the modelling approach taken in the current thesis.

1.2.3 Brief review of transient electromagnetics

1D-EM inversion

Automated routine interpretation of TEM data is mostly based on one dimensional (1D) earth models. 1D interpretation schemes resolve the subsurface conductivity from measured TEM earth responses into a 1D earth parametrisation of one, or more layers, of contrasting conductivity distributed with depth. In rigorous 1D inversion schemes, layered earth models are sought that minimise a specific measure of misfit between model and measured data and which meaningfully describe the observations either as smooth minimum structure models or as

models with sharp boundaries (e.g. Backus and Gilbert, 1967; Jackson, 1972; Jupp and Vozoff, 1975; Lines and Treitel, 1984; Huang and Palacky, 1991; Treitel and Lines, 2001).

Fullagar and Oldenburg (1984) solved the inverse least-squares problem in the frequency domain for circular loop sources. They used many more layers than observations and thus solve an under-determined inverse problem. Layers in the starting model could be sub-divided during the course of inversion. However, for incomplete and noisy data the mathematical solution is non-unique and a number of models fits the data equally well. Fullagar and Oldenburg (1984) therefore used an averaging function during model appraisal which results in a smooth model that contains only as much structure as required to fit the data.

The inversion for simple models is also known as the Occam scheme in which the smoothest model is sought, so that its features depart from the simplest case only as far as is necessary to fit the data (Constable et al., 1987). The smoothest model is found by minimising a non-linear least-squares function simultaneously to the roughness of the model, which is defined as the integrated square of the first or second derivative with respect to depth.

An over-determined least-squares problem typically allows the variation of both conductivity and thickness of a very limited number of layers. The over-determined approach may be more adequate to incorporate a priori information that may indicate a rich model structure with sharp defined layer boundaries (Commer, 2003).

Auken et al. (2004, 2005) present an interpretation approach for laterally constrained 1D inversion of 3D TEM data, where neighbouring models are constrained laterally on layer resistivities and interfaces and therefore effectively solves a 2D TEM inverse problem. Related to the approach of Auken et al., is the approach by Scholl et al. (2009) who developed a 1D joint inversion algorithm for interpreting multi-component TEM data using independent smooth models for collocated TEM data sets to invert data acquired over 3D geology.

Approximate 1D-EM imaging

Approximate 1D methods, based on a half space or a thin sheet assumption provide a rapid, first-pass interpretation of electromagnetic data, and are very widely used within the mineral exploration industry (e.g. Eaton and Hohmann, 1989; Fullagar, 1989; Smith et al., 1994; Reid and Fullagar, 1998; Christensen, 1997). Routinely employed are conductivity-depth imaging (CDI) techniques, however 1D-EM inversion is becoming increasingly common.

Conductivity-depth imaging is based on the diffusion rate of the induced current system into a homogeneous half space, allowing mappings of apparent conductivity vs depth (e.g. Raiche and Gallagher, 1985; Macnae and Lamontagne, 1987). Existing 1D conductivity-depth transformations for TEM data are designed for traditional survey geometries, such as moving-loop and fixed-loop, where data are acquired at one or more receivers using a single transmitter loop. Although these transformations are very rapid, estimation of a unique conductivity can be difficult, particularly for geometries where the receiver is located outside

the transmitter loop (e.g. Reid and Fullagar, 1998). As described in Chapter 4, Schaa et al. (2006) used magnetic field amplitudes from multi-component measurements to overcome ambiguity in apparent conductivity calculations for fixed-loop survey geometries.

Conductivity-depth imaging is complementary to rigorous inversion schemes as it may serve as an initial processing step to provide a starting model for rigorous inversion. Interpretation based on CDIs may be less biased by three dimensional (3D) effects than rigorous 1D inversion which parametrises the earth into a finite number of layers (Spies and Frischknecht, 1991, p.373). However, like 1D inversion, 1D-CDI techniques can contain artifacts when applied to data arising from 3D-TEM geology (Newman et al., 1987; Stolz et al., 1995; Scholl, 2005). Processing of TEM earth responses from complex geological settings are in general not readily amenable to rigorous or approximate 1D-TEM interpretation techniques. Therefore 3D solutions for TEM data interpretations from complex geology are essential.

3D-EM modelling

3D-TEM data interpretation is often tackled by manual trial-and-error 3D forward modelling schemes. Analytical solutions of the forward TEM problem can only be given for a small class of symmetrical and simple structures, like spheres and cylinders in free-space where conductivity boundaries correspond to constant-coordinate surfaces (Hohmann, 1988). Publications for a conductive and permeable sphere in free space in the time- and frequency-domain for a variety of sources are numerous (e.g. Debye, 1909; Wait, 1951; March, 1953; Wait, 1953, 1960; Lodha and West, 1976; Nabighian, 1970).

The problem of a sphere in a conducting full space for magnetic dipole excitation has been treated by Singh (1973), who gives an asymptotic solution which accounts for host-sphere EM interaction. A conductive sphere embedded in a layered half space has been solved in the time-domain by Lee (1974, 1980) for a coincident loop excitation. He used the Galerkin method to solve the integral equation numerically. Based on Lee's work, a semi-analytical solution was devised for a conductive and polarisable sphere in a conductive half space for a coincident loop system which separated terms for sphere response, half space response and interaction response (Lee, 1983; Lee and Thomas, 1992).

Among exact numerical solutions, the thin plate model has attracted significant use in 3D-EM modelling. Lamontagne and West (1971) solve the thin plate problem in free space for a Turam system which is a frequency-domain fixed-loop technique. Annan (1974) devised a numerical method for determining the EM response of a thin plate in free space for any type of EM source in the frequency or time domain. Of importance in understanding 3D-EM responses is the plate model in a conductive layered host which has been introduced by Lajoie and West (1976) for a Turam system. The free-space time-domain solution for a thin infinite plate, or half-plane, for dipole or circular loop excitation, was provided by Weidelt (1983). The frequency-domain EM response of a thin vertical tabular conductor situated in a two-layer earth was obtained by solving the electric field

integral equation numerically by Hanneson and West (1984). Hanneson (1992) also provided a time-domain solution for the EM response of a dipping plate in a conductive half space for the UTEM system. Walker and West (1991) devised an integral equation solution for a thin plate in a conductive host which can be used to model scattering over large ranges of conductivity.

Realistic geological 3D structures, with inclusion of topography and faults, are subject to finite differences and finite elements schemes, solving the underlying difference equations within a 3D grid (e.g. Wang and Hohmann, 1993; Druskin and Knizhnerman, 1994; Newman and Alumbaugh, 1997; Commer and Newman, 2004; Sugeng et al., 2006). However, due to the demand of discretising the entire model on a grid, the requirements for storage can easily overwhelm the computational facilities currently available.

The volume integral approach introduced by Raiche (1974); Hohmann (1975); Weidelt (1975) solved the prototype for localised regions of anomalous conductivity in an otherwise homogeneous background. Zhdanov et al. (2006) devised a 3D-TEM formulation of the integral equation method for complex structures with inhomogeneous background conductivity. The main advantage of the integral equation method is that only the scattering volume is subject to discretisation thus reducing the scale of the problem. The technique's main weakness is its restriction to low conductivity contrasts. However solutions for high conductivity contrasts with the integral equation technique have been reported recently (Farquharson and Oldenburg, 2002; Farquharson et al., 2006). Likewise Zhdanov et al. (2007) introduced an integral equation method for large conductivity contrast, based on the equations for 'integral currents', instead of the fields, where the 'integral currents' are obtained by integrating the current density over each cell.

Based on the various exact forward modelling schemes, Australia's Commonwealth Scientific and Industrial Research Organisation (CSIRO) developed geophysical software suites for EM data interpretation for the minerals exploration industry. From 2010, the Fortran 90 source code for all programs will be open source (Raiche et al., 2007). A comprehensive overview of recent rigorous 3D forward modelling techniques can be found in Avdeev (2005).

Approximate 3D-EM modelling

Approximations to the rigorous modelling schemes involve simplifications to the exact approaches described above. Commonly employed in the integral equation techniques are simplifications where the unknown total field is replaced by some kind of approximation, giving a problem of the Born type (e.g. Habashy et al., 1993; Zhdanov and Fang, 1999; Tseng et al., 2003). Born type solutions are usually restricted to low-contrast conductivity problems, but Torres-Verdin and Habashy (1994) presented a high-contrast 2.5D-EM modelling solution based on an extended Born approximation.

Approximations to the thin-plate models are attained via simple free-space loop circuits or current filaments residing in the plane of the plate (Barnett, 1984; Duncan, 1987; Lamontagne et al., 1988) which find wide use in 3D-EM modelling and inversion. McNeill et al. (1984) derive a fast, approximate transient EM

solution for a thin conductive plate buried in a conducting half-space energised by a large loop. The vortex and galvanic components are calculated in the time-domain with a single-turn wire loop and a distribution of current dipoles, respectively, disregarding EM coupling. Likewise, Liu and Asten (1993) derive approximate time-domain solutions for a thin-plate in a resistive host overlain by a thin conductive overburden. They include the EM coupling between overburden and plate in an approximate fashion by convolving the overburden-delayed driving field with a wire-loop response

Based on Liu and Asten (1993), Sattel and Reid (2001) devise an automated interpretation routine for time-domain AEM data where EM anomalies are modelled by magnetic dipoles superposed on a layered earth response which serves as a background response. The method is extended by Sattel and Reid (2006) to account for galvanic current flow which is modelled by electric dipoles. A frequency-domain solution is published by Bourgeois et al. (2000), which also employs magnetic and electric dipoles in a conductive background as an approximate model of the EM response of an anomalous volume.

3D-EM inversion

A full EM solution of the 3D inversion problem, based on volume integral equations in the frequency-domain, was provided by Eaton (1989). Wang et al. (1994) provided a solution for the 3D-EM inversion problem directly in the time-domain utilising imaging methods originally developed for seismic wave fields. Haber et al. (2007) solve the forward problem using finite volume methods in the spatial domain and a backward Euler method in the time domain. A modified Gauss-Newton strategy is employed to solve the inverse problem. A field data example, defined on a mesh-volume containing 394,440 cells took 19 days on a single Opteron 244 processor.

In the context of marine controlled source EM, a frequency-domain solution is presented by Commer and Newman (2007) who employ a non-linear conjugate gradient algorithm as their framework of the inversion scheme in a parallel computation approach. A synthetic example which involves 2,406,104 cells for three frequencies is computed on 144 processors and takes about two days.

A hybrid frequency-domain method for fast 3D-EM inversion is proposed by Cox and Zhdanov (2008) who combine a quasi linear approach, analogous to the Born approximation, with a rigorous inversion scheme. A field data example, consisting of about 300,000 cells, took about 9 hours for three frequencies on a 2.4 GHz AMD-64 processor. The review on exact EM methods by Avdeev (2005) lists further achievements in stringent 3D-EM inversion.

Approximate 3D-EM inversion

Approximate vehicles for 3D-EM inversion schemes are based in their majority on the forward modelling devices of the Born type (e.g. Zhdanov and Hursan, 2000; Torres-Verdin and Habashy, 1994). Christensen (1997) and Wolfgram et al. (2003) have described rapid quasi-2D transformations for surface and airborne

EM data. Ellis (1995) compares various exact and approximate 3D-EM modelling and inversion schemes together with 1D methods for the simulation of AEM data over a 3D conductivity earth model.

Zhdanov et al. (2002) devised a conductivity-depth transformation based on a thin-sheet model, which accounts approximately for the effect of small 3D conductive inhomogeneities on the TEM response. A number of other transformations have also been developed for electromagnetic data, based on concepts from seismic data processing (Lee and Xie, 1993; Zhdanov et al., 1996).

Farquharson and Oldenburg (1999) used approximate model sensitivities to obtain a linearised inversion scheme in order to handle larger data sets. A spatially constrained inversion, analogous to the solution of Auken et al. (2005) described earlier in the 1D inversion section, that produces quasi-3D conductivity modelling of electromagnetic EM data using a 1D forward solution is presented by Viezzoli et al. (2008, 2009). The constraints are built using Delaunay triangulation, which ensures automatic adaptation to data density variations. The method produces laterally smooth results with sharp layer boundaries that respect the 3D geological variations of sedimentary settings. In a different approach, however related to the method of Auken et al. (2005) and Viezzoli et al. (2008), is the holistic inversion approach of Brodie and Malcolm (2006) for simultaneously calibrating, processing, and inverting frequency-domain AEM data. A spline-based layered conductivity model varies laterally in each layer to retrieve a pseudo 3D structure.

The limiting EM responses, the inductive and resistive limit, are utilised for fast 3D-EM inversion of airborne data (King, 1997; Stolz and Macnae, 1997). In a separate development, Smith and Lee (2002b) have described a moment decomposition for transient electromagnetic data, which is deployed for this thesis for rapid multidimensional inversion.

3D potential field inversion

Generally, for potential field interpretation, an inversion method must introduce particular constraints, in order to reduce the number of possible solutions (Silva et al., 2001). The potential field inverse problem is non-unique because the information content in potential field data is generally insufficient to determine the size and shape of causative bodies unambiguously (Grant and West, 1965, p.210). Mathematically, it follows from Green's third theorem that a potential field can be reproduced by an arbitrarily thin source layer ('equivalent stratum'). The source layer can lie just below the observational surface, which implies that potential field data do not have intrinsic depth resolution.

Due to its simplicity and speed, the 3D potential field inversion problem is often tackled using a parametric approach which solves for the parameters of simple geometric bodies, for instance prisms or spheres with homogeneous source distribution (Grant and West, 1965; Bhattacharyya, 1980; Wang and Hansen, 1990; Zeyen and Pous, 1991). Single or multi-body parametrisation is used to model discrete changes in the properties of the subsurface and usually is an over-determined problem (Oldenburg and Pratt, 2007). Fedi et al. (2005) notes that assumption of parametric bodies leads to inversion solutions with good depth resolution.

Nonparametric methods provide a more comprehensive framework for inversion of potential field data where a general 3D physical property model of the subsurface is sought. Pure property inversion schemes most commonly adopt a uniform 3D-mesh and results usually in an under-determined problem (Fedi et al., 2005; Oldenburg and Pratt, 2007). Non-uniqueness is tackled by including constraints such as property bounds and weights (e.g. Li and Oldenburg, 1996, Silva et al., 2001).

Portniaguine and Zhdanov (2002) developed a method for 3D magnetic inversion to produce sharp images using a standard regularisation approach. The objective function consists of a misfit functional and a stabilising functional which helps generate a focused image of the subsurface. A sensitivity-based weighting scheme is applied furthermore to introduce corrections for the source distribution. The algorithm is part of the GRMAG3D package of the University of Utah Consortium for Electromagnetic Modeling and Inversion

In order to produce recovered models with sharp boundaries van Zon and Roy-Chowdhury (2006) used linear programming (LP) techniques to minimise the absolute residuals (ℓ_1 -norm). Mathematical constraints are defined implicitly via the LP formulation of the inverse problem as linear inequalities in the variables.

The University of British Columbia (UBC) Geophysical Inversion Facility (GIF) has developed 3D inversion codes for potential fields which have become de-facto industry standards (McMonnies and Gerrie, 2007). Voxel parametrisation of geology has provided the basis for the 'UBC-GIF' inversion scheme, in which the rock properties associated with each voxel act as the parameters to be optimised (Jessell, 2001). For the 'UBC-GIF' inversion scheme, geological information is accommodated via a reference model in combination with weighting functions and property bounds (Li and Oldenburg, 1996, 1998). The 'UBC-GIF' reference model typifies the area of investigation and represents the best guess for the true distribution of the physical property. The regularisation imposed by the 'UBC-GIF' inversion approach seeks a model that is smooth and deviates as little as possible from the reference model (Williams, 2008).

A different approach for potential field inversion is to use a lithologically described volume instead of voxel parametrisation alone. Lane and Guillen (2005) note that the use of 'litho-category' as the primary variable and property as the secondary variable has a natural appeal for geoscientists, because it eliminates the need for a post-inversion interpretation. The implementation of the inversion in Lane and Guillen (2005) utilises a Bayesian approach where a large number of models is generated. Both geometry and property of the litho-regions are varied during geostatistical inversion. The algorithm is part of the Intrepid Geophysics GeoModeller package (Guillen et al., 2004).

The potential field modelling and inversion framework VPmg (Fullagar et al., 2000, 2004; Fullagar and Pears, 2007; Fullagar et al., 2008) combines the various approaches of parametric, voxel parametrisation and lithological categorisation (Oldenburg and Pratt, 2007). VPmg minimises a chi-squared misfit function iteratively via a steepest descent method and incorporates 'soft' constraints such as weights and 'hard' constraints, based on petrophysical measurements. Bounds

are incorporated furthermore. In VPmg each voxel is associated with a rock type, facilitating therefore 'lithological' inversion. The VPmg framework is utilised in this thesis for inversion of TEM moments.

1.3 Approximate 3D inversion of TEM moments

The method combines the TEM moment concept with constrained potential field inversion techniques. The fast approximate 3D forward modelling scheme relies on linear superposition of TEM moments associated with sub-surface volumes. The predicted net TEM moment response of the ground is compared with the measured TEM moment response. Accumulation of TEM moment responses of magnetic dipoles, which exhibit linearity with respect to time constants, provide the basis for the approximate forward modelling approach. Rather than conductivity, the geoelectrical subsurface is delineated in terms of time constants.

The TEM moment transform is defined as a time-weighted integral of the TEM earth response. Parametrisation of both modelled and measured data is achieved by the TEM moment transform. For measurements during system off-time, where $t > 0$, the impulse response $\mathbf{I}(t)$ consists of the decaying part only with the delta function at zero time removed (Equation 1.16), the TEM moment transform, in vector notation, is then defined as (Smith and Lee, 2002b)

$$\mathbf{M}^{(n)} = \int_0^\infty \mathbf{I}(t) t^n dt \quad (n \geq 0) \quad (1.27)$$

where $\mathbf{M}^{(n)}$ is the TEM moment vector of order n with units of $\text{A} \cdot \text{s}^n / \text{m}$.

The TEM moment forward response of an anomalous volume is modelled as a discretised target 3D-response embedded in a continuous background. The background is represented as a homogeneous half space, while the target is comprised of point conductors, defined on a cubic 3D mesh. After excitation, each point conductor hosts a magnetic dipole with strength proportional to the product of local primary field, time constant and effective cell volume. Linear superposition of a dense network of point-conductors approximately reproduces the TEM moment response of a confined conductor if its time constant is assigned to each point-conductor.

The approximate 3D-TEM forward modelling algorithm implemented here, is based upon vortex currents only and ignores electromagnetic interaction between volume elements. Mutual interaction includes coupling via the magnetic field and coupling via the electric field. For the TEM moment modelling approach adopted in this thesis, negligence of electromagnetic interactions is considered a tolerable approximation. The current study exclusively makes use of the first order TEM moment ($n = 1$). The 1st TEM moment transform weights late-time responses and is equivalent to the resistive limit response (Smith and Lee, 2002b).

In effect, the transformation from multi-channel time-domain EM data into the moment-domain converts the 3D-TEM inversion problem into an approximate, linear 3D magnetic inversion problem. The relationship to the magnetostatic problem is illustrated in the following chapter. Depth resolution as provided

by the multi-channel TEM data is lost during the process of time-integration. Conductivity-depth imaging sections, which convert time to depth explicitly, may be used to generate starting models or constraints for inversion. Alternatively, depth control during inversion is based on a priori information which can be provided as geological constraints or weighting.

The potential field modelling and inversion framework VPMg is extended and modified so as to accommodate approximate 3D-TEM moment inversion. The new program can be described as a litho-inversion scheme where the model is both geological and petrophysical before, during, and after inversion, so that the lithological significance is preserved throughout the inversion process. For the TEM moment inversion scheme implemented during this project, the model space is comprised of a mesh of cubic cells where the geological setting is mapped onto the 3D mesh, i.e. a 3D analogy of a geological map so that each cell is assigned to a particular rock type, the model is therefore categorical (i.e. geology) as well as numerical (i.e. physical property).

To address the non-uniqueness of the potential field inverse problem and to limit the space of possible model solutions, inversion constraints are incorporated. If geological information is available, the inversion can incorporate the information as particular geological constraints to guide the solution towards one that is consistent with the geological knowledge.

Inversion constraints are accommodated via 'soft' constraints and 'hard' constraints (Fullagar and Pears, 2007). Property bounds designate the minimum and maximum property value allowed in each geological unit. The inversion can be restricted to a certain geological unit or combinations thereof. Soft constraints are implemented as inversion weights, either as 1D depth weights or as 3D conductivity weights. Depth weighting is a subjective, general device to counteract the geometrical decay of the potential field response in order to penalise shallow solutions. Conductivity weights are based on conductivity-depth imaging and are less subjective than depth weights and constitute a data-adaptive weighting scheme. Conductivity weights favour solutions close to the CDI models.

1.4 Thesis structure

Chapter 2 introduces the TEM moment transform. First the time-domain solution of a sphere in a dipolar and uniform field is derived. Following this, the TEM moment transform is employed to obtain the TEM moment response of a sphere. The TEM moment of a point conductor is derived. The TEM moment transform for a uniform conducting half space for a rectangular loop source is derived subsequently. All solutions are analytical and therefore very fast to evaluate numerically. The procedure for obtaining TEM moments from measured field data is delineated. For the course of this thesis, attention is restricted to the first order moment which is equivalent to the resistive limit response.

Chapter 3 presents the approximate 3D forward modelling scheme. The TEM moment response for arbitrarily shaped conductors is approximated as a combination of a continuous background response and a discrete target response,

neglecting volume interactions. The continuous background is modelled as a uniform conducting half space, whereas the discrete target is comprised as a linear combination of point conductors. The approximate forward modelling effectively calculates the TEM moment transform for arbitrarily shaped conductors by assumption of validity of superposition. The validity of neglecting the host rock EM interactions is addressed in a qualitative manner based on a semi-analytical formulation which separates terms describing sphere response, host response and interaction response. The TEM moment forward modelling is tested at two prism-models residing in a conductive host, calculated with rigorous 3D-EM.

Chapter 4 specifies the new 1D imaging technique which employs **B**-field amplitudes as obtained from multi-component TEM measurements. For the 3D inversion procedure, conductivity-depth sections serve as a preparatory process, either as initial values for cell time constants for the starting model or as a device to formulate weights assigned for inversion. Ambiguity, which is of concern when calculating apparent conductivities from single-component data for fixed-loop geometry, is not problematic when calculating apparent conductivities from multi-component **B**-field amplitudes. Unique derivation of apparent conductivity for fixed-loop geometry, based on **B**-field amplitudes, has been demonstrated during the course of this study.

Chapter 5 describes the linear potential field inversion of single-component TEM moments, utilising geological constraints. A fast steepest descent formulation, which does not require matrix inversion, is employed to recover the geoelectrical structure of the subsurface from measured TEM data. The linear inversion scheme requires computation of the initial model and associated derivatives only once, subsequent model updates are calculated via the derivatives. The TEM moment inversion methodology is tested at the response from two prism-models residing in a conductive host, calculated with rigorous 3D-EM.

Chapter 6 describes application of the fast approximate inversion scheme to measured field data acquired over a complex folded 3D target. 3D inversion of the fixed-loop field data is carried out with different starting models and constraints, so as to examine the variety of possible solutions due to non-uniqueness. Information from borehole logs assist in evaluation and plausibility of the inversion results. A conventional plate forward modelling solution is also included for comparison.

Chapter 7 presents a summary and conclusions based on previous chapters. Appendix A comments on possible further developments of the TEM moments approach.

Chapter 2

Methodology of the TEM moments approach

Introduction Parametrisation of both modelled and measured data to a minimal set of parameters has been used successfully for the interpretation of TEM data (Macnae et al., 1999; Stolz and Macnae, 1997; King, 1997). The limiting extremes at infinite and zero frequency, the inductive and resistive limit respectively, embody the essential characteristics of the transient induction process that usefully describe the data. The modelling of transient electromagnetic responses at the inductive and resistive limit is considered a suitable technique for mineral-type targets where conductivity contrasts are relatively high (Nabighian and Macnae, 2005). The inductive limit is a function of the target geometry, whereas the resistive limit displays a linear relationship with respect to the target conductivity. In the time domain, the value at zero-time for step response data is the inductive limit; the integral of the step response from zero to infinity equals the resistive limit (Lamontagne, 1975). The concept of modelling at the inductive and resistive limit has been generalised by Smith and Lee (2002b). They defined integrals of the impulse response, weighted by time raised to power n , as TEM moments. Zeroth order moment equals the inductive limit and the resistive limit is the first moment order. Higher order moments accentuate late-time and hence deeper conductive features, however late-time noise will be emphasised also. A number of publications on the subject of the moment transform of TEM data have been published by Richard Smith, Terry Lee and co-authors (2002b; 2002a; 2002c; 2005; 2006). Except for the work of Smith and Lee, and Hyde (2002), there are at this time no other publications on the use of TEM moments. However, substantial papers on modelling at the inductive and resistive limits have been published (e.g. Macnae et al., 1999; Stolz and Macnae, 1997; Reid and Macnae, 2002; King, 1997), which constitute instances of TEM moments, although until recently not identified as such.

The TEM moment of a compact body exhibits a linear relationship to its time-constant. The moment domain response for multiple targets in a resistive host is given by superposition of the responses of the individual targets. The main advantages of the TEM moments concept are the simplifications of related time-domain expressions and the processing of measured TEM data which both leads to simpler and faster processing algorithms. Eventually, parametrisation of both modelled and measured data in the moment domain, leads to a simple and very fast approximate 3D inversion scheme for interpretation of TEM data. From an interpretation perspective, use of TEM moments may facilitate detection of deep conductive features. From a computational perspective, complicated expressions of simple bodies in the time-domain, simplify in the moment domain (Hyde, 2005).

This chapter presents and explains the concept of the moment domain formulation. After introducing the definition of the TEM moment transform, emphasis is put on the derivation of the TEM moments of a sphere in a dipole and uniform field. Based on the TEM moment formulation for a sphere, the analytical TEM moment of a point-conductor is introduced. The point-conductor formulation forms the basis of the approximate 3D forward modelling scheme, described in Chapter 3. Furthermore, the TEM moments of a half space for rectangular loop excitation follows. The approximate 3D forward modelling scheme combines the TEM moment response of point-conductors and a homogeneous conducting half space. The analytical moment domain solutions provided for a half space, excited by a rectangular loop source, are derived from expressions related to the incomplete Gamma function, for the horizontal component, and to the Error function for the vertical component. Lastly, the TEM moment transform for measured data is introduced. This involves extrapolation of the measured data at early and late time using a half space model.

2.1 The TEM moment transformation

2.1.1 Moment transform definition

For measurements during system off-time, where time $t > 0$, the TEM moment transform, in vector notation, is defined as (Smith and Lee, 2002b):

$$\mathbf{M}^{(n)} = \int_0^\infty \mathbf{I}(t) t^n dt \quad (n \geq 0) \quad (2.1)$$

where $\mathbf{M}^{(n)}$ is the TEM moment vector of order n with units of $A \cdot s^n / m$. $\mathbf{I}(t)$ is the impulse response which consists of the decaying part only with the delta function at zero time removed (c.f. Equation 1.16). Mathematically, the order is not restricted to integer values; e.g. Lee et al. (2003) show the moment response of order $1/2$ for a half space with dipole excitation. Formally, the moments are undefined if the integrand does not converge on the integration interval. For example, the TEM moment transform of the impulse response for a half space due to a vertical magnetic dipole source does not strictly exist for orders $n \geq 2$ since the half space decay exhibits a $t^{-5/2}$ asymptotic behaviour (Smith et al., 2006). Mathematically, the TEM moment transform is equivalent to the Mellin transform.

2.1.2 Moments for the magnetic field and its derivative

Re-writing the defining moments integral, Equation(2.1), in terms of the magnetic field $\mathbf{H}(t)$ or its time derivative $\partial_t \mathbf{H}(t)$, assuming perfect step or impulse response and integrating by parts, the TEM moment transform is stated as:

for measurements of $\mathbf{H}(t)$ in A/m

$$\mathbf{M}^{(n)} = -n \int_0^\infty \mathbf{H}(t) \cdot t^{n-1} dt \quad n > 0 \quad (2.2)$$

for measurements of $\partial_t \mathbf{H}(t)$ in $A/(ms)$

$$\mathbf{M}^{(n)} = - \int_0^\infty \frac{\partial}{\partial t} \mathbf{H}(t) \cdot t^n dt \quad n \geq 0 \quad (2.3)$$

In this thesis, the definitions of the TEM moment in terms of the magnetic field (Equation 2.2) or its time derivative (Equation 2.3) are used. For realistic finite time ranges, the definitions given in Equations (2.2) and (2.3) are not equivalent.

2.1.3 Inductive and resistive limit as TEM moments

Inductive and resistive limits were previously introduced in Chapter 1.2.2 and have traditionally been defined in the frequency domain as the limiting values of the magnetic field response at infinite and zero frequency (Grant and West, 1965). The inductive limit is reached as the frequency is increased towards infinity whereas the resistive limit is defined as the limiting absolute value of the slope of the magnetic field response as the exciting frequency approaches zero. In terms of zeroth and first order TEM moments (Smith and Lee, 2002b) these are

$$\mathbf{M}^{(0)} = \lim_{\omega \rightarrow \infty} \mathbf{H}(\omega) \quad (2.4)$$

$$\mathbf{M}^{(1)} = \lim_{\omega \rightarrow 0} \partial_\omega |\mathbf{H}(\omega)| \quad (2.5)$$

For time-domain magnetic field measurements, the zeroth and first order TEM moments evaluate to

$$\mathbf{M}^{(0)} = - \int_0^\infty \partial_t \mathbf{H}(t) dt = \mathbf{H}(0) \quad (2.6)$$

$$\mathbf{M}^{(1)} = - \int_0^\infty t \partial_t \mathbf{H}(t) dt = \int_0^\infty \mathbf{H}(t) dt \quad (2.7)$$

The integration result in Equation (2.6) for the zeroth order moment constitutes the inductive limit whereas the first order moment in Equation (2.7) is the resistive limit.

2.2 Quasi-static time domain EM response of a sphere

In order to derive the moment-domain expression for a point-conductor in Section 2.5, the quasi-static time-domain expressions for a sphere in a dipolar field are derived first. Solutions for the electromagnetic response of a conducting sphere in free-space were given as early as 1909 by Debye (1909), who introduced scalar potentials to solve for the anomalous response for a plane wave source. March (1953) adopted Debye's approach in a geophysical context for a dipolar source. Wait (1953) started the derivation of his solution with the potential for a fictitious magnetic pole source. This approach has been adopted by Grant and West (1965) and Nabighian (1970), who derived a time-domain scalar magnetic potential for a pole source. The magnetic fields are found by taking the gradient of the pole-source potential. The dipole solution is finally obtained by differentiating the response in direction of the dipole moment (Grant and West, 1965). Smith and Lee (2002b) applied a Laplace transformation to the frequency-domain solution of Grant and West (1965) to obtain the time-domain solution of the impulse response of a sphere in a dipolar field.

2.2.1 Scalar magnetic potential of a pole source

Following Nabighian (1970), the response is obtained by solving a boundary value problem whose solution is facilitated since the external magnetic fields are derivable from a single scalar magnetic potential. The solutions of the system's differential equation, which are required for the interior of the sphere, are matched to solutions of Laplace's equation at the spherical boundary (Wait, 1960). Accordingly, displacement currents are neglected and the solution is of quasi-static nature. This assumption is valid for low enough frequencies which is usually the case for inductive EM systems.

The anomalous magnetic potential U_0 is solved for outside a permeable and conductive sphere, due to a transient magnetic pole source having time-dependence $e^{i\omega t}$ with period $2\pi/\omega$ and $i = \sqrt{-1}$. The secondary magnetic fields are then given by taking the gradient of the potential

$$\mathbf{H}^{\text{pole}}(t) = -\nabla U_0 \quad (2.8)$$

Nabighian (1970) starts by placing a transient magnetic pole source on the vertical axis (Figure 2.1) and removes the pole instantaneously at time $t = 0$ giving rise to a differential equation of the perturbed system. The differential equation is solved by introducing a vector potential \mathbf{F} for the electric field \mathbf{E} with a corresponding magnetic scalar potential U of the Lorentz gauge (Schelkunoff, 1943, p.403):

$$\mathbf{E} = -\nabla \times \mathbf{F} \quad (2.9)$$

$$U = -\frac{1}{i\mu\omega} \nabla \cdot \mathbf{F} \quad (2.10)$$

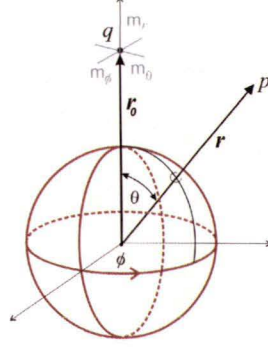


Figure 2.1 – Conducting sphere excited by a transient magnetic pole source (after Grant and West, 1965, p.517). The position of the pole source is at point q on the vertical axis. The radial distance from O to q is denoted r_0 , the radial distance to the receiver at p is denoted r . The polar angle separating r and r_0 is given by θ whereas ϕ is the azimuthal angle. Superimposed are the components of a dipole moment, m_r , m_θ and m_ϕ , where the transverse dipole moment m_θ lies in the same plane as the source q and observation point p . The transverse dipole moment m_ϕ lies perpendicular to this plane.

where μ is the magnetic permeability. Because of the polar symmetry, the vector potential \mathbf{F} has only a radial component ψ . ψ is denoted the scalar stream function of the TE (transverse electric) mode after Schelkunoff (1943),

$$\mathbf{F} = \psi \hat{\mathbf{i}}_r \quad (2.11)$$

$$U = -\frac{1}{i\mu\omega} \frac{\partial}{\partial r} \psi \quad (2.12)$$

where $\hat{\mathbf{i}}_r$ denotes the radial unit vector. The electric field vector is given by Equation (2.9) and the magnetic field vector is derived via application of Faraday's law

$$\mathbf{E} = -\nabla \times (\psi \hat{\mathbf{i}}_r) \quad (2.13)$$

$$\mathbf{H} = \frac{1}{i\mu\omega} \nabla \times \nabla \times (\psi \hat{\mathbf{i}}_r) \quad (2.14)$$

where $E_r = E_\theta = H_\phi = 0$. The stream function is a solution of the differential equation of the perturbed system

$$r^2 \frac{\partial^2}{\partial r^2} \psi + \frac{1}{\sin \theta} \frac{\partial}{\partial \theta} \left(\sin \theta \frac{\partial}{\partial \theta} \psi \right) = k^2 r^2 \psi \quad (2.15)$$

with wavenumber $k^2 = i\sigma\mu\omega - \epsilon\mu\omega^2$ where ϵ is the electrical permittivity and σ is the electrical conductivity.

The elementary solutions ψ of Equation (2.15) are proportional to products of spherical Bessel functions and Legendre polynomials. With the elementary solutions of Equation (2.15), Nabighian (1970) derives the characteristic equation of the differential equation to solve for the boundary conditions while neglecting displacement currents in the region outside the sphere. The eigenvalues of the characteristic equation are given as an infinite sum over the zeros of the Bessel function of the first kind for fractional order.

2.2.2 Secondary magnetic potential

Once the boundary conditions have been solved, the secondary magnetic potential U_0 outside the sphere can be derived using Equation (2.12). The solution Nabighian (1970) derived is

$$U_0(t) = p \sum_{\ell=1}^{\infty} a^{2\ell+1} \left(\frac{\ell/\ell+1}{(r_0 r)^{\ell+1}} P_{\ell}(\cos \theta) \right) F_{\ell}(t) \quad (2.16)$$

$$F_{\ell}(t) = 2(2\ell+1) \sum_{s=1}^{\infty} \frac{1}{x_{s,\ell}^2} \exp \left(-t \frac{x_{s,\ell}^2}{\sigma \mu a^2} \right) \quad (2.17)$$

where Equation (2.17) is given here for the non-magnetic sphere with $\mu = \mu_0$. The sphere radius is a . The zeros of the Bessel function of the first kind for order $\ell - 1/2$ are denoted $x_{s,\ell}$. The pole strength is denoted p and P_{ℓ} are the Legendre polynomials. The geometrical parameters are described in Figure 2.1 on the preceding page.

The geometric part of the solution is given as a sum of induced multipoles and the time-dependent part of the solution is given as an infinite sum of exponentials for each multipole. Each of the exponentials exhibits a time response like a simple loop circuit, the amplitude decaying with time in exactly the same way for all receiver points (Lamontagne, 1975). Each exponential in the sum of Equation (2.17) forms an eigencurrent, adopting the name from the solutions of the characteristic equation which are the eigenvalues $x_{s,\ell}$.

2.2.3 Impulse response solution

The solution in the preceding section is for a step current shut-off. If the impulse response is required, the step response is differentiated with respect to time (c.f. Equation 1.16). Carrying out the differentiation, the impulse response of the time-dependent part is given as

$$\frac{\partial}{\partial t} F_{\ell}(t) = \delta(t) F_{\ell}(t) - \frac{2(2\ell+1)}{\sigma \mu a^2} \sum_{s=1}^{\infty} \exp \left(-t \frac{x_{s,\ell}^2}{\sigma \mu a^2} \right) \quad (2.18)$$

where the term with the Dirac delta function, $\delta(t)$, has only a value at $t = 0$ and evaluates to

$$\delta(t) F_\ell(t) = 2(2\ell + 1) \sum_{s=1}^{\infty} x_{s,\ell}^{-2} \quad (2.19)$$

For measurements during the off-time, the Dirac delta response is omitted.

2.2.4 The field solutions

The gradient of the potential, Equation (2.16), solves for the secondary *magnetic pole* fields after step current shut-off:

$$H_r^{pole} = -\frac{\partial}{\partial r} U_0 = p \sum_{\ell=1}^{\infty} r_0 \frac{a^{2\ell+1}}{(r_0 r)^{\ell+2}} \ell P_\ell(\cos \theta) F_\ell(t) \quad (2.20)$$

$$H_\theta^{pole} = -\frac{1}{r} \frac{\partial}{\partial \theta} U_0 = -p \sum_{\ell=1}^{\infty} r_0 \frac{a^{2\ell+1}}{(r_0 r)^{\ell+2}} \frac{\ell}{\ell+1} P_\ell^1(\cos \theta) F_\ell(t) \quad (2.21)$$

$$H_\phi^{pole} = -\frac{1}{r \sin \theta} \frac{\partial}{\partial \phi} U_0 = 0 \quad (2.22)$$

which correspond to the frequency-domain solutions in Grant and West (1965, p.517). The secondary *magnetic dipole* field may be obtained by spatial differentiation of the monopole solution in the direction of the dipole moment (Panofsky and Phillips, 1962, p.14). Since an arbitrarily oriented dipole can be decomposed into its components in each of the cardinal directions, it is sufficient to differentiate the monopole expressions in the direction of each decomposed dipole moment at the source position $q(x_0, y_0, z_0)$ (c f. Figure 2.1).

For the derivation of any dipole expression a reciprocal feature may be invoked, that is, the differentiation with respect to the source point $q(x_0, y_0, z_0)$ may be interchanged to a differentiation with respect to the observation point $p(x, y, z)$ when it is convenient to choose so (Panofsky and Phillips, 1962, p.5). A sign change occurs when invoking the reciprocity feature. The directional derivatives of the monopole field with respect to the source point, ∇_0 , are required in the direction of the dipole axis $\hat{\mathbf{m}}$, where $\hat{\mathbf{m}}$ is given by

$$\hat{\mathbf{m}} = \frac{1}{p} (m_r \mathbf{i}_r + m_\theta \mathbf{i}_\theta + m_\phi \mathbf{i}_\phi) \quad (2.23)$$

where p is the pole strength. This expression arises from the definition of the dipole moment $m_\xi = p d\xi$ where $d\xi$ is the infinitesimal length of the dipole in direction $\xi = r, \theta, \phi$ (Grant and West, 1965, p.506 and p.517). The directional derivative operator in the direction of $\hat{\mathbf{m}}$ is given by

$$(\hat{\mathbf{m}} \cdot \nabla_0) = \frac{1}{p} \left(m_r \frac{\partial}{\partial r_0} + m_\theta \frac{1}{r_0} \frac{\partial}{\partial \theta_0} + m_\phi \frac{1}{r_0 \sin \theta_0} \frac{\partial}{\partial \theta_0} \right) \quad (2.24)$$

Applying the operator, Equation (2.24), to the magnetic pole fields, Equations (2.20)–(2.22), yields the expressions

$$\mathbf{H}_r^{dipole} = \frac{m_r}{p} \frac{\partial}{\partial r_0} \left(H_r^{pole} \mathbf{i}_r + H_\theta^{pole} \mathbf{i}_\theta \right) \quad (2.25)$$

$$\mathbf{H}_\theta^{dipole} = \frac{m_\theta}{p} \frac{1}{r_0} \frac{\partial}{\partial \theta_0} \left(H_r^{pole} \mathbf{i}_r + H_\theta^{pole} \mathbf{i}_\theta \right) \quad (2.26)$$

$$\mathbf{H}_\phi^{dipole} = \frac{m_\phi}{p} \frac{1}{r_0 \sin \theta_0} \frac{\partial}{\partial \theta_0} \left(H_r^{pole} \mathbf{i}_r + H_\theta^{pole} \mathbf{i}_\theta \right) \quad (2.27)$$

where the subscript of \mathbf{H}_ξ^{dipole} , ($\xi = r, \theta, \phi$) refers to the direction of the magnetic dipole moment and where the dipole moments m_ξ ($\xi = r, \theta, \phi$) have units $A \cdot m^2$. The derivatives are evaluated when both, source and observation point, lie in the same plane, or when the dipole transmitter lies perpendicular to this plane (Figure 2.2).

For a particular dipole transmitter orientation with dipole moment m_τ , the dipole solutions have the general form

$$\mathbf{H}^{dipole} = \frac{m_\tau}{4\pi} \sum_{\ell=1}^{\infty} a^{2\ell+1} \mathbf{G}_\ell(P_\ell, P_\ell^1, \theta) \cdot F_\ell(t) \quad (2.28)$$

where the functions \mathbf{G}_ℓ describe the geometric response as described in subsequent sections. The components of the geometrical response are dependent on dipole source orientation and are defined by the terms in square brackets in subsequent Equations (2.29)–(2.33). In the following field expressions, the first subscript refers to the orientation of the magnetic dipole source and the second subscript denotes the magnetic field component.

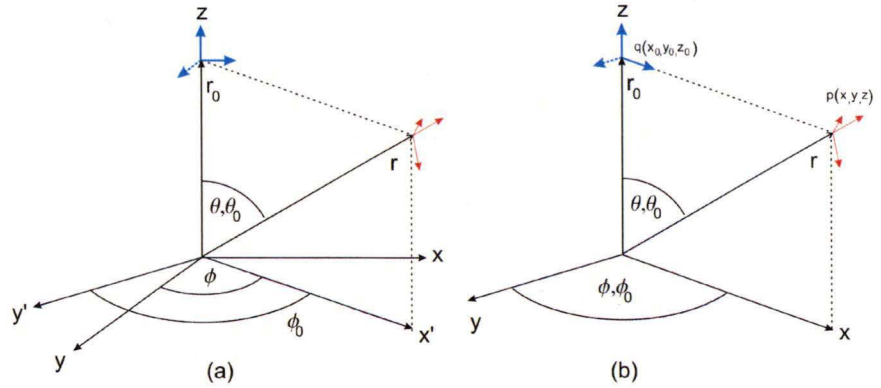


Figure 2.2 – Coordinate system for secondary magnetic fields for a conductive sphere in a dipolar field. The left Figure (a) shows two fixed coordinate systems, offset by angle $\phi - \phi_0$. The primed frame is referenced with respect to the transmitter, the other with respect to the observation point. The frame depicted in (b) shows where the two frames coincide when the transverse transmitter dipole lies in the same plane as the observation point, i.e. $\phi - \phi_0 = 0$. Another case where both frames coincide is when $\phi - \phi_0 = \pi/2$.

Solution for radial dipole source The solution for a radial dipole source is straightforward with

$$\mathbf{H}_r^{dipole} = \frac{m_r}{p} \frac{\partial}{\partial r_0} \left(H_r^{pole} \mathbf{i}_r + H_\theta^{pole} \mathbf{i}_\theta \right)$$

thus, the following components are obtained (Grant and West, 1965, 17-45, p 517):

$$H_{r,r}(t) = -\frac{m_r}{4\pi} \sum_{\ell=1}^{\infty} a^{2\ell+1} \left[\frac{\ell(\ell+1) P_\ell(\cos \theta)}{(r r_0)^{\ell+2}} \right] \cdot F_\ell(t) \quad (2.29)$$

$$H_{r,\theta}(t) = -\frac{m_r}{4\pi} \sum_{\ell=1}^{\infty} a^{2\ell+1} \left[\frac{\ell P_\ell^1(\cos \theta)}{(r r_0)^{\ell+2}} \right] \cdot F_\ell(t) \quad (2.30)$$

$$H_{r,\phi}(t) = 0$$

Solution for transverse dipole source The solution for a transverse dipole source, lying in the plane of the source and the observation point, follows with

$$\mathbf{H}_\theta^{dipole} = \frac{m_\theta}{p} \frac{1}{r_0} \frac{\partial}{\partial \theta_0} \left(H_r^{pole} \mathbf{i}_r + H_\theta^{pole} \mathbf{i}_\theta \right)$$

The magnetic dipole source is synthesised from two monopoles lying in the $\phi - \phi_0 = 0$ plane, and has constant unit vectors. Under differentiation, the unit vectors evaluate to zero. The magnetic field vectors can be differentiated with respect to the observation coordinate θ , invoking the reciprocal property, thus (Fullagar, pers. comm.)

$$\begin{aligned} \mathbf{H}_\theta^{dipole} &= \frac{m_\theta}{p} \frac{1}{r_0} \left(\frac{\partial}{\partial \theta_0} H_r^{pole} \mathbf{i}_r + H_r^{pole} \frac{\partial \mathbf{i}_r}{\partial \theta_0} \right) + \frac{m_\theta}{r_0} \left(\frac{\partial}{\partial \theta_0} H_\theta^{pole} \mathbf{i}_\theta + H_\theta^{pole} \frac{\partial \mathbf{i}_\theta}{\partial \theta_0} \right) \\ &= -\frac{m_\theta}{p r_0} \left(\frac{\partial}{\partial \theta} H_r^{pole} \mathbf{i}_r + \frac{\partial}{\partial \theta} H_\theta^{pole} \mathbf{i}_\theta \right) \end{aligned}$$

With the derivative of the associated Legendre polynomial (see next section), the transverse dipole gives rise to the following components (Grant and West, 1965, 17-48, p.518)

$$H_{\theta,r}(t) = \frac{m_\theta}{4\pi} \sum_{\ell=1}^{\infty} a^{2\ell+1} \left[\frac{\ell P_\ell^1(\cos \theta)}{(r r_0)^{\ell+2}} \right] \cdot F_\ell(t) \quad (2.31)$$

$$H_{\theta,\theta}(t) = -\frac{m_\theta}{4\pi} \sum_{\ell=1}^{\infty} a^{2\ell+1} \left[\frac{\ell^2 P_\ell(\cos \theta) - \frac{\ell}{\ell+1} \cos \theta \frac{P_\ell^1(\cos \theta)}{\sin \theta}}{(r r_0)^{\ell+2}} \right] \cdot F_\ell(t) \quad (2.32)$$

$$H_{\theta,\phi}(t) = 0$$

Solution for transverse perpendicular dipole source The magnetic field due to a dipole source, synthesised from two monopoles aligned perpendicular to the plane of the source and the observation point, i.e. in the $\phi - \phi_0 = \pi/2$ plane, does not produce a radial and polar magnetic field component at the observation point (Figure 2.2). However, the change in the \mathbf{i}_θ unit vector will produce a ϕ component (Fullagar, pers. comm.)

$$\begin{aligned} \mathbf{H}_\theta^{dipole} &= \frac{m_\phi}{p} \frac{1}{r_0 \sin \theta_0} \frac{\partial}{\partial \theta_0} \left(H_r^{pole} \mathbf{i}_r + H_\theta^{pole} \mathbf{i}_\theta \right) \\ &= -\frac{m_\phi}{p r_0} \csc \theta H_\phi^{pole} \mathbf{i}_\phi \end{aligned}$$

where again the reciprocal feature has been invoked and $\sin \theta = \sin \theta_0$. Thus, using the derivative of the associated Legendre polynomial, the magnetic field evaluates as (Grant and West, 1965, 17-49, p.518)

$$\begin{aligned} H_{\phi,r}(t) &= 0 \\ H_{\phi,\theta}(t) &= 0 \\ H_{\phi,\phi}(t) &= -\frac{m_\phi}{4\pi} \sum_{\ell=1}^{\infty} a^{2\ell+1} \left[\frac{\frac{\ell}{\ell+1} \csc \theta \cdot P_\ell^1(\cos \theta)}{(r r_0)^{\ell+2}} \right] \cdot F_\ell(t) \end{aligned} \quad (2.33)$$

2.2.5 Evaluation of associated Legendre polynomials

The first derivative of P_ℓ is denoted P_ℓ^1 and is known as the associated Legendre polynomial. Derivatives of the associated Legendre polynomial of the first order can be evaluated using suitable recurrence relationships¹, e.g. Arfken (1985, p.669) which evaluate with $x = \cos \theta$ to

$$(1-x^2)^{1/2} P_\ell^{1'}(x) = \frac{1}{2} P_\ell^2(x) - \frac{1}{2} \ell(\ell+1) P_\ell(x) \quad (2.34)$$

$$P_\ell^2(x) = 2 \frac{x}{(1-x^2)^{1/2}} P_\ell^1(x) - \ell(\ell+1) P_\ell(x) \quad (2.35)$$

where the prime denotes differentiation with respect to the argument, then

$$P_\ell^{1'}(\cos \theta) = \frac{1}{\sin \theta} \left(\frac{\cos \theta}{\sin \theta} P_\ell^1(\cos \theta) - \ell(\ell+1) P_\ell(\cos \theta) \right) \quad (2.36)$$

thus the derivative for the associated Legendre polynomial of first order is

¹There are two sign conventions for associated Legendre polynomials; some authors include a factor of $(-1)^m$ where m is the order of the associated polynomial. Here, the definition of Grant and West (1965, p 223) is used which does not include the factor.

$$\frac{\partial}{\partial \theta} P_\ell^1(\cos \theta) = -\sin \theta \cdot P_\ell^{m'}(\cos \theta) \quad (2.37)$$

$$= \ell(\ell+1) P_\ell(\cos \theta) - \cot \theta P_\ell^1(\cos \theta) \quad (2.38)$$

When the receiver and dipole source are coincident, the separation angle θ will be zero in which case the terms involving the division by $\sin \theta$ have the limiting value

$$\left. \frac{P_\ell^1(\cos \theta)}{\sin \theta} = \frac{\ell(\ell+1)}{2} \right|_{\theta=0} \quad (2.39)$$

2.3 TEM response of a sphere in a uniform field

In a uniform field, the solutions reduce to just the $\ell = 1$ term. The uniform field approximation is valid if the sphere dimension is small relative to the distance to the source. If the source and observation point are more than about one sphere radius away from the sphere surface, the first dipole moment will strongly predominate, however higher order multipoles are still prevalent. For shallow conductors at a distance $\lesssim 0.1$ radius, a large number of multipoles need to be considered (West and Macnae, 1991, p.30). Lodha and West (1976) report that in most cases, where the sphere is close to source and observation point, 15 multipoles are sufficient. Dyck et al. (1980, 1.2) notes that the multipole expansion of $\ell = 10$, for a dipole-dipole system, achieves an accuracy of better than 1%, provided that both transmitter and receiver are at least one radius away from the surface of the sphere. As a guideline, the uniform field approximation is adequate if the source and observation points are at least in a distance of about seven times the sphere radius (Telford et al., 1985, p.347). This restriction is relaxed for large loop systems where the generated primary field is intrinsically more uniform than a dipole source.

Assuming a radial magnetic dipole source at a distance such that the uniform field conjecture holds true, the solutions for $H_{r,r}$ (Equation 2.29) and $H_{r,\theta}$ (Equation 2.30) for the uniform field approximation, are

$$H_{r,r} = H_0 \frac{2 \cos \theta}{r^3} a^3 \cdot F_1(t) \quad (2.40)$$

$$H_{r,\theta} = H_0 \frac{\sin \theta}{r^3} a^3 \cdot F_1(t) \quad (2.41)$$

The axial primary field of the magnetic dipole source is

$$H_0 = -\frac{m_r}{4\pi r_0^3} \quad (2.42)$$

where m_r is the magnetic moment of the radial dipole transmitter. The time-dependent part for step-current shut-off evaluates as

$$F_1(t) = 6 \sum_{s=1}^{\infty} x_{s,\ell}^{-2} \cdot \exp\left(-t \frac{x_{s,\ell}^2}{\sigma \mu a^2}\right) \quad (2.43)$$

For the uniform field response of the time derivative of the magnetic field, $\partial_t F_1$ (Equation 2.18 on page 32) is substituted for the time-dependent part, viz

$$\frac{\partial}{\partial t} F_1(t) = -\frac{6}{\sigma \mu a^2} \sum_{s=1}^{\infty} \exp\left(-t \frac{x_{s,\ell}^2}{\sigma \mu a^2}\right) \quad (2.44)$$

The uniform field response is equivalent to the response of a magnetic dipole oriented in the direction of the polar axis, located at the sphere centre and exhibiting a transient moment.

2.4 TEM moments of a sphere

The TEM moment transform of order n for a sphere in a dipolar field for step current shut-off follows from Equation (2.2) and (2.28):

$$\mathbf{M}^{(n)} = \frac{m_\tau}{4\pi} \sum_{\ell=1}^{\infty} a^{2\ell+1} \mathbf{G}_\ell \cdot n \int_0^\infty t^{n-1} \cdot F_\ell(t) \quad (2.45)$$

The components of the geometrical response \mathbf{G}_ℓ are dependent on the dipole source orientation and can be inferred by comparison with the terms in square brackets in Equations (2.29) to (2.33). Integration of the time-dependent part of the step response $F_\ell(t)$ yields

$$\begin{aligned} n \int_0^\infty F_\ell(t) \cdot t^{n-1} dt &= 2(2\ell+1) n \sum_{s=1}^{\infty} \frac{1}{x_{s,\ell}^2} \int_0^\infty t^{n-1} e^{-k t} dt \\ &= 2(2\ell+1) \Gamma(n+1) \pi^{2n} \tau^n \sum_{s=1}^{\infty} x_s^{-2(n+1)} \\ &= \pi^{2n} \tau^n f_\ell(n) \end{aligned} \quad (2.46)$$

where $\tau^n = (\mu \sigma a^2)^n / \pi^{2n}$ is the sphere time constant, raised to the n -th power; and where

$$f_\ell(n) = 2(2\ell+1) \Gamma(n+1) \sum_{s=1}^{\infty} x_s^{-2(n+1)} \quad (2.47)$$

where x_s denote zeros of the Bessel function of the first kind for order $\ell - 1/2$ (Equation 2.16). The integral in Equation (2.46) has been evaluated using the definition of the Gamma function (Abramowitz and Stegun, 1965, 6.1.1)

$$\Gamma(z) = k^z \int_0^\infty t^{z-1} e^{-k t} dt \quad (z > 0) \quad (2.48)$$

where

$$k = \frac{x_{s,\ell}^2}{\sigma \mu a^2} \quad (2.49)$$

Comparison with the solution of Smith and Lee (2002b, Eq 25), who derived the result for the impulse response by direct integration, demonstrates equivalence. Thus, the TEM moment response of a sphere in a dipolar field is given by

$$\mathbf{M}^{(n)} = \pi^{2n} \frac{m_\tau}{4\pi} \tau^n \sum_{\ell=1}^{\infty} a^{2\ell+1} \mathbf{G}_\ell \cdot f_\ell(n) \quad (2.50)$$

2.4.1 Evaluation of sum of Bessel zeros.

The infinite sum of Bessel zeros occurring in the solution of the TEM moment transform of the sphere (Equation 2.46) can be solved analytically for moment orders up to $n = 4$ as reported by Smith and Lee (2002a). The evaluation of the sum of Bessel zeros is given by Watson (1944, p.502)

$$z_\nu(n) = \sum_{s=1}^{\infty} x_s^{-2(n+1)} \quad (2.51)$$

where ν is the order of the Bessel function. In this case $\nu = \ell - \frac{1}{2}$ where ℓ is the order of the current multipole expansion. The equations for the Bessel zeros up to order 4 are

$$z_\nu(0) = \frac{1}{2^2(\nu+1)} \quad (2.52)$$

$$z_\nu(1) = \frac{1}{2^4(\nu+1)^2(\nu+2)} \quad (2.53)$$

$$z_\nu(2) = \frac{1}{2^5(\nu+1)^3(\nu+2)(\nu+3)} \quad (2.54)$$

$$z_\nu(3) = \frac{5\nu+11}{2^8(\nu+1)^4(\nu+2)^2(\nu+3)(\nu+4)} \quad (2.55)$$

$$z_\nu(4) = \frac{7\nu+19}{2^9(\nu+1)^5(\nu+2)^2(\nu+3)(\nu+4)(\nu+5)} \quad (2.56)$$

In case of point conductor TEM moments, which follows in the next section, the sum over the zeros of the Bessel function may be expressed as a Bernoullian number² β_r (Watson, 1944; Smith and Lee, 2002a), with

$$z_{1/2}(n) = \frac{2^{2n+1}}{(2n+2)!} |\beta_{2n+2}| \quad (2.57)$$

The Bernoullian numbers are tabulated, for example Abramowitz and Stegun (1965, p.810) list the first 60 Bernoullian numbers.

2.5 Point conductor TEM moments

The general form of the TEM moment of a sphere in a dipolar field was given earlier in Equation (2.50). The first term in the summation includes a factor of a^3 . Therefore, if the time constant of a small sphere is identical to the time constant of a large sphere, i.e. if σa^2 is invariant, then $\mathbf{M}^{(n)}$ of the small sphere

²Smith and Lee (2002b) report a typographic error in the discussion of Bessel zeros in Watson (1944). the second last equation on page 502 of Watson needs to be corrected by changing β_r to β_{2r} .

will be approximately equal to $\mathbf{M}^{(n)}$ of the large sphere provided the difference in their volumes is taken into account. The quality of the approximation is governed by the size of the second and subsequent terms in the summation:

$$\mathbf{M}^{(n)} = \pi^{2n} \frac{m_\tau}{4\pi} \tau^n \sum_{\ell=1}^{\infty} a^{2\ell+1} \mathbf{G}_\ell \cdot f_\ell(n) \quad (2.58)$$

$$= \pi^{2n} \frac{m_\tau}{4\pi} \tau^n a^3 \cdot \left(\mathbf{G}_1 \cdot f_1(n) + \sum_{\ell=1}^{\infty} a^{2\ell} \mathbf{G}_{\ell+1} \cdot f_{\ell+1}(n) \right) \quad (2.59)$$

Suppose the product $\tau^n a^3$ is maintained constant as the sphere radius decreases. In the limit as a approaches zero, the contribution from the second and subsequent terms in the expansion becomes negligible, and the n -th TEM moment for a point conductor may be defined as (Fullagar, 2007b)

$$\mathbf{M}^{(n)} = f_1(n) \pi^{2n} \frac{m_\tau}{4\pi} \tau^n a^3 \cdot \mathbf{G}_1 \quad (2.60)$$

The different contributions to the point conductor moment are readily identified: transmitter-moment m_τ , time constant τ , effective volume a^3 , geometry \mathbf{G}_1 and the constant part arising from the moment transform. Changing the effective volume does not affect the time constant and, vice versa, a change of the time constant does not modify the effective volume. The point-conductors approach is equivalent to the uniform field approach. However, proximity of the point conductor to the transmitter is immaterial because the point conductor occupies no volume, so higher order multipoles are never involved.

For a radial transmitter dipole, the TEM moment of a point conductor resolves to

$$\mathbf{M}^{(n)} = H_0 \cdot \tau^n a^3 \cdot \left(\frac{2 \cos \theta_{\hat{\mathbf{i}}_r} + \sin \theta_{\hat{\mathbf{i}}_\theta}}{r^3} \right) \cdot f_1(n) \pi^{2n} \quad (2.61)$$

where the primary field is defined via (Equation 2.42)

$$H_0 = -\frac{m_\tau}{4\pi r_0^3} \quad (2.62)$$

Of interest is the first order TEM moment of a point conductor which finds use in the approximate forward modelling scheme described in Chapter 3. For an arbitrarily oriented magnetic dipole source, the first order TEM moment can be written more generally as:

$$\mathbf{M}^{(1)} = \eta \cdot \frac{3 \left(\hat{\mathbf{b}} \cdot \hat{\mathbf{r}} \right) \hat{\mathbf{r}} - \hat{\mathbf{b}}}{4\pi r^3} \quad (2.63)$$

where $\hat{\mathbf{b}}$ and $\hat{\mathbf{r}}$ are unit vectors parallel to primary field \mathbf{H}_0 and \mathbf{r} respectively, and where η is defined as

$$\eta = H_0 2\pi a^3 f_1(1) \pi^2 \tau = 2\pi a^3 \left(\frac{\sigma \mu a^2}{15} \right) H_0 \quad (2.64)$$

which agrees with the frequency domain resistive limit expression given by Grant and West (1965, p 496,17-15) for a non-permeable conducting sphere in a uniform field. η is the magnetic dipole moment of a sphere (Grant and West, 1965, p 495) in the resistive limit, which is equivalent to the first order TEM moment.

By introducing the sphere volume $V = 4/3\pi a^3$, the result for the first order TEM moment of a point conductor has the more simple form:

$$\begin{aligned} \mathbf{M}^{(1)} &= \eta \cdot \frac{3(\hat{\mathbf{b}} \cdot \hat{\mathbf{r}}) \hat{\mathbf{r}} - \hat{\mathbf{b}}}{4\pi r^3} \\ &= \frac{\pi^2}{10} H_0 V \tau \cdot \frac{3(\hat{\mathbf{b}} \cdot \hat{\mathbf{r}}) \hat{\mathbf{r}} - \hat{\mathbf{b}}}{4\pi r^3} \\ &\approx H_0 V \tau \cdot \frac{3(\hat{\mathbf{b}} \cdot \hat{\mathbf{r}}) \hat{\mathbf{r}} - \hat{\mathbf{b}}}{4\pi r^3} \end{aligned} \quad (2.65)$$

Thus the 1st TEM moment of a point conductor is analogous to the response of a magnetic dipole, with dipole moment aligned in the direction of the primary field, and proportional to the product of primary field, volume and time constant $H_0 V \tau$. For further references, the point-conductor formula is written as

$$\mathbf{M}^{(1)} = \mathbf{G} \tau \quad (2.66)$$

where

$$\mathbf{G} = H_0 V \frac{3(\hat{\mathbf{b}} \cdot \hat{\mathbf{r}}) \hat{\mathbf{r}} - \hat{\mathbf{b}}}{4\pi r^3} \frac{\pi^2}{10} \quad (2.67)$$

2.5.1 Primary field

The primary field \mathbf{H}_0 may result from sources other than magnetic dipoles. The forward modelling algorithm in Chapter 3 is described in the context of fixed-loop EM. For a rectangular loop source in free space, under the quasi-static approximation, the primary field for a point-conductor can be calculated deploying the law of Biot-Savart (Fullagar, 2007b). The net magnetic field H_y along a wire of the transmitter loop in x -direction is given by

$$H_y = \frac{I}{4\pi} z_0 \int_{x_1}^{x_2} \frac{dx}{r^3} = \frac{I}{4\pi} \frac{z_0}{y_0^2 + z_0^2} \left(\frac{x}{r}\right)^2 \quad (2.68)$$

with $r = \sqrt{x^2 + y_0^2 + z_0^2}$ the distance from cell centre to an infinitesimal linear current element of the wire carrying a current I . Integration is carried out between the wire endings x_1 and x_2 . A similar approach is adopted for the remaining wire segments of the transmitter loop. The primary field \mathbf{H}_0 for a point-conductor is obtained by the sum of the net magnetic fields of each transmitter wire segment.

In the case of a magnetic dipole source, the primary field at the cell centre is obtained by invoking the familiar dipole formula (e.g. Smith and Lee, 2002a), viz.

$$\mathbf{H}_0 = \frac{m_{tx}}{4\pi r^3} (3(\hat{\mathbf{m}}_{tx} \cdot \hat{\mathbf{r}}_{tx}) \hat{\mathbf{r}}_{tx} - \hat{\mathbf{m}}_{tx}) \quad (2.69)$$

where m_{tx} is the magnitude of the magnetic moment of the source dipole with unit vector $\hat{\mathbf{m}}_{tx}$. The unit vector $\hat{\mathbf{r}}_{tx}$ is parallel to the position vector connecting transmitter and cell centre

2.6 Comparison with magnetostatic solution

In magnetostatics, the property being sought is the magnetic susceptibility χ . The magnetisation \mathfrak{M} is related to the applied magnetic field \mathbf{H}_0 as (Blakely, 1995, p.87)

$$\mathfrak{M} = \chi \mathbf{H}_0 \quad (2.70)$$

where it is assumed that χ is not dependent on field intensity. The magnetostatic potential at an observation distance \mathbf{r} is then given (Grant and West, 1965, p.308) as

$$A(\mathbf{r}) = - \int_V \mathfrak{M} \nabla \frac{1}{r} dV \quad (2.71)$$

$$= - \int_V \chi \cdot \mathbf{H}_0 \cdot \nabla \frac{1}{r} dV \quad (2.72)$$

The moment expressions for the sphere with uniform field excitation for step-current shut-off can be re-written as a gradient of a magnetic scalar potential. By inspection of Equation (2.63) a scalar potential for the TEM moments is found to be

$$A(\mathbf{r}) = \eta \frac{\hat{\mathbf{m}} \cdot \hat{\mathbf{r}}}{4\pi r^3} \quad (2.73)$$

where $\eta = H_0 2\pi a^3 f_1(1) \pi^2 \tau$. All quantities have been defined earlier in Section 2.4. The potential itself can be written as a Green's function potential

$$A(\mathbf{r}) = - (\eta \hat{\mathbf{m}}) \cdot \nabla \frac{1}{4\pi r}$$

the quantity in brackets may be identified as the magnetic dipole moment of the sphere directed parallel to the inducing field \mathbf{H}_0 . Introducing the volume magnetisation (Blakely, 1995, p.93) of a sphere

$$(\eta \hat{\mathbf{m}}) = \frac{4}{3} \pi a^3 \cdot \mathfrak{M} \quad (2.74)$$

the magnetisation can then be expressed as

$$\mathfrak{M} = \frac{3}{2} \mathbf{H}_0 \cdot \tilde{f}_1 \quad (2.75)$$

where $\tilde{f}_1 = f_1(1) \pi^2 \tau$, and the potential can therefore be identified outside a sphere with volume V_s as

$$A(\mathbf{r}) = - \int_{V_s} \mathfrak{M} \nabla \frac{1}{r} dV \quad (2.76)$$

$$= - \frac{3}{2} \tilde{f}_1 \int_{V_s} \mathbf{H}_0 \cdot \nabla \frac{1}{r} dV \quad (2.77)$$

The derivation of the potential is completely analogous to that of the magnetostatic potential as described in Grant and West (1965, p.212f.). The expression can be further simplified by noting that

$$\tilde{f}_1 = \frac{\pi^2 \tau}{15} \quad (2.78)$$

The magnetostatic potential for the TEM moment response can then be expressed as

$$A(\mathbf{r}) = -\frac{\pi^2}{10} \int_{V_s} \tau \cdot \mathbf{H}_0 \cdot \nabla \frac{1}{r} dV \quad (2.79)$$

$$\simeq -\int_{V_s} \tau \cdot \mathbf{H}_0 \cdot \nabla \frac{1}{r} dV \quad (2.80)$$

The time constant τ , replaces the magnetic susceptibility χ in the magnetostatic formulation of the 1st TEM moment (c.f. Equation 2.72). In effect, the moment transformation converts the TEM inversion problem into a magnetic inversion problem.

2.6.1 Program implementation

The discourse so far concentrated on the TEM moment response of a conductive sphere in the field of a magnetic dipole source. For uniform field excitation, or equivalently, for point-conductors, the expressions describing the secondary response simplify considerably. Altogether, the TEM moment expressions are of simpler form than their time-domain counterparts. Both, time-domain and moment-domain solutions for dipole and uniform field excitation have been implemented in a Fortran 95 program. This section illustrates some examples as calculated with the TEM moments program.

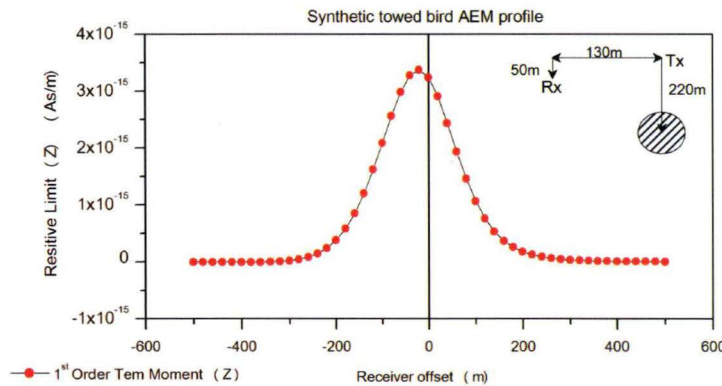


Figure 2.3 – Synthetic towed bird AEM profile of 1st TEM moment. The profile shows the z-component of the \mathbf{M}^1 TEM moment (resistive limit) of a conductive sphere in free space for uniform field excitation. The sphere is centred at (0E, 0N, -220z), radius is 50m and conductivity is 0.1S/m. The AEM Tx-Rx system consists of a receiver offset by 130m horizontally and 50m vertically from a vertical dipole transmitter (of unit moment). The plotting point is at the receiver. This profile agrees with the resistive limit response of the sphere as shown in Smith and Lee (2002b, Fig.2).

In order to establish validity of the TEM moments program, the synthetic profile shown in Figure 2.3 was calculated using the TEM moments formulation for the first moment order. The example is taken from Smith and Lee (2002b, Fig 2) and shows an airborne EM response over a conducting sphere. Shown is the z-component of the first order TEM moment which is equivalent to the resistive limit response of the sphere. The AEM Tx-Rx system consists of a receiver offset by 130m horizontally and 50m vertically from a vertical dipole transmitter (of unit moment). The calculated profile corresponds almost exactly to the profile presented in Smith and Lee (2002b, Fig 2) to the extent that it can be evaluated from the diagram without access to the original digital data.

To further validate the calculations of the TEM moments program, the time-domain response for a conductive sphere is compared with the result as computed with program SPHERE (Dyck et al., 1980). SPHERE calculates the eigenvalues of the characteristic equation (Nabighian, 1971, Eq.10) for eigencurrents up to 300. The maximum capacity of the multipole expansion of SPHERE is $\ell = 10$. The TEM moments program evaluates the eigencurrents, that is the sum of Bessel-zeros, by implementation of a look-up-table containing a wide range of Bessel-zeros for multipole orders up to $\ell = 25$. A convergence criterion, dependent on the sphere time-constant, terminates the sum of Bessel-zeros.

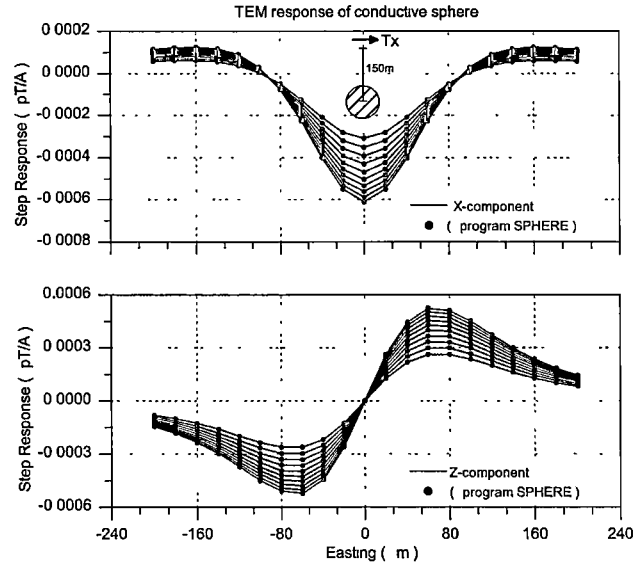


Figure 2.4 – Synthetic fixed transmitter profile for a conducting sphere centred at (0E, 0N, -150Z). Units are given in terms of the magnetic flux density B . The sphere has a radius of 50m and a conductivity of 50S/m. Step response recordings are at 20m intervals from -200E to 200E over the centre line of the sphere for channel delay times: 0.8813, 1.069, 1.313, 1.619, 2.006, 2.506, 3.144, 3.956, 4.994, 6.313 (msec). The transmitter is a horizontal magnetic dipole with dipole moment (1,0,0) fixed at 0E,0N. Calculations are carried out for multipole order $\ell = 10$. Superimposed are the responses from the program SPHERE (Dyck et al., 1980).

The example shows the response of a conducting sphere excited by a horizontal magnetic dipole and is depicted in Figure 2.4. The horizontal dipole source is centred at (0E,0N), 150 m above the centre of a sphere. The sphere has a radius of 50 m with a conductivity of 50 S/m. Step response recordings are at 20 m intervals from -200E to 200E over the centre line of the sphere. The order of the multipole expansion is 10 in order to account for induced higher multipoles. The time-domain response curves from SPHERE and the TEM moments program in Figure 2.4 plot essentially on top of each other. The results are identical to about the sixth significant Figure. Differences arise due to the different implementations of the evaluation of the sum over the Bessel-zeros. The geometrical response in both programs are exactly the same. Temporal and spatial contributions are calculated separately.

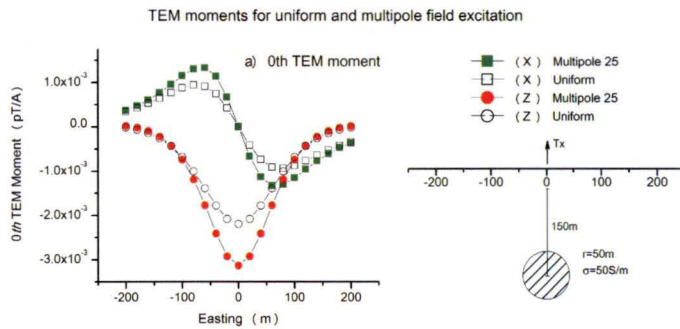


Figure 2.5 – Comparison of 0-th TEM moment for uniform and dipole field excitation. Synthetic recordings are obtained at 20m intervals along the mid-line over a sphere buried at (0E, 0N, -150m) with radius of 50m and conductivity of 50S/m. The vertical dipole transmitter is placed over the top of the sphere at 0E, 0N. Shown are the X and Z components for uniform field excitation and for multipoles up to order $\ell = 25$. The uniform field is calculated for $\ell = 1$.

The validity of the point-conductor or uniform-field approach is tested in Figure 2.5 which shows the zeroth order TEM moment response for the same model configuration as is shown in Figure 2.4, except here for a vertical magnetic dipole source at (0E,0N). The zeroth TEM moment for uniform field excitation is compared to the dipole field excitation, here for multipoles up to 25 in order to achieve the highest accuracy possible.

The zeroth TEM moment equals the inductive limit (Equation 2.6) and shows the largest difference between uniform and dipole field excitation. For the model under consideration, the sphere radius is large compared to source and observation distances, so that the field is non-uniform over the volume of the sphere and higher order multipoles are induced. When the observation points are at greater distances, i.e. at eastings larger than ± 130 m, both uniform field and dipole field responses are quite similar. Since the highest order multipoles decay most rapidly, the inductive limit exhibits the largest differences between uniform and dipole field excitation.

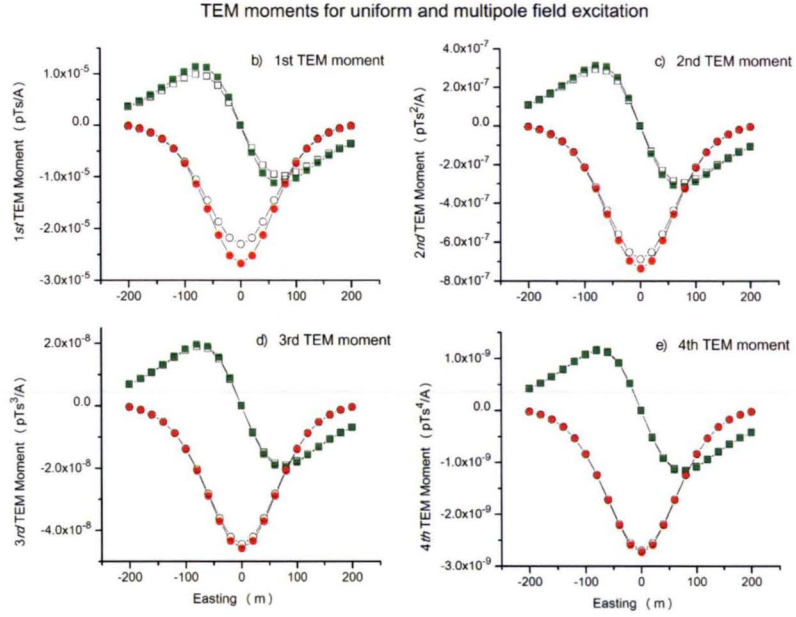


Figure 2.6 – Comparison of 1-st – 4-th TEM moment for uniform and dipole field excitation. The configuration is like in Figure 2.5. Higher order TEM moments for uniform and dipole field excitation agree better than lower order TEM moments.

As the response progresses towards the resistive limit, the eigencurrents of the highest order multipoles have already decayed, and the uniform field matches the dipole field to a higher degree as can be seen in Figure 2.6 (b), which depicts the 1st order TEM moment (resistive limit). Second to fourth order TEM moments are shown, respectively, in panel (c) to (e) in Figure 2.6. The fourth order TEM moment for uniform field excitation is virtually indistinguishable from the dipole field response. The dominance of the $s = 1$ term in Equation (2.51) results in the better agreement for the higher order TEM moments (Smith and Lee, 2002a).

2.7 The TEM moment of a half space for a rectangular loop source

In the following, analytical expressions for the first order TEM moments for a half space with rectangular loop excitation are derived for the vertical and horizontal magnetic field components. The forward modelling concept uses a continuous conducting half space as the response of the background. TEM moments for horizontally layered structures excited by a magnetic dipole source have previously been derived by Smith and Lee (2002c). In the limit when the layer has infinite depth extent, a first order half space moment is obtained. The concept for the half space moment has been extended to fractional order by Lee et al. (2003). Hyde (2005, p.83) derives the vertical half space moment for order up to $n = 1.4$ for a circular loop source. These previous results are suitable for airborne EM, but they are not generally applicable to ground TEM, which commonly employs large rectangular loop systems.

2.7.1 The vertical-component half space TEM moment

Raiche (1987) derived the analytical solution of the transient EM response of a conductive half space for rectangular loop excitation with step-current shut-off. His solution describes the electromagnetic force dB_z/dt induced in the receiver. The B_z response is given by integrating Raiche's solution with respect to time. The time integral of the B_z response subsequently provides the vertical TEM moment response of order one. For consistency reasons, the development of the equations will here be given in terms of the magnetic field \mathbf{H} , where it is understood that the magnetic permeability is that of free space. The expression for the dH_z/dt time-integral is given as the sum of the results for each line segment of the transmitter loop, viz.

$$H_z = G(x, y, t) \Big|_{(y_1, x_2)}^{(y_1, x_1)} + G(x, y, t) \Big|_{(x_2, y_1)}^{(x_2, y_2)} + G(x, y, t) \Big|_{(y_2, x_1)}^{(y_2, x_2)} + G(x, y, t) \Big|_{(x_1, y_2)}^{(x_1, y_1)}$$

where sub- and superscripts in brackets denote the corners of the transmitter loop. The response for a line segment of the transmitter loop evaluates as (Fullagar, 2002)

$$G(x, y, t) = \frac{I}{8\pi x^3} \left[\frac{1}{\gamma^2} \left(2 + \frac{x^2}{\rho^2} - 2\gamma^2 x^2 \right) \frac{y}{\rho} \operatorname{erf}(\gamma \rho) - \frac{2}{\sqrt{\pi}} \frac{x^2 y}{\rho^2 \gamma} e^{-\gamma^2 \rho^2} - \frac{2}{\gamma^2} e^{-\gamma^2 \rho^2} \operatorname{erf}(\gamma y) \right]_{\gamma=0}^{\gamma(t)} \quad (2.81)$$

where $G(x, y, t)$ denotes the vertical magnetic field; x and y denote corresponding coordinates of the ends of the line current relative to the receiver and $r = \sqrt{x^2 + y^2}$. Also,

$$\gamma = \frac{\sqrt{\sigma \mu}}{4t}, \quad t > 0 \quad (2.82)$$

where t denotes the channel delay time.

The 1st TEM moment is given by the time-integral of the expression for $G(x, y, t)$ in Equation (2.81); for evaluation the integration variable is expressed in terms of γ with

$$dt = -\frac{\mu \sigma}{2\gamma^3} d\gamma \quad (2.83)$$

and the integration of G can be expressed as

$$K(x, y, t) = - \int_t^\infty G(x, y, t) dt = -\frac{\sigma \mu}{2} \int_0^{\gamma(t)} \frac{G(x, y, t)}{\gamma^3} d\gamma \quad (2.84)$$

The solution of this integral is given as (Fullagar, 2002)

$$K(x, y, t) = \left[\frac{\sigma\mu}{2} \frac{1}{4\gamma^2} G(x, y, t) + \frac{\eta}{2\gamma^2} \right]_0^{\gamma(t)} + I \frac{\sigma\mu}{16\pi} x \int_0^{\gamma(t)} e^{-\gamma^2 x^2} \frac{\text{erf}(\gamma y)}{\gamma} d\gamma \quad (2.85)$$

where η is defined by

$$\eta = I \frac{\sigma\mu}{16\pi} x \left(-\frac{y}{\rho} \text{erf}(\gamma \rho) + \text{erf}(\gamma y) e^{-\gamma^2 x^2} \right) \quad (2.86)$$

The $n = 1$ moment is equivalent to the complete time integral of the H-field response after step-current shut-off. Therefore, from Equation (2.84)

$$M_z^1 = \left[\frac{\sigma\mu}{2} \frac{1}{4\gamma^2} G + \frac{\eta}{2\gamma^2} \right]_0^\infty + I \frac{\sigma\mu}{16\pi} x \int_0^\infty e^{-\gamma^2 x^2} \frac{\text{erf}(\gamma y)}{\gamma} d\gamma \quad (2.87)$$

where the integral term is analytical with

$$\int_0^\infty \frac{e^{-\gamma^2 x^2}}{y} \text{erf}(\gamma y) d\gamma = \sinh^{-1} \left(\frac{y}{x} \right) \quad (2.88)$$

The term in brackets in Equation (2.87) vanishes at early time since, as $\gamma \rightarrow \infty$, the expression is zero and in the late time, when $\gamma \rightarrow 0$, the term also approaches zero. Thus follows the expression for the first order vertical moment response due to one side of a rectangular loop source (Fullagar, 2007b):

$$M_z^1(x, y) = I \frac{\sigma\mu}{16\pi} x \cdot \sinh^{-1} \left(\frac{y}{x} \right) \quad (2.89)$$

In Figure 2.7 the 1st order z-component TEM moments are shown for a resistive (1 mS/m) and a conductive (200 mS/m) half space with rectangular loop source excitation. Synthetic recordings are obtained at 50 m intervals along the centre line of a rectangular loop source with side lengths 250E×500N, centred at (0E, 0N). In order to recognise the effect of the integration over a finite time range, as is realised with the incomplete TEM moments, the TEM moment response of both incomplete and complete moments are on display in Figure 2.7. The incomplete moments are calculated by evaluating Equation (2.84) between the integration limits t_1 and ∞ , where t_1 is the first channel delay time; subsequently the moment contribution from t_N to ∞ is subtracted, where t_N denotes the last channel delay time. The complete moments are computed using Equation (2.89). For the spline-integrated TEM moments, the time-domain solution is numerically integrated between the first and last channel delay time. The contribution between 0 and t_1 is denoted 'head' contribution and the term 'tail' is used for

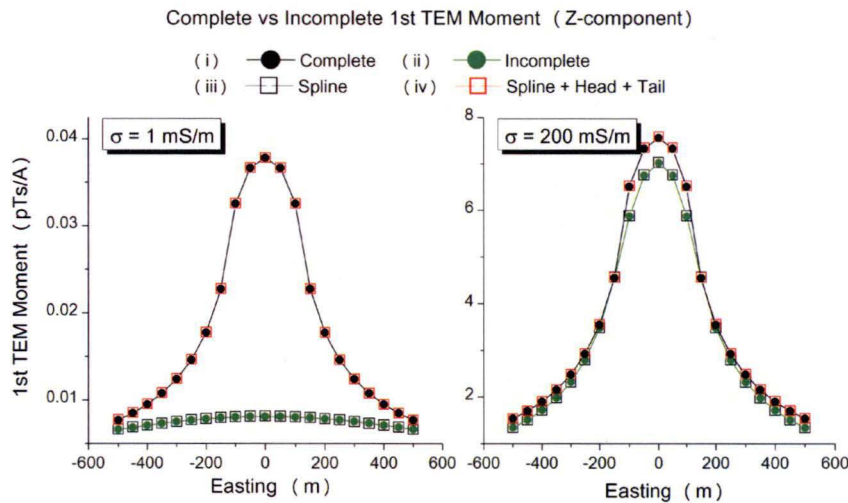


Figure 2.7 – First order vertical TEM moment of a half space with rectangular loop source. The left panel shows the result for a resistive half space of 1 mS/m whereas the right panel shows the response for a conductive half space with 200 mS/m . Several responses are recorded: (i) the complete 1st TEM moment as given by Equation (2.89); (ii) the incomplete moment given by evaluation of Equation (2.84) between the first and last channel delay time; (iii) the spline-integrated result of the time-domain response between the first and last channel; (iv) summed response from contributions from 0 to the first channel ('head') and last channel to infinity ('tail'), and the spline-integrated response. Channel delay times correspond to the SMARTTEM instrument channels (Chapter 1, Table 1.2).

the part between t_N and ∞ , both of which are calculated employing Equation (2.84) together with Equation (2.89). The summed response of splined-integrated moments, together with 'head' and 'tail' equals the complete TEM moment. This example illustrates the method of calculation of TEM moment data for a half space for which measurements are only available over finite time ranges. The numerical integration scheme provides a suitable approximation. The spline integration is based on the methods described in Davis and Rabinowitz (1975, pp.50-55 and pp.367-377).

2.7.2 The horizontal-component half space TEM moment

The expression for the horizontal components of the magnetic field due to a horizontal electrical dipole over a conducting earth is given by Ward and Hohmann (1988, p.236). For a rectangular loop source the galvanic terms which

are included in the expression can be neglected, leaving the inductive terms

$$H_x^{dip}(t) = \frac{I}{32\pi} \frac{dy}{t} \left[I_0(z) - I_2(z) \right] \cdot e^{-z} \quad (2.90)$$

where I is the transmitter current, I_0 and I_2 are, respectively, the modified Bessel functions of the first kind of zeroth and second order with argument $z = \sigma\mu_0 r^2/8t$, and dy indicates the electrical dipole direction. With the use of the following recurrence relation for modified Bessel functions (Abramowitz and Stegun, 1965, p.376)

$$I_{\nu-1}(z) - I_{\nu+1}(z) = \frac{2\nu}{z} I_{\nu}(z) \quad (2.91)$$

the expression can be further simplified, thus

$$H_x^{dip}(t) = \frac{I}{2\pi r^2} \frac{dy}{t} I_1(z) \cdot e^{-z} \quad (2.92)$$

The expression (Equation 2.92) for the horizontal magnetic field due to a horizontal electrical dipole needs to be integrated with respect to time to solve for the first moment expression. Integration around the loop wires yields the response of a rectangular loop source.

Integrating expression (2.92) with respect to time directly leads to a divergent integral, which can be seen by comparing the following expression from Luke (1962, §4.6)

$$\int_0^\infty e^{-t} t^p I_s(t) dt = \frac{\Gamma(p+s+1) \Gamma(-p-1/2)}{2^{s+1} \Gamma(1/2) \Gamma(s-p)} \quad (2.93)$$

subject to the conditions $p+s > -1$ and $p < -\frac{1}{2}$, thus for $p = -2$ and $s = 1$ one condition is violated for this solution. However, for a rectangular loop source, for every dipole on the near side of the loop there is a contribution from an oppositely oriented dipole on the other (parallel) side of the loop and an analytical expression can be derived by considering the opposing electrical dipoles together. Let r_1 and let r_2 denote the radial distances to the opposing dipoles on far and near side of the transmitter loop respectively. The moment net response (Fullagar, 2007b) is expressed as

$$\begin{aligned} \int_0^\infty H_x^{net}(t) dt &= \int_0^\infty (H_x^{near}(t) - H_x^{far}(t)) dt \\ &= \int_0^\infty \left(\frac{1}{2\pi r_1^2} e^{-z} I_1(z) - \frac{1}{2\pi r_2^2} e^{-\kappa z} I_1(\kappa z) \right) dt \end{aligned} \quad (2.94)$$

where

$$\kappa = \left(\frac{r_2}{r_1} \right)^2 \quad (2.95)$$

In order to solve for the first order moment the time integration is bisected into two integrations from 0 to t and from t to ∞ . The integral expressions over

the finite time ranges are called incomplete moments borrowing the name from the incomplete Gamma functions involved.

Setting

$$g(t) = z = \frac{\mu\sigma r^2}{8t} \Rightarrow dt = -\frac{\mu\sigma r^2}{8z^2} dz \quad (2.96)$$

If $g(t_1) = z_1$, $g(t_N) = z_N$ then the general expression for the TEM moment response for two opposing, y-directed electrical dipoles is

$$\int_{t_1}^{t_N} H_x^{net}(t) dt = -Idy \frac{\sigma\mu}{16\pi} \int_{z_1}^{z_N} \left(\frac{e^{-z}}{z^2} I_1(z) - \frac{e^{-\kappa z}}{\kappa z^2} I_1(\kappa z) \right) dz \quad (2.97)$$

Net moment response for $t_1 = 0$ and $t_N = t$

The integration limits transform as $g(t_1) = z_1 = \infty$ and $g(t_N) = z' = z$. The modified Bessel functions in the integral is replaced by its defining series expansion (Abramowitz and Stegun, 1965, p.375)

$$I_1(z) = \sum_{n=0}^{\infty} \frac{z^{2n+1}}{2^{2n+1} n! (n+1)!} \quad (2.98)$$

Substituting the series expansion then gives:

$$\begin{aligned} \int_0^t H_x^{net}(t) dt = \\ -Idy \frac{\sigma\mu}{16\pi} \sum_{n=0}^{\infty} \frac{1}{2^{2n+1} n! (n+1)!} \int_{\infty}^{z'} (e^{-z} z^{2n-1} - \kappa^{2n} e^{-\kappa z} z^{2n-1}) dz \end{aligned} \quad (2.99)$$

The individual integrals can easily be solved by recognising that they conform to the definition of the incomplete Gamma function (Abramowitz and Stegun, 1965, p.260), viz.

$$\int_{\infty}^{z'} e^{-z} z^{2n-1} dz = -\Gamma(2n, z') \quad (2.100)$$

$$\kappa^{2n} \int_{\infty}^{z'} e^{-\kappa z} z^{2n-1} dz = -\Gamma(2n, \kappa z') \quad (2.101)$$

which gives the result for the incomplete net-moment response between $t_1 = 0$ and $t_N = t$

$$\int_0^t H_x^{net}(t) dt = -Idy \frac{\sigma\mu}{16\pi} \sum_{n=0}^{\infty} \frac{\Gamma(2n, z') - \Gamma(2n, \kappa z')}{2^{2n+1} n! (n+1)!} \quad (2.102)$$

Net moment response for $t_1 = t$ and $t_N = \infty$

The integration limits are given by $g(t_1) = z'$ and $g(t_N) = 0$. The solution of the integral between these integration limits is similar to (2.102), except here the $n = 0$ term is problematic due to the upper integration limit. Separating the $n = 0$ term yields

$$\begin{aligned}
 -I dy \frac{\sigma \mu}{16\pi} \sum_{n=0}^{\infty} \frac{1}{2^{2n+1} n! (n+1)!} \int_{z'}^0 (e^{-z} z^{2n-1} - \kappa^{2n} e^{-\kappa z} z^{2n-1}) = \\
 -I dy \frac{\sigma \mu}{16\pi} \left\{ \frac{1}{2} \int_{z'}^0 \left(\frac{e^{-z}}{z} - \frac{e^{-\kappa z}}{z} \right) + \right. \\
 \left. \sum_{n=1}^{\infty} \frac{1}{2^{2n+1} n! (n+1)!} \int_{z'}^0 (e^{-z} z^{2n-1} - \kappa^{2n} e^{-\kappa z} z^{2n-1}) \right\} \quad (2.103)
 \end{aligned}$$

The first integral due to the $n = 0$ term is solved by using the series expansion of the exponential function which gives rise to the following equation (Fullagar, 2007b),

$$\begin{aligned}
 \frac{1}{2} \int_{z'}^0 \left(\frac{e^{-z}}{z} - \frac{e^{-\kappa z}}{z} \right) &= \frac{1}{2} \sum_{k=0}^{\infty} \int_{z'}^0 \left(\frac{(-1)^k z^{k-1}}{k!} - \frac{(-\kappa)^k z^{k-1}}{k!} \right) dz \\
 &= \int_{z'}^0 \left(\frac{1}{z} - \frac{1}{z} \right) dz + \frac{1}{2} \sum_{k=1}^{\infty} \int_{z'}^0 \left(\frac{(-1)^k z^{k-1}}{k!} - \frac{(-\kappa)^k z^{k-1}}{k!} \right) dz \\
 &= -\frac{1}{2} \sum_{k=1}^{\infty} \left(\frac{(-z')^k}{k k!} - \frac{(-\kappa z')^k}{k k!} \right) \quad (2.104)
 \end{aligned}$$

The series expression in Equation (2.104) can furthermore be expressed in terms of Euler's constant $\tilde{\gamma}$, the Exponential Integral E_1 and a logarithm (Abramowitz and Stegun, 1965, p.229). The Exponential Integral is then expressed as an

incomplete Gamma function (Abramowitz and Stegun, 1965, p.230), viz

$$\begin{aligned}
 -\frac{1}{2} \sum_{k=1}^{\infty} \left(\frac{(-z')^k}{k k!} - \frac{(-\kappa z')^k}{k k!} \right) &= \\
 &= -\frac{1}{2} (-\tilde{\gamma} - \ln(z') - E_1(z') + \tilde{\gamma} + \ln(\kappa z') + E_1(\kappa z')) \\
 &= \frac{1}{2} (\ln(z') - \ln(\kappa z') + \Gamma(0, z') - \Gamma(0, \kappa z')) \\
 &= \frac{1}{2} \left(\Gamma(0, z') - \Gamma(0, \kappa z') + \ln\left(\frac{1}{\kappa}\right) \right) \quad (2.105)
 \end{aligned}$$

The expressions in Equation (2.103) for all $n > 0$ are well behaved and can be expressed in terms of the incomplete Gamma function as in Equation (2.100) and Equation (2.101). Therefore the contribution to the horizontal TEM moment between t and ∞ evaluates to

$$\begin{aligned}
 \int_t^{\infty} H_x^{net}(t) dt &= \\
 -I dy \frac{\sigma \mu}{16\pi} \left\{ -\frac{\ln(\kappa)}{2} + \frac{\Gamma(0, z') - \Gamma(0, \kappa z')}{2} + \sum_{n=1}^{\infty} \frac{\Gamma(2n, z') - \Gamma(2n, \kappa z')}{2^{2n+1} n! (n+1)!} \right\} \\
 = -I dy \frac{\sigma \mu_0}{16\pi} \left\{ -\frac{\ln(\kappa)}{2} + \sum_{n=0}^{\infty} \frac{\Gamma(2n, z') - \Gamma(2n, \kappa z')}{2^{2n+1} n! (n+1)!} \right\} \quad (2.106)
 \end{aligned}$$

Net moment response for $t_1 = 0$ and $t_N = \infty$

The integration limits transform as $g(t_1) = 0$ and $g(t_N) = \infty = z'$ and the integral can be solved with the results of the incomplete moments from the previous sections establishing the complete net-moment (Fullagar, 2007b),

$$\begin{aligned}
 \lim_{t_N \rightarrow \infty} \int_0^{t_N} H_x^{net}(t) dt &= \\
 \lim_{z' \rightarrow \infty} -I dy \frac{\sigma \mu}{16\pi} \left\{ -\frac{\ln(\kappa)}{2} + \sum_{n=0}^{\infty} \frac{\Gamma(2n, z') - \Gamma(2n, \kappa z')}{2^{2n+1} n! (n+1)!} \right\} \\
 = I dy \frac{\sigma \mu_0}{16\pi} \frac{\ln(\kappa)}{2} \quad (2.107)
 \end{aligned}$$

since $\lim_{z' \rightarrow \infty} \Gamma(2n, z') = 0$ and $\lim_{z' \rightarrow \infty} \Gamma(2n, \kappa z') = 0$

Horizontal-component TEM moment for a rectangular loop source

The result for the complete net-moment (Equation 2.107) can be solved by integrating analytically around the transmitter loop. With the definition of κ (Equation 2.95) it follows

$$M_x^1 = I \frac{\sigma \mu}{32\pi} \int_{y_1}^{y_2} \ln \left(\frac{y^2 + x_2^2}{y^2 + x_1^2} \right) dy \quad (2.108)$$

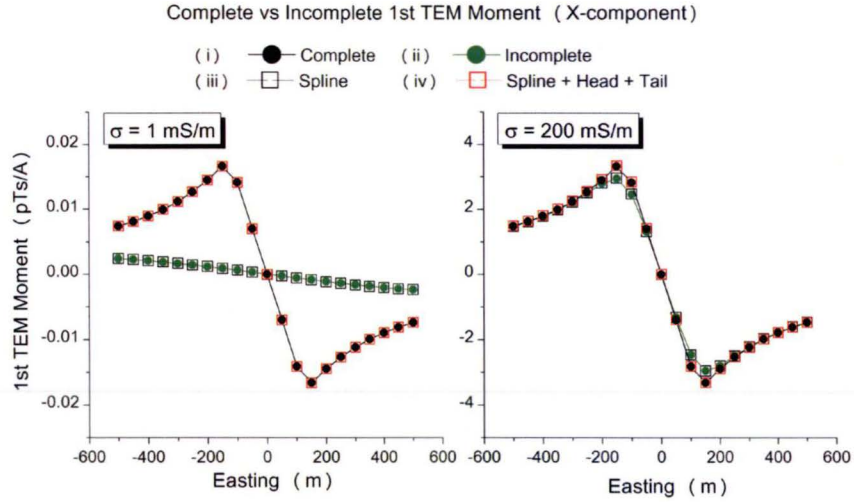


Figure 2.8 – First order horizontal (x) TEM moment of a half space with rectangular loop source. The configuration is the same as in Figure 2.7. Several responses are recorded: (i) the analytical complete TEM moment via Equation (2.107); (ii) the incomplete moment as evaluated using a combination of Equation (2.102) and Equation (2.106); (iii) numerical integration between t_1 and t_N labelled 'Spline'; (iv) the summed response of spline-integration, 'head' and 'tail'.

where $|x_2| < |x_1|$. Using

$$\int_{y_1}^{y_2} \ln(y^2 + a^2) dy = \left[y \ln(y^2 + a^2) - 2y + 2a \tan^{-1}\left(\frac{y}{a}\right) \right]_{y_1}^{y_2}, \quad (2.109)$$

the horizontal complete TEM moment for a rectangular loop source over a half space is given as (Fullagar, 2007b)

$$M_x^1 = I \frac{\sigma \mu}{32\pi} \cdot \left[y \ln\left(\frac{y^2 + x_2^2}{y^2 + x_1^2}\right) + 2x_2 \tan^{-1}\left(\frac{y}{x_2}\right) - 2x_1 \tan^{-1}\left(\frac{y}{x_1}\right) \right]_{y_1}^{y_2} \quad (2.110)$$

For finite time ranges, integration around the loop is performed numerically (Press et al., 2002, p.1054).

On display in Figure 2.8 are x-components of the complete and incomplete TEM moments of a half space with rectangular loop source. Shown are the responses for a resistive half space of 1 mS/m (left) and a conductive half space with 200 mS/m (right). As was the case for the vertical component in Figure

2.7, synthetic recordings are simulated at 50 m intervals along the centre line of a rectangular loop source with side lengths $250\text{E} \times 500\text{N}$, centred at $(0\text{E}, 0\text{N})$. The complete moment (i) is calculated with Equation (2.107). The incomplete moment (ii) is evaluated using a combination of Equation (2.102) and Equation (2.106) for integration limits t_1 and t_N . A numerical spline-based integration between first and last channel solves for the response labelled 'Spline' (iii) which is identical to the analytical incomplete moment response. The summed response of spline-integration, 'head' and 'tail' (iv) equals the analytical complete moment. Because induced currents will decay much faster for a resistive half space, the incomplete TEM moment gives a 'flat' anomaly shape. For a conductive half space, the incomplete and complete TEM moments are nearly identical because induced currents decay much slower.

2.8 TEM moments of measured data

The complete TEM moments are defined for a time-range from 0 to ∞ . Clearly, measured data only exist over a finite time range. In addition, measured data are for non-ideal waveforms exhibiting the effects of previous transmitter pulses. Retrieving the complete TEM moments as closely as possible for a set of measured data over a finite time range is important for the 3D inversion of TEM moments in order to maintain the linearity with respect to the time constant. The inversion benefits from the linear relationship. Incomplete TEM moments defined over finite time-ranges do not exhibit this linear relationship, rendering the inversion process non-linear. Although the inversion scheme is capable of non-linear inversion, the execution time will increase significantly.

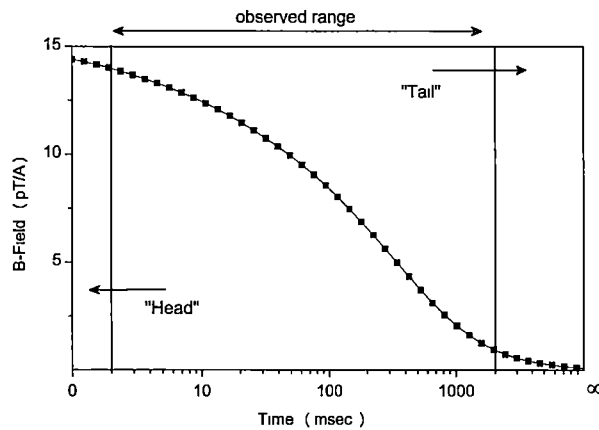


Figure 2.9 – Schematic of Head and Tail contribution to TEM moment response. Very early times are denoted 'head' and very late times 'tail' contributions. 'Head' and 'tail' responses are calculated by extrapolation, based on a half space conductivity model for the times in question.

Chapter 3

Approximate 3D modelling of TEM moments

Introduction Approximate 3D modelling computes the TEM response of the ground with accuracy traded for speed so as to accelerate the computations. The forward model solution presented in this chapter employs TEM moments of a dense network of point conductors (magnetic dipoles) to approximate the EM response of 3D targets. Electromagnetic interactions are ignored and linear superposition of point-conductor responses yields the approximate TEM moment response of the 3D target. Consequently, computation of the combined response of a 3D assembly of point-conductors is very fast.

The 3D forward modelling approach presented here is described in the context of fixed loop EM ground systems. However the method is flexible and applicable to moving-loop as well to airborne problems. The model volume is divided into a 3D grid comprised of cubic cells. Typically, for ground-loop TEM, the model contains the transmitter loop and should extend well beyond the receiver locations to avoid edge effects. The depth of penetration is judged with reference to conductivity-depth pseudo-sections and the vertical model dimension is selected accordingly. Because point conductors are derived for cubic cells, all subcells of the model space are of fixed cubic dimension and may range from centimetres to hundreds of meters, depending on the size of the target and computer memory. The 3D model space is referred to as 'Voxel', which is the terminology of GOCAD (Paradigm™) for a three-dimensional set of voxels (Jessell, 2001; Mallet, 2002). GOCAD is a commercial software solution for modelling geological objects in 3D.

The TEM moment forward response is modelled as a combination of a continuous background and a discrete target response. The background is represented as a homogeneous half space, while the target is comprised of a distribution of point conductors on the 3D grid. For the background response, analytical expressions are utilised for the first order TEM moment of a half space excited by a rectangular loop source. The moment contribution of a point-conductor is computed using a simplified form of the expression for a sphere in free space which is proportional to its time constant. Linear superposition of a dense net-

work of point-conductors approximately reproduces the TEM moment response of a confined conductor if the time constant of the conductor is adopted by each point-conductor. 3D forward modelling of time constants employing point conductors is scale invariant, i.e. given a conductor's time constant, the TEM moment response does not substantially change with subcell dimension

This chapter describes the implementation of the TEM moment forward algorithm for arbitrary anomalous volumes. The algorithm described herein is implemented as a set of Fortran 95 modules. Following the introduction of the background response, the target response is described and the linear superposition of point conductors is tested for free space examples. The section thereafter qualitatively analyses the impact of ignoring host-rock EM interaction. The chapter concludes with a comparison between exact and approximate (point conductor) TEM moment responses for 3D targets in a conducting half space. The exact moments are calculated via integration of decays generated by rigorous 3D algorithms.

3.1 Background response

Approximate 3D modelling of TEM moments requires addition of a continuous background response to a discrete target response. The discrete target response is defined from superposition of the responses of point conductors defined on a 3D grid (Section 3.2). In the basic formulation of the forward algorithm each point conductor inherits the orientation of the primary field, therefore the magnetic dipole orientations associated with each point conductor are effectively frozen in the directions of the primary field, which as a consequence prohibits current diffusion. For this reason a continuous background is introduced, so that the TEM moment response of the host-rock is treated as a continuous background response in the model. The background response is computed as the 1st order TEM moment of a homogeneous conducting half space, introduced previously in Chapter 2, Equations (2.89) and (2.107).

In ground-loop TEM, the near-transmitter zone is most responsive at early delay times and ground sensitivity is pronounced in the vicinity of the transmitter loop. Since the target algorithm effectively approximates free-air responses of 3D conductors, the half space response represents the air-earth interface as well as the pronounced sensitivity near the transmitter loop. Moreover, the induced migrating host-current is characterised by the TEM moment response of a continuous conducting half space. Thus, the half space response captures early-time and near-transmitter responses as well as the late time response of an extensive unbounded medium. This concept underlies the assumption, discussed in Section 3.4, that electromagnetic interactions between host and target may tolerably be ignored. As a first step in data interpretation, conductivity-depth imaging is carried out which yields a conductivity model from which a half space conductivity may be inferred. Generally, the background model is not restricted to half space models, and can be extended to layered earth models. For the algorithm discussed herein, the background will always be composed of a conducting half space due to its computational simplicity and speed.

3.2 Discrete target response

The target is defined on a 3D grid and is comprised of closely-packed cubic cells, each containing a point conductor at its centre. Electromagnetic interaction between volume elements is ignored. Effectively, the discrete target response is the sum of the contributions from a dense network of point conductors, or magnetic dipoles, where each dipole inherits the orientation of the exciting primary field. The effect of the primary magnetic field is described in Section 3.2.2.

The calculations are in terms of the time constant of the associated point conductor of each cell. In this formulation, the forward algorithm is scale invariant, so that different subcell sizes give almost the same TEM moment response for the same time constant. Summation of the TEM moment responses of all cells approximately reproduces the TEM moment response if the point conductors inherit the time constant of the body to which they belong.

The point conductor formulation is mathematically equivalent to the formulation of a sphere under uniform excitation. However, in the point conductor approach, the effective volume is the volume of the cubic cell, not the volume of a sphere, where the time constant, not the conductivity, is adopted as the electrical property of the cell. This is because the TEM response from an extensive conductive body should be almost independent of the cell size used to model it. If conductivity were maintained constant as cell size is decreased, the time constant would decrease in proportion to $L \times L$, where L is the cube dimension.

3.2.1 Calculating the target response

For the forward algorithm, only the first order TEM moment $\mathbf{M}^{(1)}$ is used, which has been defined in Chapter 2 (Equation 2.7). For confined conductive bodies in free space the first order TEM moment is proportional to the time constant τ . In this sense, applying the moment transform linearises the TEM problem. Implementation of the approximate 3D TEM forward modelling scheme consists of superposition of the TEM moments of all constituents of a subcelled anomalous volume together with the background response. Superposition relates the TEM moment at a particular measurement location (x, y, z) , to a distribution of point conductors (Equation 2.66) and is stated for the 1st-order TEM moment as (e.g. Blakely, 1995, p.197)

$$\mathbf{M}(x, y, z)^{(1)} = \mathbf{M}_0(x, y, z)^{(1)} + \sum_{k=1}^K \mathbf{G}_k(\mathbf{r}_k) \tau_k \quad (3.1)$$

where $\mathbf{M}_0(x, y, z)^{(1)}$ denotes the background moment discussed earlier, K is the number of cells defined for the anomalous volume and summation is carried out over k ; \mathbf{r}_k is the position vector that connects the observation point (x, y, z) and cell centre of the k -th cell; τ_k is the time constant of the k -th cell. \mathbf{G}_k is the geometrical coupling factor of the k -th cell which corresponds to a point-conductor or magnetic dipole at the cell centre and was given earlier by Equation (2.67):

$$\mathbf{G}_k(\mathbf{r}_k) = B_{0,k} V_k \frac{3(\hat{\mathbf{b}}_k \cdot \hat{\mathbf{r}}_k) \hat{\mathbf{r}}_k - \hat{\mathbf{b}}_k}{4\pi r_k^3} \frac{\pi^2}{10} \quad (3.2)$$

where $B_{0,k}$ is the magnitude of the primary magnetic induction at the centre of the k -th cell, and V_k is the volume of the k -th cell.; $\hat{\mathbf{r}}_k$ is the unit vector parallel to position vector \mathbf{r}_k . In the simplest form of the forward algorithm, the unit vector $\hat{\mathbf{b}}$ is parallel to the primary field vector \mathbf{B}_0 .

The point conductor formulation is consistent with the analytic solution for the TEM moment of a sphere if the product τV is maintained constant as the sphere radius decreases; in the limit, the TEM moment response equals that of a point conductor which has previously been defined in Equation (2.60). In the context of fixed-loop TEM, the primary magnetic field is calculated for a rectangular loop source in free space employing the law of Biot-Savart. Other inductive sources however, like magnetic dipoles for AEM, can easily be adopted. Equation (3.1) is implemented as a set of Fortran 95 modules as the principal algorithm for calculating the TEM moment response of a 3D target.

3.2.2 Effect of primary field and conductivity gradient

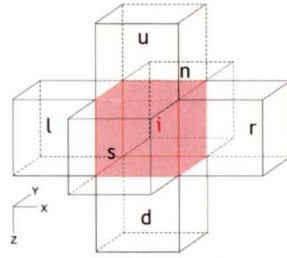


Figure 3.1 – Local subcell and adjacent cells in 3D mesh.

Using point-conductors, current migration effects in compact conductors cannot be replicated because induced vortex currents are in effect confined to each subcell and the currents always flow perpendicular to the primary field direction at the point conductor location. However, current flows preferentially parallel to the boundaries of good conductors, i.e. orthogonal to conductivity gradients. Thus EM induction is controlled by the component of the inducing field which is parallel to the local conductivity gradient. During this study, the algorithm used for inversion (Chapter 5) exclusively employs the basic formulation (Equation

3.2) where the point conductor inherits the orientation of the primary field. However, a modified forward algorithm which adjusts the components of the primary field according to the conductivity gradient is in an experimental stage (c.f. Appendix A). The modified forward algorithm defines local 'next-neighbour' gradients based on the difference in conductivity or time constants of adjacent cells. Denoting the current cell with subscript 'i' and the six adjacent cells with subscripts 'l', 'r' and 'n', 's' and 'u', 'd' (Figure 3.1), the differences are defined as:

$$\begin{aligned} \Delta_x^p &= \tau_r - \tau_i & \Delta_y^p &= \tau_n - \tau_i & \Delta_z^p &= \tau_d - \tau_i \\ \Delta_x^n &= \tau_l - \tau_i & \Delta_y^n &= \tau_s - \tau_i & \Delta_z^n &= \tau_u - \tau_i \end{aligned}$$

where superscripts 'p' and 'n' refer to the values of the 'positive' or 'negative' face. Attached to the definitions of the local gradients are two conditions. First,

if the time-constant of a cell is below a threshold, the time-constant is treated as zero during assignment of the difference. Second, if the ratio of the involved cell time-constants are within a certain margin, they are treated as equal during assignment of the difference. One way to define a conductivity or time constant gradient is to adopt them from the differences with maximum amplitude (Fullagar, 2008a):

$$\begin{aligned}\nabla\tau_j &= \frac{\Delta_j^p}{L} & \text{if } |\Delta_j^p| \geq |\Delta_j^n| \\ \nabla\tau_j &= \frac{\Delta_j^n}{L} & \text{otherwise}\end{aligned}$$

where $\nabla\tau_j$ are the components of the gradient of τ with $j = x, y$ or z and where L is the cell dimension.

Gradient contrasts define geometric boundaries of geoelectrical structures. Certain structures impose a strong constraint on the induced vortex current flow, for example a horizontal slab where currents will predominantly flow in the horizontal plane of the slab at late times if the lateral extent is much larger than the vertical extent. In order to model this current flow correctly, the effective primary field has to be adjusted accordingly. Strong gradients (hence conductor boundaries) can be identified if the differences of the adjacent cells are tested accordingly. If a possible boundary is detected, the gradient is set to the most reasonable direction. According to this simple model, the effective inducing field \mathbf{B}_σ , acting on the target cell is the component of the primary field in the direction of the conductivity gradient; thus

$$\mathbf{B}_\sigma = (\mathbf{B}_0 \cdot \hat{\mathbf{n}}_\sigma) \hat{\mathbf{n}}_\sigma \quad (3.3)$$

where \mathbf{B}_0 is the primary field and where $\hat{\mathbf{n}}_\sigma$ is the unit vector in the direction of the gradient $\nabla\tau_j$. Thus \mathbf{B}_σ is zero if the primary field is perpendicular to the conductivity gradient; this tallies with the physical notion of null coupling. If the conductivity gradient is zero, the unmodified primary field in zero gradient cells is adopted.

3.2.3 3D grid time constants

As the model space is subdivided into a 3D grid of cubic cells, each cell is assigned a time constant. The time constant of a confined conductor serves to classify the conductor quality. The time constant is defined as the time interval over which the late-time signal decreases to $1/e$ of its initial value, i.e. characterises the exponential decay. A general expression for the time constant (Nabighian and Macnae, 1991, p.467) can be given as

$$\tau = K \cdot \mu\sigma \cdot A \quad (3.4)$$

with K a numerical coefficient and A a geometrical coefficient proportional to the effective cross-section of the conductor. Usually, the geometrical factor will be difficult to estimate for geologically realistic objects.

For the 3D grid it is reasonable to regard the time constant τ_k of a cubic cell as approximately equal to that of a sphere having the same volume and conductivity; this is implicitly the position taken by Newman and Hohmann (1988, eq.35). The sphere time constant (Kaufman and Eaton, 2001, p 172) for a sphere with radius a and conductivity μ is defined by:

$$\tau_s = \frac{\sigma \mu a^2}{\pi^2} \quad (3.5)$$

From the condition of equal volumes for sphere and cubic cell, the radius is calculated as:

$$V = L^3 = \frac{4\pi}{3} a^3 \Rightarrow a = \left(\frac{6}{\pi}\right)^{1/3} \left(\frac{L}{2}\right) \quad (3.6)$$

and on this basis, the time constant τ_k of a cubic cell in the 3D model grid can be defined as:

$$\tau_k = \sqrt[3]{\left(\frac{6}{\pi}\right)^2 \left(\frac{L}{2}\right)^2} \frac{\sigma \mu}{\pi^2} \approx \frac{\sigma \mu L^2}{25.6} \quad (3.7)$$

where L is the cubic cell dimension.

Simple structures such as spheres and thin plates in free space have analytical expressions for their time constants which are employed for testing the approximation as illustrated in subsequent Section 3.3. Generally however, the time constant of a complex body is an empirical quantity as estimated from the time-domain decay curves by fitting an exponential to the late time part of the decay response (Nabighian and Macnae, 1991, p.459). Estimation of reliable time constants is furthermore complicated if the target resides in a conductive host-rock environment.

The following procedure automatically calculates the time constant from an observed TEM moment response. In the context of forward modelling, observed response means here the response for a certain model as obtained by other methods and third-party software. Because the time constant has a linear relationship with respect to the first-order TEM moments, a simple linear regression fits the amplitudes of the observed response to the amplitudes of the model response as calculated from an initial estimate of cell time constants with the point conductor algorithm. Initial estimates may be based on time constant analysis of the decays or apparent conductivities from conductivity-depth imaging are assigned as initial time constants. The result of the linear regression rescales the initial estimate of the cell time constants to fit the observed response in a least-squares sense.

Let $\mathbf{d} \in \mathbb{R}^N$ be the data vector of the observed response for N data points and $\mathbf{c}(\boldsymbol{\tau}) \in \mathbb{R}^N$ the vector of the calculated response as a function of the cell time constants $\boldsymbol{\tau} \in \mathbb{R}^K$ for K cells. The relationship between observed and model TEM moments is linear with respect to time constants:

$$\mathbf{d} = \mathbf{c}(\boldsymbol{\beta} \cdot \boldsymbol{\tau}) = \boldsymbol{\beta} \cdot \mathbf{d}(\boldsymbol{\tau})$$

Therefore, if the factor β is known, initial estimates of cell time constants can be rescaled as to match the observed response as close as possible. The rescaling factor β is found by minimising the sum of squares of measurement misfits for a set of N data points, viz.:

$$\min S = \sum_{n=1}^N (d_n - \beta \cdot c_n)^2, \quad (3.8)$$

Setting the derivative with respect to β to zero, and solving for β results in:

$$\beta = \frac{\sum d_n c_n}{\sum c_n^2} \quad (3.9)$$

As a measure of the quality of the fit, the dimensional root-mean-square (RMS) can be utilised; the RMS is quoted in data units and is defined as

$$\text{RMS} = \sqrt{\frac{1}{N} \sum_{n=1}^N (d_n - c_n)^2}$$

3.3 Linear superposition of point conductors

In the following section the linear superposition of TEM moment responses from point conductors is illustrated for the examples of a large sphere and a thin vertical plate, both situated in free space and excited by a rectangular loop source. In both examples the anomalous volume is subjected to discretisation into subcells with dimension $L = 2$, $L = 5$ and $L = 10$ where each subcell contains a point conductor at its centre with the time constant of its 'parent' conductor. The number of cells, K , of the subcelled volume is given by the ratio of the anomalous volume, V_A , to the subcell volume V_L .

3.3.1 Subcelled sphere in free space

Let a large sphere have a radius of $R=50$ m and a time constant of $\tau \simeq 0.32$ msec (conductivity is 1 S/m). Depth-to-top of the sphere is 200 m and centre-coordinates are (0E, 0N). The sphere is energised by a fixed transmitter loop, centred at (450E, 0E) with side lengths of 100 m \times 200 m. A survey line traverses the centre of the sphere at 20 m intervals from -200E to 200E.

The exact z-component of the first order TEM moment of the large sphere together with the approximate response for three different subcell sizes is depicted in Figure 3.2. The exact sphere response was calculated with the TEM moment program introduced earlier in Chapter 2.6.1. Each subcell response was calculated for the same time constant as the large sphere. Subcells whose centres lie within the radius of the large sphere are members of the subcelled volume. The number of cells for each subcell dimension of 2 m, 5 m and 10 m are, respectively,

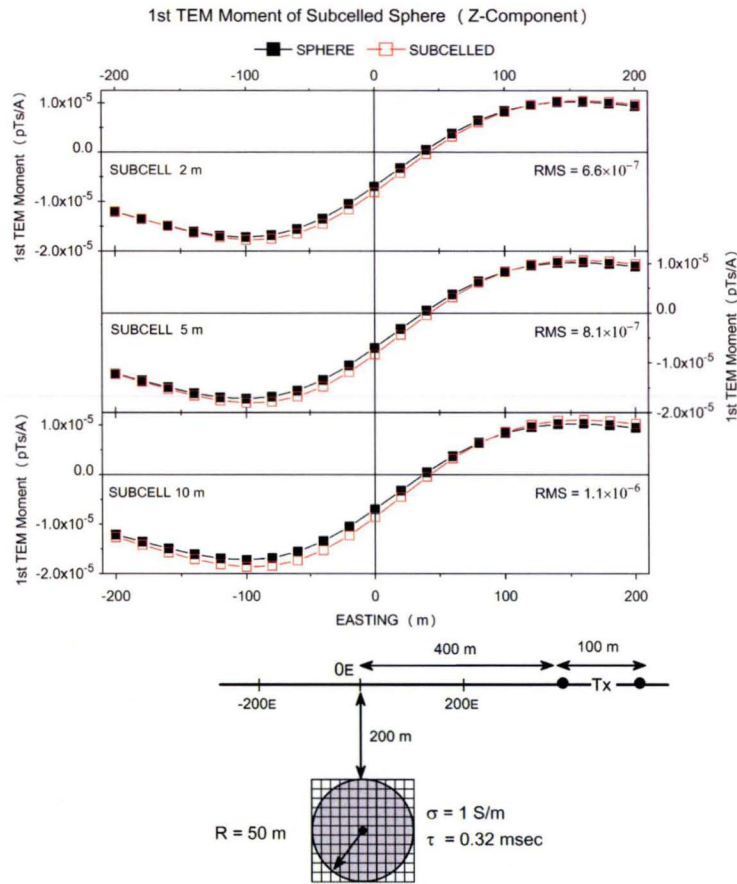


Figure 3.2 – TEM moment response of a subcelled sphere in free-space for a 50 m sphere energised by a fixed transmitter loop. The panels show the responses for the subcelled sphere for various subcell dimensions of 2 m (top), 5 m (middle) and 10 m (bottom). Superimposed is the response of the large sphere in the dipole approximation (uniform field excitation). The number of cells for each subcell dimension are $V_2 = 65450$, $V_5 = 4189$ and $V_{10} = 524$.

$V_2 = 65450$, $V_5 = 4189$ and $V_{10} = 524$. The large sphere response has been calculated as a dipole term at the sphere centre (uniform field excitation) which is acceptable given the distance to the transmitter loop which is approximately $9R$ (c.f. Chapter 2.3). In fact, the RMS misfit between the uniform field approximation and the exact response for multipoles up to order 15 is very small with $\text{RMS} = 2.9 \times 10^{-7}$ pTs/A. The differences between the response curves of the large sphere as calculated for the uniform field approximation and the subcelled sphere are small, which is indicated by the RMS values in the plot of Figure 3.2.

The least-squares optimisation (discussed in Section 3.2.3) for the sphere and the approximated response curves give the following values

$$\beta_2 = 0.99 \quad \beta_5 = 0.97 \quad \beta_{10} = 0.94$$

where the subscript denotes the subcell dimension. The least-squares values are close to unity, demonstrating that the time constant value is close to the optimal value in a least-squares sense. The subcell size with $L=2$ gives the most accurate response because of the higher degree of discretisation.

3.3.2 Subcelled plate in free space

The next example illustrates the TEM moment response of a subcelled thin-plate in free space. A plate and a sphere respond differently to the primary exciting field. A sphere supports current flow in any direction; in the case of the plate, the effective inducing field \mathbf{B}_σ (Equation 3.3) is the component of the primary field in the direction perpendicular to the plane of the plate where the strongest conductivity gradient occurs (Figure 3.3). As described in Section 3.2.2, eddy currents in each subcell will be aligned perpendicular to the local primary field vector in the basic form of the forward algorithm. For the plate example, the calculations are carried out twice: first with the basic configuration employing the full primary field, and then with the simple gradient scheme where only the primary field component is accepted which is perpendicular to the plane of the plate as to simulate the true plate / primary field interaction (Figure 3.3).

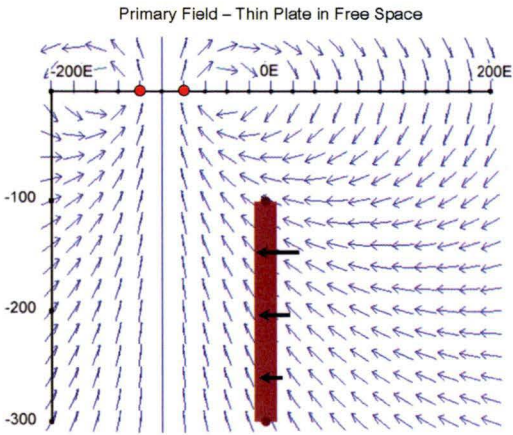


Figure 3.3 – Primary magnetic field at the location of a thin plate in free space. The effective, inducing component of the primary field is perpendicular to the plane of the plate. The inducing component is schematically indicated by the superimposed black arrows at the plate location. The transmitter loop location is indicated by the two red circles on the Easting axes.

The time constant of a thin plate is given by Lamontagne (1975, p.160) and Nabighian and Macnae (1991, p.470) as

$$\tau_p = \mu \cdot t \sigma_p \ell / 10 \quad (3.10)$$

where $t\sigma_p$ is the plate's conductance; t the plate's thickness, σ_p its conductivity and ℓ is an average dimension of the plate, calculated as $\ell = 1.815 \sqrt{(area/\pi)}$, which follows by equating the time constant of a disk with radius a and conductance S to the plate's time constant (Fullagar, 2007b). The time constant of a disk with conductance S and radius a is given by Kaufman and Eaton (2001, p.233) as

$$\tau_d = \mu \cdot S \cdot a / 5.51 \quad (3.11)$$

In the following model the plate has a conductivity of 2 S/m and a width of $t = 20$ m; strike length and depth extent are $SL = 300$ m and $DE = 200$ m respectively. Based on Lamontagne's formula, the time constant of the plate evaluates as $\tau_p = 1.26$ msec. A fixed rectangular transmitter loop is centred at (-100E, 0N) with side lengths of $100E \times 150N$. A survey line traverses the centre of the plate at 20 m intervals from -200E to 200E. Time domain calculations are carried out for 45 channel delay times ranging from 0.01 msec to 1400 msec. As in the sphere example the subcell dimensions are $L = 2$, $L = 5$ and $L = 10$ where each subcell contains a point conductor at its centre with the same time constant as the 'parent' plate.

The plate response was calculated with the plate modelling software MAXWELL (Duncan and Perry, 2008) using the 'thick plate' option and subsequently transformed to the moment domain by numerical integration, employing splines (Davis and Rabinowitz, 1975). MAXWELL employs the concept of current filaments as an approximation to the EM response of a thin plate (Barnett, 1984; Duncan, 1987). The MAXWELL solution simulates a thick plate by placing multiple plates on the external faces.

The z-component of the first order TEM moment of the plate together with the subcelled response for three different subcell sizes is shown in Figure 3.4. The Figure displays the result of the subcelled responses as calculated with two variants of the forward algorithm: the full primary field and the horizontal primary field component. The displayed response curves for the gradient method are for a re-scaled time constant of $\tau_{fit} \simeq 2.16$ msec as obtained from the least-squares fit. The relative large rescale factor for τ_{plate} may result from the approximate nature of the MAXWELL solution for a thick plate. The least-squares optimisation give the following values for the various subcell sizes

$$\beta_2 = 2.17 \quad \beta_5 = 2.17 \quad \beta_{10} = 2.17$$

The rescale factors are all identical up to the second figure, because the subcells all fit neatly into the plate volume. Only the response of the subcelled volume as calculated with gradient method gives a reasonable good fit to the plate response, especially at the location of plate. The differences between the subcelled response (gradient method) and the plate response is indicated by the RMS value which for all subcell dimensions is 0.002 pTs/A, about a third from the peak plate response.

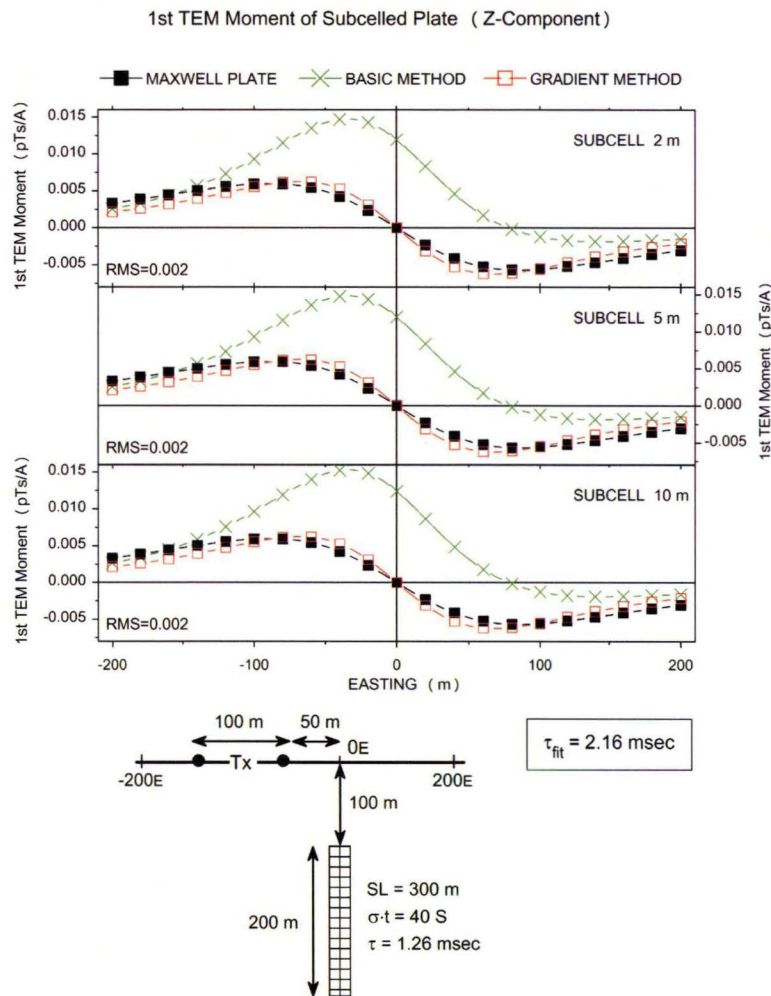


Figure 3.4 – TEM moment response of a subcelled thin plate in free-space for a plate with a conductivity of $\sigma = 2 \text{ S/m}$; thickness $t = 20 \text{ m}$, strike length $SL=300 \text{ m}$ and depth extent of $DE=200 \text{ m}$. The panels show the responses for the subcelled plate for various subcell dimensions. The number of cells for each subcell dimension are $V_2 = 65450$ $V_5 = 4189$ $V_{10} = 524$. The subcelled responses are calculated with the basic method (full primary field) and with the gradient method (horizontal primary field component). The response curves for the gradient method are calculated for cell time constants which have been rescaled with a least-squares fit with $\tau_{\text{fit}} = 2.16 \text{ msec}$ (see text). Superimposed is the response of the thin plate as calculated with MAXWELL. Only the gradient method can give a good fit to the plate response. The RMS values are given for the gradient method.

3.3.3 Proximity of transmitter source

Since the point conductor response is also a function of the primary field vector \mathbf{B}_0 , the question arises how the proximity of the transmitter loop affects the accuracy of the approximate TEM moment response. It is expected that if a shallow target in proximity to the transmitter is represented by a dense cubic network of point conductors, the TEM moment response will still be fairly accurate, provided the subcells have been assigned the appropriate time constants. However, since the point conductor model is unable to replicate current migration effects in large conductors because of the 'frozen dipole direction' (Section 3.2.2), it is important to distinguish compact conductors from unbounded conductors. A conductor is considered compact if it has a typical dimension which is not much greater than the transmitter loop dimension. If a conductor is located close to the transmitter loop and can be considered very large in relation to the transmitter loop, it will behave like an unbounded conductor. The background response, however, will (hopefully) capture the response of an extensive conductor.

The following examples illustrate the effect of a transmitter loop close to a compact subcelled volume. In the first example a sphere with a radius of $R = 50$ m and time constant of 0.32 msec ($\sigma = 1$ S/m) is placed at different depths, with depth-to-top $R/2$, R , $2R$ and $4R$, and excited by a fixed square transmitter loop centred over the top of the sphere. In the second example a small, shallow sphere with a radius of 1 m is excited by a fixed square transmitter loop for different loop sizes; the sizes of the transmitter loop are, respectively, R , $2R$ and $4R$.

For the first example the subcell dimension is $R/10$ (5 m) which resulted in an accurate approximation when the transmitter loop is far away (Figure 3.2). Because the transmitter in the following examples is relatively close to the sphere, the exact TEM moment responses of the sphere have been calculated by taking into account higher order multipoles up to 15 (c.f. Section 2.3). Additionally, calculations are repeated for the dipole approximation (uniform field excitation). The square transmitter loop is centred at (0E,0N) with side lengths of $2R$ (100 m). A survey line traverses the centre of the sphere at 20 m intervals from -200E to 200E. The vertical component TEM moment results are depicted in Figure 3.5. If the cubic cells are assigned the time constant of the large sphere, the subcelled response overshoots the peak sphere response, but becomes more accurate as the sphere is moved to greater depths. At receiver locations larger than ± 100 Easting, the response curves effectively coincide.

The second example illustrates the effect of transmitter loop size on the TEM moment response for a shallow, small subcelled sphere. The radius of the sphere is $R = 1$ m, depth-to-top is $R/2$. The time constant of the sphere is $\tau = 1.3 \times 10^{-4}$ msec ($\sigma = 1$ S/m) and the subcell dimension is $R/20$ (0.1 m), resulting in 4224 cells for the subcelled sphere with a volume ratio of 0.991. The results are shown in Figure 3.6 and illustrate that the response of the shallow, subcelled sphere gets more accurate as the transmitter loop gets larger.

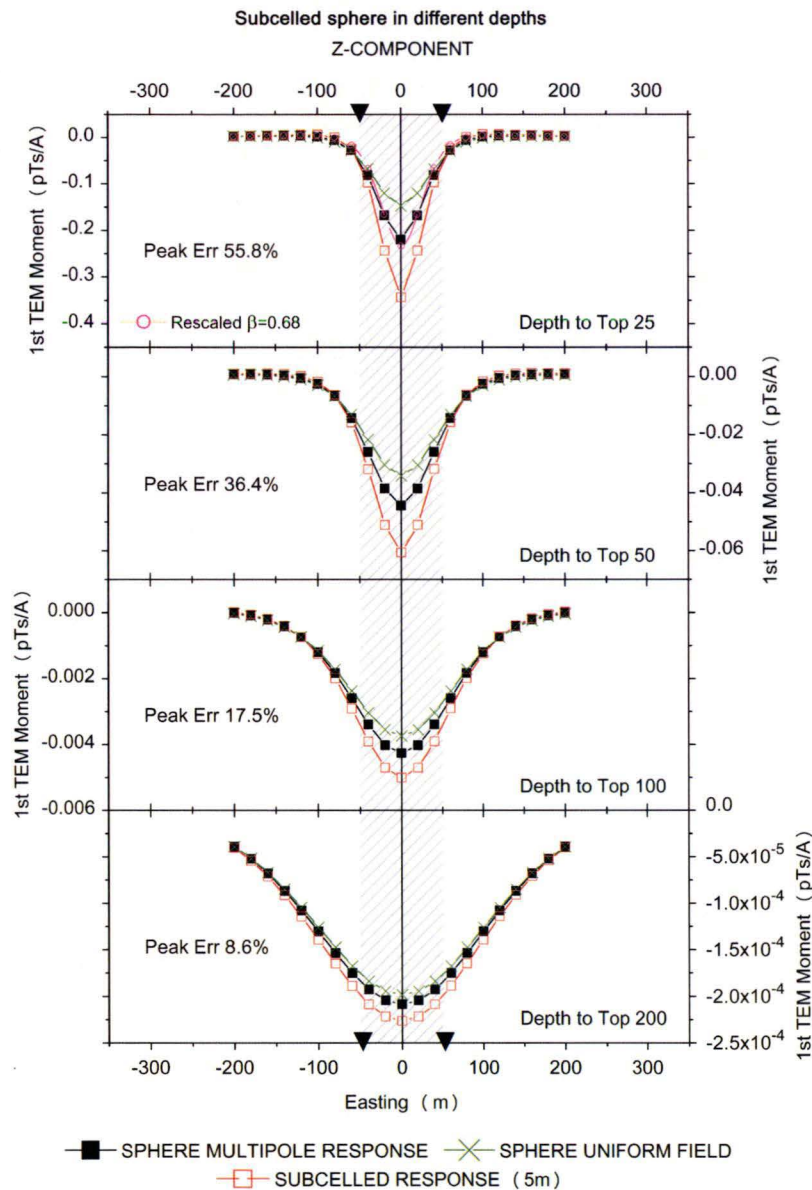


Figure 3.5 – Superposition of point conductor responses for a sphere in different depths. The sphere has a radius of 50 m and a time constant of 0.32 msec. Cubic cell dimension is 5 m. The fixed transmitter loop is centred above the sphere at coordinates (0E,0N) with side lengths of 100 m as indicated by the triangles on the Eastings axis. The grey-shaded area illustrates the location of the sphere. The vertical component TEM moment responses of the large sphere are displayed for uniform field excitation and for multipole field excitation. The error values indicate the relative error at the peak location as compared with the multipole response.

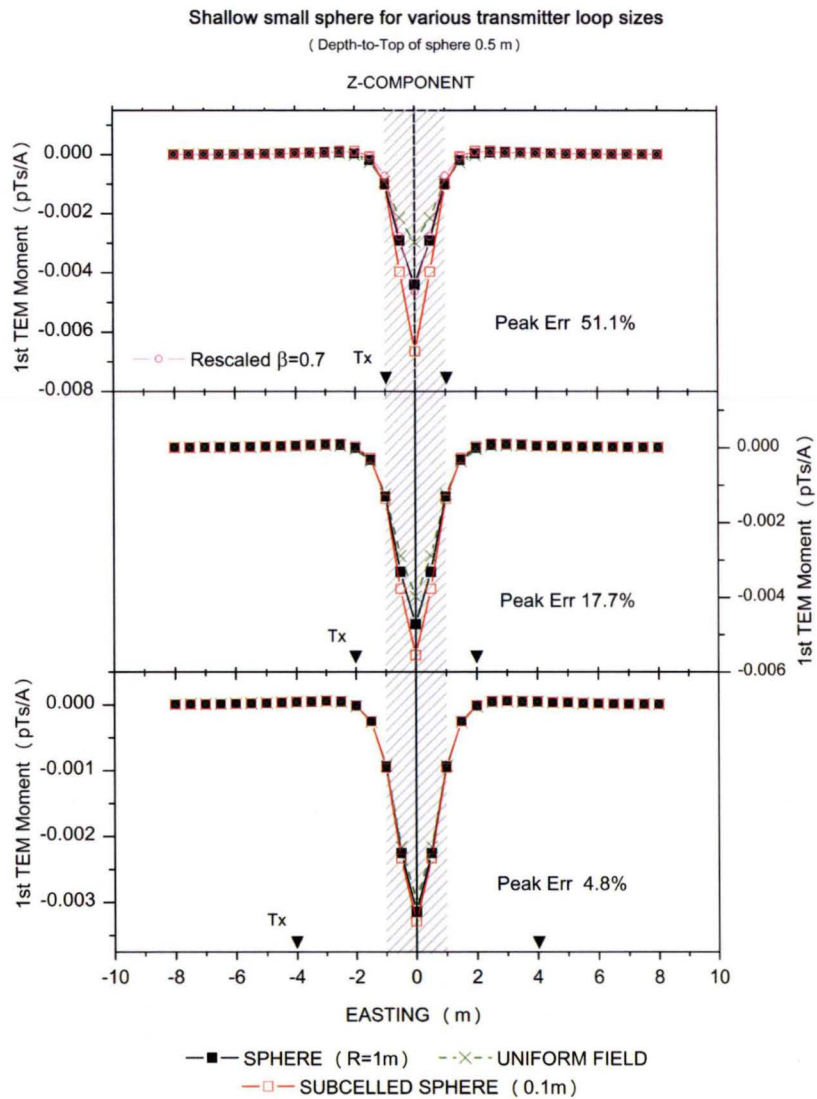


Figure 3.6 – Exact and approximate vertical component TEM moment response for a small shallow sphere for various transmitter loop sizes. A survey line traverses over the centre of the small sphere at intervals of $R/2$ m from $-8R$ to $8R$. Sphere radius is 1 m with time constant $\tau = 1.3 \times 10^{-4}$ msec. The subcells have dimension $L = 0.1$. On display are curves for the subcelled response, the sphere response for multipole expansion up to 15 and for the uniform field approximation. The transmitter loop varies from R (top panel) to $2R$ (middle panel) and for $4R$ (bottom panel). The error values indicate the relative error at the peak location as compared with the multipole response.

Generally, the subcelled sphere responses for both examples match the target responses more accurately for conditions where the primary field can be considered uniform. The primary field is less variable and more uniform at greater depths as it is likewise beneath the large transmitter loop at all depths. This is noticeable from the bottom panels in Figures 3.5 and 3.6 where the differences of the large sphere responses for the uniform field approximation and the multipole expansion are small.

The shapes of the approximate TEM moment anomalies resemble the exact profiles. The subcelled TEM moment responses for both examples with the largest errors have been subjected to the linear least-squares scheme (with respect to the multipole sphere response) and the rescaled response is superimposed in the top panels of both Figures 3.5 and 3.6 (open circles mark the rescaled response). The rescaled approximate TEM moment response curves closely resemble the multipole sphere response. The rescale factor in case of the large sphere is $\beta = 0.68$ which gives a rescaled time constant of $\tau = 0.22$ msec and in case of the small sphere $\beta = 0.7$, giving a time constant of $\tau = 8.9 \times 10^{-5}$ msec. The approximate forward modelling algorithm recovers the profile shape very well, albeit for a smaller time constant.

3.4 Effect of host-rock

The approximate TEM moment forward algorithm presented above ignores possible electromagnetic interactions between cells comprising the anomalous volume. Because the TEM moment method is intrinsically a late-time method, mostly, this approach is justified in resistive environments. Neglect of interactions, however, may lead to systematic errors in conductive environments where the effect of one conductive volume modifies the transient electromagnetic field of neighbouring volumes.

This section explores the inaccuracy associated with the TEM moment method when neglecting electromagnetic interaction for the case of a sphere in a uniform host. The analysis is based on the results of Lee (1980) which are greatly simplified in Lee (1983) in which an asymptotic semi-analytical formulation for the transient coincident loop EM response of a conductive sphere buried in a conducting half space is presented. Lee's formulation is convenient, since it decouples the combined electromagnetic response into individual terms for half space, sphere and interaction. Thus Lee represents the net dB/dt response as the sum of three contributions,

$$V = V_h + V_s + V_i \quad (3.12)$$

where V_h is the half space voltage response for a coincident loop with step current shut-off (e.g. Raiche and Spies, 1981); V_s is the contribution from the sphere as if it were placed in free space; and V_i denotes the interaction term.

The interaction term includes both, inductive and galvanic coupling between host and sphere (Chapter 1.2.2). Galvanic coupling arises due to electrical charges which develop at surfaces dividing domains with different conductivity values. If axial symmetry is exhibited, and the primary electrical field does not intersect surfaces between media characterised by different conductivities, only inductive coupling arises (Kaufman and Keller, 1985, p.483).

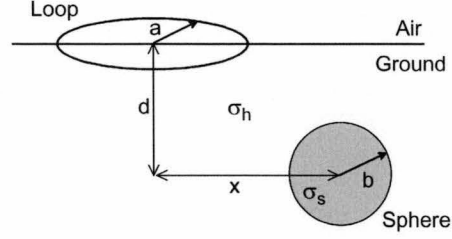


Figure 3.7 – A coincident loop system traversing a buried sphere after Lee (1983, Fig.1). The loop radius is a ; sphere radius is b . The host conductivity is denoted by σ_h and the sphere conductivity by σ_s . The horizontal distance from the loop centre to the sphere centre is defined as x and the vertical distance as d . The presented expressions for the secondary voltage response are primarily accurate for $\sigma_h \mu d^2 / t \lesssim 0.2$ (Lee and Thomas, 1992).

Figure 3.7 shows a sphere of radius b and conductivity σ_s buried in a conducting half space with conductivity σ_h . A coincident loop system with radius a records the transient voltages for an ideal step current shut-off. From Lee (1983), the time-domain voltage-response functions V_h , V_s and V_i for coincident loop measurements are given by:

$$\begin{aligned}
 V_h &= \frac{a \mu I_0 \sqrt{\pi}}{t} \frac{\sqrt{\sigma_h \mu a^2}}{\sqrt{4t}} \sum_{k=0}^{\infty} \frac{2(-1)^k (2k+2)!}{k! (k+1)! (k+2)! (2k+5)} \left(\frac{\sigma_h \mu a^2}{4t} \right)^{k+1} \\
 V_s &= \frac{3 \mu b^3 I_0 \pi}{a^2 \beta^2} \cdot (\mathcal{G}_1^2 + \mathcal{G}_2^2) \cdot \sum_{n=1}^{\infty} \exp(-n^2 \pi^2 t / \beta^2) \\
 V_i &= \frac{2}{5} \alpha^3 a \mu I_0 \mathcal{G}_1 J(t) + \frac{2}{3} \frac{\mu b^3}{a^2} \cdot (\mathcal{G}_1^2 + \mathcal{G}_2^2) \cdot C(t) \\
 &\quad + \frac{4}{3} \frac{\mu I_0 b}{t^{6/2}} \mathcal{G}_3^2 \cdot (\sigma_h \mu b^2)^{4/2} + \frac{a^2}{b^2} \frac{\sqrt{\pi}}{4} \frac{x \mu I_0}{t^{7/2}} (\sigma_h \mu b^2)^{5/2} \mathcal{G}_3
 \end{aligned} \tag{3.13}$$

where I_0 is the transmitter current; $\alpha^2 = \sigma_h / \sigma_s$, $\beta^2 = \sigma_s \mu b^2$; the functions \mathcal{G}_1 , \mathcal{G}_2 and \mathcal{G}_3 give the geometrical parts of the response and are given in detail in Lee (1983, Eq.8, Eq.9 and Eq.10); $C(t)$ and $J(t)$ are the time dependent functions of the interaction term and are given as (Lee, 1983, Eq.14 and Eq.13):

$$C(t) = \alpha^3 \left\{ \left(\frac{2t}{\beta^2} - \frac{2}{3} \right) \cdot J(t) - \frac{\beta^3 \sqrt{\pi}}{12 t^{5/2}} \right\} \tag{3.14}$$

$$J(t) = -2\sqrt{\pi} \beta \sum_{n=1}^{\infty} \frac{\exp(-\beta^2 n^2 / t)}{n} \left(\frac{3\beta^2 n^2}{2t^{5/2}} - \frac{n^4 \beta^4}{t^{7/2}} \right) + \frac{\sqrt{\pi} \beta}{2t^{3/2}} - \frac{\Gamma(\frac{5}{2}) \beta^3}{3t^{5/2}} \tag{3.15}$$

Special attention is drawn to the time-dependent function $J(t)$ of the interaction term, Equation (3.15), which characterises the response of a sphere in a conductive host at later times. Lee (1983) showed that the $J(t)$ function represents a series of fields which collectively at later times decay like $t^{-7/2}$. Eventually, the $J(t)$ term will dominate the exponential sphere transient at late times but can be significant less than the host rock contribution which decays like $t^{-5/2}$ for voltage response measurements (see also Lee, 1982). This is in contrast to the EM response of a sphere in a highly resistive host which decays as a single exponential at late times.

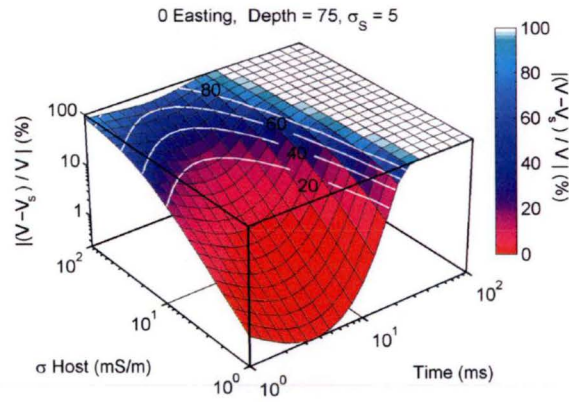
The expressions in Equation (3.13) are used to calculate normalised TEM profiles for a range of delay times and half space conductivities. The normalised responses are displayed as surface plots which represent the percentage error when the effect of the host rock is neglected. Two different sets of normalised responses are calculated. In the first set, the contribution of the host is emphasised and in the second set, the effect of neglecting the interaction term is accentuated. The normalised host response and the normalised interaction response are respectively calculated as

$$\text{Normalised host response} = \left| \frac{V - V_s}{V} \right| \quad (3.16)$$

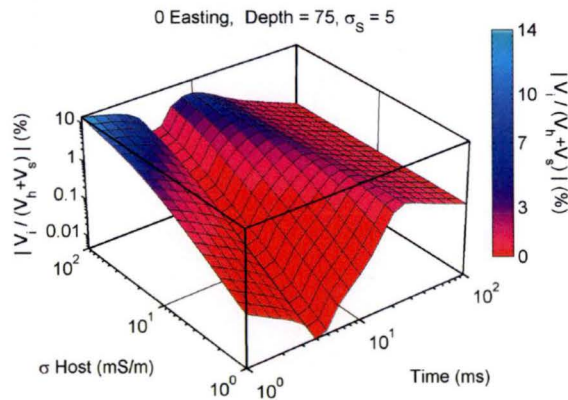
$$\text{Normalised interaction response} = \left| \frac{V_i}{V - V_i} \right| \quad (3.17)$$

The surface plots in Figure 3.8 show the normalised responses for both cases when the loop is centred directly above the sphere when interactions are solely inductive. The model parameters are given in the caption of the figures. The surface of Figure 3.8a illustrates the first case $|(V - V_s)/V|$ which may be understood as defining the percentage error which is incurred if host rock contribution is neglected as compared to the free-space sphere response (see also Lee and Thomas, 1988, Fig.12). Figure 3.8b illustrates the second case $|V_i/(V - V_i)|$ which represents the percentage error contribution which arises by neglecting the interaction term. Corresponding surface plots when the loop is not in axial symmetry with the sphere, and therefore gives rise to galvanic coupling, are depicted in Figure 3.9.

At early to intermediate times and low to medium half space conductivities, the influence of the sphere is mostly perceptible as seen in both Figures 3.8a and 3.9a, indicated by the broad curved feature in red. This region at intermediate delay times from ~ 1 -10 msec and for a conductivity range from ~ 1 mS/m to 10 m/Sm, characterises the visibility window where the target is detectable (Kaufman and Eaton, 2001, p.440). For $t \gtrsim 10$ msec the relative contribution of the host grows rapidly; here, the target decays exponentially, and the interaction term as a power-law of $t^{-7/2}$; the host response, which decays as $t^{-5/2}$, is pre-dominant and eventually, the sphere is undetectable.

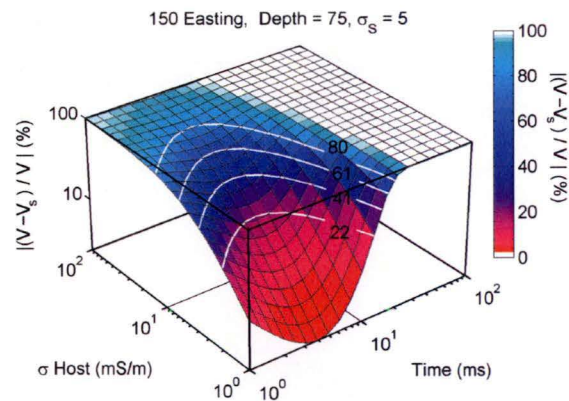


(a) Surface of normalised TEM responses $|(V - V_s)/V|$ at 0 Easting. The broad curved feature in red indicates the influence of the sphere's predominance mostly at early to intermediate times and low to medium half space conductivities. The effect of the host is predominant at higher half space conductivities and late times. At 10 msec and for $\sigma_h = 10$ mS/m, $V = 6.282 \times 10^{-6}$ Volt/Amp (c.f. Lee, 1983, Fig.7) .

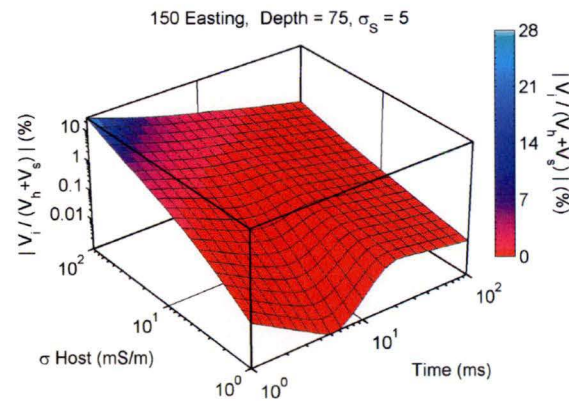


(b) Surface of normalised TEM responses $|V_i / (V_h + V_s)|$ at 0 Easting. The surface represents the error when calculating the TEM response as the sum of host and sphere and ignoring host rock interaction. At high conductivities and at early time, the error is as high as $\sim 14\%$. At late times the error is below 3%, independent of the host conductivity. Because of the axial symmetry of the measurement configuration at 0 Easting, V_i comprises inductive coupling only .

Figure 3.8 – Surface of normalised TEM responses of a buried sphere in a conducting host recorded directly above the sphere at 0 Easting. The radius of the coincident loop is $a = 100$ m and the sphere radius is $b = 50$ m. The sphere is buried at $d = 75$ m and has a conductivity of $\sigma_s = 5$ S/m. Delay times range from 1–100 msec and half space conductivities range from 1–100 mS/m.



(a) Surface of normalised TEM responses $|(V - V_s)/V|$ at 150 Easting. The broad curved feature in red indicates the influence of the sphere's predominance mostly at early to intermediate times and low to medium half space conductivities. Host-rock is predominant already at medium half space conductivities and intermediate times.



(b) Surface of normalised TEM responses $|V_i / (V_h + V_s)|$ at 150 Easting. As compared with the error-surface at 0 Easting, the error values are much higher due to galvanic coupling effects at far offsets. At high conductivities and at early time, the error is as high as ~28%. At late times the error is small and weakly dependent on the host conductivity.

Figure 3.9 – Surface of normalised TEM responses of a buried sphere in a conducting host recorded at 150 East. The radius of the coincident loop is $a = 100$ m and the sphere radius is $b = 50$ m. The sphere is buried at $d = 75$ m and has a conductivity of $\sigma_s = 5$ S/m. Delay times range from 1–100 msec and half space conductivities range from 1–100 mS/m.

Figures 3.8b and 3.9b illustrate the effect of the interaction term at 0 Easting, directly above the sphere and at 150 Easting, respectively. A sign change occurs in the surface plot for 0 Easting at ~ 4 msec which results in discontinuities on a logarithmic scale. The error reaches a minimum at the zero cross-over where the sphere response is the strongest and the detectability of the sphere is maximal. At earlier times, < 4 msec, and with increasing host conductivity, the effect of the interaction term reaches a maximum of $\sim 14\%$. With increasing host conductivity and at time > 4 msec the error values increase until ~ 12 msec where the effect of the interaction term declines independently of the host conductivity. At later times the host response with a decay rate of $t^{-5/2}$ is predominant over the interaction term with a decay rate of $t^{-7/2}$. Except for the zero-crossover, the surface plot in Figure 3.9b exhibits similar characteristics where a maximum occurs of 28% at early time and high host conductivity. The surface is generally more flat at Easting 150 than at Easting 0 due to weaker responses, however the relative errors are larger due to the additional contribution arising from galvanic coupling.

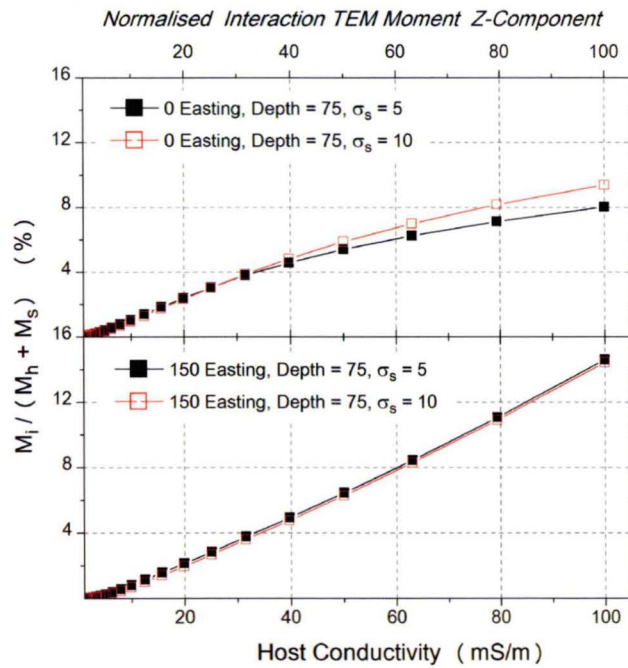


Figure 3.10 – Normalised incomplete TEM moment of the interaction term for a range of host conductivities at 0 Easting (top) and at 150 Easting (bottom). The radius of the coincident loop is $a = 100$ m and the sphere radius is $b = 50$ m. Calculations are for a sphere buried at $d = 75$ m which has a conductivity of $\sigma_s = 5$ S/m. The calculations are repeated for a sphere with a conductivity of 10 mS/m. Half space conductivities range from 1–100 mS/m.

The calculated coincident loop voltages of the sphere-in-host responses have been transformed to (incomplete) first order TEM moments by numerical integration between the first and last channel where channel times range from 1 – 100 msec. The model is that of Figures 3.8 and 3.9. The calculations have been repeated for the same model but for a sphere with a conductivity of 10 mS/m. The TEM moments at 0 Easting and at 150 Easting are shown for a range of host conductivities from 1 mS/m–100 mS/m in Figure 3.10. For both sphere conductivity values, the error values when neglecting host-rock interaction are as high as ~8% at 0 Easting and are about ~15% at 150 Easting for large host conductivities. The maximum normalised TEM moment error values due to neglecting interaction are smaller than the corresponding maximum time-domain values. Conductivity values as large as 100 mS/m are typically found in weathered layers and sedimentary rocks (Figure 1.1), however host-rock conductivity and therefore the error values will usually be lower.

From the field behaviour of the TEM moment response of a buried sphere for coincident-loop surveys it may be deduced that the main contributions in conductive environments arise from the sphere and the half space with a minor contribution from the interaction term which depends mostly on the host conductivity. Therefore, 3D forward modelling can reasonably be realised as a superposition of free-space responses of point conductors in a homogeneous conducting background.

3.5 Comparison with fully 3D electromagnetic modelling schemes

The fully 3D electromagnetic modelling software MARCO (Xiong and Tripp, 1995; Raiche et al., 2007) was employed to calculate the transient response for two distinct prism models embedded in a conductive host. The moment transformed TEM decays of the prism responses are compared with the combined TEM moment response of discrete target and continuous background. MARCO is a 3D-EM integral equation solver, designed to model multi-block targets in a layered earth. The synthetic time-domain data has been transformed to the moment domain by a numerical integration scheme, as was outlined in Section 2.8 of Chapter 2.

The two models can be considered 'extreme' in their dimensions and, for the second model, also in its conductivities. The first example models an extensive horizontal slab with moderate conductivity of 1 S/m in a rather resistive 1 mS/m host, whereas the second example models an extensive vertical dyke with high conductivity of 50 S/m in a fairly conductive host of 50 mS/m. The models are primarily designed to challenge the forward algorithm with two difficult, nearly unbounded, models which exemplify large ore deposits at great depths.

In contrast to the previous free-space examples, the prism models here are embedded in a conducting half space, so that very early and very late time will

be associated with the response of the host-rock. Because the MARCO prism responses are for a finite time-range, but the moment transform is the time-integral from zero to infinity, extrapolation is carried out at very early ('head') and very late times ('tail') by virtue of Equation (2.112). The extrapolation at early and late time uses an analytical half space model for the times in question which captures the near transmitter loop response and the response of an extensive unbounded medium respectively. In case of measured field data, the half space models are based on conductivity-depth images or can rely on borehole logs, if available. For the forward modelling examples, the half space conductivity is known beforehand and is employed for the extrapolation of the 'head' and 'tail' moment contribution.

3.5.1 Horizontal slab in resistive host

The first example is for a conductive, extensive horizontal slab model with dimensions $800\text{E} \times 800\text{N} \times 300\text{Z}$ embedded in a more resistive host. The horizontal slab model is depicted in Figure 3.11. Because the transmitter-loop is much smaller than the lateral dimensions of the slab, the model virtually represents a layered conductive structure. The slab model is designed so as to test whether the forward algorithm (Equation 3.1) is able to replicate the response of a massive horizontal volume in a conducting medium.

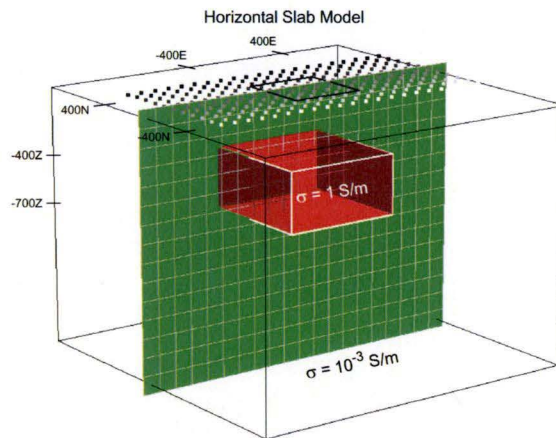


Figure 3.11 – Horizontal slab model in resistive host. Subcell size of the slab is 10 m, giving a total of 192,000 cells for the volume of the slab. Each subcell has been assigned the time constant of the slab model, which is $\tau_{slab} = 2.61$ msec.

The slab has a conductivity of 1 S/m and the half space conductivity is 1 mS/m. The depth-to-top centre coordinates are (0E,0N,-400Z). The fixed, square transmitter loop is centred over the slab at (0E,0N) with side lengths of 500 m. Survey lines for Northings from -500N to 500N, separated by 100 m, traverse the prism model from -500E to 500E at 50 m intervals. Synthetic vertical B-field step response recordings were calculated for 45 channel delay times ranging from 0.1 msec to 1340 msec (Chapter 1, Table 1.2). The time domain data is subsequently transformed to first order TEM moments by a spline-based numerical integration scheme and extrapolated using 'head' and 'tail' moment contributions for the half space conductivity value of 1 mS/m.

There is no formula applicable for the time constant of the thick horizontal slab in a conducting environment, therefore the time constant is empirically found from the time-domain decay curves. The decay curve and time constant fit are displayed in Figure 3.12 which shows the empirically estimated time constant. The time constant is estimated as

$$\tau_{slab} \simeq 2.6 \text{ msec}$$

The model space is defined by the Voxet on display in Figure 3.11. The model subcell dimension is 10 m, giving a total number of 192,000 cells for the volume of the slab. All slab-subcells contain a central point conductor with time constant of $\tau = 2.6 \text{ msec}$. The vertical TEM moment response curves are displayed in Figure 3.13. The agreement between the MARCO model and the subcelled TEM moments is remarkably good as is also evident from the RMS values which are very small as compared with the peak amplitude response at all Northings. The least-squares optimisation, as calculated for the entire data set, for the MARCO model response and the subcelled response curves gives the following value $\beta_{slab} = 1.01$. The least-squares value is close to unity, demonstrating that the assumed time constant of 2.6 msec is close to the optimal value in a least-squares sense.

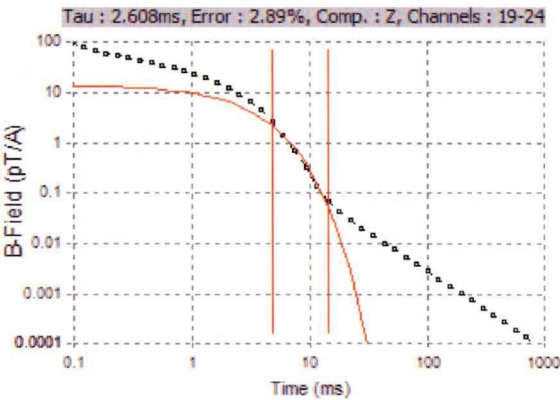


Figure 3.12 – Time constant decay curve of horizontal slab at 0 East of survey line 0 North. The late-time response of the horizontal slab is noticeable at intermediate times. The late-time response for channels > 24 decays with a power-law.

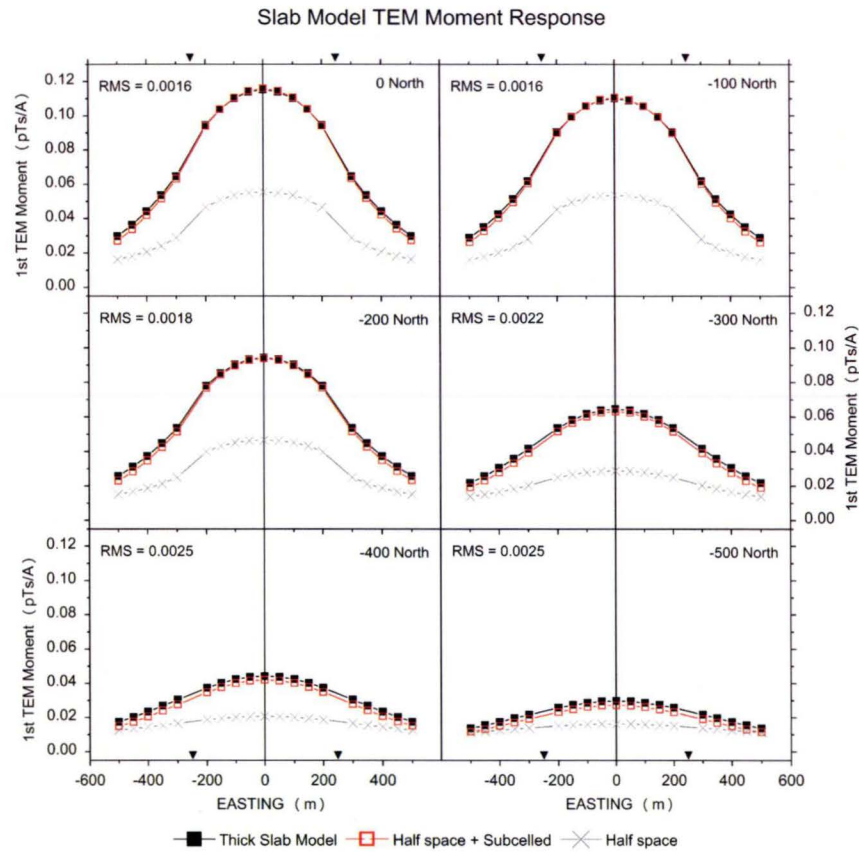


Figure 3.13 – Vertical component TEM moment response curves at a range of Northings for the horizontal slab model. The subcellled TEM moment responses are calculated for cell time constants of 2.6 msec, equivalent to the empirical slab time constant. The triangles on the Easting axes indicate the position of the Tx-loop. TEM moment response of 1 mS/m host shown in grey.

3.5.2 Vertical dyke in conductive host

The second example shows the TEM moment response of a highly conductive, extensive vertical dyke model embedded in a conductive host. The dimensions of the vertical dyke are $100\text{E} \times 1400\text{N} \times 1000\text{Z}$ with depth-to-top centre coordinates $(750\text{E}, 0\text{N}, -400\text{Z})$. Conductivity of the dyke is 50 S/m and the host conductivity is 50 mS/m. The vertical dyke model is depicted in Figure 3.14a. The model is a simplistic representation of a massive sulfide deposit in a conducting environment. For such a model, given the host conductivity and the target strike, host-rock EM interaction can be expected including current channelling at early time (Section 1.2.2). The model is designed as to test whether the forward algorithm is able to replicate the response of a plate-like massive vertical volume in a highly conducting medium when host-rock EM interaction is ignored.

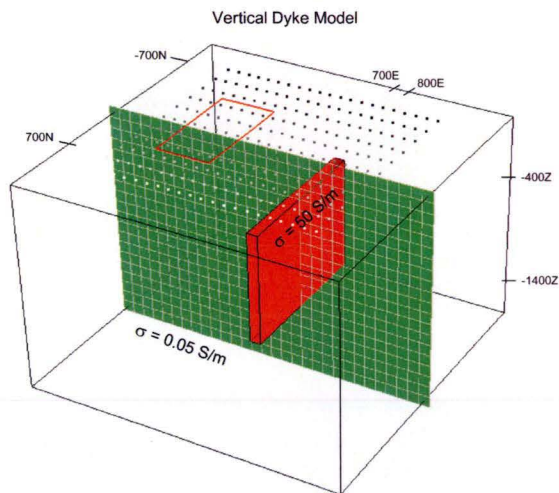
A fixed, rectangular transmitter loop is centred at (0E,0N) with side lengths of 500E×1000N. East-west survey lines, separated by 200 m, run at Northings -1000N to 1000N and traverse the prism model from -500E to 1500E at 100 m intervals. Synthetic step response Bz-decays were computed for 45 channel delay times ranging from 0.1 msec to 1340 msec (Table 1.2), which subsequently have been transformed to first order TEM moments, using 'head' and 'tail' moment contributions for the half space conductivity value of 50 mS/m.

The synthetic decay curves are employed to estimate the time constant of the vertical dyke, because Lamontagne's time constant formula (Equation 3.10) is correct only for free-space plates, but invalid for plates in a highly conducting half space. Moreover, the formula is not strictly valid for an extensive plate where the plate dimensions are larger than the dimension of the transmitter loop (Lamontagne, 1975, p.144). The time constant, based on the transient decays, was difficult to evaluate because of the predominance of the host contribution. At stations west from the plate, all decays exhibit a power law decay from intermediate times onwards, only at stations east from the dyke could an exponential be fitted to the decays. The time-domain decays at selected stations together with the time-constant fit at 0 Northing are shown in Figure 3.14b. Based on the decay curves at 0 Northing and 1200 Easting, the estimated value for the dyke's time constant is

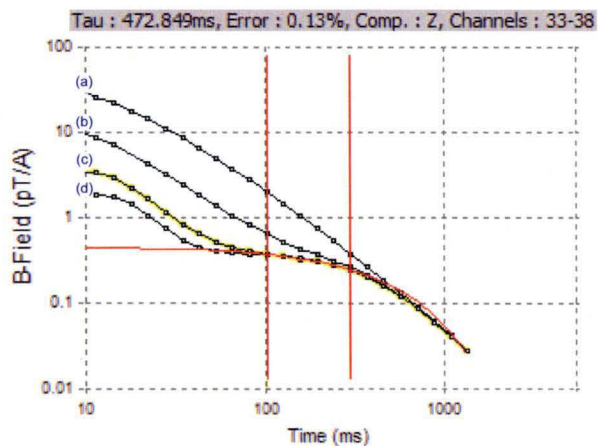
$$\tau_{dyke} = 475.2 \text{ msec}$$

The dyke model was discretised into 10 m subcells where each cell has been assigned the time constant of the dyke; there are in total 140,000 cells filling the volume of the vertical dyke. The vertical TEM moment results of the subcelled dyke together with the TEM moment response of the MARCO model are displayed in Figure 3.15. Due to the relatively high host conductivity, the TEM moment response curves are close to the host response. 'Stripped' TEM moment responses (after subtraction of host response) are on display in Figure 3.16 in order to emphasise the isolated response from the vertical dyke.

Because the target will predominantly support eddy current flow in the plane of the plate, the calculations are shown for the conductivity gradient method. The panel for 0-North in Figure 3.15 also superimposes the result as calculated using the standard form (full primary field) of the forward algorithm. The half space response is plotted as well. For this example, the bulk of the response is due to the host. The TEM moments of the MARCO response and the subcelled dyke are very close at all Northings, as is also indicated by the associated RMS values which are small as compared with the TEM moment response curves. Small deviations become apparent at large receiver offsets, East from the dyke position. The TEM moment response curves have been subjected to the linear least-squares fit which produces an optimal time constant value as to fit the the MARCO response. The least-squares factor evaluates as $\beta_{dyke} = 1.005$ and is close to unity, demonstrating that the assumed time constant value τ_{dyke} is close to the optimal value in a least-squares sense.



(a) Vertical dyke model in conductive host. Subcell size of the dyke is 10 m, giving a total of 140,000 cells for the volume of the dyke. Each subcell has been assigned the time constant of the dyke model, which is estimated as $\tau_{dyke} = 475.2 \text{ msec}$.



(b) Time constant decay curves of vertical dyke at various stations. The decays are at 0 Northing for Eastings 700 (a), 1000 (b), 1200 (c) and at 1300 (d). The decay curves for stations labelled 'c' and 'd' exhibit the response of the dyke. The other response curves mostly display a power-law decay for the entire time range. The yellow curve (c) indicates the decay used for estimating the time-constant.

Figure 3.14 – Vertical dyke model (top) and time constant analysis (bottom).

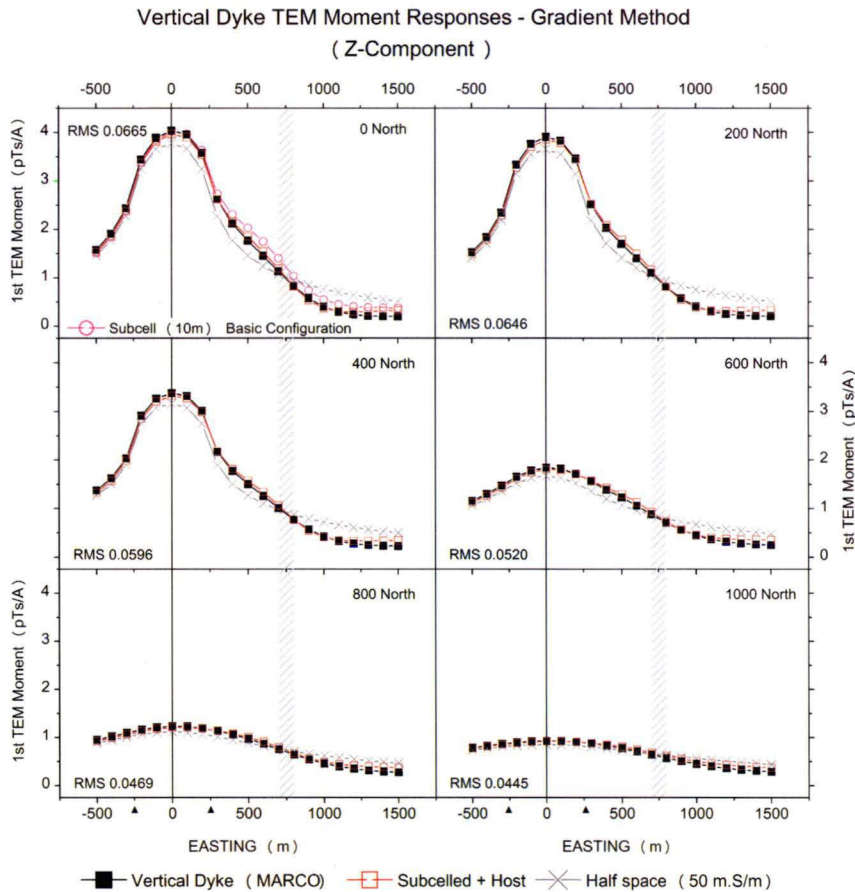


Figure 3.15 – 'Full' Z-component TEM moment response profiles at a range of Northings over vertical dyke model. The Figure shows the response curves as calculated with the conductivity gradient method for Northings from 0N to -1000N. The panel for 0N also shows the response as calculated using the basic configuration of the forward algorithm. On display are the TEM moment responses for the vertical dyke (MARCO), the point conductor response from the subcells and the host response. Triangles on the Easting axes indicate the position of the Tx loop; the grey shaded area indicate the position of the dyke.

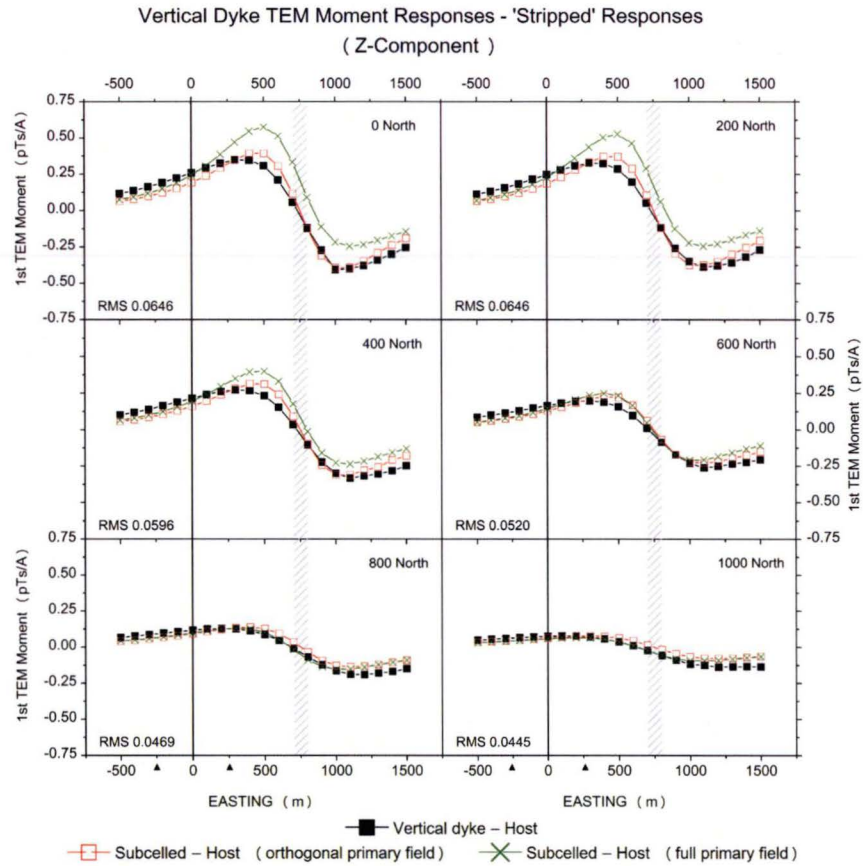


Figure 3.16 – 'Stripped' Z-component TEM moment response profiles at a range of Northings over vertical dyke model. The figure shows the TEM moment response curves with the host response of 50 mS/m subtracted. On display are the "true" residual response curves as calculated with MARCO, the point conductor response curves of the subcelled volume as calculated with the gradient method (orthogonal primary field) and with the basic form (full primary field) of the forward algorithm. At large receiver offsets, east from the plate the residual responses from the subcelled volume diverge somewhat from the MARCO residuals.

In case of the point conductor approach, host-rock EM interaction is ignored which is included in case of the MARCO result. The TEM responses at most stations west of the dyke decay with a power law for the entire time range, characterising the host rock response. The stripped TEM moment response curves in Figure 3.16 are shown for the basic form (full primary field) and for the gradient (orthogonal primary field) forward algorithm. As can be expected, the gradient method matches the stripped MARCO response more closely because of the plate-like target characteristic. At large receiver offsets East from the target, the deviations between the MARCO and the subcelled response are noticeable, interpreted to be most likely a residual of the host rock response.

3.6 Concluding remarks

The forward algorithm of the TEM moment inversion scheme was presented in this chapter. The algorithm relies on linear superposition of TEM moment responses of point conductors which comprise the subcelled anomalous volume. The forward algorithm is posed in terms of the time constant of the prospective target, resulting, therefore, in a scale invariant formulation, independent of subcell size. The TEM moment response is linear with respect to the cell time constant, consequently simplifying the TEM problem. Time constants can simply be rescaled employing a linear regression as to match the target response curves.

The free space examples in Section 3.3 showed that the subcelled volume of a sphere approximately matches the parent conductor, independent of subcell size. In the case of a free space plate, the time constants of the subcelled volume had to be rescaled as to match the plate response, presumably due to the approximate nature of the plate response. The TEM moment algorithm gives more reliable results in conditions where the primary field can be considered uniform, as delineated in Section 3.3.3.

The purely inductive algorithm is put to the test in Section 3.5 where the TEM moment responses of two extensive prismatic models embedded in a conductive environment are compared with the result from the point-conductor forward algorithm. The prism models are calculated using an exact integral Equation solver which includes host-rock EM interaction. The time constants of the subcelled volume are found by inspection of the associated time decays of the prism responses. The response of the subcelled model using the point conductor approach compares favourably for both examples, building confidence in the approach. At far receiver offsets, in the case of the more conductive vertical dyke example, small deviations, as compared to the exact model response, become apparent which are interpreted to be a consequence of the negligence of host rock EM interaction.

The negligence of host rock EM interaction is analysed in a qualitative manner in Section 3.4. Estimation of the TEM moment response as a combination of a continuous background and a discrete target response is a rational approximation for the modelling of 3D targets.

Chapter 4

1D imaging of TEM data

Introduction The objective of 1D imaging of TEM data is to retrieve an approximate portrayal of the geoelectrical subsurface structure which plausibly explains a set of observations. In the context of the project, the 1D imaging scheme serves as a preparatory process for the 3D inversion procedure. Due to the time-integration of the TEM decays, the TEM moment transform loses depth resolution. The loss of depth resolution may be compensated for by the preliminary result of the 1D imaging scheme, which is encompassed to the 3D inversion as an element of a starting model.

Among the varieties of 1D imaging schemes, conductivity-depth-imaging, or CDI, is a familiar form of processing of TEM recordings (c.f. Chapter 1). In this thesis, CDIs portray the subsurface geoelectrical structure as cross sections of apparent conductivity versus depth via 'stitching' of 1D conductivity-depth curves. It constitutes a very fast low-cost technique to provide an image of the conductivity directly from observed data which provides fast preliminary results. The CDIs effectively serve as a starting model for 3D inversion where the apparent conductivity-depth pairs serve either as a way to assign initial property values or for formulating 3D inversion weights.

Sensible portrayals of the subsurface conductivity in the CDIs are advantageous in order to condition the 3D inversion, since misleading conductivity-depth sections may lead to spurious features in 3D inversion. However well-defined for in-loop measurements, apparent conductivity is either dual-valued or undefined for vertical component ground-loop TEM measurements over a half space outside the transmitter-loop, both for step and impulse response data (Spies and Eggers, 1986). On a uniformly conductive ground, non-uniqueness arises because the vertical and horizontal components of the magnetic induction $\mathbf{B}(t)$ (and $\partial_t \mathbf{B}$) are not monotonically decreasing with time. Computing apparent conductivity from vertical component fixed-loop TEM data can be problematic, therefore, for receiver positions located outside the Tx-loop. In particular, if $B_z < 0$, for stations outside the loop, the apparent conductivity is extremely high at mid- to late-times.

Specifying a sensible apparent conductivity in an automatic fashion can be difficult, complicating generation of apparent conductivity-depth pseudo-sections for fixed-loop and slingram TEM (Fullagar and Reid, 1992; Reid and Fullagar, 1998). Reid and Fullagar calculated both apparent conductivities, and rejected the one which was associated with decrease of apparent depth with time. Here, apparent depth conveys the notion of the depth to the physical current maximum (electric field maximum) in a half space of conductivity equal to the apparent conductivity at the time in question for impulse response measurements (Fullagar, 1989). Calculating apparent depths has been generalised for \mathbf{B} -field data, in which case the apparent depth is the depth of the maximum B_z in the half space (Fullagar, 2002).

It is well known that CDIs may contain artifacts when converting TEM data to apparent conductivity due to non-uniqueness. However, the artifacts are not always solely due to non-uniqueness, but may also arise from 3D geology — any anomaly which includes two peaks or which includes a cross-over is prone to artifacts. For example a single conductor with a cross-over anomaly will produce two conductive zones in the CDI for vertical component TEM data.

The total magnetic induction amplitude ($|\mathbf{B}|$) on a homogeneous ground, however, is a non-increasing function of time. Consequently, if multi-component fixed loop \mathbf{B} -field data are available, an unambiguous apparent conductivity can be derived from $|\mathbf{B}|$ -data at all times. Generally, \mathbf{B} -field data is preferable over impulse response data for computing apparent conductivity (e.g. Spies and Eggers, 1986). In the case of $\partial_t \mathbf{B}$ measurements, CDIs can be calculated from 'quasi- $|\mathbf{B}|$ ' data: impulse response data can be time-weighted and summed to yield quasi- $|\mathbf{B}|$ amplitudes which expedites computation of apparent conductivities more reliable than single component $\partial_t \mathbf{B}$ data (Schaa et al., 2006). In the inductive limit, the EM response is unrelated to conductivity and apparent conductivity from magnetic induction amplitudes is undefined, however. Computing apparent conductivity from $|\mathbf{B}|$ or quasi- $|\mathbf{B}|$ amplitudes facilitates generation of more accurate conductivity-depth sections from fixed loop TEM.

This chapter establishes the unambiguous derivation of apparent conductivities from $|\mathbf{B}|$ -field amplitudes. The technique's suitability is first demonstrated on synthetic layered earth models. The recovered layered conductivity structure from conductivity-depth imaging resembles the true layered model without artifacts. Extension to 3D environments follows. The conductivity-depth imaging scheme is demonstrated at a vertical prism model and a horizontal prism model residing in a conductive host. Furthermore conductivity-depth imaging of a dipping plate in a conductive host is illustrated. Apparent conductivities from $|\mathbf{B}|$ -field amplitudes is shown to be less biased by 3D effects than conventional CDI interpretation which are based on the vertical component only. The method can then recover a smoothed representation of the 3D geoelectrical structure of the subsurface. Lastly, the imaging technique is demonstrated on multi-component \mathbf{B} -field data, acquired across a Proterozoic metavolcanic sedimentary sequence hosting Pb-Zn-Cu-Ag mineralisation.

4.1 Apparent conductivity

Apparent conductivity is defined as the conductivity of a homogeneous half space which produces the same response for a given EM configuration as the actual measurement over an inhomogeneous earth. The concept of apparent conductivity is considered a convenient data transformation for transient electromagnetic data, because it effectively normalises the theoretical variations in the response due to measurement configuration over a homogeneous half space. Derivation of reliable apparent conductivities is desirable, but not always possible, because apparent conductivity derived from single component transient electromagnetic data is often non-unique (Spies and Eggers, 1986). When the receiver is offset from the centre of the transmitter loop, the apparent conductivity is dual-valued or undefined for single component impulse or step response-data. Non-unique behaviour of the apparent conductivity occurs because the transient B_x and B_z components on a uniform half space do not decay monotonically with time (Figure 4.1). Apparent conductivity based on $|\mathbf{B}|$ -field amplitudes, however, is unique over a homogeneous conducting ground. Derivation and examination of unambiguous apparent conductivity from $|\mathbf{B}|$ -field amplitudes is the subject in this and subsequent sections.

The units of apparent conductivity are Siemens per metre (S/m); the algebraic inverse is known as apparent resistivity which is measured in Ohm-metre ($\Omega \cdot m$). The only instance where the apparent conductivity is equal to the true subsurface conductivity is in the case of a homogeneously conducting earth. Analytical formulae for apparent conductivity can only be derived in the asymptotic cases for very early and very late time. Spies and Frischknecht (1991) provide a comprehensive list of asymptotic formulae for a variety of measurement configurations. The asymptotic formulae, however, are not applicable to intermediate times where a sign change occurs. This is commonly observed for separated loop systems. In order to calculate an apparent conductivity defined over the entire measurement time range, a single parameter inversion of the half space response is implemented (Fullagar, 1989; Reid, 1994; Reid and Fullagar, 1998). The single parameter inversion technique is here applied to generate unique apparent conductivities from total field amplitudes.

4.2 Unambiguous apparent conductivity from magnetic field amplitudes

The following section describes the derivation of apparent conductivities from \mathbf{B} -field amplitudes. If o_n denotes the observed $|\mathbf{B}|$ -field response at the n -th channel, and c_n^i the calculated $|\mathbf{B}|$ -field half space response at the n -th channel and i -th iteration, then the χ^2 misfit measure is defined as

$$(\chi^2)_n^i = \left(\frac{o_n - c_n^i}{\epsilon_n} \right)^2 \quad (4.1)$$

where ϵ_n is the error associated with the observation of the n -th channel, where the error is assumed to be a realisation of a normal random distribution with zero mean. The error may be characterised as a fraction of the observed data via

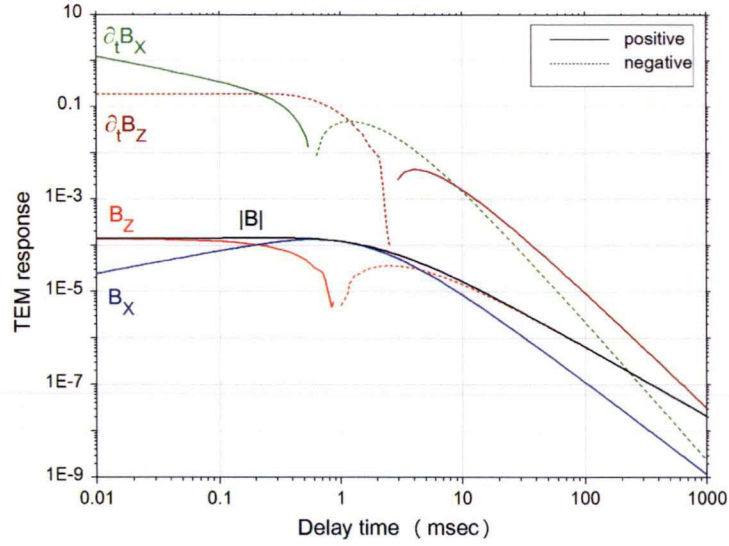


Figure 4.1 – Fixed loop TEM decay curves over a homogeneous half space with conductivity $0.1S/m$. Displayed are response curves for B_x , B_z and $|B|$ in $\mu T/A$ and for $\partial_t B_x$ and $\partial_t B_z$ in $\mu V/Am^2$. The transmitter loop is $250 \times 250m$, and the receiver is at dimensionless offset X/L of 1.5 (X is the receiver offset and L denotes the transmitter side length). Only the $|B|$ decay is monotonic.

$$\epsilon_n = pcerr \times \left(\frac{o_n}{100} \right) \quad (4.2)$$

where $pcerr$ is a parameter controlling the desired degree of fit between observed data and half space model.

The inversion proceeds iteratively to solve for an apparent conductivity which minimises the χ^2 misfit measure. The χ^2 misfit at the $(i+1)$ -th iteration is related to the misfit at the i -th iteration by the following first-order approximation (Reid, 1994, p.35):

$$(\chi^2)_n^{i+1} = (\chi^2)_n^i + \delta\sigma \left(\frac{\partial (\chi^2)_n^i}{\partial \sigma} \right) \quad (4.3)$$

where $\delta\sigma$ is the unknown conductivity perturbation. The perturbation is chosen so that the χ^2 target misfit at the next iteration is zero, thus

$$(\delta\sigma)^i = \frac{(\chi^2)_n^i}{\partial_\sigma (\chi^2)_n^i} \quad (4.4)$$

where $(\delta\sigma)^i$ is an estimate for the conductivity perturbation at the i -th iteration. The derivative of the χ^2 misfit measure is given as

$$\frac{\partial (\chi^2)_n^i}{\partial \sigma} = -2 \left(\frac{o_n - c_n^i}{\epsilon_n} \right) \frac{1}{\epsilon_n} \frac{\partial c_n^i}{\partial \sigma} \quad (4.5)$$

The derivative of the χ^2 misfit measure utilises the first derivative of the total magnetic induction with respect to the inversion parameter σ .

$$\frac{\partial c}{\partial \sigma} = \frac{1}{|\mathbf{B}|} \cdot (B_x \partial_\sigma B_x + B_y \partial_\sigma B_y + B_z \partial_\sigma B_z) \quad (4.6)$$

where the sub- and superscript (n and i) have been omitted for convenience. Expressions for the derivatives of the horizontal and vertical components of the \mathbf{B} -field will be given in section 4.2.1 below.

For a single parameter inversion, the expected value of a χ^2 random variable with zero mean and normalised by its variance is 1. Thus, the inversion is considered successful if the misfit measure is equal or less than 1. If the misfit is larger than 1, the conductivity is perturbed by $\delta\sigma^i$ and from an updated conductivity $\sigma^{i+1} = \sigma^i + \delta\sigma^i$, a new half space model is computed. The process is repeated until an apparent conductivity is found which reduces the χ^2 misfit measure to a value less than 1. If convergence cannot be achieved in a specified maximum number of iterations, the inversion fails. The inversion is deemed to have stalled, if the data does not fit into any half space model.

4.2.1 Derivatives of magnetic field amplitude

The half space response of the magnetic field amplitudes due to step-current shut-off of a rectangular transmitter loop is calculated directly in the time-domain using analytical expressions. The analytical expression for the vertical component $B_z(t)$ half space response is obtained via analytic integration of the expression for the impulse response from a line current segment (Fullagar, 2002). Recalling Equation (2.81) in terms of the magnetic induction \mathbf{B} :

$$G(x, y, t) = \frac{\mu I}{8\pi x^3} \left[\frac{1}{\gamma^2} \left(2 + \frac{x^2}{\rho^2} - 2\gamma^2 x^2 \right) \frac{y}{\rho} \operatorname{erf}(\gamma\rho) - \frac{2}{\sqrt{\pi}} \frac{x^2}{\rho^2} \frac{y}{\gamma} e^{-\gamma^2 \rho^2} - \frac{2}{\gamma^2} e^{-\gamma^2 \rho^2} \operatorname{erf}(\gamma y) \right]_{\gamma=0}^{\gamma(t)} \quad (4.7)$$

where $G(x, y, t)$ denotes the vertical magnetic field; x and y denote corresponding coordinates of the ends of the line current relative to the receiver and $r = \sqrt{x^2 + y^2}$. Also,

$$\gamma = \frac{\sqrt{\sigma\mu}}{4t}, \quad t > 0$$

where t denotes the channel delay time. The net B_z response is then given by the summing of the contributions $G(x, y, t)$ from each side of the transmitting loop.

Recalling Equation (2.92), the horizontal component of the quasi-static magnetic field at any point on the surface of a homogeneous half space of conductivity σ due to step current shut-off of an ungrounded y -directed electric dipole is (Ward and Hohmann, 1988, p.236):

$$B_x^{dip}(t) = \frac{I dy}{2\pi r^2} I_1(z) \cdot e^{-z} \quad (4.8)$$

where $z = \sigma\mu_0 r^2/8t$, I is the transmitter current, I_1 is the modified Bessel function of the first kind of order 1, and dy indicates the electrical dipole direction. Integrating Equation (4.8) around the transmitter loop perimeter yields the horizontal component of the magnetic induction. Integration of this expression along the y-sides of the loop, defines the x-component, and vice-versa. Numerical integration is performed with a Romberg integration scheme (Press et al., 2002). The magnetic induction amplitude is then given by

$$|\mathbf{B}(t)| = \sqrt{B_x(t)^2 + B_y(t)^2 + B_z(t)^2} \quad (4.9)$$

The total magnetic induction, $|\mathbf{B}(t)|$, may be computed from multi-component step response measurements. The total magnetic field for a homogeneous half space is a non-increasing function of time as was shown earlier in Figure 4.1. It is therefore intrinsically well-behaved for determination of apparent conductivity, except in the inductive limit (c.f. Chapter 1.2.2).

If only windowed impulse response measurements are available, amplitudes of a quasi-step response, referred to as quasi- $|\mathbf{B}|$, may be calculated via a time-weighted summation (approximate integration). For the n -th channel, quasi- B , for a single component k , is defined as

$$Q_n^k = \sum_{j=n}^J t_j \cdot \partial_t B_j^k \quad (4.10)$$

where J is the total number of channels; t_j the delay time for channel j ; $\partial_t B_j^k$ the time derivative of a magnetic field component k , and Q_n^k is the quasi- B value for the corresponding field component k and channel n . Quasi- $|\mathbf{B}|$ amplitudes are computed as per Equation (4.9).

The time derivatives of the vertical and horizontal magnetic field components can be taken directly from Raiche (1987) for the vertical component, and from Ward and Hohmann (1988, p.237, Eq.4.181) for the horizontal component with the galvanic terms neglected. The expression in Ward and Hohmann (1988) is numerically integrated along the transmitter loop sides. Apparent conductivity based on quasi- $|\mathbf{B}|$ is dual valued, but is usually ‘virtually unique’ (c.f. Fullagar and Reid, 1992) insofar as only one of the alternative values is geologically plausible. Overall, apparent conductivity can be derived more reliably from quasi- $|\mathbf{B}|$ than from impulse response data.

In order to compute the apparent conductivities, the derivatives with respect to conductivity are needed for the various components of \mathbf{B} or $\partial_t \mathbf{B}$. The horizontal component $\partial_\sigma B_x$ is found by integrating the expression for the electrical dipole $\partial_\sigma B_x^{dip}$ around the transmitter loop perimeters. The conductivity derivative for a horizontal electrical dipole of the horizontal component of magnetic induction is found to be:

$$\partial_\sigma B_x^{dip}(t) = \frac{\mu I dy}{16\pi t} \left(\mu_0 (I_0 - I_1) - \frac{8t}{r^2 \sigma} I_1 \right) \cdot e^{-z} \quad (4.11)$$

where the Bessel function arguments are $z = \mu \sigma r^2 / 8t$. The integration of Equation (4.11) along the y-sides of the transmitter loop gives the x-component, $\partial_\sigma B_x$, and integration along the x-sides gives the y-component, $\partial_\sigma B_y$.

The analytical expression for the vertical derivative, $\partial_\sigma B_z$, is found by differentiating Equation (4.7) with respect to σ which results in (Fullagar, 2002):

$$\partial_\sigma B_z = -\frac{\mu}{4\gamma^2} \cdot \partial_t B_z \quad (4.12)$$

where $\partial_t B_z$ is Raiche's analytical formula for computation of the impulse response of a homogeneous half space for a rectangular transmitter loop (Raiche, 1987, Eq.8).

In case that apparent conductivity is computed for quasi- $|\mathbf{B}|$ amplitudes, the conductivity derivatives of the voltage responses are needed. Differentiation with respect to σ of the expressions in Ward and Hohmann (1988, p.237, eq.4.181), yields

$$\partial_\sigma (\partial_t B_x^{dip}) (t) = \frac{\mu^2 I dy}{16\pi t^2} \left[2z \cdot (I_0 - I_1) - \left(1 + \frac{1}{z} \right) \cdot I_1 \right] \cdot e^{-z} \quad (4.13)$$

As before, integrating the dipole expression along the y-sides of the transmitter loop gives the x-component, $\partial_\sigma (\partial_t B_x)$, and integration along the x-sides gives the y-component, $\partial_\sigma (\partial_t B_y)$. The vertical derivative $\partial_\sigma (\partial_t B_z)$ is given as (Fullagar, 2002)

$$\partial_\sigma (\partial_t B_z) (x, y, t) = \left[\frac{\mu \gamma^2}{2t} \cdot x \cdot e^{-x^2 \gamma^2} \operatorname{erf}(y \cdot \gamma) \right]_{y_1}^{y_2} \quad (4.14)$$

where (x, y_1) and (x, y_2) are the coordinates of the ends of the line current relative to the receiver.

4.3 Time-depth transformation

The time-depth transformation assigns an apparent depth to the apparent conductivity for a given channel delay time. The procedure is based on that proposed by Fullagar (1989), but adapted for \mathbf{B} -field data. In the original algorithm for $\partial_t B_z$ -field data, the assigned apparent depth at a particular channel was the depth to the physical current maximum in a half space with apparent conductivity at the given channel. For \mathbf{B} -field data (and $|\mathbf{B}|$ -amplitudes), the apparent depth is the depth of the maximum B_z in the half space. The $|\mathbf{B}|_{max}$ depth is the same as the $B_{z_{max}}$ depth: the maximum \mathbf{B} -field is located on the axis of the Tx-loop. The $|\mathbf{B}|_{max}$ depth is approximately $\sqrt{(t/\sigma\mu)}$ (Fullagar, 2009, pers. comm.).

The concept of diffusion depth was introduced in the context of TEM by Nabighian (1979). He described the downward and outward diffusion of the induced eddy current system in a conducting half space as a diffusing *smoke ring* blown by the transmitter loop. The TEM response at the surface of a half space can be approximated by a single current filament of the same shape as the transmitter loop which moves downward and outward from the transmitter with increasing time (c.f. Chapter 1). The current filament has a diffusion velocity of $v = 2/\sqrt{(\pi\sigma\mu t)}$. The current filament, or image current, however diffuses downward and outward from the transmitter loop at an angle of $\sim 47^\circ$ with respect to the surface; the physical current maximum at an angle of $\sim 30^\circ$. This is so because the 'equivalent current filament', which has an infinite current density, must always be deeper than the maximum of the actual distributed current system. Accordingly, depths calculated based on the current filament approximation always exceed those based on the position of the physical current maximum for the same delay time and conductivity (Reid, 1994, p.100).

4.4 Total B-field CDI processing for layered earth models

Model studies of two- and three-layered models have been conducted in order to investigate the performance of the conductivity-depth transformation for total magnetic field responses over a layered earth. A Fortran 95 program has been written to compute the frequency- and time-domain layered earth response for fixed-loop sources. The vertical component of the **B**-field response for a rectangular loop source with step current excitation was calculated in the frequency domain using the method of Poddar (1983): applying reciprocity, the receiver coil was regarded as the transmitter and its electric field was integrated around the transmitter loop. The layered earth Hankel transform kernels were taken from Kauahikaua (1978), with the half space response defined analytically in a separate term outside the Hankel integral. This approach has been adopted previously by Anderson (1984).

The horizontal **B**-field components were derived by integrating the horizontal electric dipole response along the loop sides. The integral expression for a horizontal dipole is given in Kauahikaua (1978) and in Anderson (1984). All Hankel transforms have been evaluated with the double precision filter coefficients of Guptasarma and Singh (1997). A Romberg integration scheme then solves for the integration along the transmitter loop perimeters. The frequency domain solutions of the vertical and horizontal components are subsequently transformed to the time domain using the double precision cosine filter coefficients of Anderson (1983). The transient **B**-field is splined and the time derivative of the spline is accepted as the $\partial_t \mathbf{B}$ value (e.g. Raiche, 1998). Figure 4.2 demonstrates the result for apparent conductivities for 2-layered earth models and Figure 4.3 shows the results for 3-layered earth models and illustrate the processing of the TEM decays to apparent conductivity versus depth.

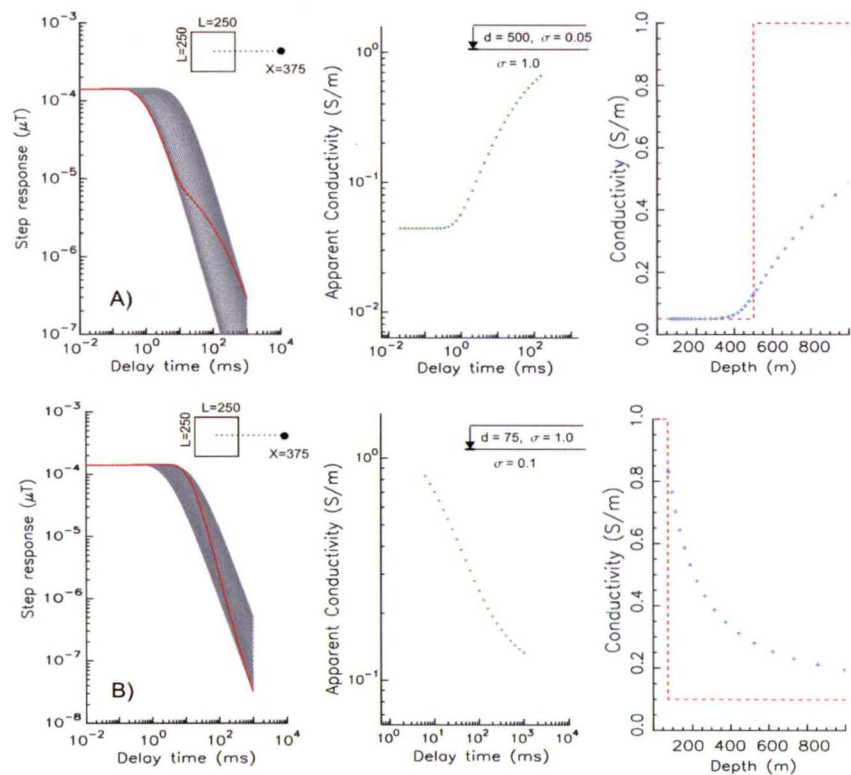


Figure 4.2 – Apparent conductivities for 2 layered earth models. The model decay curve (red) is shown on the left hand panel. The grey curves show the decay for each apparent conductivity. The centre panel shows the apparent conductivities as plotted against channel delay time. The model parameters are specified as well in the centre panel. Conductivity/depth curves are shown on the right hand panel. The upper panels refer to a thick resistive layer over a conductive basement. The lower panels refer to a thin conductive layer over a resistive basement. The right hand panel shows the depth-transformed apparent conductivities with the true conductivity-model superimposed (dashed red curve).

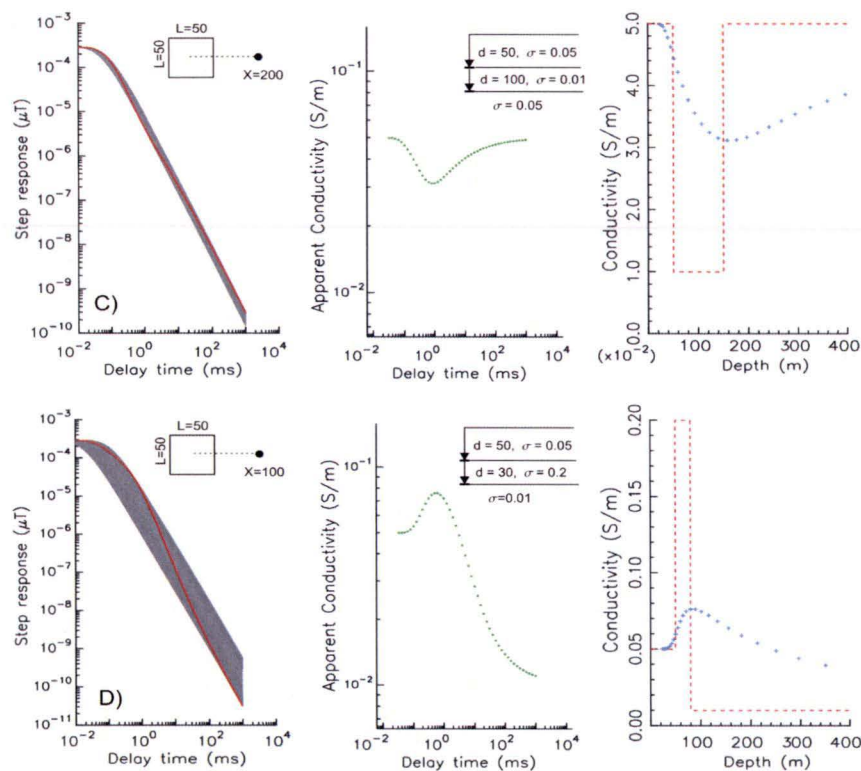


Figure 4.3 – Apparent conductivities for two 3-layer models. The model parameters are specified in the centre panel. The upper panels refer to a thick resistive layer embedded in a more conductive host. The lower panels refer to a thin conductive layer under resistive cover and over a resistive basement. Synthetic recordings are at respective receiver-transmitter offsets of 200 m and 100 m for a square transmitter loop with side lengths 50 m. The right hand panel shows the depth-transformed apparent conductivities with the true conductivity-model superimposed (dashed red curve).

The layered earth test-models, referred to as model A to D, test the theoretical variations possible in stratified media. Synthetic fixed-loop soundings were computed along a mid-line of the fixed transmitter loop. The 2-layered earth models, referred to as A and B, represent, respectively, a resistive overburden over a conductive basement and a conductive cover over a resistive basement. Model A exhibits an initial fast decay in the overburden and subsequently a slow decay rate in the conductive basement. The situation in model B is opposite: the decay is slow in the conductive cover and faster in the resistive basement.

Figure 4.2 shows the results for the 2-layered earth model at a receiver location outside a 250×250 m transmitter loop. The results of the three-layered earth models at a receiver location outside a 50×50 m transmitter loop are shown in Figure 4.3. The 3-layered earth models, referred to as C and D, represent a conductive layer in a resistive host (C) and a resistive layer embedded in a more conductive host (D). The layers introduced in model C and D respectively decreases or increases the decay rate of the induced current systems.

Moving from left to right, the three panels in Figures 4.2 and 4.3, display the main stages of the processing from $|\mathbf{B}|$ -field versus time to conductivity versus depth curves. The leftmost panel shows the $|\mathbf{B}|$ decay curve of the model (red) at one offset, with total magnetic field half space decays superimposed for the apparent conductivity at each delay time. The dimensionless transmitter-receiver offset, X/L (where X denotes the receiver offset, L the long side of the transmitter), selected for display is 1.5 for models A and B, 4.0 for C and 2.0 for D. In the second panel, the apparent conductivity is plotted as a function of delay time at the selected offset. The right hand panel shows the depth-transformed apparent conductivities at the selected offset, with the true conductivity-model superimposed (dashed red curve). Depths correspond to maximum B_z depth in a half space. At each receiver station, a depth-conductivity profile is obtained. The apparent conductivities are assigned to depth points directly beneath the receiver station.

To obtain a conductivity-depth pseudo section, the depth profiles from all receivers are interpolated or 'stitched'. Pseudo-sections for the two-layer examples (models A and B) and the three-layer examples (models C and D) are depicted in Figures 4.4a and 4.4b respectively. The interpolation procedure uses an *inverse distance to a power* gridding method which is a weighted average interpolator. The recovered models, as shown in the conductivity-depth pseudo sections, give a smoothed portrayal of the layered geoelectrical structures. The depth-to-top of all layers are correctly depicted. The depth-to-top of the second layers in the three-layered models, are underestimated which is a consequence of the diffusion method.

The inductive limit is encountered at large transmitter-receiver (Tx-Rx) offsets, and/or early delay times and/or for high conductivity. At the inductive limit the B -field response is independent of ground conductivity and a function of the Tx-Rx geometry only. Apparent conductivity is therefore undefined. Data at (or above) the inductive limit can easily be excluded from apparent conductivity calculations. Hence the undefined regions (in white) at shallow depth and far offset in the conductivity-depth pseudo-sections for models A, B, and C (Figure 4.4a and 4.4b).

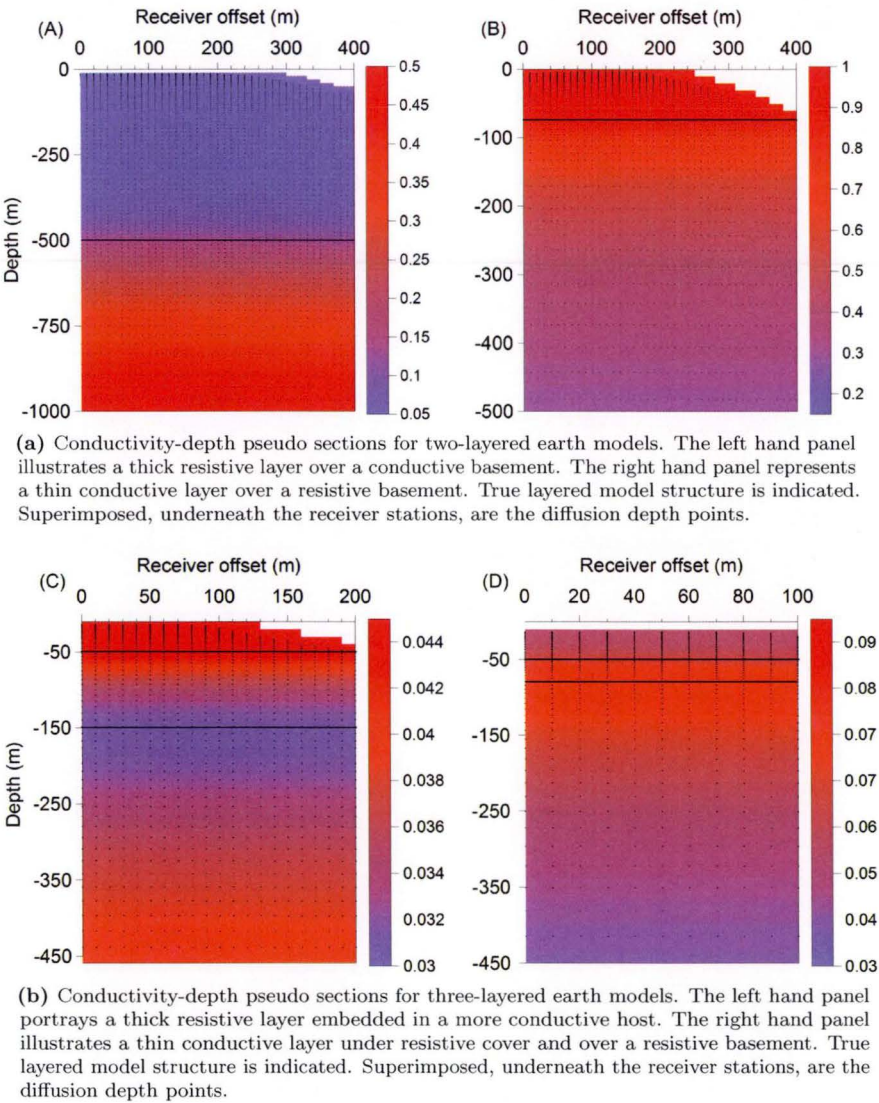


Figure 4.4 – CDIs for two-layered earth (top) and for three-layered earth (bottom).

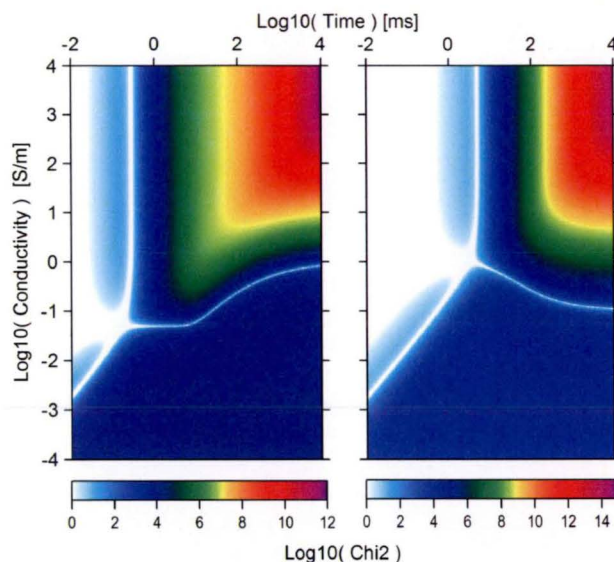
4.4.1 Unambiguous total magnetic field apparent conductivity

Non-uniqueness of separated loop apparent conductivity arises because the EM response is not necessarily either strictly increasing or decreasing. As a consequence, CDIs based on single-component data may contain artifacts which show spurious conductive regions. In 3D environments, apparent conductivity may not be well defined since any given half space model cannot fit the 3D TEM response. As a result thereof, in order to fit the response, artificial conductive regions may originate which give a misleading picture of the subsurface geoelectrical structure.

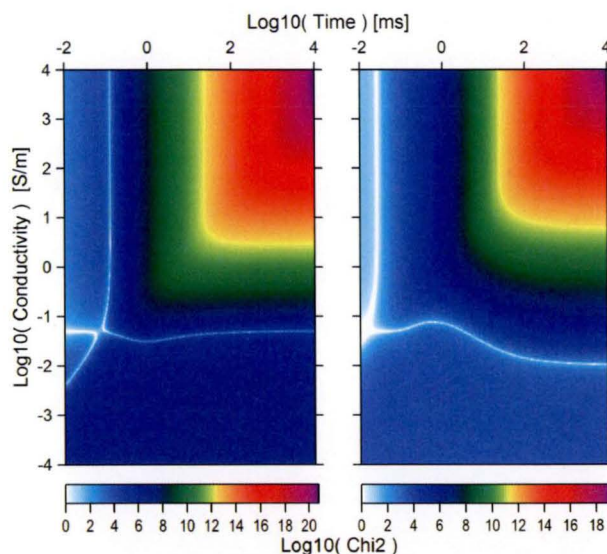
Over a layered half space, the apparent conductivities based on $|\mathbf{B}|$ -field amplitudes are unique except at very early time, when the inductive limit is encountered and the ground TEM response is independent of conductivity. A unique apparent conductivity can be found because the decay of $|\mathbf{B}|$ TEM data over a conductive half space is always monotonically decreasing with time. Based on the layered earth models, previously introduced in Figures 4.2 and 4.3, the following discourse examines the non-uniqueness of apparent conductivity based on amplitudes of the magnetic flux density.

Mathematically, uniqueness manifests in single solutions for the χ^2 misfit function, previously introduced in Equation (4.1). In order to obtain all possible minima of the χ^2 misfit for layered models A to D, the χ^2 minima for a wide range of conductivities and times have been calculated. Images of the χ^2 -misfit in time-conductivity space reflect the behaviour of the inversion inasmuch as they define the regions where apparent conductivity is defined. The χ^2 -misfit images have been calculated for 7 decades of conductivity at 100 points per decade and 4 decades of time at 50 points per decade. For each apparent conductivity and time, a half space response was calculated for the appropriate transmitter-receiver geometry, and the χ^2 -misfit was computed for each of the four layered models. The χ^2 -misfit is then represented as a function of conductivity and time.

χ^2 -misfit images for total magnetic field are shown in Figure 4.5a for models A and B and in Figure 4.5b for models C and D. Areas along the left boundary in each panel, grading from blue to white, are associated with the inductive limit response. The inductive limit is attained only at the very earliest times and is extensive in model A and B. Apparent conductivity is undefined in these zones. The inductive limit extends to later times for model B because of the high conductivity of its uppermost layer. The thin blue-white curvilinear running from left to right across the images connects the (conductivity, time) pairs for which χ^2 drops below unity. For almost the entire time-range there is only one minimum χ^2 corridor for each model, demonstrating the unique nature of apparent conductivities computed from $|\mathbf{B}|$ values. The shape of the corridor reflects the geoelectrical structure of the corresponding model.

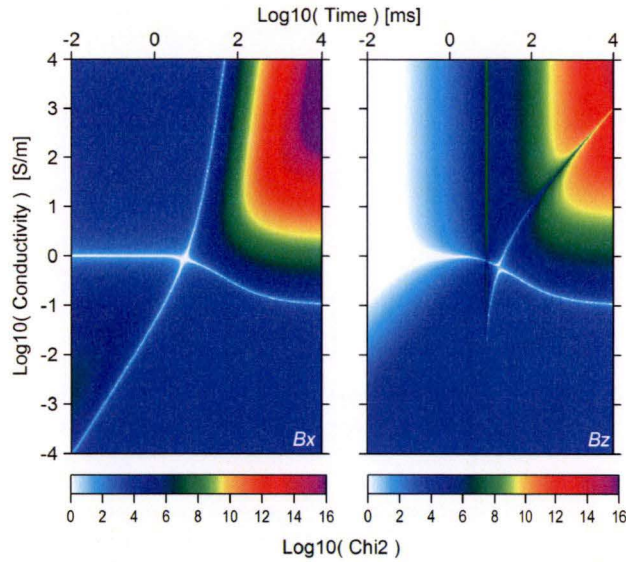


(a) χ^2 -misfit images of total magnetic field apparent conductivities for models A (left) and B (right), at dimensionless offset $X/L = 1.5$. A single narrow corridor of low misfit can be traced across to the right side of each image and reflects occurrence of a unique apparent conductivity. The inductive limit is attained only at the very earliest times and is extensive in model A and B (blue-white region at upper left).

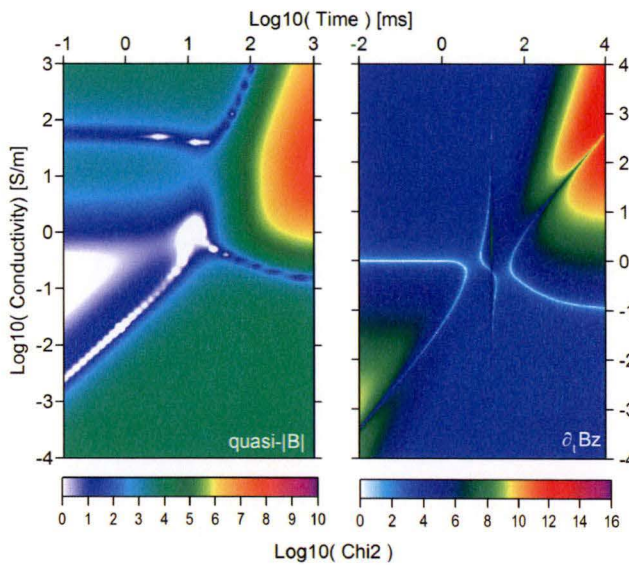


(b) χ^2 -misfit images of total magnetic field apparent conductivities for models C (left) and D (right) at dimensionless offsets $X/L = 4$ and $X/L = 2$ respectively. A single narrow corridor of low misfit can be traced across to the right side of each image and reflects occurrence of a unique apparent conductivity.

Figure 4.5 – χ^2 -misfit images of total magnetic field apparent conductivities for two- and three-layered earth models.



(a) Images of χ^2 -contour of B_x and B_z responses for model B at a transmitter-receiver dimensionless offset of 1.5. The χ^2 -contour for B_z illustrates the non-unique nature of single component step response apparent conductivity. The B_x response is non-unique at early and intermediate times but, like $|B|$, exhibits essentially unique behaviour at late times.



(b) χ^2 -contour plots for quasi- $|B|$ and $\partial_t B_z$ for model B at a transmitter-receiver dimensionless offset of 1.5. Processed multi-component data quasi- $|B|$ is virtually non-unique, inasmuch that only the lower branch of χ^2 -minima is geologically plausible. In contrast, the single component data $\partial_t B_z$ exhibits non-unique behaviour. At intermediate time, the apparent conductivity is undefined or multi-valued.

Figure 4.6 – Comparison with quasi- $|B|$ and single component data.

4.4.2 Comparison with quasi $|\mathbf{B}|$ -field amplitudes and single component data

The panels in Figure 4.6a show χ^2 -misfit images (for model B) for the horizontal and vertical components of \mathbf{B} . Apparent conductivity based on B_x is also ‘virtually unique’ at late times. The intersection of the two corridors at intermediate times signifies the peak B_x response; apparent conductivity is unique at that point. The χ^2 -misfit image for B_z reflects the impact of the inductive limit at early times. The apparent conductivity is unique as B_z starts to decay, for as long as B_z remains negative. Apparent conductivity is dual valued at later times, when B_z is positive. The χ^2 -misfit image for quasi- $|\mathbf{B}|$ in Figure 4.6b combines characteristics from the $\partial_t B_z$ image and the $|\mathbf{B}|$ image¹. The two minimum χ^2 corridors are well separated at all times. Early time apparent conductivity is problematic, but at later times the quasi- $|\mathbf{B}|$ apparent conductivities are ‘virtually unique’, since one conductivity can be rejected as geologically untenable. The χ^2 -misfit image for $\partial_t B_z$ includes intermediate regions with no minima; apparent conductivity is undefined there. Some χ^2 minima in the centre of the image are associated with the zero-crossing of the decay curve. The shown χ^2 -misfit images for single components $\partial_t B_z$, and B_z exhibit two minimum χ^2 corridors, hence two apparent conductivities, at most delay times. In all panels the shape of the lower late time apparent conductivity corridor reflects the geoelectrical structure of the model.

4.5 CDIs of 3D structures

Performance of the conductivity-depth conversion for 3D structures is investigated in the following section. For layered earth structures, apparent conductivity is well defined at all times (except in the inductive limit) if generated from total-field amplitudes. The CDI routine is based on the unbounded half space response and the exponential decays associated with compact conductors are ‘foreign’ to it. Therefore, 3D structures may exhibit characteristics which may lead to spurious features in the CDIs.

Three types of simple 3D structures are considered below to test the degree to which the CDIs reflect the true conductivity distribution. First, the response of a vertical prismatic body buried in a conducting host is transformed to a conductivity-depth section. This experiment is repeated for the same prism at a different depth. Second, the response of a flat lying slab in a conductive host is subjected to conductivity-depth conversion. The last example shows the CDI of a dipping plate in a conductive host.

¹The χ^2 -image for quasi- $|\mathbf{B}|$ has been calculated on a coarser grid due to computational expenditure

4.5.1 Vertical prism in a moderately conducting host

The following model consists of a vertical prism with dimensions $120 \times 800 \times 400$ (E-W, N-S, Z). The prism has a conductivity of 2 S/m buried in a host with conductivity of 2 mS/m . Conductivity-depth sections from total-field amplitudes and Z-components are obtained for two different burial depths: (a) depth-to-top is 200 m , (b) depth-to-top is 400 m . The model configuration is shown in Figure 4.7. The step response is calculated with the integral Equation solver MARCO (CSIRO) which calculates the EM response of prisms in a layered host.

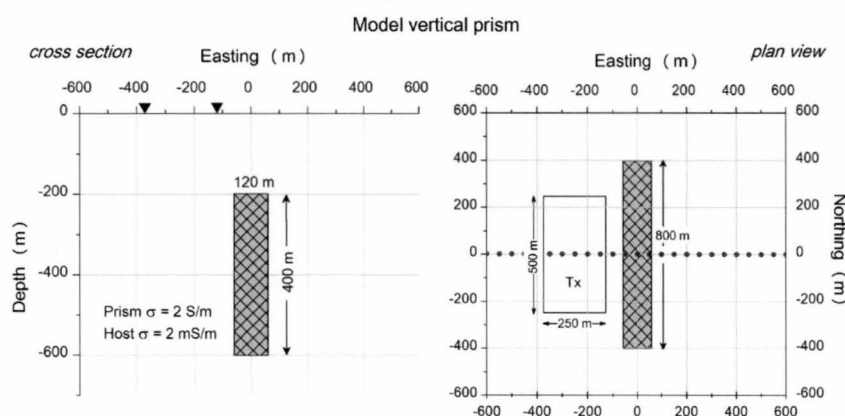


Figure 4.7 – Vertical prism model for a synthetic fixed-loop survey. The configuration shown is for model (a) where depth-to-top is 200 m . The second model (b) is identical but has depth-to-top of 400 m . Synthetic recordings are obtained over the centre-line of the model at 50 m intervals from -600 East to 600 East . The channel delay times are consistent with the SMARTEM channels (Table 1.2).

The step response of the prism (a) for the Z-component is depicted in Figure 4.8 on the left panel, the right panel shows the X-component. The Z-component responses on negative Eastings, $< -50 \text{ m}$, are all flat, and the decay curves of the Z-component are virtually half space responses at all times at these locations. A crossover anomaly in the Z-component is apparent at positive receiver offsets $\sim 200 \text{ m}$ from the Tx-loop centre and indicative of termination of the subsurface conductor. The first three channels are mostly influenced by the host; cross-overs of the first three channels at far offsets, $\sim 500 \text{ E}$, $\sim 550 \text{ E}$, $\sim 600 \text{ E}$, are due to the 'smoke ring' current passing the receivers. The horizontal component will always be zero at the loop centre over homogeneous ground; here, however, it shows some distortions due to the presence of the anomalous prism. At the location of the prism, the absolute value of the X-component is maximum.

The conductivity-depth sections for $|\mathbf{B}|$ and B_z are shown in Figure 4.9a for a burial depth of 200 m and in Figure 4.9b for a burial depth of 400 m . Because of the resistive host, currents have already diffused to a depth of $\sim -200 \text{ m}$ at the first channel delay time. A conductive high has been defined in all CDIs, indicative of a conductive 3D feature. The profiles of both, $|\mathbf{B}|$ -field amplitude

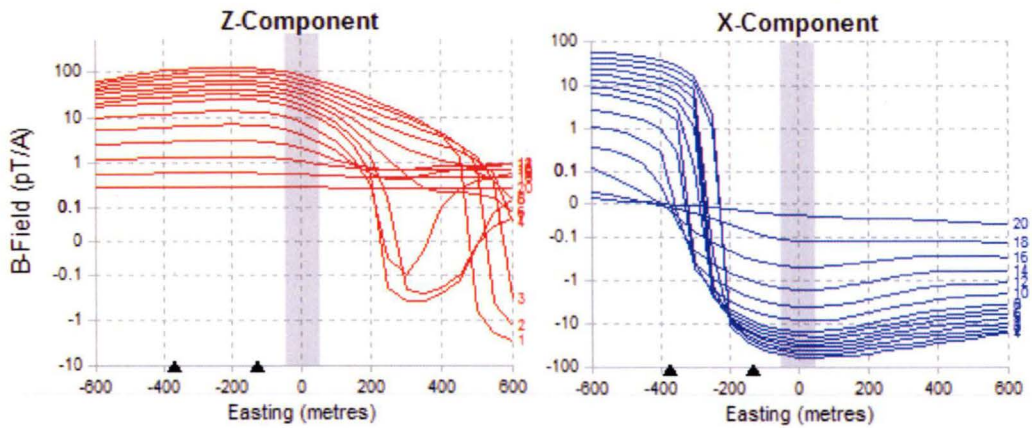
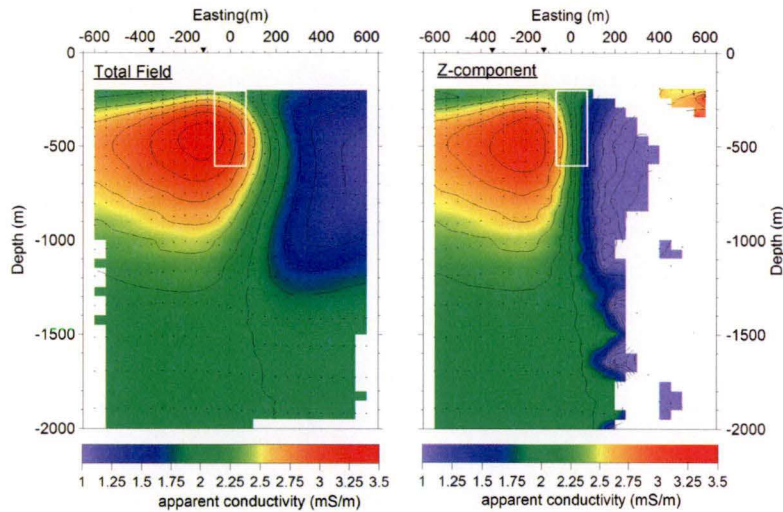


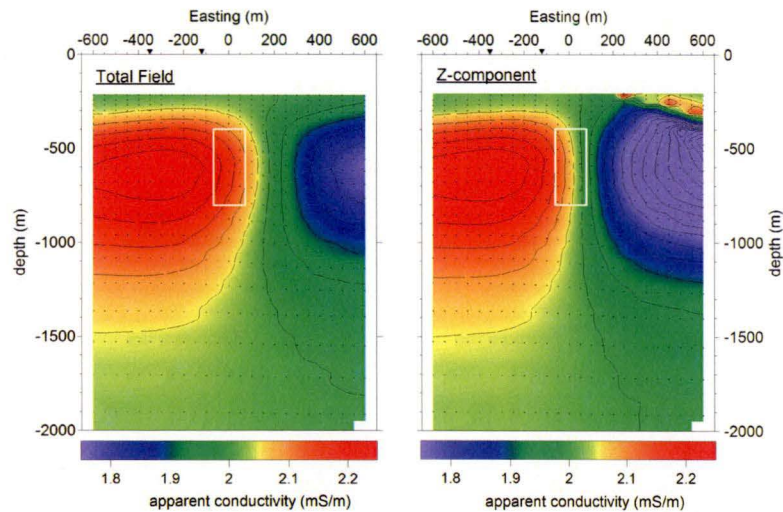
Figure 4.8 – Stacked profiles TEM step responses of Z-component (left) and X-component (right) over a vertical prism at 200 m depth in a resistive host. Black triangles indicate Tx loop wires. Gray band marks projected position of the prism. Red / blue numbers refer to Rx channels. The responses are calculated with the integral Equation solver MARCO.

and Z-component, are similar, however the Z-component CDI exhibits spurious conductive features at large, positive, receiver offsets. The conductive zone extents much further east in the $|\mathbf{B}|$ -CDI, coinciding with the lateral extent of the buried prism, whereas the conductor is cut short on the B_z CDI by virtue of the cross-over (Figure 4.8). Non-uniqueness of B_z apparent conductivity becomes an issue in the vicinity of the cross-over: as B_z approaches zero the most acceptable apparent conductivity is zero, the alternative being extremely large. On the other hand, $|B_x|$ is maximum at the B_z zero crossing, with the result that the true extent of the conductor is more faithfully captured in the $|\mathbf{B}|$ -field amplitudes CDI.

The conductive zone is extended further west, external to the true prism beneath the transmitter loop; this attribute is more pronounced in model (b). At receiver offsets near the transmitter and away from the prism, the EM response is mostly that of the host, however slightly increased due to the presence of the conductive body. Apparent conductivity will consequently characterise the higher EM response amplitudes at these offsets, resulting in the extended conductive zone to the west. Another characteristic of the prism CDIs is the separation between conductive high on the west and conductive low on the east of the buried prism which is a consequence of the transmitter-receiver offsets. At far offsets, on the eastern side of the prism, the EM responses have smaller amplitudes resulting in lower apparent conductivities. The CDIs for the prism at 400 m depth display virtually the same behaviour, however the result is a more smoothed image of the true model due to larger diffusion depths. The good indication of depth is noteworthy in both cases.



(a) CDI of 2 S/m vertical prism at 200 m depth from total-field data (left panel) and from Z-component step response data (right panel). Superimposed is the true model and the data points as obtained from the conductivity-depth conversion. The CDI on the right hand panel displays regions where no conductivity is defined. Here, apparent conductivity is undefined. Due to the complicated behaviour of the Z-component at far receiver offsets, east from the prism (Figure 4.8), no half space model fits the response. In addition, a spurious conductive feature is apparent at Eastings > 400E on the right hand panel. The half space conductivity of 2 mS/m is depicted very good in both CDIs.



(b) CDI of 2 S/m vertical prism at 400 m depth. At greater depths, the conductive zones depicted in both CDIs are broader due to increased diffusion depths. As in model (a), the Z-component CDI consists of artifacts, apparent at Eastings > 200E.

Figure 4.9 – CDIs of vertical prisms in a moderately conducting host.

4.5.2 Horizontal slab in conductive host

A thick horizontal slab in a conductive host is modelled with MARCO. The model is shown in Figure 4.10 and displays a square prism with 500 m side lengths and with 200 m depth extent; depth-to-top is 300 m. The resulting EM response is symmetric with respect to zero Easting where the amplitudes of the Z-component are maximum and the X-component has a cross-over. The response characteristics are suitable for conductivity-depth conversion of Z-component data. The resulting CDIs from the single component as well as the multi-component data give similar results.

Figure 4.11 shows the resulting CDIs with the true prism superimposed. The depicted depth-to-top in both CDIs concurs with the true depth of the slab, however the main conductive zone is located below the actual prism and extends to deeper depths. Since the decays have increased amplitudes over the centre of the conductive body, apparent conductivities reflect a conductive half space which match these amplitudes over the centre. On the other hand, amplitudes are not increased ($|B|$) or diminished (B_z) at the prism edges, thus apparent conductivities will be lower here. As a consequence the conductive zone will extent deeper over the centre of the body. The conductive zone is somewhat broader in the total-field CDI which is a consequence of higher amplitude values of the total-field response at the flanks of the prism. Here, the Z-component has smaller amplitudes, the X-component however has maximal amplitudes over the lateral extents of the body resulting in higher total-field amplitudes. The half space conductivity from the model can be inferred from the depicted CDIs (blue region).

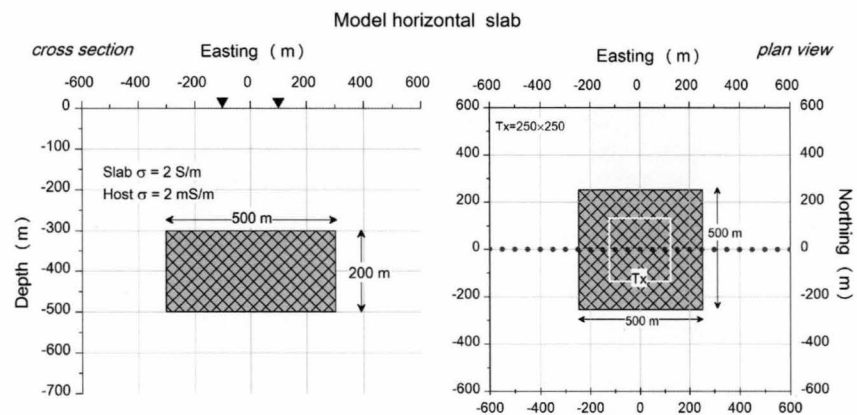


Figure 4.10 – Horizontal slab model for a synthetic fixed-loop survey. Recordings are obtained over the centre-line of the model at 50 m intervals (SMARTeM channels, Table 1.2). The transmitter loop is centred over the slab with side lengths proportional to the slab side lengths. The model configuration results in a symmetric TEM profile.

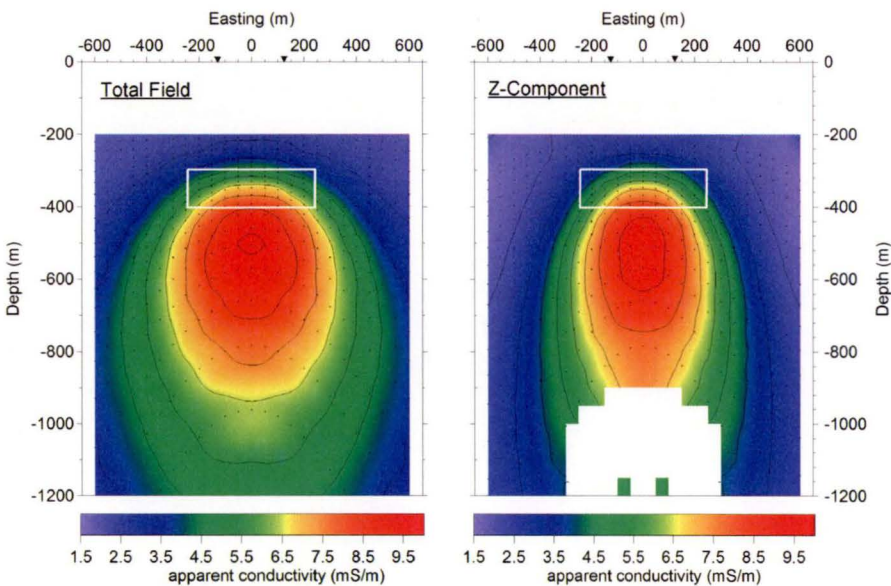


Figure 4.11 – CDI of horizontal slab. The left hand panel shows the CDI from B-field amplitudes whereas the right hand side shows the CDI obtained from the vertical component of the step response. The true model is superimposed together with the data points as obtained from the conductivity-depth conversion. Both CDIs depict the actual depth-to-top of the prism.

4.5.3 Dipping plate in a conductive host

This section investigates how the response of a plate conductor transforms under conductivity-depth imaging. Since the conductive region is confined to a bounded and very narrow region, it can be anticipated that conductivity-depth imaging is less indicative of the true conductive region because of the diffusive nature of the imaging scheme, which is based on unbounded half space decays. Nonetheless, conductivity-depth sections of the plate models based on total-field data is suggestive of conductive 3D features, which is not always the case for CDIs obtained from Z-component data. The model configuration is depicted in Figure 4.12. The models are calculated with the EM modelling program LEROI (CSIRO) which computes the full EM response of conductive plates in a layered earth.

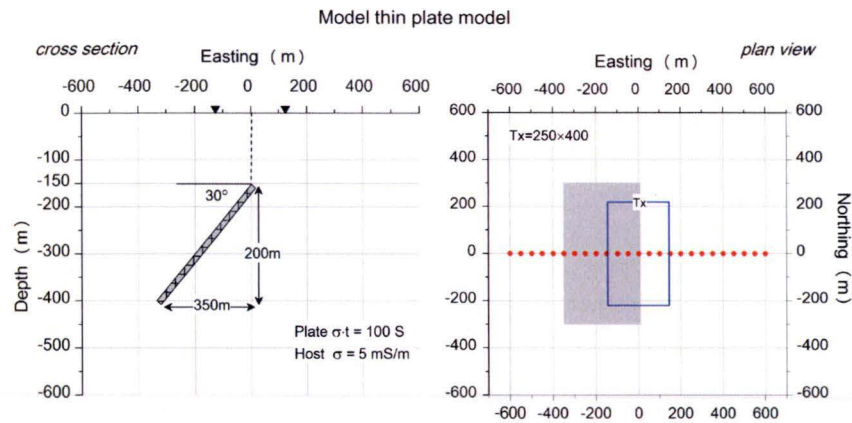


Figure 4.12 – Dipping plate model for a synthetic fixed-loop survey. Recordings are obtained over the centre-line of the model at 50 m intervals (SMARTeM channels). The conductance of the plate in both cases is 100 S in a conductive host of 5 mS/m.

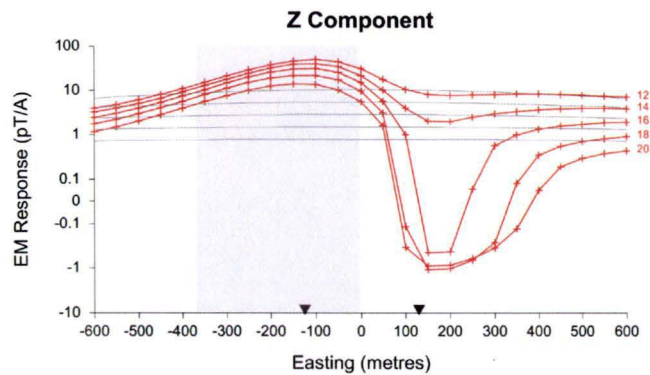


Figure 4.13 – Z-component TEM decay of dipping plate underneath transmitter loop for every second channel from 12 to 20. The selected channels chosen for display, show the transition from mainly host influenced decay to mainly plate influenced decay. Superimposed (in grey) are the responses from the host only. The grey shaded area indicates the position of the plate in plan view and the triangles on the abscissa axis display the transmitter position. The cross-overs of channel 18 and 20 approximately mark the edge of the buried conductor. The positive lobes of the anomaly profile is directed towards the transmitter loop, and in this case, over the conductive feature.

The stacked profile of the Z-component is shown in Figure 4.13 from channels 12 to 20 for every second channel. It depicts the transition from mainly host-influenced to mainly plate-influenced response. For comparison, the host response is superimposed. The zero crossing is indicative of the edge of the buried conductor. The positive lobes of the response are directed towards the transmitter loop, which, for this particular model geometry, coincides with the orientation of the plate. Because of this model characteristic, apparent conductivity is well-defined for the Z-component CDI at the location of the anomalous conductive volume (Figure 4.14).

The depicted conductive zones in both CDIs for total-field and Z-component, Figure 4.14, extent to great depths and does not reproduce a plate conductor. Nevertheless, the emergence of the conductivity gradient in both CDIs coincides with the location of the plate. This is typically observed in CDIs for plate-like conductors. It can be furthermore observed that the top of the conductive zone approximately coincides with the plate's dip along its depth extent. The top of the plate, however, is not honoured in both CDIs. The CDI from Z-component data on the right hand panel, exhibits broad white patches where no conductivity-depth data is defined due to the negative responses at far Eastings.

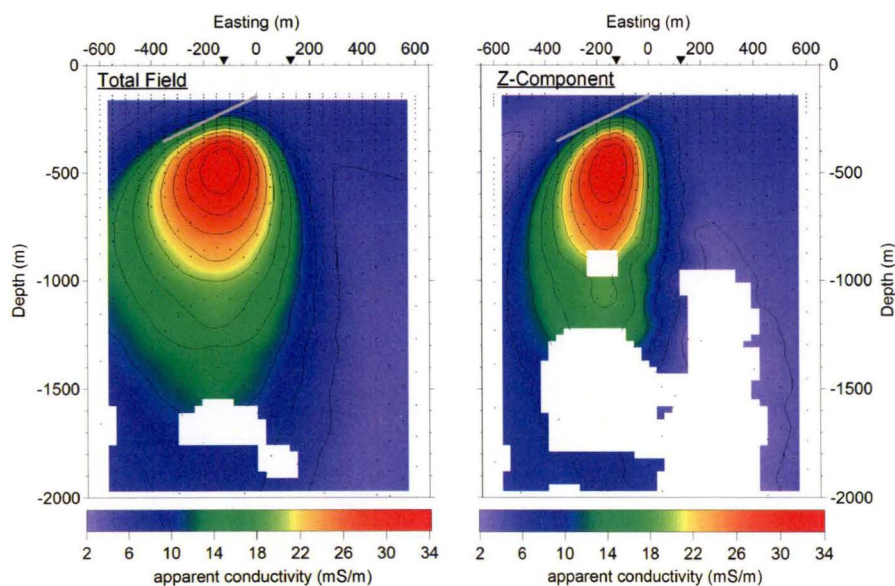


Figure 4.14 – CDI of dipping plate underneath the transmitter loop from B-field amplitudes (left) and from Z-component step responses (right). Superimposed are the plate models and the data points from the conductivity-depth conversion. Both CDIs give a good indication of the depth to the centre of the plate whereas the top of the plate is not honoured in both CDIs. The Z-component CDI shows extensive editing for Eastings $> 100\text{ m}$ at depths where the white patches occur. Apparent conductivity is undefined here. The half space conductivity displayed in both CDIs agrees with the model half space conductivity (5 mS/m).

4.6 Field data example

Apparent conductivities derived from $|\mathbf{B}|$ measurements have been used to generate a conductivity-depth image from multi-component B-field data. The fixed-loop TEM data were acquired across a Proterozoic metavolcanic sedimentary sequence hosting Pb-Zn-Cu-Ag mineralisation buried in a resistive environment. The transmitter loop had dimensions 400×800 m, with the long side of the loop oriented north-south, perpendicular to the survey line. The loop was centred at (11050E, 7900N), and the TEM data were recorded on line 7600N. Receiver station spacing was 50 m or 100 m. The transmitter on and off times were 900 ms (0.2778 Hz fundamental), with a turnoff ramp of 0.5 ms. A low temperature SQUID sensor was used, in conjunction with a SMARTTEM receiver. Channel centre times ranged from 0.1 ms to 710.31 ms (Table 1.2).

Figure 4.15 displays the response curves from channels 1 to 41 for every fourth channel. Shown are the Z-component, X-component and the total-field amplitudes, calculated from all three (Z,X,Y) components. The data is very clean, even at 700 ms after shut-off. A cross-over in B_z is evident near 10500E, indicating termination of a conductor below. The anomaly shape of the response curves suggests a west-east dipping conductor extending below the transmitter loop. Even at very late channels, the transients have not decayed to zero and exhibit responses from a conductive feature. This advocates that the conductive body is thick.

As a first estimate, the response has been modelled by a west-east dipping plate residing in a resistive host as shown in Figure 4.16a. The plate modelling was carried out with the integral Equation solver LEROI. The plate parameters are given in the caption of Figure 4.16a where the measured B_z response is superimposed. It can be seen that the anomaly shape of the plate resembles the anomaly response curves of the measured data. Noticeable, however, is the rapid decay of the plate response, even for a relative high conductance of 500 S. Higher conductance values renders the response towards the inductive limit of the plate and does not improve the fit, which substantiates the suggestion of a thicker conductor.

The response data for all components (X,Y,Z) from the plate model as well from the observed data have been converted in conductivity-depth pseudo images. CDIs were generated in two stages. first, apparent conductivities were computed at each delay time, then depths were assigned according to the depth of the maximum B_z in a half space with conductivity equal to the apparent conductivity at the time in question. The resulting pseudo-sections for the B-field amplitudes are imaged and contoured in Figure 4.16b. The apparent conductivities are very low at early times, with the result that the CDIs are blank at shallow depths; current has already diffused hundreds of metres through schists and quartzites before the first delay time. The CDIs of both data sets, measured and synthetic, have similar conductive zones at comparable depths. However the main conductive zone is located at a deeper depth in the CDI of the measured data and consists of a smoother transition zone from low to high conductive values which probably reflects a thicker body. Also, the apparent conductivities are much higher than those which could be obtained for the plate model. The conductive zone of the plate is much deeper than the actual model.

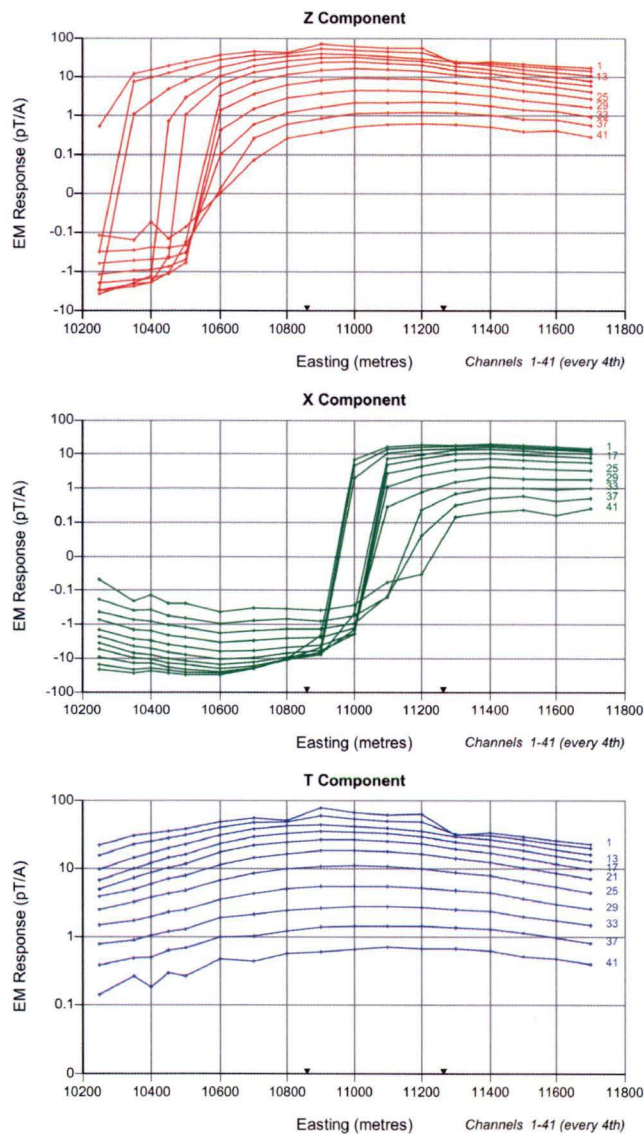
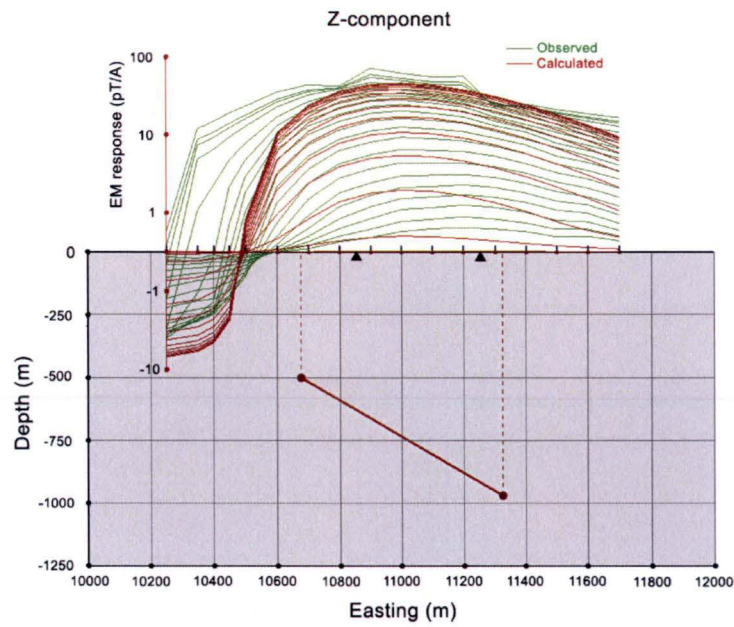
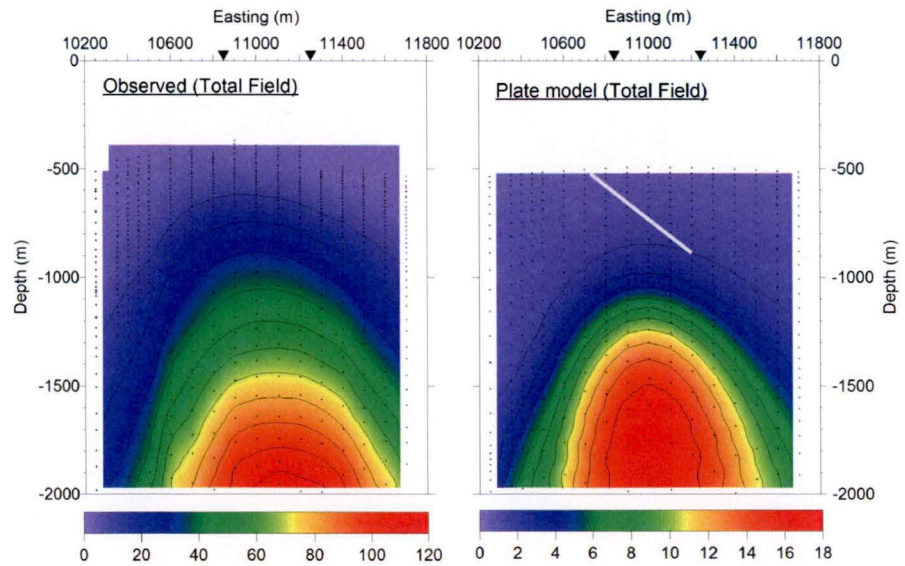


Figure 4.15 – Stacked profiles for field data fixed loop TEM. Arrows indicate the position of the $400m \times 800m$ transmitter loop. Readings are taken every 50 or 100m. To avoid cluttering in the Figures, responses are shown for every fourth channel (all channels from 1 to 41). The B_z cross-over near 10500E is interpreted to mark the edge of a buried conductor. Shown are also the X-component and the total-field amplitudes as calculated from Z-, X-, and Y-component.



(a) Plate model and observed data (Z-component). The plate strike length is 700 m with depth extent of 600 m. It has a dip of 40° and a dip direction of 90° . The conductance of the plate is 500 S buried in a resistive background of 0.2 mS/m



(b) Conductivity-depth pseudo-sections from measured (left) and modelled (right) multi component fixed loop TEM field data.

Figure 4.16 – Z-component of measured field data and plate model (top) together with total-field CDIs for measured and modelled data (bottom).

4.7 Concluding remarks

Conductivity-depth pseudo sections from $|\mathbf{B}|$ -field amplitudes can provide a better image of discrete or truncated conductors than CDIs based on individual components, since zero crossings of a single component are not depicted as resistive zones. Data acquired in 3D environments translate to $|\mathbf{B}|$ CDIs which exhibit 3D features. Conductivity-depth images from $|\mathbf{B}|$ -field amplitudes supplements interpretation of TEM 3D data, however careful analysis of the decay response curves is required to elucidate the 3D characteristic.

The EM responses of thick prismatic bodies translate well to conductivity-depth images as obtained from $|\mathbf{B}|$ -field amplitudes. Vertical prismatic bodies, offset from the transmitter loop, tend to produce an elongated conductive high in the $|\mathbf{B}|$ -CDI towards the transmitter loop, but reliably images the top and the edge away from the transmitter; on the opposite side, a resistive zone manifests in the CDI (Figure 4.9a). The result for the flat lying slab is analogous.

In case of plate-like conductors, however, the underlying geoelectrical structure may not be faithfully captured in the CDIs and cannot be easily identified as a conductive plate. This is because the CDI routine is based on the unbounded half-space response, which cannot 'capture' the response of the bounded, narrow plate-conductor very well. Notwithstanding these complexities, processing \mathbf{B} -field amplitudes general results in CDIs which identify 3D structures whereas the use of Z-component data alone may result in incoherent images of the subsurface. Principal guidance in interpretation of total-field CDIs from 3D environments is not given by the conductive high depicted in the image, but by the conductivity gradient, i.e. edges of the conductive zone where the conductivities start to deviate from the background response.

The measured field-data is interpreted, as a first approximation, as a dipping plate. While not quite sufficient to assess the conductivity of the target, it may reveal geometrical parameters, like dip and depth extent, of the target. The total-field CDI of the measured data, as well as the plate model, exhibit significant similarities and establishes some confidence in the interpretation of the data. The plate model, as captured in the CDI, locates the conductive zone at much deeper depths than the actual model. In consequence, the CDI from the measured data may reflect analogous behaviour. In addition, the transition zone from background conductivity to higher conductivity seems to mark the edge of the dipping conductor. As can be recognised from the contour lines, the dip approximately agrees with the plate model. The lateral extent of the conductive zone is interpreted to approximately reflect the depth extent of the target. When comparing the CDI for the field data with the 'best-fitting' plate, the two results are alternative preliminary interpretations. The CDI defines the conductivity of the host nicely, and provides an image of a laterally-localised conductor. In the absence of any independent 'a priori' information it is difficult to prefer one interpretation over the other.

In summery, CDIs from \mathbf{B} -field amplitudes assist in interpretation of 3D structures without producing spurious features and therefore may well provide a starting model for 3D inversion. The CDIs provide initial estimates of time-

constants for the 3D inversion scheme or can be encompassed as inversion weights which favour solutions close to the CDI models. CDI processing fits half space responses to TEM data which may exhibit 3D-TEM characteristics, therefore exponential decays associated with compact conductors cannot unambiguously be imaged. This limitation is addressed by allowing for confined conductors as implemented in the fast, approximate 3D-TEM inversion scheme, which is discussed in the next chapter.

Chapter 5

3D Inversion of TEM moments

Introduction Three-dimensional geophysical inversion of EM data aims to give an idealised estimate of the 3D geoelectrical structure of the subsurface which can meaningfully describe a set of observations. Inversion is a numerical process whereby an initial model is adjusted to improve the fit between the measured geophysical data and the corresponding calculated data based on the model (Fullagar et al., 2008). Inversion proceeds as an optimisation problem by minimising an objective function which is a metric that measures the difference between observed and modelled data. At minimum, a geophysical model defines a distribution of one or more physical properties in the subsurface. The present study incorporates geological constraints in an innovative and novel approach for fast, integrated 3D inversion of parametrised TEM data where recovered model parameters after inversion define the geoelectrical structure of the subsurface in terms of time constants.

Rigorous 3D inversion of time-domain electromagnetic data is an onerous challenge, mainly due to computational requirements. TEM measurement configurations can easily result in problems too slow for practical inversion on standard computation facilities. However, 3D inversion of TEM data is feasible using the method described here. First, the TEM moment methodology effectively compresses the number of data points by integrating the response data with respect to time, thus reducing a decay to a single value. This results in a smaller numerical problem which is faster and less demanding in terms of memory. Second, using TEM moments, EM interaction may tolerably be ignored, therefore facilitating linear superposition of TEM moment responses which reduces the computation time remarkably. Third, the approximate forward calculation utilises analytical TEM moment expressions, so that calculations are fast. Fourth, if posed in terms of the time constant, the TEM moment transform renders the non-linear time-domain problem into an approximate linear moment-domain problem. Derivatives of linear inverse modelling schemes are model independent, therefore expediting successive model updates via initially calculated derivatives which accelerates the inversion process substantially. Furthermore, the 3D inversion scheme employs a fast steepest descent method; computationally expensive matrix inversion is not required. The reduction in accuracy with respect to

fully 3D-EM solutions is accepted as a trade-off for much improved speed of calculation. Typically, for ground-TEM, the described 3D inversion problem, completes in minutes rather than hours or even days, thus facilitating flexible data interpretation where various different models can be subject to analysis in a short time frame.

Because of the time-integration of the TEM moment transform, depth resolution is lost and conditioning the inversion becomes essential. In effect, the moment transformation converts the 3D TEM inversion problem into a 3D magnetic inversion problem. Thus, a potential field inverse problem is solved where non-uniqueness is significant, i.e. multitudinous source distributions explain the data equally well. Non-uniqueness is balanced by including geological information in the inversion and/or by utilising standard potential field inversion devices, such as depth weights and property bounds (Oldenburg and Pratt, 2007; Li and Oldenburg, 1998, 1996).

For fast, approximate inversion of TEM moments the VPmg inversion approach has been adopted. VPmg is a gravity, gravity gradient, and magnetic 3D modelling and inversion program, designed for integrated interpretation utilising geological constraints (Fullagar et al., 2000, 2004; Fullagar and Pears, 2007; Fullagar et al., 2008). VPmg inversion proceeds from a geological litho-model, defined on a 3D grid, which reflects the available geological knowledge, so that each cell is assigned to a rock type. The underlying model is both geological and petrophysical (categorical and numerical) before, during, and after inversion, so that the lithological significance is preserved throughout the inversion process. Fullagar and Pears (2007) mention that VPmg allows for flexible property inversion, since preservation of domain boundaries implies retention of rock type designation. Therefore property changes can be restricted to a particular geological domain, if desired. The greater flexibility, as compared with property-only inversion styles, can be attributed to the fact that the underlying model is categorical as well as numerical.

For inversion of TEM moments, selected domains of the categorical model are subdivided into cubic cells, each carrying a point conductor at its centre. The 3D inversion of TEM moments furthermore distinguishes 'background' and 'target' response which can each be subject to individual optimisation. As described in Chapter 3, the background is comprised of a conducting half space whereas the target is effectively a distribution of cells in free space. The recovered model time constants define the geoelectrical structure of the subsurface. During inversion, the time constants associated with each point conductor are subject to iterative adjustment so as to fit the observed data.

This chapter describes the inversion method developed to produce a 3D distribution of time constants that explain a given set of TEM moments. First, the details of the 3D inversion of TEM moments is delineated, subsequently model preparation and examples are presented. The examples concentrate on inversion of the Z-component TEM moments of the horizontal slab and vertical dyke model, which have been previously introduced in Chapter 3. In order to test the inversion algorithm and examine the variability of the inversion results due to non-uniqueness, the inversion proceeds from different starting models so as to explore some of the range of acceptable models. For different starting models and constraints, the inversion could recover time constant models which approximately indicated the location of the true conductive body.

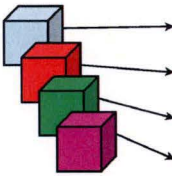
5.1 Overview of the inversion algorithm

The following section is meant as a qualitative overview of the TEM moment inversion program developed during this study. The TEM moment inversion program builds on the VPmg potential fields framework and is referred to as VPem3D. VPmg has been developed to specifically address enforcement of geological constraints, in particular drill hole information, so as to reduce the inherent ambiguity of interpretation of potential field data. This is achieved in VPmg by assigning each cell to a rock type, so that the geological significance of boundaries is preserved. In VPmg, the subsurface is discretised into close-packed identical rectangular prisms, and internal contacts divide each prism into cells. After inversion the model is fully recognisable as a geological model, i.e. comprised of lithological or structural domains.

Usually, the rock types of interest are distinguished on the basis of their physical properties where rock properties are derived from drill core or hand samples, or logged downhole. Petrophysical properties provide the link between mineralogy and geophysics, and hence between geology and geophysics (Fullagar and Pears, 2007). Based on the measurements, geological models are comprised of surfaces, mainly litho-stratigraphic boundaries and structures, which divide the ground into rock type domains. The surfaces are interpolated between mapped or drilled points on geological contacts and structures. Away from the borehole logs, the geological model can be highly interpretative in nature, however.

Fullagar and Pears (2007) note that algorithms operating on geological models can exert a greater degree of control over rock properties and permit flexibility in the conduct of inversion. For example, property changes during inversion can be confined to selected rock types and property bounds can be linked to each geological unit. Property bounds designate the minimum and maximum property value allowed in each cell. Adoption of a categorical model structure does not limit options for property inversion: 'unconstrained' property inversion can be performed on a categorical model, with changes restricted to specific units or permitted throughout the entire subsurface.

For TEM moment inversion, a uniform 3D grid is adopted, comprised of cubic cells with a point conductor at the centre of each (Chapter 3). The geological model is mapped onto the 3D grid, subdivided into distinct geological units which results in a simplified litho-model of the underground and therefore facilitating geologically constrained inversion. The model is defined within a continuous conducting background, modelled as a half space, which may optionally be held fixed or variable during inversion. The 3D model is categorical (i.e. geology) as well as numerical (i.e. property). Each cell is explicitly assigned to a geological unit. The geological units can be homogeneous or heterogeneous. If a geological unit is homogeneous, all its constituent cells share the same property value. If a geological unit is heterogeneous, each of its cells has an individual property value. Inversion of the properties of heterogeneous units produces intra-unit variations of property values, bounded by specified minimum and maximum values. Figure 5.1 illustrates schematically the litho-categorical property table for a model.



Category	Start τ (msec)	Min τ (msec)	Max τ (msec)
Quartzite Schist	0	0	0
Iron Formation	100	0	1000
Aluminous Schist	0	0	0
Pink Gneiss	0	0	0

Figure 5.1 – Parametrisation of rock property model after Fullagar and Pears (2007). Each cell of the geological model belongs to a predefined geological category. The cell properties, in this case time constants τ , are assigned accordingly so that the lithological significance of each cell is captured and carried through inversion. In this example, only the category where ore mineralisation is expected is 'active' for inversion and a start value and bounds are assigned. The property bounds designate the minimum and maximum property value allowed in each cell for each category. If lower and upper bounds are identical, the unit is deactivated.

Heterogeneous property inversion Heterogeneous property inversion for single-component TEM moments is fully supported in the current implementation of the TEM moment inversion algorithm. This inversion style can be described as an extended 'UBC-GIF' inversion style. Like 'UBC-GIF' inversion, heterogeneous property inversion of TEM moments is based on a regular 3D grid where each cell is allocated a property value but additionally also to a rock type, so that the geological integrity is preserved throughout the inversion process.

The number of active parameters is usually larger than the number of data so that an 'under-determined' problem is solved. Consequently, there is a large degree of freedom which is limited by introducing constraints. The inversion proceeds on defined geological units. The properties of all cells within each unit lie between the bounds defined for that unit. The heterogeneous property inversion proceeds as a conventional inversion style where an objective function is minimised in a least squares sense. The details of the inversion are described in Section 5.2 below. Alternatively, inversion proceeds by subjecting individual model cells to random property perturbations; the perturbation is accepted if it produces a reduction in misfit. For this thesis, the conventional heterogeneous property inversion style is exclusively utilised.

Homogeneous property inversion If a geological unit is assumed to be of homogeneous conductivity, the same property is assigned to each cell which belongs to the particular unit. Homogeneous units can be designated as active or inactive during inversion. If a unit is active, lower and upper bounds define the permissible range of property values. Homogeneous property inversion is a discrete body inversion to find a relatively small number of homogeneous body parameters (Oldenburg and Pratt, 2007). It may serve to examine the degree to which the data can be explained by inter-unit variability alone. The assumption of homogeneity is often a useful starting point when very little is known about

local rock properties; inversion can then define the optimal 'average' property (Fullagar and Pears, 2007). The number of active parameters during homogeneous property inversion is usually less than the number of data so that the problem is 'over-determined'. Because there are only a few active parameters, homogeneous property inversion is fast, even if the model is large and geometrically complex.

Homogeneous property inversion is not utilised for inversion of the discrete target response in the current study. The employed optimisation procedure of the background response, however, is a special case (single-parameter) of homogeneous property inversion.

Geometry inversion The geological contacts that define the litho-units of the geological model can be subject to inversion themselves thus constituting geometry inversion. In geometry inversion, the geological surfaces are manipulated to achieve an improved fit between observed and calculated data. The geological significance of contacts is preserved so that the model is still recognisable as a geological model after inversion. During geometry inversion, the properties of all cells are fixed. In VPmg, geometry inversion proceeds by successive adjustments of the horizontal cell boundaries, therefore defining an 'adaptive mesh' (Fullagar and Pears, 2007; Fullagar et al., 2008). Geometry inversion of TEM moments has yet to be implemented.

5.1.1 Rock property constraints

Non-uniqueness is an issue in potential field inversion techniques because multitudinous source distributions produce equally valid mathematical solutions. That is to say, from Green's third theorem it follows that a potential field can be reproduced by an arbitrarily thin source layer or 'equivalent stratum' (Grant and West, 1965, p.214). Discretisation of data and source give rise to an under-determined problem (if there are more model parameters than data points) and the presence of noise add to the ambiguity of the inverse problem (Fedi et al., 2005; Oldenburg and Li, 2005). Non-uniqueness is addressed by including geological and petrophysical information to ensure the solution is consistent with prior knowledge and/or by imposing a set of quantitative weights that approximate geological expectations when geological data is lacking (Williams, 2008). Geological maps, surface samples from trenching or underground drifts and drill holes may supply geological context and actual physical property measurements. In addition, magnetic and gravity potential field data provides further information for categorising and for geological interpretation (McMonnies and Gerrie, 2007; Oldenburg and Pratt, 2007). For inversion of TEM moments within the VPmg framework, inversion constraints can be classified in 'bound', 'hard' and 'soft' constraints, where hard constraints are based on measurements and soft constraints are flexible and subjective to a certain degree.

If geological/petrophysical context is supplied via a geological litho-model, the inversion may be geologically constrained by only allowing cells to change which belong to a specified unit where ore mineralisation is expected. Such a case is explored in Chapter 6 which demonstrates 3D inversion of measured TEM field data. The main challenge is the assembly of the geological model which is the result of an interdisciplinary geoscientific cooperative effort.

Bound constraints Property bounds enforce a particular range of property values within a region where the physical properties are known to vary within the supplied bounds. Bound constraints are most commonly employed and may be applied globally, to all cells, or different bounds can be applied to sub-sets of cells, for instance to individual units of the model (Fullagar and Pears, 2007). In geometry inversion, pierce points and drill trajectories can be expressed as bounds of designated contacts during inversion in VPMg (Fullagar et al., 2008).

Hard constraints Hard constraints reflect ground-truth, primarily based on rock property measurements logged downhole or measured on drill core, and are incorporated in the rock property model as fixed property cells. In VPMg, the property of a cell in an heterogeneous unit can be held to a fixed value if petrophysical measurements are located within it (Fullagar and Pears, 2007). In the context of geometry inversion, hard constraints are pierce point constraints which preserve drilled contact positions during geometry inversion (Fullagar et al., 2008).

Soft constraints In addition to 'hard' constraints, multiplicative weighting factors may be applied, referred to as 'soft' constraints. In VPMg, property changes can be limited in the vicinity of fixed cells, since rock property usually exhibit a degree of correlation over a certain length range (Fullagar and Pears, 2007). In general, the concept of multiplicative weights for TEM moment inversion are designed so as to counteract the geometrical decay of the potential field response with distance from the sensor so that all cells have an equal likelihood of containing sources. Two variations of weights are considered below: vertically (1D) defined depth weights and spatially (3D) defined conductivity weights. Depth weights are intended so as to counteract shallow solutions. Alternatively, conductivity weights can be applied which are calculated using apparent conductivity / depth pairs from the CDIs. The conductivity weighting scheme can be applied to favour solutions which preserve the spatially defined conductive regions as seen in the CDIs. The implementation of soft constraints is described in Section 5.2.6 below. In the context of geometry inversion, soft constraints are multiplicative weights which limit the movement of unconstrained contacts which are located in the neighbourhood of a pierce point (Fullagar et al., 2008).

5.1.2 Discrete target and continuous background response

Because the TEM moment forward calculation is the linear combination of a continuous background and a discrete target response, the inversion algorithm distinguishes between 'background' and 'target' response. The target is the sought-after anomalous volume comprised of a distribution of cell time constants defined in the geological litho-model. The background is calculated as the TEM moment response of a continuous half space (Section 3.1). Background conductivity can be optimised in conjunction to the inversion of the target response. Mostly, the assumption of an homogeneous half space as a background model is geologically artificial, however numerically convenient since it captures early-time and near-transmitter responses as well as the late time response of an extensive unbounded medium.

The background conductivity is inferred from the conductivity-depth images. If in situ measurements are available, for example from bore hole logs, they may serve as a measure of conductivity for the half space model. Given an estimate of the half space conductivity, the background is isolated from the measured TEM data vector during inversion by simply subtracting the half space TEM moment response from the measured TEM data vector ('stripped response'). The remainder of the TEM moment data vector is treated as the target response, which effectively arises from a distribution of conductive cells situated in free space. The background may either be optimised simultaneously or held fixed at a predefined conductivity value for the half space. Optimisation of the background response proceeds by means of a simple linear regression, whereas the 3D target response is subject to a steepest descent inversion technique.

5.1.3 The starting model

The starting model comprises an initial time constant estimate for the discrete target model and also an estimate of the background conductivity. The voxelised time constant model τ^0 together with encompassed hard and soft constraints constitutes the starting model for the discrete target. The inversion constraints favour particular desired features. An initial estimate of the background conductivity, for example from CDIs, constitutes the starting model for the background.

In the absence of in-situ data from boreholes, as is the case in greenfield exploration, a starting model may be purely conceptual. In this case VPem3D may be initialised with a minimum structure model; for example an uncategorised discrete target model where all cells are initialised with zero time constants, together with a weighting scheme, in conjunction with an estimate of the background conductivity. In the case of a minimum structure model where all time constants are initialised with zero, the starting model is here referred to as a 'zero starting model'. Depending on the details of the starting model, different recovered models will be obtained after inversion which may all be equally valid mathematically.

A time constant model τ^0 may also be initialised with starting values based on the apparent conductivity values interpolated from CDIs; such a model is referred to as a 'CDI starting model'. Cell time constants based on CDI values are calculated as described in Section 3.2.3 via a simple linear regression which automatically scales the cell conductivities so as to fit the observed TEM moment response to the calculated moments. Because conductivity is linearly related to the time constant, the rescaled conductivities are accepted as a first approximation to the time constants. Since the inversion distinguishes between a continuous background and a discrete target response, the estimate of the background conductivity is first subtracted from the CDIs so that the rescaled conductivities are associated with the target response only.

5.2 The inverse problem

Measured data contain always contributions which are not captured in the forward model response, altogether referred to as 'noise', so that the model response after inversion is only as accurate as defined by this noise-level. The noise-level, or data uncertainty is user-defined and is assumed to be a normal

random variable with zero-mean. Usually the data uncertainty is defined as a fraction of the measured data amplitudes. The 3D model response, which is defined as the combined response of target and background, is adjusted during inversion until its response reproduces the measured data to the predefined desired accuracy as defined by the data uncertainty.

The target response, which consists of the TEM moment response with the background removed, is attributed to a distribution of cells in free space. The background is treated separately and is optionally subject to a simple linear least-squares optimisation. In this section, the target model inversion is described first. The background optimisation is discussed in Section 5.2.5.

Let the time constants of all cells be represented by the parameter vector τ ,

$$\tau = (\tau_1, \tau_2, \dots, \tau_K)^T \in \mathbb{R}^K, \quad (5.1)$$

where K denotes the number of cells of the discretised 3D model space. \mathbb{R}^K denotes the K -dimensional Euclidean vector space. Let the N TEM moments derived from a set of imperfect TEM measurements be represented by the data vector \mathbf{d} ,

$$\mathbf{d} = (d_1, d_2, \dots, d_N)^T \in \mathbb{R}^N, \quad (5.2)$$

where previously an estimate of the background has been subtracted. Associated with the measurements are the data uncertainties \mathbf{q} ,

$$\mathbf{q} = (q_1, q_2, \dots, q_N)^T \in \mathbb{R}^N. \quad (5.3)$$

During inversion a 3D time constant model is sought that adequately explains the set of measured TEM moments which satisfies the relationship

$$\mathbf{d} = \mathbf{f}(\tau) \quad (5.4)$$

where \mathbf{f} represents the TEM moments calculated for the time constant model τ and is a vector valued function with $\mathbf{f} : \mathbb{R}^K \rightarrow \mathbb{R}^N$. Parameter estimation involves the iterative construction of a time constant model by linearised improvement of a starting model τ^0 . Linear approximation of $\mathbf{f}(\tau)$ around τ^0 gives (Jupp and Vozoff, 1975)

$$\mathbf{d} \approx \mathbf{f}(\tau^0) + \mathbf{D}\delta\tau \quad (5.5)$$

where $\delta\tau$ denotes the sought-after perturbation vector which is defined via $\tau = \tau^0 + \delta\tau$. $\mathbf{D} \in \mathbb{R}^{N \times K}$ is the Jacobian or sensitivity matrix where each element measures the sensitivity of the n -th data value to the k -th parameter

$$D_{nk} = \frac{\partial f_n(\tau)}{\partial \tau_k} \quad (5.6)$$

For a linear problem, above Equation (5.5) is exact

The inverse problem in VPem3D attempts to minimise error-weighted residuals between observed and calculated data by finding a new perturbation vector $\delta\tau^i$ at successive iterations i . From Equation (5.5), the inverse problem follows with

$$\mathbf{Q}(\mathbf{d} - \mathbf{c}^i) = \mathbf{QD}\delta\tau^i \quad (5.7)$$

where \mathbf{Q} is a diagonal matrix consisting of the data uncertainties with $\mathbf{Q} = \text{diag}(1/q_1, 1/q_2, \dots, 1/q_N)$ and where $\mathbf{c}^i = \mathbf{f}(\tau^i)$ denotes the calculated forward model solution at the i -th iteration. At iteration $(i+1)$, the model response $\mathbf{c}^{i+1} = \mathbf{f}(\tau^i + \delta\tau^i)$ is approximated via

$$\mathbf{c}^{i+1} \approx \mathbf{c}^i + \mathbf{D}\delta\tau^i \quad (5.8)$$

which is exact in the linear case.

5.2.1 Objective function

A variety of inversion schemes exist for obtaining an optimised solution, e.g. Meju (1994). A mathematical review of various inversion schemes can also be found in Soleimani (2008). Here, a fast steepest descent method, originally implemented in VPMg, is employed for inversion of the target response. The steepest descent method successively corrects a model estimate in direction of the negative gradient of a misfit measure. Matrix inversion is not required. The misfit is measured by means of an objective function $S(\tau)$ which is here defined in terms of a least-squares criterion. The least-squares criterion is an element of the family of ℓ_p -norm solutions, derived from a maximum-likelihood formulation which gives rise to various probabilistic inversion schemes (c.f. Tarantola, 2005). The most commonly employed measure is the dimensionless norm of the ℓ_2 type, equivalent to the least-squares criterion. The ℓ_2 norm arises naturally from the assumption of a Gaussian distribution of errors so that the misfit is governed by a Chi-squared distribution and the objective function is commonly referred to as the χ^2 misfit function. It measures the degree of misfit between model response and observed data as the Euclidean distance. The χ^2 random variable is defined in terms of the weighted residuals as

$$S(\tau) = \chi^2 = (\mathbf{d} - \mathbf{c})^T \mathbf{Q}^T \mathbf{Q} (\mathbf{d} - \mathbf{c}) \quad (5.9)$$

For inversion, the χ^2 -misfit is subject to minimisation for which the method of steepest descent is utilised as described in the next section. Because the expected value of a χ^2 random variable is 1, if normalised by N , the recovered model after inversion is regarded as acceptable if the χ^2 -misfit of the model is 1 or less (e.g. Oldenburg and Li, 2005). The inversion is also terminated if the maximum number of iterations is completed, or if the misfit does not decrease on successive iterations and is stalled.

The solution for the linear inverse problem, arising for vertical component TEM moments is described here. In linear inverse problems, sensitivities are model independent, which expedites successive model corrections via initially calculated sensitivities. Recalculating an updated forward model and sensitivities after each iteration is therefore not necessary. For the linear inversion of the vertical TEM moments, the forward model response at the i -th iteration is simply

$$\mathbf{c}^i = \mathbf{G}\tau^i \quad (5.10)$$

where \mathbf{G} is the TEM moment forward operator, or kernel, with elements G_{nk} (Equation 3.2) which quantifies the contribution of a point conductor in the k -th cell to the n -th observation (c.f. Li and Oldenburg, 1998).

If each cell is assigned a point conductor with individual time constant and the heterogeneous inversion problem is solved, the model space under consideration is typically comprised of a large number of cells. An alternative approach is to treat defined geological units homogeneously and the homogeneous inversion problem is solved. Both, the under- and over-determined cases, utilise a steepest descent inversion technique, but their computational details differ somewhat.

Summed up briefly, the inversion procedure involves the following steps:

0. Construct a starting model and define constraints
1. Compute the forward model
2. Test for convergence or exit criteria
 - a true: exit
 - b false: proceed to step 3.
3. Compute the gradient of the misfit and the step length
4. Update the model and data
6. Return to step 2.

5.2.2 The method of steepest descent

The inversion proceeds by successive approximation, seeking at each stage a change in the parameter vector which can reduce the magnitude of the misfit vector. In order to find an optimal solution τ^* , the descent method iteratively minimises the misfit measure $S(\tau)$. From an initial parameter-estimate τ^0 , the method generates a series of new estimates, until it converges to a minimum of the misfit function

At the start of the i -th iteration let τ^i be the current parameter-estimate of the function's minimum. The i -th iteration then consists of the computation of the perturbed parameter value $\delta\tau^i$ in direction of the steepest descent from which the new estimate τ^{i+1} is obtained, according to equation

$$\tau^{i+1} = \tau^i + \delta\tau^i \quad (5.11)$$

In the *method of steepest descent*, the perturbed parameter vector $\delta\tau^i$ is given by

$$\delta\tau^i = -\alpha^i \cdot \nabla S(\tau^i) \quad (5.12)$$

where α^i is a scalar known as the step length. Thus the perturbation is anti-parallel to the gradient of the misfit. During inversion, the perturbation vector $\delta\tau^i$ is tested if it exceeds a pre-defined size and truncated accordingly in order to avoid large 'jumps' in the solution space; truncation is applied one vector component at a time. The truncation size is user-defined and passed via an inversion control-file.

At each iteration i a new step length and descent direction is chosen, subject to the descent condition

$$S(\tau^{i+1}) < S(\tau^i) \Leftrightarrow S(\tau^i + \delta\tau^i) < S(\tau^i) \quad (5.13)$$

The step length α^i is found by evaluating the minimum of $S(\tau^{i+1})$, thus

$$\alpha^i = \arg \min_{\alpha} S(\tau^i + \delta\tau^i) \quad (5.14)$$

where 'arg min' denotes the argument for which the minimum is attained.

5.2.3 Under-determined case ($K > N$)

The under-determined case commonly occurs for heterogeneous property inversion. In order to maximise computational speed, summations over N data are preferable to summations over K parameters (Fullagar, 2007a). To obtain an updated parameter vector, τ^{i+1} , the descent method (Equation 5.12) requires the computation of the perturbed parameter vector $\delta\tau^i$ at each iteration i . Writing out the normalised objective function (Equation 5.9) for the next iteration $i + 1$ gives.

$$S(\tau^{i+1}) = \frac{1}{N} \sum_{n=1}^N \left(\frac{d_n - c_n^{i+1}}{q_n} \right)^2 \quad (5.15)$$

where c_n^{i+1} is the model update via Equation (5.8) for the n -th data point, viz.

$$c_n^{i+1} = c_n^i + \sum_{k=1}^K D_{nk} \delta\tau_k^i \quad (5.16)$$

where $\delta\tau_k^i$ is the perturbation in the descent direction, previously given in Equation (5.12). Substituting Equation (5.16) into (5.15) gives

$$S(\tau^{i+1}) = \frac{1}{N} \sum_{n=1}^N (e_n^i + \delta e_n^i)^2 \quad (5.17)$$

where

$$e_n^i = \frac{(d_n - c_n^i)}{q_n} \quad (5.18)$$

denotes the weighted residual at the i -th iteration and where δe_n^i is the change in residuals. Recalling Equation (5.12) it follows that

$$\delta e_n^i = -\alpha^i \sum_{k=1}^K \frac{1}{q_n} D_{nk} \nabla_k S(\tau^i) \equiv -\alpha^i \Delta_n^i \quad (5.19)$$

where the gradient of the objective function for the k -th parameter evaluates as

$$\nabla_k S(\tau^i) = -\frac{2}{N} \sum_{n=1}^N \left(\frac{d_n - c_n^i}{q_n} \right) \cdot \frac{1}{q_n} D_{nk} \quad (5.20)$$

The step length α^i is obtained by minimising $S(\tau^{i+1})$ with respect to α^i (Equation 5.14). At the minimum is

$$\frac{\partial}{\partial \alpha^i} S(\tau^{i+1}) = 0$$

Therefore, substituting from Equation (5.19) into (5.17) and differentiating,

$$-\frac{2}{N} \sum_{n=1}^N (e_n^i - \alpha^i \cdot \Delta_n^i) \Delta_n^i = 0 \quad (5.21)$$

Hence, the step length that minimises $S(\tau^{i+1})$ is given by (Fullagar, 2007a)

$$\alpha^i = \frac{\sum_n^N e_n^i \Delta_n^i}{\sum_n^N (\Delta_n^i)^2} \quad (5.22)$$

where summations are over N data. With a new step length at each iteration, a new model is calculated via Equation (5.11) and the model response is updated via Equation (5.8).

5.2.4 Over-determined case ($N > K$)

The over-determined case commonly occurs for homogeneous property inversion. In order to maximise computational speed, summations over K parameters are preferable to summations over N data (Fullagar, 2007a). The objective function is given by the χ^2 -misfit according to Equation (5.9),

$$S(\tau^i) = \frac{1}{N} \sum_{n=1}^N \left(\frac{d_n - c_n^i}{q_n} \right)^2 \quad (5.23)$$

The gradient for the k -th parameter evaluates the same as Equation (5.20). The step length is chosen to simply scale the steepest descent perturbation as needed to halve the χ^2 -misfit,

$$\nabla S(\tau^i) \cdot \delta\tau = -\frac{S(\tau^i)}{2}, \quad (5.24)$$

and with $\delta\tau = -\alpha \cdot \nabla S$ (Equation 5.12) follows for the scaling factor α^i ,

$$\alpha^i = -\frac{S(\tau^i)}{2 \cdot \|\nabla S(\tau^i)\|^2}, \quad (5.25)$$

where the squared magnitude of the gradient of the χ^2 -misfit is given via (Fullagar, 2007a)

$$\|\nabla S(\tau^i)\|^2 = \sum_{k=1}^K \left(\frac{\partial S}{\partial \tau_k} \right)^2 \quad (5.26)$$

where summations are over K parameters. Thus, iteration proceeds as in Equation (5.11) by computation of the gradient and the scaling factor at each iteration step.

5.2.5 Background optimisation

The background response is modelled as the TEM moment response of a continuous conducting half space. The background-portion of the measured TEM moment response is initially estimated from a half space conductivity, as most commonly inferred from CDIs. The background-portion is subtracted from the measured TEM moments and during inversion, an optimisation procedure optionally finds the optimal half space conductivity in a least-squares sense so as to fit the

background-portion of the TEM moment response. This optimisation is closely analogous to 'enclosing half-space' optimisation in VPmg.

The first order TEM moment of the half space response is linear with respect to the half space conductivity σ_h . For any wire-segment of the transmitter loop, the half space TEM moment responses can be calculated, respectively for the vertical and horizontal component if needed, using Equations (2.89) and (2.107) in Chapter 2. The background conductivity can be fixed or variable. If variable, then during each iteration the current estimate of the background response is subject to a simple least squares regression. By assumption, the observed TEM moment vector \mathbf{o} is given by

$$\mathbf{o} = \mathbf{t} + \sigma_h \cdot \mathbf{b} \quad (5.27)$$

where \mathbf{t} is the target response and \mathbf{b} is background. The spatial variation in background is controlled by survey geometry, but its amplitude is linearly dependent on conductivity σ_h . Let an estimate of N 'observed' background TEM moments at the i -th iteration be represented by the data vector $\tilde{\mathbf{d}}^i$,

$$\tilde{\mathbf{d}}^i = \mathbf{o} - \mathbf{t} \quad (5.28)$$

The background $\tilde{\mathbf{d}}^i$ is calculated by subtracting an estimate of the discrete target response from the observed TEM moments. The initial background response $\tilde{\mathbf{d}}^0$ is calculated for the starting conductivity value σ_h^0 which is based on CDIs or in-situ measurements. The objective is to find a new half space conductivity at each iteration which gives an improved fit to the 'measured' background. That is, at each iteration a scaling factor β^i is sought to rescale the half space responses and half space conductivity, viz.

$$\tilde{\mathbf{d}} = \beta^i \cdot \tilde{\mathbf{d}}^0 \quad (5.29)$$

The least squares fitting proceeds by minimising the sum of squares of measurement misfits for a set of N data points, and was also applied in Section 3.2.3 of Chapter 3 for calculating initial estimates of cell time constants. The required scaling factor is

$$\beta^i = \frac{\sum_n \tilde{d}_n \cdot \tilde{d}_n^0}{\sum_n (\tilde{d}_n^0)^2} \quad (5.30)$$

5.2.6 Implementation of rock property constraints

Bound constraints Property bounds for each unit are usually enforced during inversion. For TEM moment inversion, typically a positivity constraint is employed, i.e. a lower bound of zero, in order to ensure non-negative time constants. Time constant analysis from the TEM decays or previous inversion results may serve as guidelines to incorporate upper bounds. If conductivity measurements are available, the 'conversion factor' is applied which re-scales the conductivities so as to match the measured data. The conversion factor is based on a least-squares regression, introduced earlier in Section 5.1.3.

For homogeneous and heterogeneous property inversion, VPem3D checks whether bounds of the actual unit have been reached when updating the properties after inversion. The optimisation problem for the property inversion cases may be stated as

$$\begin{aligned} &\text{minimise: } S(\tau) \\ &\text{subject to: } \tau_{min} < \tau < \tau_{max} \end{aligned}$$

In practise each value of the updated parameter is tested, and if a bound has been exceeded, the associated cell time constant is truncated at the bound value for the associated unit.

Hard constraints It was mentioned earlier in this chapter that hard inversion constraints in VPmg capture 'ground-truth' which reflect geological information in form of drill pierce points and petrophysical information, primarily based on downhole logs or core measurements. For TEM moment inversion, which recovers time constants, the aforementioned 'conversion factor' is applied to measured conductivities. The re-scaled conductivity is accepted as a time-constant 'measurement'. Hard constraints are implemented as cell property values, via the supplied rock property model. During inversion the assigned cell properties are held fixed.

Soft constraints Soft constraints in VPem3D are implemented as multiplicative weights, either as 1D depth weights or as 3D conductivity weights, in order to, respectively, penalise shallow solutions or to promote particular features as seen in the corresponding CDIs. The weights, 1D or 3D, are encompassed as a diagonal weight matrix $\mathbf{W} \in \mathbb{R}^{K \times K}$. The weights are applied to the sensitivity matrix \mathbf{D} . The columns of \mathbf{D} relate to parameters, i.e. time constants of individual cells. The weights modify the relative importance of each cell parameter. Accordingly, those elements of the perturbation vector $\delta\tau^i$ with weight near unity will be accentuated during inversion relative to elements with small weights. Zero weights set parameter changes to zero, and hence exclude them from inversion.

The inverse problem (Equation 5.7) is adjusted so as to accommodate the weighting matrix as follows:

$$\mathbf{Q}(\mathbf{d} - \mathbf{c}^i) = \mathbf{QDW}(\mathbf{W}^{-1}\delta\tau^i) \quad (5.31)$$

where $(\mathbf{W}^{-1}\delta\tau^i) \equiv \delta\tilde{\tau}^i$ denotes the vector of unknowns. The problem is solved with the steepest descent method as described earlier. A new model is obtained upon 'unweighting' the solved perturbation, viz.

$$\delta\tau^i = \mathbf{W}\delta\tilde{\tau}^i \quad (5.32)$$

An updated time constant model and model response is then obtained, respectively, via Equations (5.11) and (5.8).

Calculation of the weight factors The following section describes computation of 1D depth weights and 3D conductivity weights. The 1D depth weights are designed so as to counteract the geometrical decay of the forward operator \mathbf{G} (Equation 3.2) and to force conductivity variation to greater depth. The depth weights are calculated according to the following empirical function (G.Pears, Mira Geoscience, pers. comm., 2008)

$$w(z, s_0, d_0) = \tanh(s_0 \cdot (z - d_0)) \quad (5.33)$$

where z denotes the depth to the k -th cell and where s_0 denotes a 'slope' factor. The slope factor affects the decay rate of the weights: a smaller value gives a more slowly decaying weighting scheme as depicted in Figure 5.2. The reference depth d_0 forces the weights to greater depths by introducing a surficial layer with zero weights. These depth weights decay more slowly than the 'UBC-GIF' depth weights for magnetic inversion, which are defined via a $z^{-3/2}$ dependence (Li and Oldenburg, 1996). By introducing a 'slope' and 'depth' parameter, the VPem3D depth weights offer some flexibility to smoothly accentuate different depths.

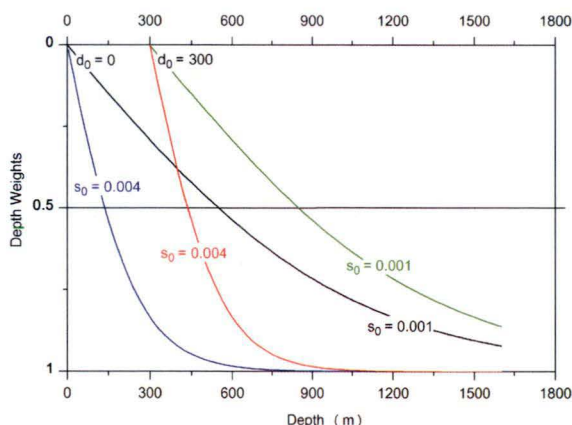


Figure 5.2 – VPem3D depth weights for various 'slope' and 'depth' factors s_0 and d_0 . Smaller s_0 tend to accentuate deeper features and d_0 counteracts the strong influence of the transmitter at shallow depth. Zero weights prevent parameter changes and weights near unity emphasise parameter changes.

The best choice for s_0 is subjective; it may be chosen by preliminary inspection of accompanying conductivity-depth sections; for example if conductivity occurs at large depth, a smaller slope factor may be chosen and vice versa. Adequate inversion results from synthetic examples were obtained if s_0 was chosen so that the weights decayed to about 0.5 at the depth where the conductive high emerges in the CDI. The reference depth d_0 is introduced in order to exclude surficial layers which neutralises the impact of the strong transmitter footprint at shallow depths. The factor d_0 is chosen according to the CDI sections where

the transition from background to higher conductivity values occurs. Selection of s_0 and d_0 is further illustrated at two synthetic examples in subsequent sections.

The 3D conductivity weights are based directly on interpolated conductivity/depth pairs from the CDIs and are less subjective than depth weights. This approach directly reflects the diffusive transient field decay so that conductivity weights inject depth resolution which is required for TEM moment inversion. Caution is needed if the CDIs contain artifacts or cannot be considered an authentic, generalised representation of the geoelectrical subsurface. In that case the weights would impose spurious features and the inversion may fail.

Apparent conductivity values are mapped between 0 and 1 and assigned as spatial 3D weights distributed according to their assigned location. The 3D weights are simply obtained by a linear mapping of the apparent conductivities via:

$$w(\sigma_a) \Big|_{(x,y,z)} = 1 - \left(\frac{\sigma_a}{\sigma_{max}} \right) \Big|_{(x,y,z)} \geq 0 \quad (5.34)$$

where σ_a is the apparent conductivity at location (x, y, z) ; σ_{max} is the maximum occurring apparent conductivity value of the entire data set so that the maximum occurring weight is 1. Because the weights are mainly specified to counteract the geometric decay of the target response, that is the response without background, the estimated background has been subtracted from the CDI values before calculating the weights. Conductivity weights give priority to conductivity structures as seen in the CDIs and penalise solutions deviating from the CDIs.

5.3 3D Inversion example Horizontal Slab

The following section illustrates heterogeneous property inversion of TEM moments for the thick horizontal slab buried in a resistive environment previously introduced in Section 3.5.1 (Chapter 3). The synthetic example is for a fixed-loop system with instantaneous current shut-off. The recordings are for 45 channels with finite widths where channel centre times range from 0.01 msec to 1359 msec and comply with the SMARTEM instrument (c.f. Chapter 1, Table 1.2). All B-field components are computed in pT/A. The 'observed' TEM moment vector is calculated from the time-domain EM response as computed with MARCO. Only the moment transformed MARCO Bz-field decays are inverted. The number of data points is 231. The TEM moments as obtained from the MARCO responses are extrapolated at early and late time to provide complete TEM moments (c.f. Equation 2.112). 5% random Gaussian noise was added to the complete TEM moments. During inversion, components of the perturbation vector $\delta\tau$ are truncated at a maximum possible change of 0.2 msec in order to avoid large 'jumps' in the solution. The value for the step-size is chosen as a fraction of the estimated time constant of the slab τ_{slab} . The examples were computed on a standard Pentium 4 2.8-GHz processor from 2006.

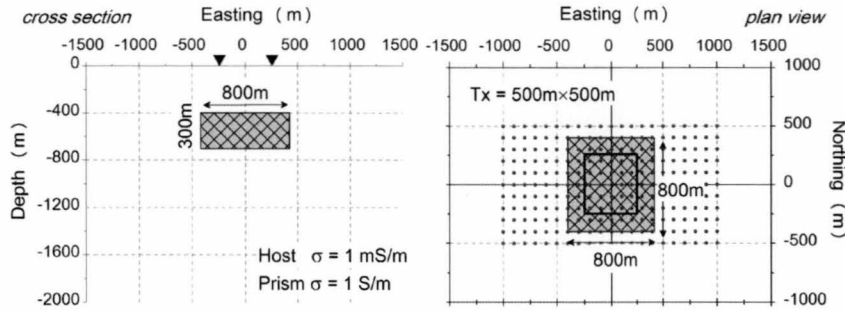


Figure 5.3 – Horizontal slab model with a conductivity of 1 S/m in 400 m depth in 1 mS/m host. Fixed-loop TEM survey lines from -500N to 500N traverse the model area with receivers from -1000E to 1000E at 100 m intervals. There are in total 231 receiver stations. All three B-field components are computed at 45 channels complying with the SMARTEM instrument (Table 1.2). Transmitter on and off times are 2000 ms (0.125 Hz fundamental).

The model is depicted in Figure 5.3; it shows a thick horizontal slab centred at (0E,0N) with depth-to-top of 400 m and dimensions $800\text{E} \times 800\text{N} \times 300\text{Z}$. The conductivity contrast between host and target is 1000, since the host has a conductivity of 1 mS/m and the slab a conductivity of 1 S/m. The time constant of the slab has been estimated from the decay curves as $\tau_{\text{slab}} \simeq 2.6\text{ msec}$, as is illustrated in Chapter 3. A fixed, square transmitter loop, with side lengths of 500 m, is directly above the prism. Model dimensions are $3\text{ km} \times 2\text{ km} \times 2\text{ km}$ for east, north and depth, respectively. The model is discretised into 25 m cubic cells which amounts to a total of 768,000 cells. Not all cells will participate, however, depending on the model setup for inversion as described below.

TEM moments of horizontal slab Figure 5.4 shows the complete vertical component TEM moments as calculated from the 'MARCO' decays via Equation (2.112). The complete TEM moment is the sum of the 'incomplete' TEM moment and the 'head' and 'tail' contributions. The 'incomplete' TEM moments are the moment transformed decays between the first and last channel delay time. 'Head' and 'tail' are calculated by extrapolating the magnetic field data using a half space model at early and late times. Panel 0N in Figure 5.4 also shows the 'incomplete' TEM moment together with the 'head' and 'tail' contribution. For the resistive half space model, the 'tail' contribution is practically zero since the B-field response has already decayed to zero for the 'tail' time range. 5% random Gaussian noise has been added to the complete TEM moments, which translates to a data uncertainty of about $\sim 0.004\text{ pTs/A}$ relative to the highest occurring TEM moment amplitude. The noise contaminated TEM moments are input for inversion with assumed data uncertainty of 0.004 pTs/A for all data points.

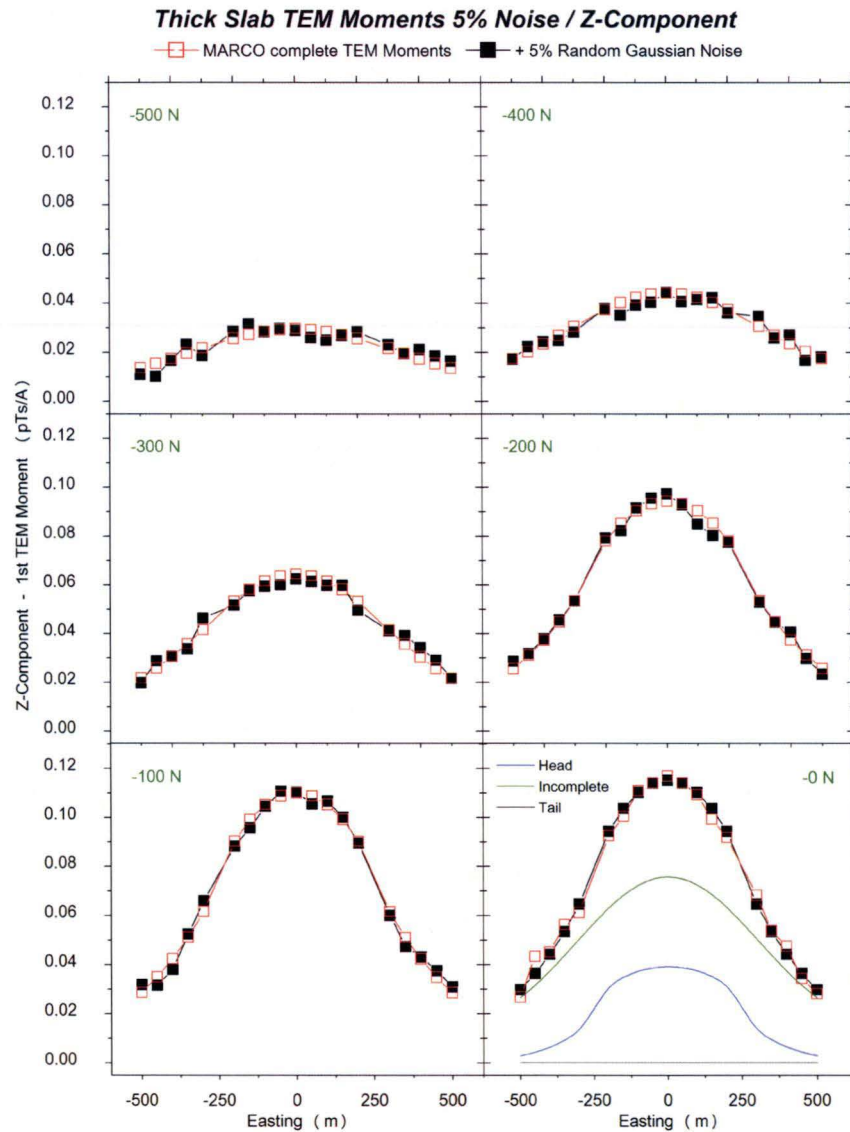


Figure 5.4 – TEM Bz-moments of horizontal slab with 5% random Gaussian noise added. Superimposed in panel 0N are the 'incomplete' TEM moment together with the 'head' and 'tail' contribution.

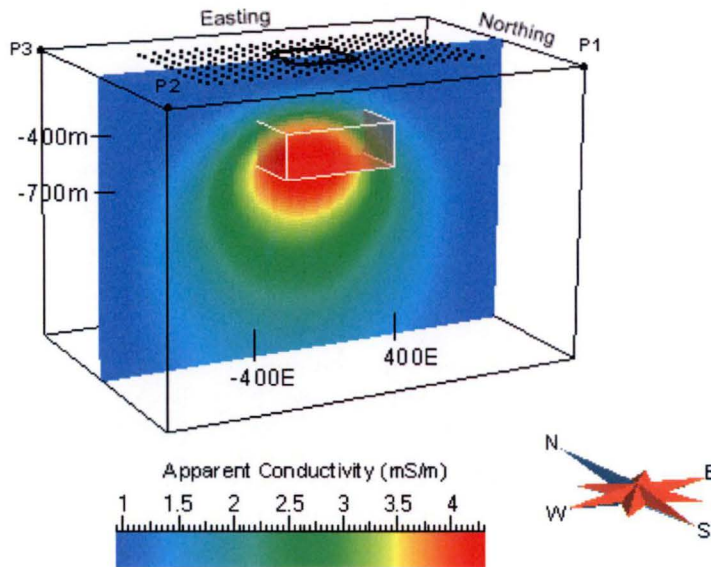


Figure 5.5 – Conductivity-depth sections based on total B-field amplitudes for the horizontal slab model. The highest conductivities are centred at about -750 m, near the base of the prism. Apparent conductivities in larger distances from the prism depict the half space conductivity of 1 mS/m. Lateral model dimensions are indicated by corners P1= (1500E, -1000N), P2= (-1500E, -1000N) and P3= (-1500E, -1000N). Vertical model extent is 2000 m.

Conductivity-depth sections A conductivity-depth image of the TEM decays of the horizontal slab model are shown in Figure 5.5 which depicts an eastwest CDI-section through the centre of the model (0N). The CDIs are calculated from total B-field amplitudes using all three components (c.f. Chapter 4). Apparent conductivities range from about 1 mS/m to about 5 mS/m. The apparent conductivity value of 1 mS/m depicts the host conductivity of the model and may serve as an estimate of the host conductivity during inversion. Interpolated apparent conductivities extend to larger depths than the actual slab. However, the conductive high, depicted in the CDIs, is a good first approximation to the location of the slab. The top of the conductor is well defined by the conductivity gradient in the CDI, and lateral position of the conductor is well defined in plan. The base of the conductor is not well defined. Interpolated conductivity- depth pairs are utilised to initialise the CDI starting model and to calculate the conductivity weights for the zero starting model.

Depending on the starting models and constraints used, recovered time constant models after inversion may exhibit significant differences due to the non-unique nature of the TEM moments inversion. A preferred time constant model may only be identified after exploring some of the range of acceptable models so as to develop an understanding of the variability of the results (Williams, 2008). In order to test the inversion algorithm and examine the variability of the inversion results due to non-uniqueness, 3D inversion is carried out with four different starting models and constraints:

1. Unconstrained-starting model:

The starting model is initialised with zero time constants in all cells and without any constraints. 3D inversion of the unconstrained-starting model involves all cells. No positivity constraints are imposed. The unconstrained inversion has the largest degree of freedom and is expected to fit the data very well. In general, solutions for the unconstrained inversion do not reflect the true subsurface conductivity structure and illustrates the importance of encompassing constraints.

2. CDI-starting model:

The time constant starting model τ_0 is generated from CDI pseudo-sections. The CDI-starting model includes an inactive 'layer-unit' of 200 m at the top and an active unit which occupies the remainder of the model Voxet. The vertical extent of the 'layer-unit' is chosen according to the CDI sections which show the transition from background conductivity to higher conductivity values at a depth of about 300 m (Figure 5.5). The active unit is set up with a positivity constraint for the time constants. Only the cells in the active unit take part in the inversion. No weighting scheme is applied. For the CDI-starting model, the background conductivity is variable and subject to optimisation. The CDI-starting model is useful for providing depth-information for inversion of TEM moments.

3. Zero-starting model with conductivity weights:

The zero-starting model is useful when there is little prior knowledge of the target, as for example in greenfields exploration. Here, the zero-starting model is combined with conductivity weights. This setup is closely related to the CDI starting model and depth information is injected via the weights based on CDI values (Section 5.2.6). The zero-starting model with conductivity weights favours solutions which bear resemblance to the CDIs. All cells of the model Voxet take part in the inversion. A positivity constraint for the time constant of all cells is enforced. The background conductivity is held fixed during inversion.

4. Zero-starting model with depth weights:

The zero-starting model is conditioned with depth-weights. To illustrate the effect of depth weights, two different depth weighting schemes are employed (Equation 5.33). First, the weights are calculated with parameters $s_0 = 0.004$ and $d_0 = 200$. The choice of s_0 and d_0 was guided by the CDI sections so that the weights have decayed to ~ 0.5 at the centre of the conductive high at 750 m depth (Figure 5.5). Second, the weights are calculated with parameters $s_0 = 0.0005$ and $d_0 = 350$. The weights are more slowly decaying with a value of ~ 0.2 at 750 m depth. The depth factor d_0 is chosen so as to coincide with the top of the conductive high in the CDIs. The half space conductivity is held to a fixed value of 1 mS/m.

5.3.1 Unconstrained starting model

In unconstrained inversion of static magnetic data one expects to achieve a good fit to the data, with the changes in susceptibility concentrated near the receiver stations at the ground surface (Oldenburg and Pratt, 2007). For TEM moment inversion, the significant difference with respect to inversion of static magnetic data is the presence of a primary magnetic field which varies from cell to cell. The transmitter footprint, and therefore model sensitivities, is strong in the vicinity of the transmitter, so that changes do not only appear at the top near the receivers but also near the transmitter.

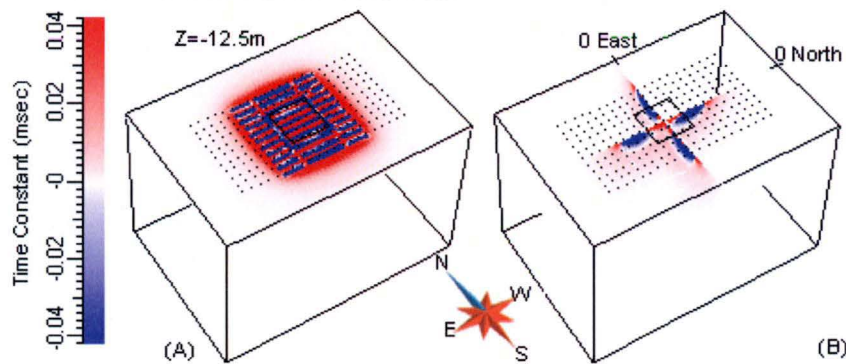


Figure 5.6 – Recovered time constant model after inversion of the horizontal slab TEM Bz-moments based on the unconstrained starting model. Figure (A) shows a horizontal section at 12.5 m depth. Figure (B) shows an eastwest and northsouth section which highlight the distribution of time constants with depth. Because the recovered model is clustered near the surface, the time constant values are very small.

Figure 5.6 shows the recovered time constant model after unconstrained inversion of vertical component TEM moments. Although inversion was successful, the recovered structure bears no resemblance to the thick slab model and manifests the non-unique nature of the inverse problem. Panel (A) in Figure 5.6 displays a horizontal section at a depth of 12.5 m. The time constant pattern in the top layer is complex and alternates between negative values along the survey lines and positive values in between, with reversed polarity inside the transmitter loop. At far receiver offsets the time constants are zero. The figure in (B) shows cross-sections through the centre of the model. The recovered conductive region is at shallow depths. The time constants are mostly positive inside the transmitter loop whereas outside the loop, the time constants are mostly negative. The polarity in time constants reflects the orientation of the primary field of the transmitter inside and outside the loop. Because the cell point conductors adopt the primary field direction, the cell time constants are negative outside the loop so as to reproduce a positive TEM moment response. The half space conductivity was held to a fixed value of 1 mS/m during inversion.

Vertical component TEM moment profiles of the recovered time constant model are shown in Figure 5.7 and appear to be better than the noise level. Because no constraints were applied, variations in the recovered time constant model are concentrated at the top so that the data is overfitted. Overfitting usually implicates that an unrealistic model has been generated with excessive

structure in order to fit the noise which also explains the relative high number of 76 iterations (Oldenburg and Li, 2005, p.16). Initial misfit was $\chi^2 = 51.3$; final misfit was $\chi^2 = 0.9$. Inversion succeeded after 16 min. and 19 sec. (16:19 min).

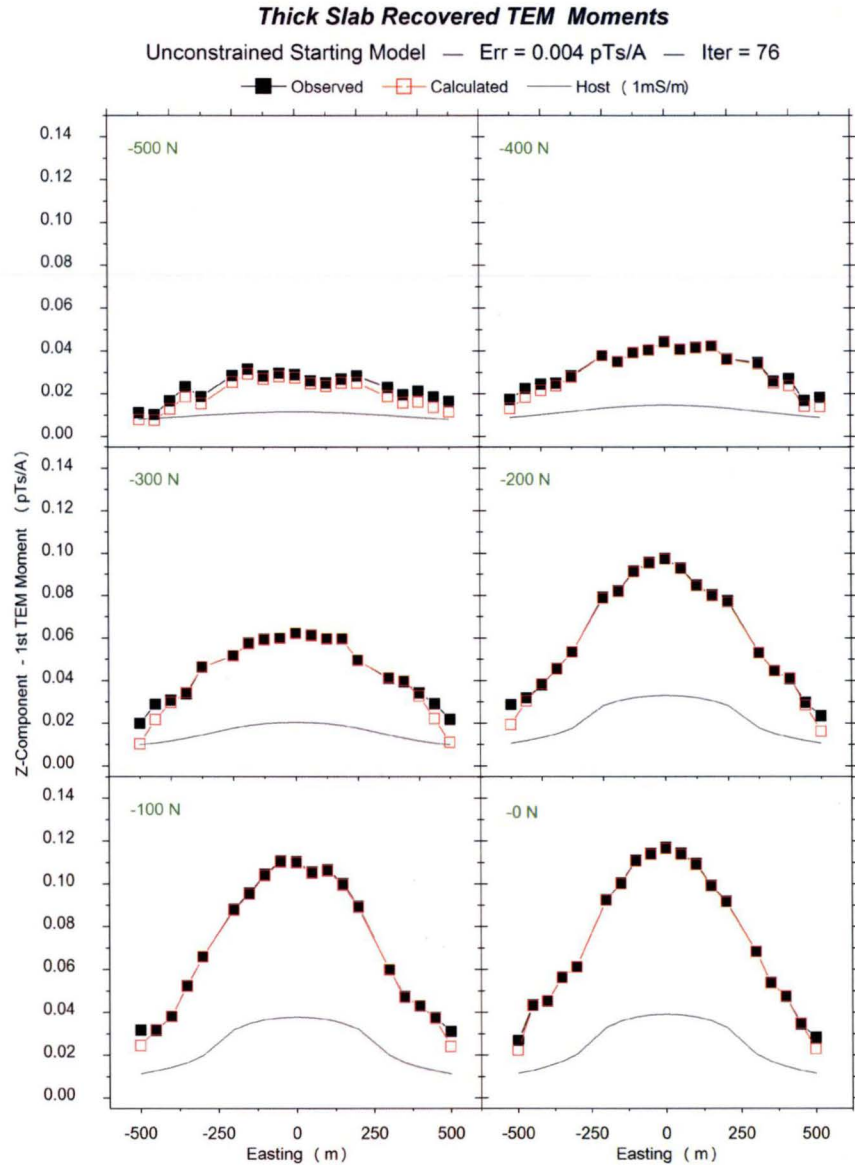


Figure 5.7 – Recovered Bz-TEM moment responses based on unconstrained starting model. The recovered time constant model gives rise to TEM moment responses which also fits the noise with a fit of better than 0.004 pTs/A after 76 iterations.

5.3.2 CDI starting model

An eastwest cross-section through the recovered time constant model, based on the CDI starting model for the horizontal slab, is shown in Figure 5.8. The starting model was initialised with time constants based on apparent conductivity values which have been rescaled using a least-squares multiplicative factor of $\beta = 0.7$ as described earlier in Section 5.1.3 and Chapter 3.2.3. No weighting scheme was applied. The starting model consists of an inactive 'layer-unit', extending 200 m below the surface, and the active unit, defined as the remainder of the model. The 'layer-unit' effectively suppresses the strong influence of the transmitter loop at shallow depths. The active unit consists of 700,800 cells. A positivity constraint has been employed.

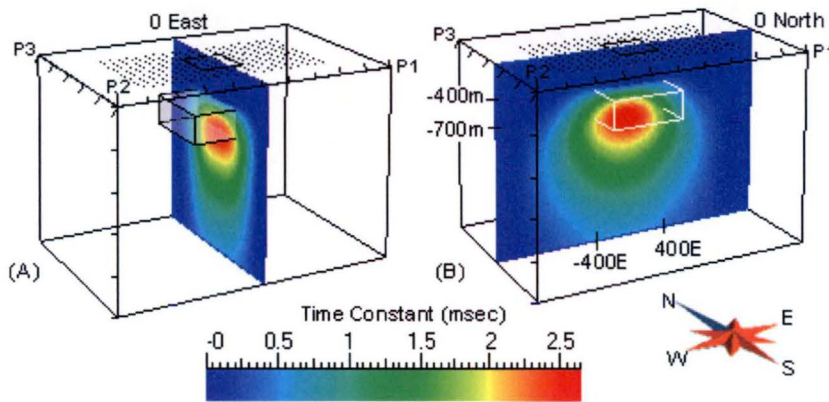


Figure 5.8 – Cross-section through recovered time constant model after inversion of the vertical component horizontal slab TEM moments using the CDI starting model. Inversion was successful after 2 iterations. Figure (A) shows a northsouth section and Figure (B) an eastwest section through a region of elevated time constants at the model centre. The recovered model is in distinct resemblance to the CDI starting model.

During inversion, the background conductivity was held variable and subject to least squares optimisation at each iteration. In order to test the optimisation, the start value was based on a 'bad' guess of 0.5 mS/m. After inversion, the half space conductivity was 0.71 mS/m which somewhat underestimated the true background conductivity (1 mS/m). The recovered time constant model has a distinct resemblance to the CDI starting model. The maximum recovered time constants are in good agreement with the estimated time constant value of the slab ($\tau_{slab} \simeq 2.6$ msec).

Together with the TEM moments of the recovered time constant model, Figure 5.9 depicts the TEM moments of the starting model. The starting model provided a good fit to the data with a misfit of $\chi^2 = 2.24$. Accordingly, the inversion succeeded after 2 iterations with a minimum change to the starting model. Runtime was 14:22 min. Because the starting time constant model τ_0 was initialised with time constants larger than zero, the forward model calculation took considerably longer than for the starting models based on a zero time constant model.

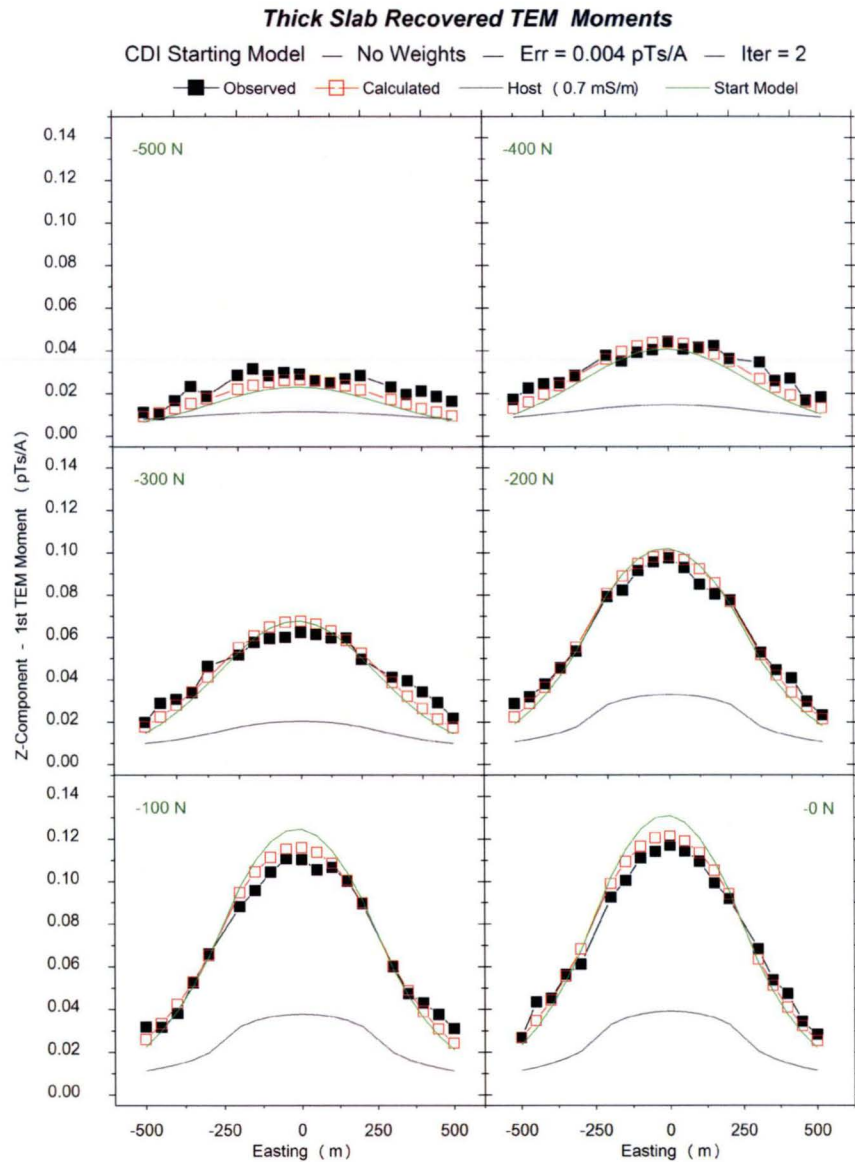


Figure 5.9 – Recovered vertical component TEM moment responses based on CDI starting model. Half space conductivity after inversion was 0.71 mS/m. The calculated TEM moments fit the the observed data set to better than 0.004 pTs/A. The TEM moment response of the CDI starting model provides a good fit to the data. The inversion was successful after 2 iterations.

5.3.3 Zero starting model with conductivity weights

Closely related to the CDI starting model is the zero starting model with conductivity weights. All cells of the model Voxet take part in the inversion. A positivity constraint for all model parameters is enforced. The conductivity weights are shown in Figure 5.10 (A). On display is an eastwest section through the model centre (0N). Parameter changes are favoured for cells associated with high starting conductivity. Away from the conductive high, the conductivity weights approach zero. Cells associated with a zero weight are effectively turned off and will not change during inversion. Zero weights occur where apparent conductivity equals the host conductivity (1 mS/m) or smaller.

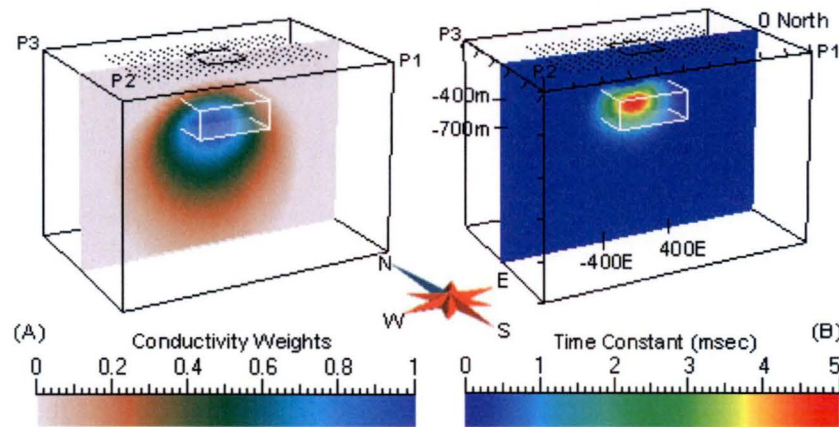


Figure 5.10 – Conductivity weights and recovered time constant model after inversion for zero starting model. The left panel (A) shows an eastwest section (0N) through the starting model with the conductivity weights on display. The right panel (B) shows the same cross-section through the centre of the recovered time constant model.

An eastwest cross-section through the model centre of the recovered time constant model after inversion is shown in Figure 5.10 (B). In contrast to the recovered time constant model of the CDI starting model, the recovered time constants here are mostly confined to the volume of the horizontal slab. The highest occurring time constant is ~ 5 msec, which is about double the estimated time constant of the horizontal slab (2.6 msec). The TEM moment response is shown in Figure 5.11. Initial misfit was $\chi^2 = 51.3$ for an uncertainty of 0.004 pTs/A and inversion succeeded after 4 iterations with a runtime of 9:17 min. Because initial calculation of the forward model is avoided when using a zero starting model, the runtime is significantly shorter than for the CDI starting model.

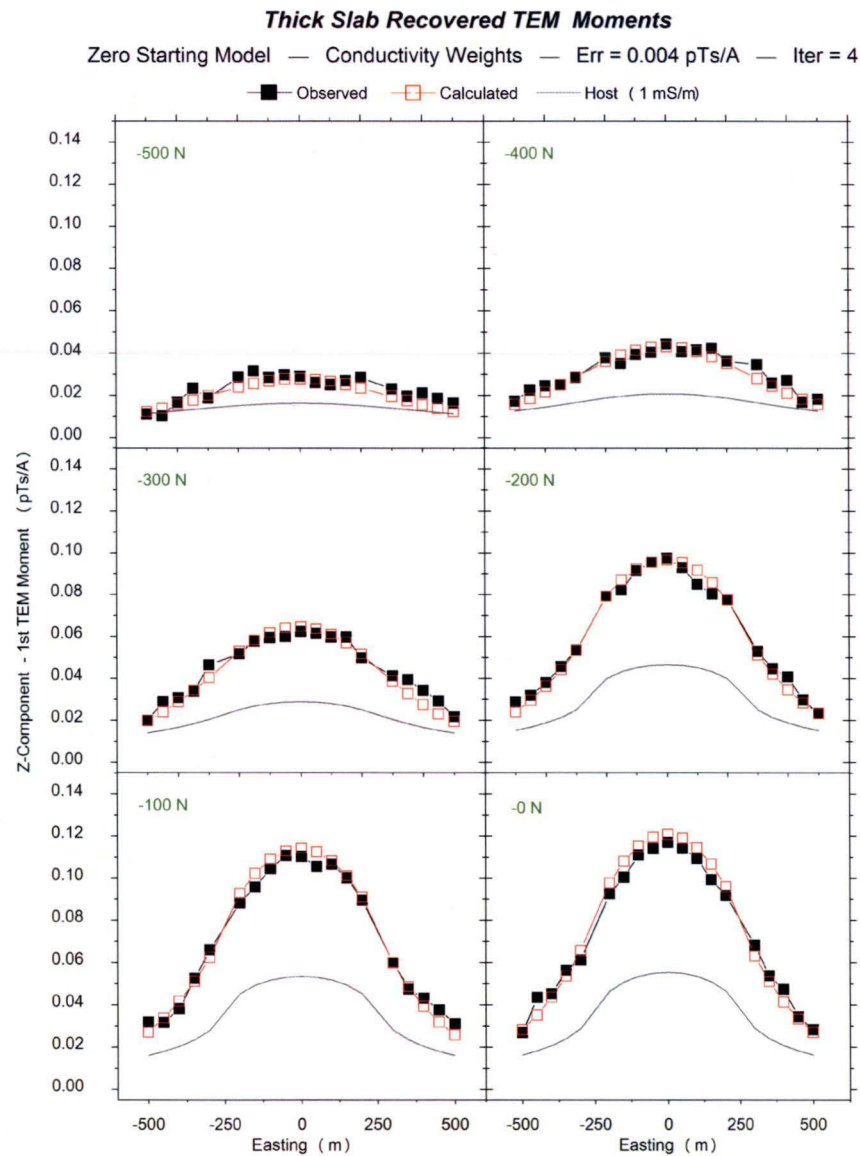


Figure 5.11 – Recovered vertical component TEM moment responses based on the zero starting model with conductivity weights. The inversion was successful after 4 iterations. The calculated TEM moments fit the the observed data set to better than 0.004 pTs/A. During inversion, the half space conductivity was held fixed to 1 mS/m.

5.3.4 Zero starting model with depth weights

The zero starting model is here conditioned with depth weights. As previously described, the inversion based on the zero starting model with depth weights is carried out for two different weighting schemes. First, a weighting scheme is devised calculated with parameters $s_0 = 0.004$ and $d_0 = 200$, referred to as weighting scheme (a). Second, inversion is carried out for a weighting scheme based on factors $s_0 = 0.0005$ and $d_0 = 350$, referred to as weighting scheme (b). The smaller 'slope' factor gives a more slowly decaying weighting scheme which forces the weights to greater depths. Figure 5.12 shows an eastwest cross-section through the centre of the model (0N) for weighting scheme (b).

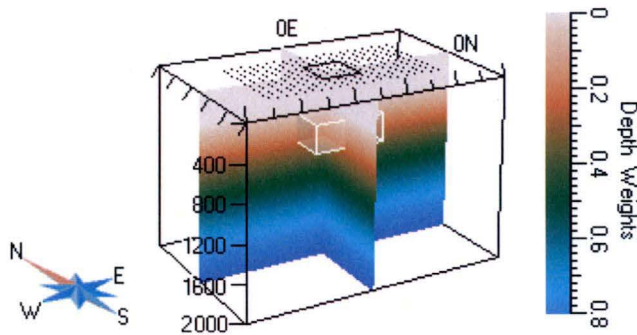
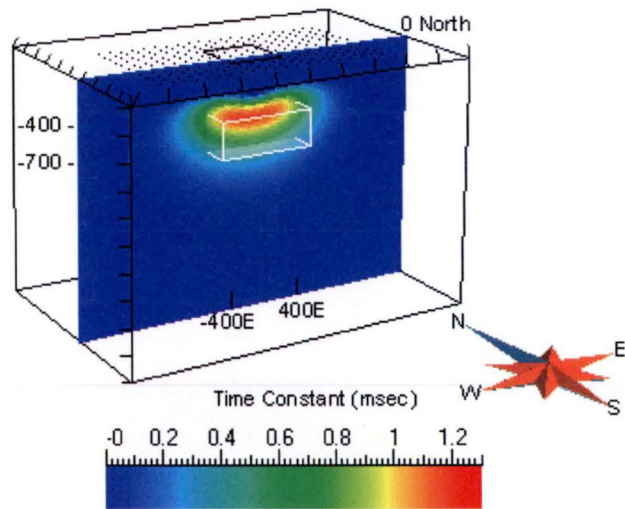


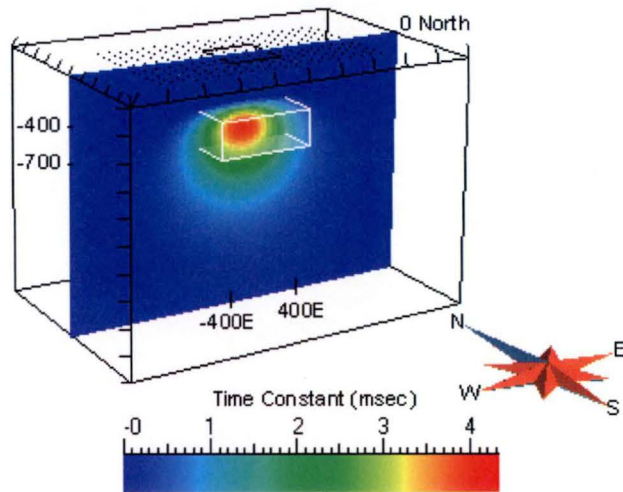
Figure 5.12 – Depth weighting scheme calculated for a 'slope' factor of $s_0 = 0.0005$ and a 'depth' factor of $d_0 = 350$ (c.f. Equation 5.33).

The recovered model after inversion with weighting scheme (a) is shown in Figure 5.13a. The figure shows an eastwest section through the model centre (0N). All cells of the model were restricted to non-negative time constants. A region of elevated time constants approximately coincides with the horizontal slab, however somewhat shifted above the upper edge of the slab. Compared with the previous result based on conductivity weights (Figure 5.10), the region of elevated time constants is disseminated throughout a larger volume. The inversion was successful after 4 iterations with a runtime of 9:45 min. During inversion, the half space conductivity was held to a fixed value of 1 mS/m. Initial misfit was $\chi^2 = 51.3$ for an uncertainty of 0.004 pTs/A.

Figure 5.13b shows the recovered time constant model based on weighting scheme (b). The recovered model shows the region of elevated time constants mostly confined to the volume of the horizontal slab. The inversion succeeded after 6 iterations; runtime was 10:32 min. As before, the half space conductivity was held to a fixed value of 1 mS/m. Both inversion results, based on different depth weighting schemes, give a solution which fit the TEM data to a data uncertainty of better than 0.004 pTs/A and demonstrates the inherent non-unique nature of the inverse problem. Figure 5.14 shows the TEM moment response profiles of the recovered time constant model for weighting scheme (b).



(a) Recovered time constant model based on zero starting model with depth weights for $s_0 = 0.004$ and $d_0 = 200$. The recovered time constant model broadly coincides with the position of the slab however appears somewhat elevated above the top of the horizontal slab.



(b) Recovered time constant model based on zero starting model with depth weights for $s_0 = 0.0005$ and $d_0 = 350$. The recovered time constant high is largely confined within the volume of the horizontal slab.

Figure 5.13 – Recovered time constant models for a thick horizontal slab based on a zero starting model conditioned with two different depth weighting schemes.

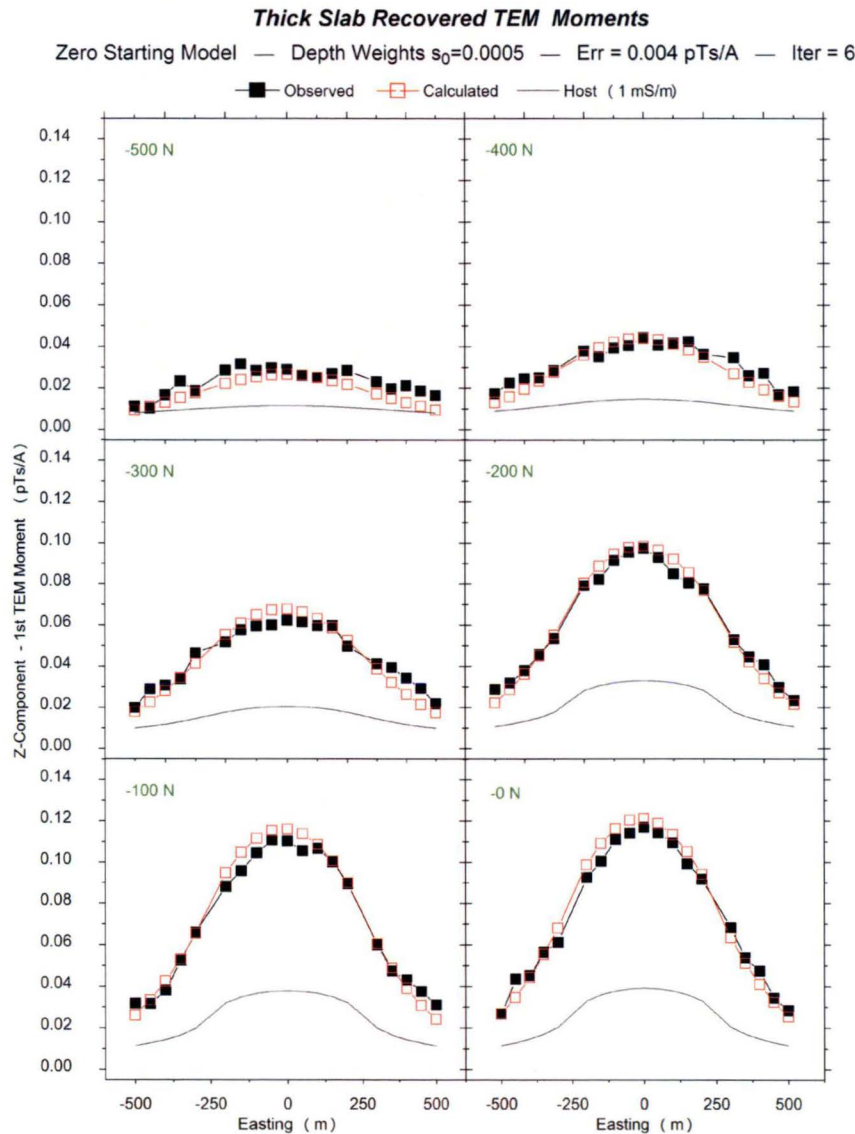


Figure 5.14 – Recovered vertical component TEM moment responses based on the zero starting model with depth weights for a factor of $s_0 = 0.0005$ and $d_0 = 350$. The inversion was successful after 6 iterations. The calculated TEM moments fit the the observed data set to better than 0.004 pTs/A. During inversion, the half space conductivity was held fixed to 1 mS/m.

5.3.5 Review of inversion results for horizontal slab model

Heterogeneous property inversion of the vertical component TEM moments for the horizontal slab model have been conducted for four different starting models. All inversions concluded successfully with a misfit of $\chi^2 \leq 1$ after inversion. Due to the non-unique nature of the TEM moments inversion, the recovered time constant models exhibit significant differences, depending on the starting models and constraints used. The non-unique nature is illustrated most clearly by the inversion result for the unconstrained starting model which generated a shallow time constant model after 76 iterations with very low time constant values, clustered near the transmitter loop and receivers. The TEM moment response for this model fits the noise-level, i.e. overfits the data which also explains the high number of iterations.

Inversion parameters of the various schemes employed are displayed in Table 5.1. Initial χ^2 -misfits for the starting models initialised with zero time constants are identical; this misfit characterises the difference between the measured TEM moments and the 1 mS/m background response. The CDI starting model has a considerably smaller initial misfit. The small misfit is indicative of the fairly accurate image of the horizontal slab model provided by the conductivity-depth sections. Consequently, after only 2 iterations the inversion for the CDI starting model succeeded and the resulting time constant model retains a distinct resemblance to the CDI sections. When the zero starting model is conditioned with conductivity weights, inversion generated an acceptable time constant model after 4 iterations, confined by the volume of the slab. Likewise, when conditioned with depth weights, successful inversions generated time constant models in fairly good agreement with the horizontal slab after only a few iterations.

Table 5.1 – Inversion parameters of the horizontal slab model. Number of data points is 231. Data uncertainty is $q = 0.004$ pTs/A and maximum step size $\delta\tau = 0.2$ msec.

Starting-model	σ_{host} (mS/m) (start / final)	χ^2_{start}	Iter.	Time (min.sec)	# Active Parameters
'Unconstrained'	1.0 / 1.0	51.3	76	16.19	768,000
'CDI'	0.5 / 0.71	2.24	2	14:22	700,800
'Zero' 3D-weights	1.0 / 1.0	51.3	4	9:17	768,000
'Zero' 1D-weights (a)	1.0 / 1.0	51.3	4	9:45	768,000
'Zero' 1D-weights (b)	1.0 / 1.0	51.3	6	10:32	768,000

5.4 3D Inversion example Vertical Dyke

The second example illustrates heterogeneous property inversion of the TEM moment response of the extensive vertical dyke model embedded in a conductive host, previously introduced in Section 3.5.2 (Chapter 3). In this second example the extensive target is offset from the transmitter loop. As in the previous example of the horizontal slab, all B-field components are calculated in pT/A at 45 'SMARTTEM' channel delay times for a fixed-loop layout. East-west survey lines along -1000N to 1000N at 200 m intervals traverse the model area with receiver stations between -500E and 1500E at 100 m intervals yielding 231 data points. The fixed transmitter loop has side lengths of 500E×1000N and is centred at (0E,0N) with the eastern wire 450 m west from the nearest edge of the dyke. The dimensions of the vertical dyke are 100E×1400N×1000Z; it is centred at (750E,0N) with depth-to-top of -400 m. Conductivity of the dyke is 50 S/m and the host conductivity is 0.05 S/m. The time constant of the model was previously estimated from the TEM decays as $\tau_{dyke} \simeq 475$ msec (Chapter 3.5.2). The model, shown in Figure 5.15, is comprised of 50 m cubic cells with a total of 180,000 cells

Synthetic step response recordings were computed at times ranging from 0.1 msec to 1340 msec with MARCO. The moment transformed MARCO Bz-field decays constitute the observed data vector where 5% random Gaussian noise have been added. The TEM moments as obtained from the MARCO responses are extrapolated at early and late time using Equation (2.112) to provide the complete TEM moments. The components of the perturbation vector $\delta\tau$ are not permitted to exceed the predefined step-size of 3.5 msec during inversion. The value for the step-size was chosen as a small fraction of τ_{dyke} . The examples were computed on a standard Pentium 4 2.8-GHz processor from 2006.

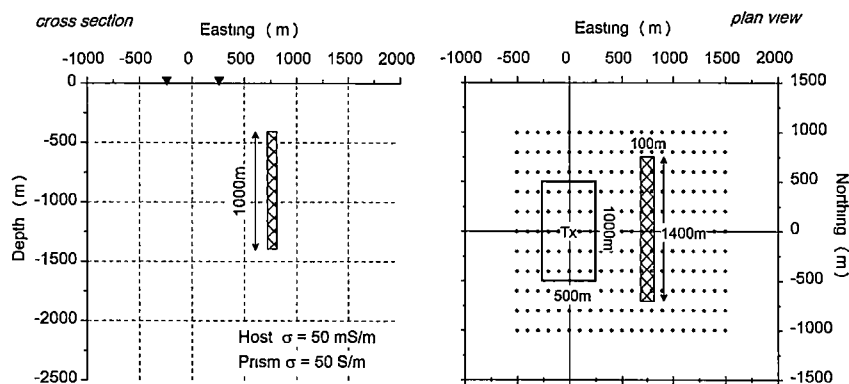


Figure 5.15 – Section and plan of vertical dyke model. Depth-to-top is 400 m, width is 100 m, strike is 1400 m and depth extent is 1000 m. The dyke is buried in a conductive host (50 mS/m). The conductivity of the target is 50 S/m. Fixed-loop TEM survey lines from -1000N to 1000N at 200 m intervals traverse the model area with receivers from -500E to 1500E every 100 m. There are in total 231 receiver stations.

Conductivity-depth sections Figure 5.16 shows an eastwest conductivity-depth section through the centre of the model (0N). The apparent conductivities are calculated from total B-field amplitudes using all three components (Chapter 4). Overall, the CDIs present a diffuse image of the vertical dyke. The depth-to-top and depth-extent of the prism are represented fairly accurately in the CDI, but there is a broad conductive area west of the vertical dyke which extends below the transmitter loop. On the eastern side of the dyke, the apparent conductivities are smaller than the host conductivity of 50 mS/m. This apparent conductivity pattern, as calculated from B-field amplitudes, is typically seen for vertical prisms buried in conducting hosts (c.f. Chapter 4.5.1). Away from the conductive regions, the host conductivity of 50 mS/m is recovered. Maximum apparent conductivity is 74 mS/m.

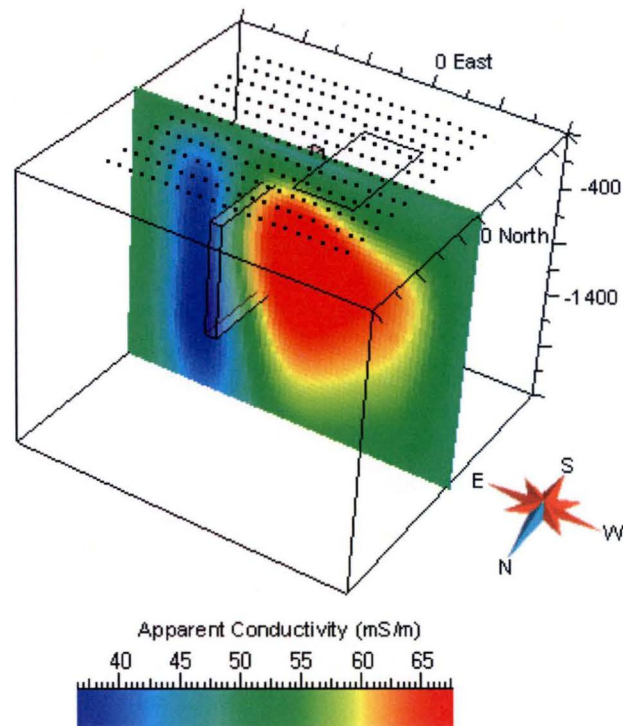


Figure 5.16 – Conductivity-depth section of vertical dyke model based on total B-field amplitudes for an eastwest cross-section through the centre of the model (0N). The CDI depicts the depth-to-top and the depth-extent of the prism fairly accurately. A broad conductive region extends west of the dyke, underneath the transmitter loop. Apparent conductivities east from the dyke are smaller than the host conductivity of 50 mS/m. Maximum apparent conductivity is 74 mS/m.

As in the example of the horizontal slab various starting models are constructed in order to examine the variability of the inversion results due to non-uniqueness and to test the algorithm for a different model where the transmitter is offset from the target:

1. CDI-starting model:

The time constant starting model τ_0 is initialised with cell time constants based on the CDIs. The CDI-starting model is furthermore categorised into an inactive 'layer-unit' of 200 m at the top and an active unit which occupies the remainder of the model Voxet (165,600 cells). The vertical extent of the 'layer-unit' is motivated by CDI sections where the transition from background conductivity to higher conductivity values occur at a depth of about 300–400 m (Figure 5.16). A positivity constraint is imposed on the time constants of the active unit. No weighting scheme is applied. For the CDI-starting model, the half space conductivity is variable during the inversion process and subject to optimisation. The host conductivity is initialised with a value of 30 mS/m.

2. Zero-starting model with conductivity weights:

The zero-starting model is initialised with conductivity weights and a positivity constraint. All cells of the model Voxet take part in the inversion. The conductivity weights are calculated from the CDI-based conductivity model of the dyke (Equation 5.34). The half space conductivity is held to a fixed value of 50 mS/m as estimated from the CDI sections.

3. Zero-starting model with depth weights:

The zero-starting model is conditioned with depth-weights. As before, the time constants are constrained to non-negative values. The weights are based on a 'slope' factor of $s_0 = 5 \times 10^{-4}$ and a 'depth' factor of $d_0 = 200$. The weights decay to a value of 0.5 at a depth of ~ 1200 m where the maximum conductivity in the CDIs occur (Figure 5.16). The inversion is carried out with a fixed half space conductivity of 50 mS/m and is repeated where the half space conductivity is subject to optimisation as well.

TEM moments of vertical dyke Figure 5.17 shows the vertical TEM moment response from the vertical dyke model. Because the model is symmetric with respect to 0N, and the noise does not vary significantly, only the southern lines from -1000N to 0N are shown.

As before, moment transformation of the synthetic Bz-TEM decays, including 'head' and 'tail', produces the complete TEM moments. 5% random Gaussian noise has been added to the complete TEM moments. The noise contaminated vertical component TEM moments are input for inversion. For a noise level of 5%, the data uncertainty for inversion translates to about 0.15 pTs/A with respect to the maximum TEM moment amplitude at 0N.

Because the strong host response obscures the response from the dyke, the 'stripped' responses are shown in Figure 5.18. For the 'stripped' responses, the 50 mS/m host response has been subtracted from the 'full' TEM moments. The 'stripped' TEM moments depict an estimate of the free-space response of the vertical dyke prism. At 750E, the 'stripped' responses exhibit a zero cross-over, which is indicative of the Bz response of the vertical dyke

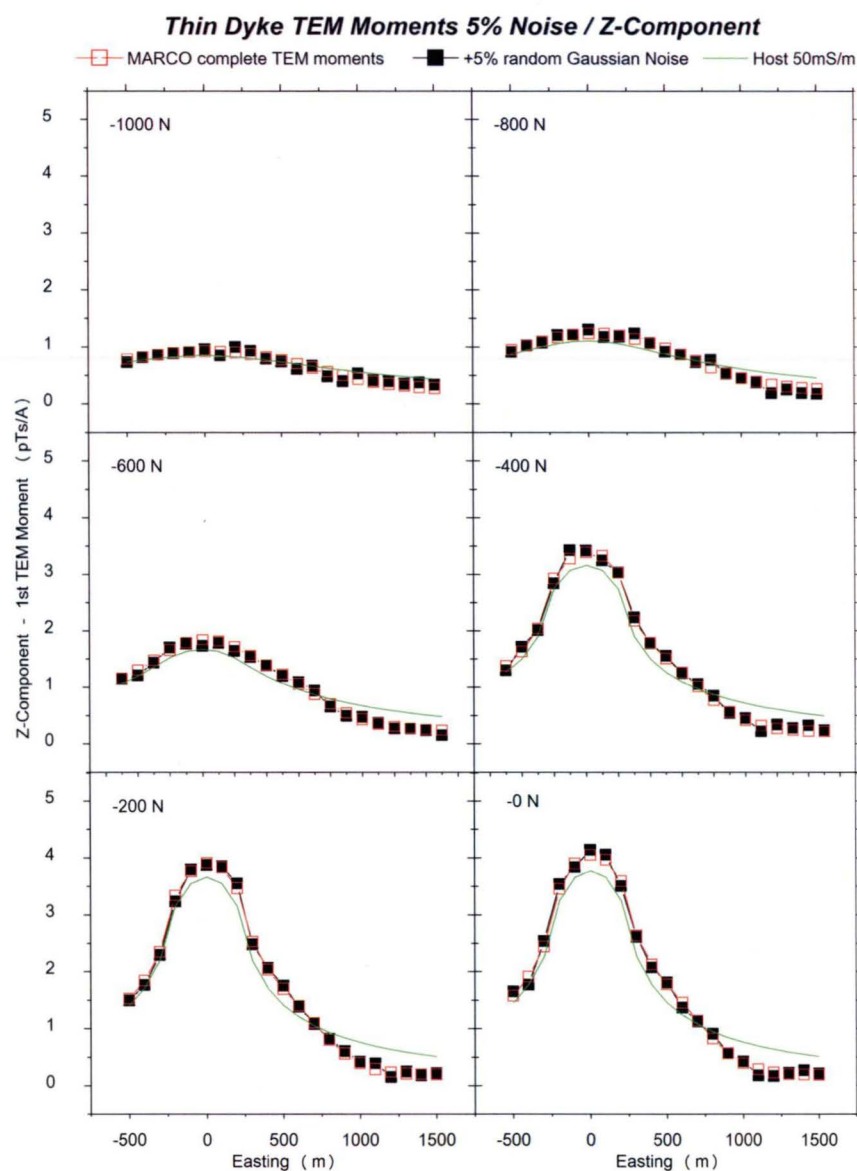


Figure 5.17 – TEM Bz-moments of vertical dyke model as calculated from moment transformed 'MARCO' decays. Superimposed are the TEM moments with 5% random Gaussian noise; these are input for inversion. The 50 mS/m background TEM moments are shown also.

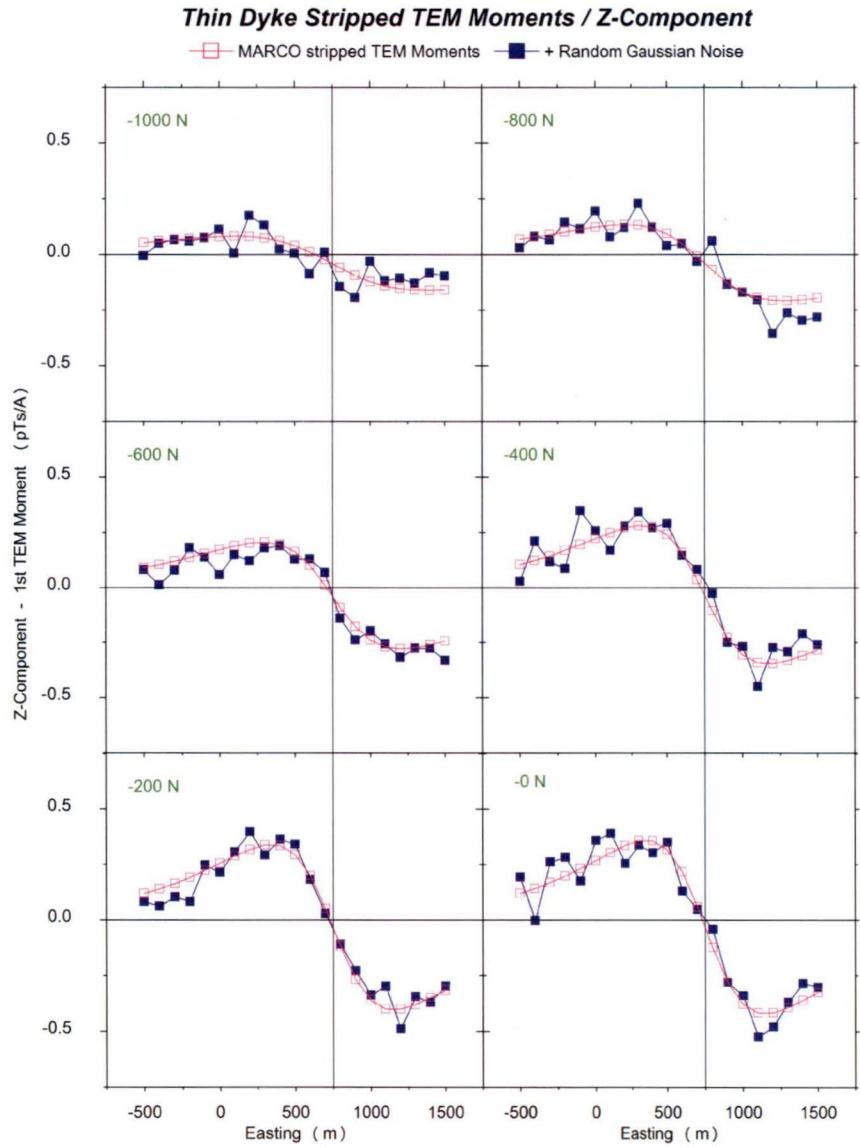


Figure 5.18 – ‘Stripped’ Bz TEM moments of vertical dyke model where the background TEM moments have been subtracted from the ‘full’ TEM moments. The stripped TEM moments depict an estimate of the free-space response of the vertical dyke prism. Because the noise level is based on the ‘full’ TEM moments, the noise level appear higher in the stripped response, so that 5% noise is more severe than in the previous case: host contribution is more significant. Zero-crossovers occur over the centre of the vertical dyke at 750E.

5.4.1 CDI starting model

Initial time constant values are assigned to each cell of the active unit after the apparent conductivities have been rescaled with a least-squares multiplicative factor of $\beta = 2.6$ (Section 5.1.3). Figure 5.19 shows cross-sections through the recovered time constant model after inversion. The recovered time constant model bears resemblance to the CDI starting model, however the region of elevated time constants has shifted eastwards and towards the upper part of the dyke. Panel (A) displays an eastwest section through the model centre at 0 North, panel (B) shows a northsouth section through the vertical dyke prism at 750 East and panel (C) presents a horizontal section at a depth of 525 m where the maximum time constant value is found. The time constant values are well below $\tau_{dyke} \simeq 475$ msec, which was based on time constant analysis of the MARCO decays (Chapter 3). Since elevated time constants are distributed throughout a larger volume than the vertical dyke, the recovered time constant values are smaller than τ_{dyke} so as to reproduce the TEM moments

Also shown in Figure 5.19 (D) is a 3D iso-volume of the recovered time constant model where only time constants greater than 40 msec are displayed. The elevated recovered time constants larger than 40 msec are clustered around the location of the original vertical dyke model but extend somewhat westwards towards the transmitter loop as is noticeable in the eastwest cross-section of panel (A). The westward extension of the recovered model is also seen in the CDI sections of the model. The conductivity model is based on total B-field amplitudes which is not necessarily ideal for inversion of Bz TEM moments. Inversion of $|\mathbf{B}|$ TEM moments may produce a model which resembles the dyke more closely. $|\mathbf{B}|$ TEM moments inversion is the subject of future work (Appendix A).

The half space conductivity was initiated with a 'bad' guess of 30 mS/m. After inversion, the half space conductivity was ~ 45 mS/m. The vertical component TEM moment response of the recovered time constant model is shown in Figure 5.20. On display are the responses for three survey lines at -800N, at -400N, and at 0N. The responses at line -800N are outside the transmitter loop and approximately over the edge of the vertical dyke. The TEM moment responses at -400N are near the transmitter wire and traverses the vertical dyke. The responses at 0N are recorded across the centre of the loop and dyke. The left hand side shows the 'full' TEM moments and the right hand side shows the 'stripped' responses where the host response for 45 mS/m has been subtracted.

Figure 5.20 also shows the Bz TEM moment response of the starting model for three survey lines. The TEM moments of the starting model approximately corresponds to the observed TEM moments with an initial misfit of the starting model of $\chi^2 = 2.27$. The inversion of the noise contaminated TEM moments, based on the CDI starting model, succeeded after 15 iterations with a runtime of 4:15 min.

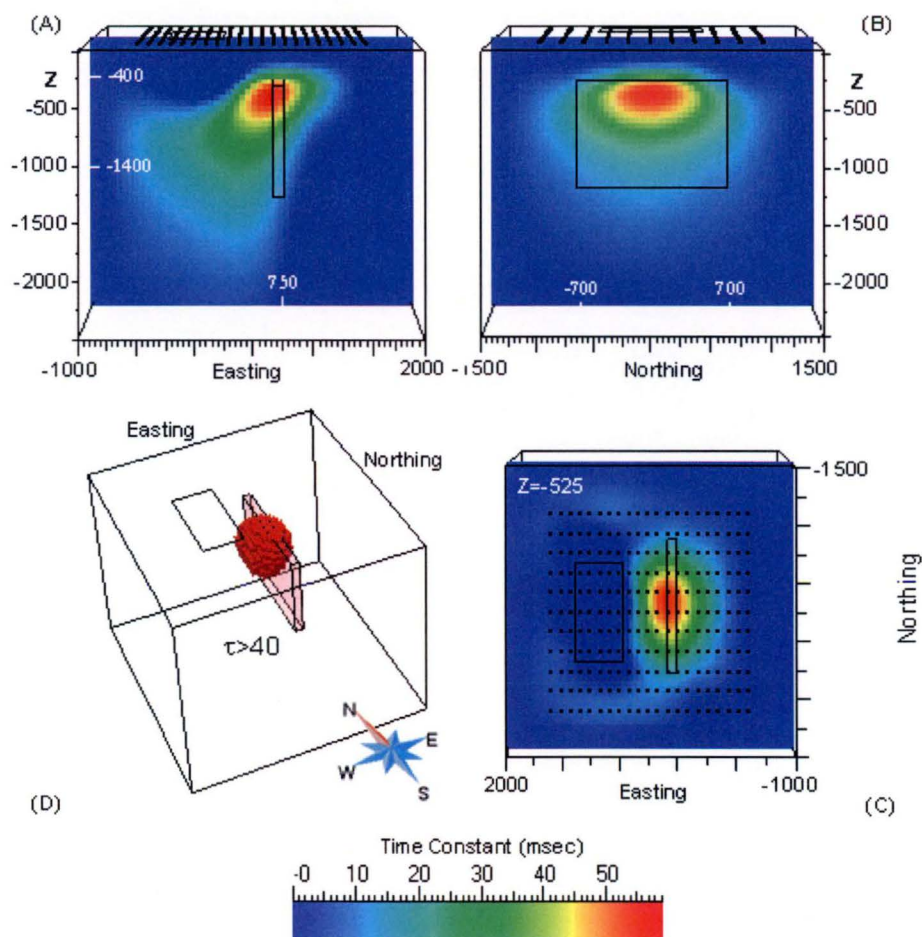


Figure 5.19 – Cross-sections for (A) 0N, (B) 750E and (C) plan at depth 525 m through recovered time constant model after inversion of the vertical dyke TEM moments using the CDI starting model. Inversion was successful after 15 iterations. The recovered model bears resemblance to the CDI starting model, however the region of elevated time constants has shifted eastwards and towards the upper part of the dyke. The iso-volume in panel (D) is for time constants larger than 40 msec.

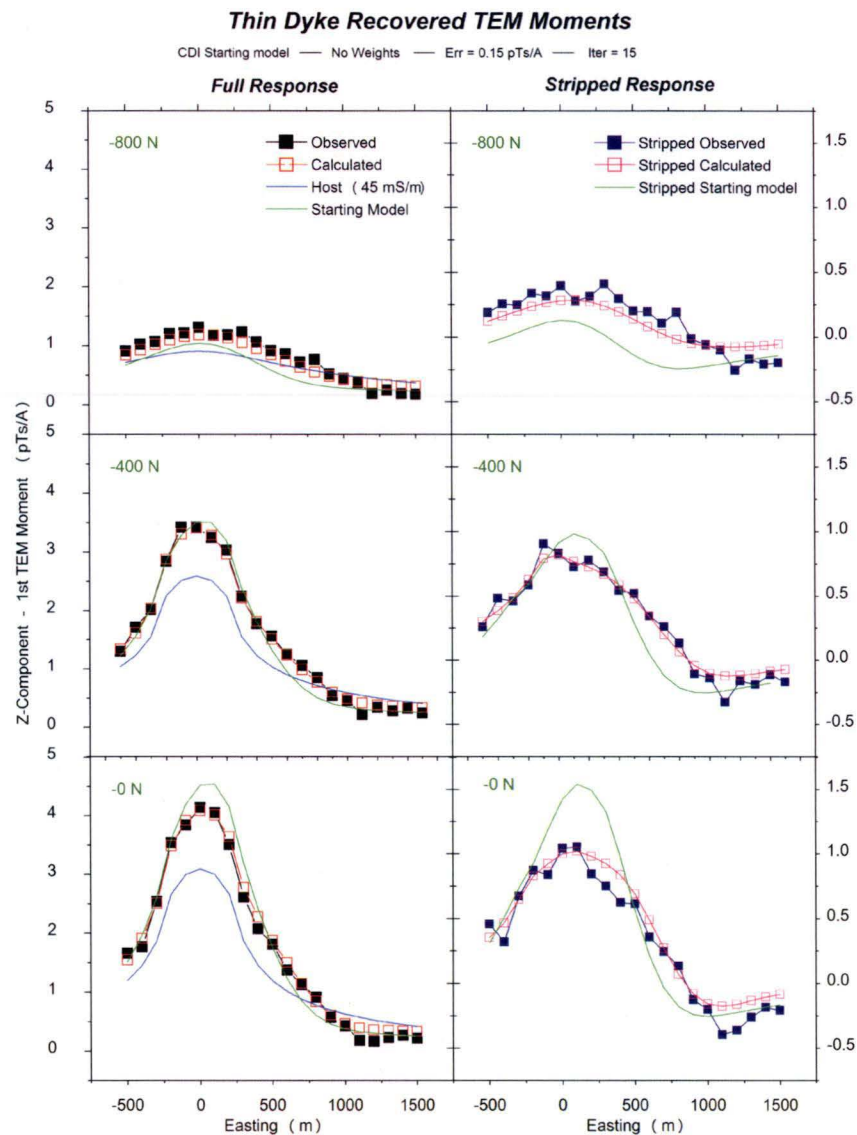


Figure 5.20 – Bz TEM moment responses of recovered time constant model based on the CDI starting model. On display are TEM moments for three survey lines at -800N, at -400N and at 0N, which run, respectively, outside the transmitter loop, just inside the transmitter loop and over the transmitter loop centre. The left hand side displays the 'full' TEM moments and the right hand side the 'stripped' responses without the host response.

5.4.2 Zero starting model with conductivity weights

For the zero starting model with conductivity weights, all cells are active during inversion. A positivity constraint for the time constants was enforced during inversion. An eastwest cross-section of the conductivity weights is shown in Figure 5.21. Larger weights are associated with higher conductivities. Zero conductivity weights are associated with the half space conductivity or smaller values. A sharp transition from higher weights near the centre of the prism to zero weights occurs east of the dyke, so that changes in the parameter vector are prohibited east of the dyke.

The recovered time constant model after inversion is shown in Figure 5.22. The dyke is accurately located in plan (Panel C), and its upper part is accurately located in section (Panels A and B). The recovered geoelectrical structure is mostly confined to the volume of the vertical dyke, however it is clustered in the upper third of the dyke model. The maximum values of the recovered time constants are larger than 300 msec, close to the time constant estimate for the vertical dyke ($\tau_{dyke} = 475$ msec).

As before, the 'full' and 'stripped' vertical component TEM moment profiles are shown for three lines in Figure 5.23. The half space conductivity was held fixed at its true value of 50 mS/m. Initial misfit was $\chi^2 = 4.74$ for the data uncertainty of 0.15 pTs/A and the inversion was successful after 67 iterations; runtime was 5:52 min.

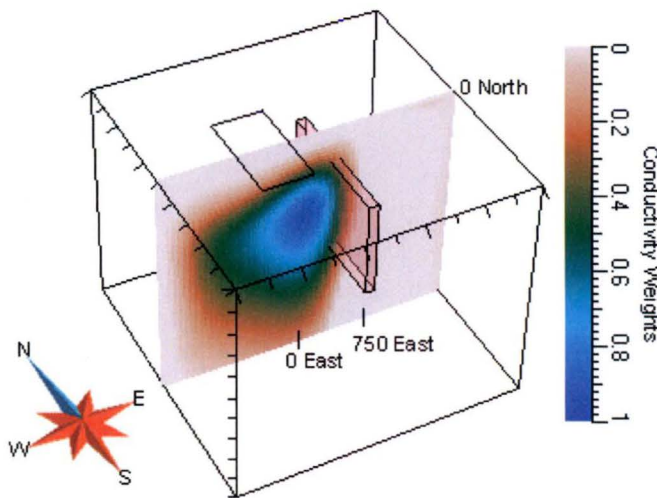


Figure 5.21 – Conductivity weights for vertical dyke model for an eastwest cross-section through the centre of the model (0N). Changes in the time constant for cells associated with high conductivity are preferred, whereas parameter changes are penalised for low conductivity cells. Cells associated with a zero weight are effectively turned off and will not change during inversion. Zero weights occur predominantly at the top of the model and east of the vertical dyke.

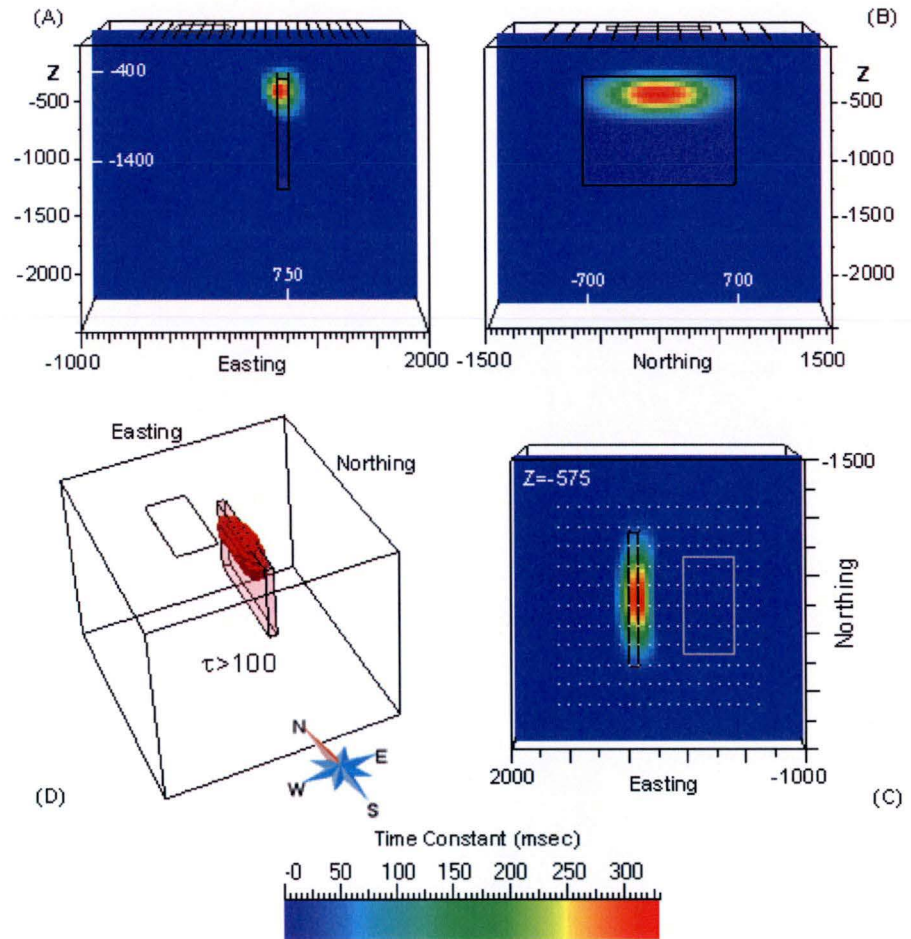


Figure 5.22 – Recovered time constant model of vertical dyke data assuming a zero starting model with conductivity weights. The recovered time constant model seems concentrated near the top of the dyke. Panel (A) displays an eastwest section through the model centre at 0 North; panel (B) shows a northsouth section through the vertical dyke prism at 750 East and panel (C) presents a horizontal section at a depth of 575 m where the maximum time constant value is found. Panel (D) is a 3D iso-volume of the recovered time constant model where only time constants greater than 100 msec are displayed.

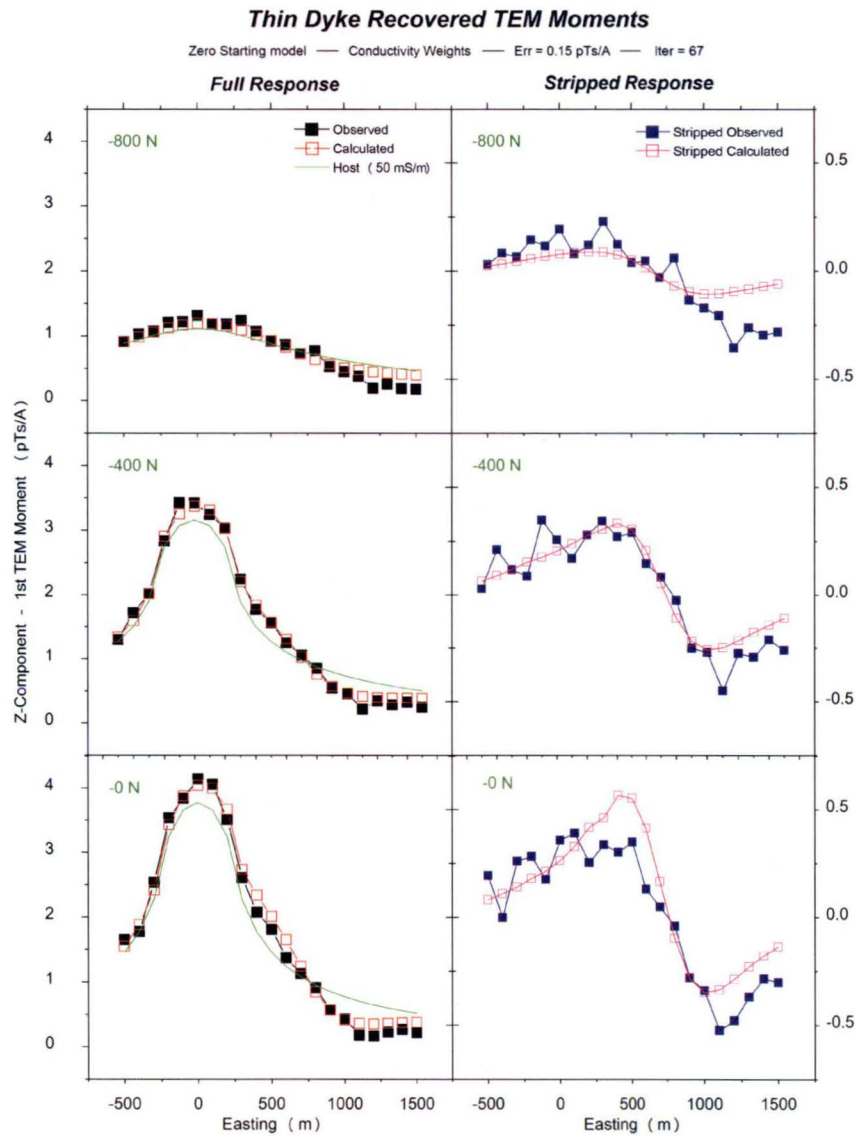


Figure 5.23 – Bz TEM moment responses of recovered time constant model for the zero starting model with conductivity weights. The left hand side displays the 'full' TEM moments and the right hand side the 'stripped' responses without the host response. During inversion, the host conductivity was held fixed at 50 mS/m.

5.4.3 Zero starting model with depth weights

A depth weighting scheme, based on weights calculated with $s_0 = 5 \times 10^{-4}$ and $d_0 = 200$, is employed to condition the depth of the causative volume. The weights are shown in Figure 5.24. Inversion is carried out with a fixed background conductivity (50 mS/m) and is repeated with a variable conductivity in order to examine the impact of a variable background when the background conductivity is relatively high. Optimisation for the background conductivity is based on an initial 'bad' guess of 30 mS/m.

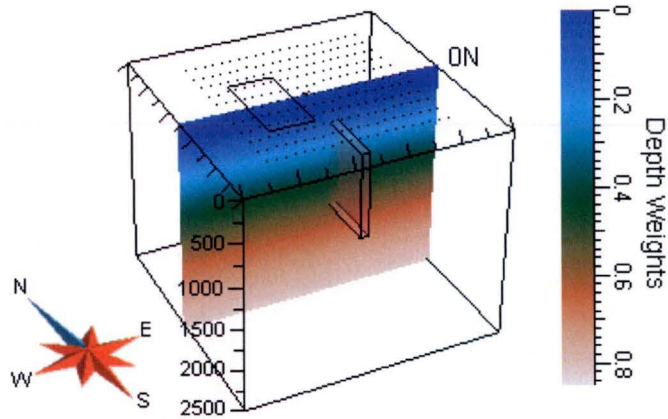


Figure 5.24 – Depth weighting scheme based on $s_0 = 5 \times 10^{-4}$ and $d_0 = 200$. The weights decay to a value of ~ 0.5 at a depth of ~ 1200 m which coincides with the maximum conductivity of the CDIs.

Figure 5.25 shows the recovered time constant model with the fixed half space conductivity of 50 mS/m. Elevated values of the recovered time constants are found at depths broadly coinciding with the upper half of the vertical dyke model. However large time constant values are distributed throughout a large volume extending well above the vertical dyke. The top of the recovered time constant model is at $d_0 = 200$ m. Initial misfit was $\chi^2 = 4.7$ for the data uncertainty of 0.15 pTs/A; inversion succeeded after 91 iterations; runtime was 6:33 min.

The inversion was repeated for the variable host conductivity (starting value 30 mS/m). The result is depicted in Figure 5.26. The recovered time constant model has a distinct resemblance to the result for the fixed half space conductivity. After inversion, the half space conductivity was 46.7 mS/m. The recovered time constants are spread out within a greater volume of the model in order to account for the 'missing' host conductivity. Initial misfit was $\chi^2 = 4.1$ for the data uncertainty of 0.15 pTs/A; inversion was successful after 49 iterations; runtime was 4:36 min.

Because the background response is very strong, a fixed background conductivity during inversion imposes a strong constraint so that the inversion requires a considerable number of iterations in order to achieve a fit to the data. Having a variable host conductivity gives less restrictive constraints with more degrees of freedom so that the inversion finds a solution more readily. The TEM moment responses are shown in Figure 5.27 for the recovered time constant model for the fixed background.

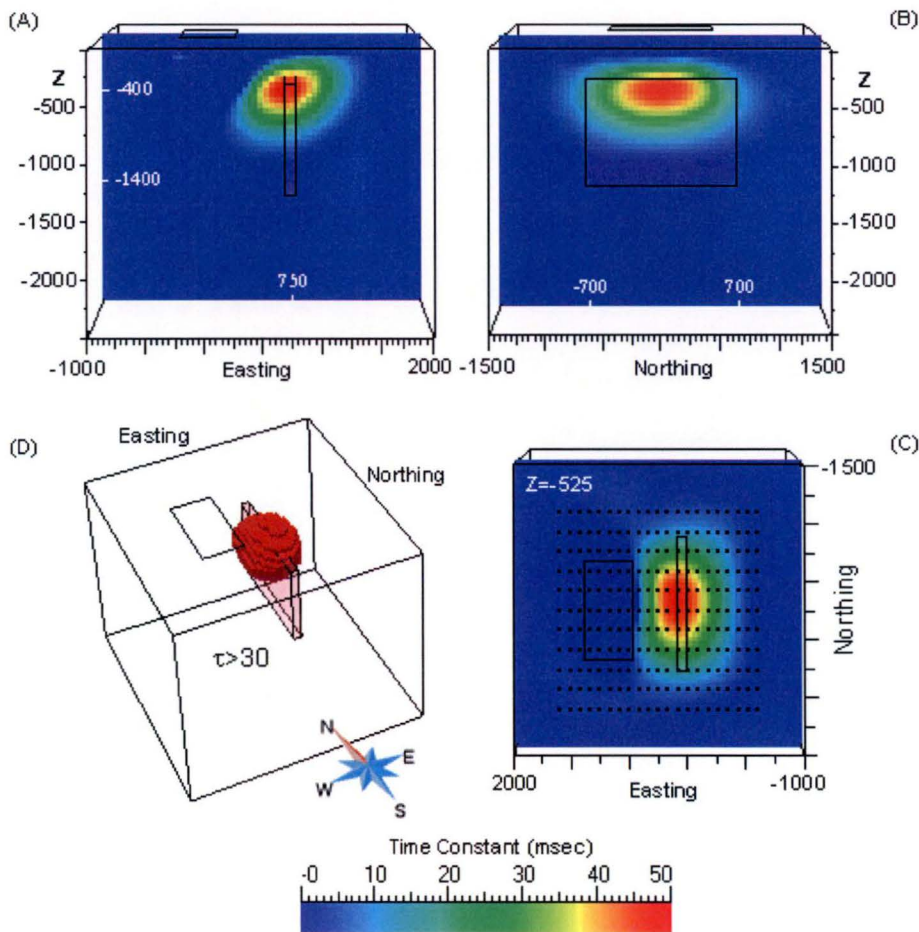


Figure 5.25 – Recovered time constants for the vertical dyke model based on a zero starting model conditioned with depth weights ($s_0 = 0.0005$ and $d_0 = 200$). The half space conductivity was held fixed during inversion (50 mS/m). The recovered time constant model approximately coincides with the upper third of the vertical dyke model, but somewhat extends laterally and above the dyke. Highest time constant value of ~55 msec is found at a depth of 525 m (C). The iso-surface in panel (D) shows elevated time constants larger than 30 msec.

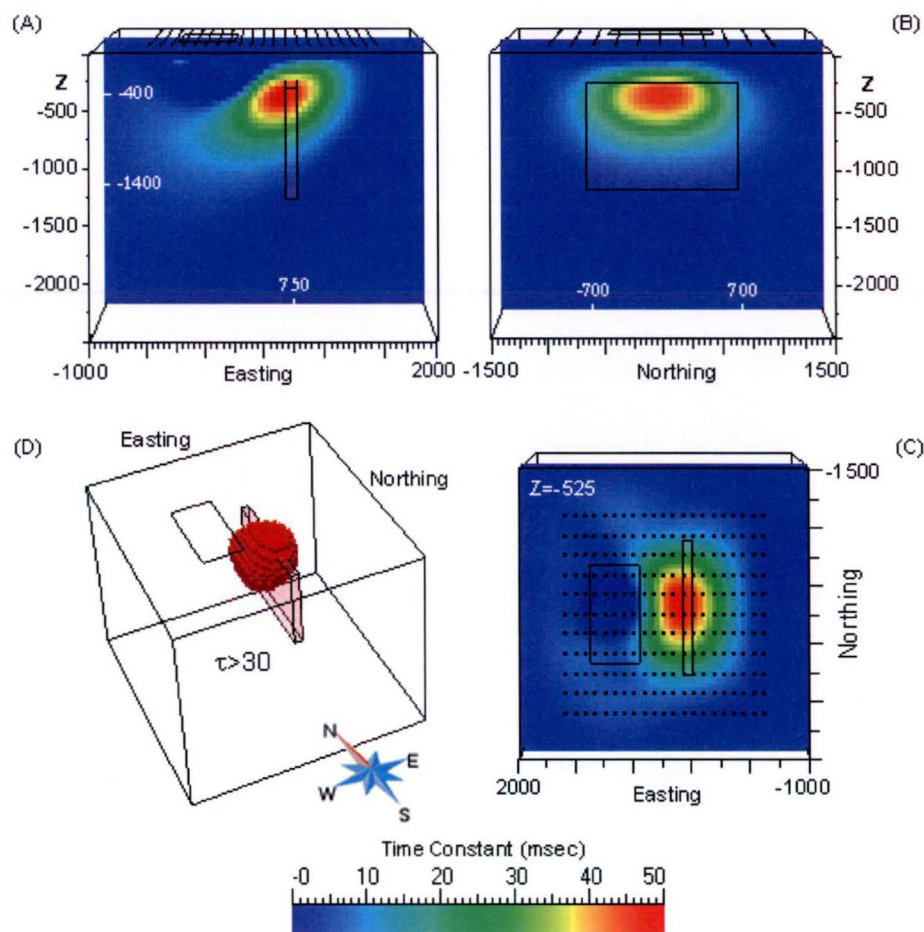


Figure 5.26 – Recovered time constants for the vertical dyke model based on a zero starting model conditioned with depth weights ($s_0 = 0.0005$ and $d_0 = 200$). The half space conductivity was variable during inversion (start value 30 mS/m; final value was 46.7 mS/m). The recovered time constant model approximately coincides with the upper third of the vertical dyke model, but somewhat extends laterally and above the dyke. Highest time constant value of ~50 msec is found at a depth of 525 m (C). The iso-surface in panel (D) encloses cells with time constants larger than 30 msec.

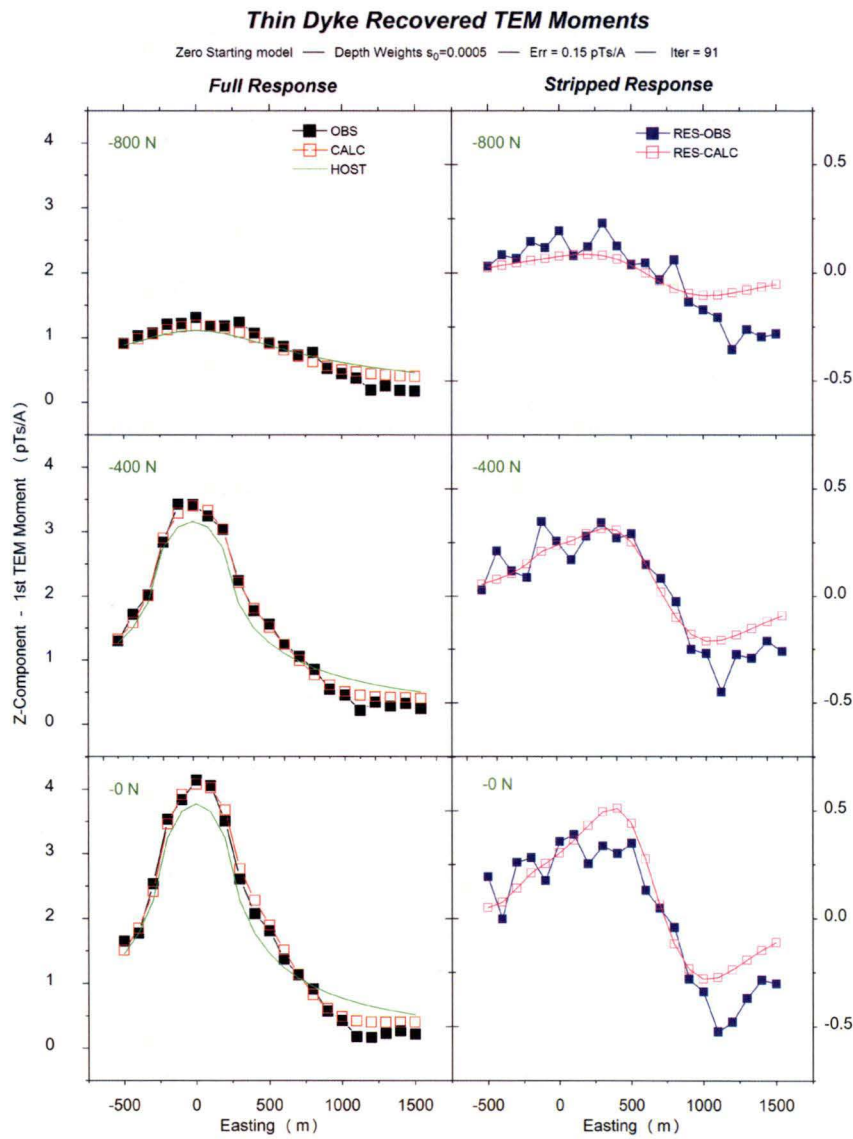


Figure 5.27 – Vertical component TEM moment response profiles of recovered time constant model based on zero starting model conditioned depth weights. The 50 mS/m background conductivity was held fixed during inversion. On display are three survey lines at -800N, at -400N and at 0N with the left hand side displays the 'full' TEM moments and the right hand side the 'stripped' responses.

5.4.4 Review of inversion results for vertical dyke model

Heterogeneous property inversion of the Z-component TEM moments for the vertical dyke was carried out for a CDI starting model, a zero starting model conditioned with conductivity weights and a zero starting model conditioned with depth weights. Five percent Gaussian random noise was added to the Z-component TEM moments, which translates to a data uncertainty of about 0.15 pTs/A. Depending on the starting models and constraints used, various differences arose in the recovered time constant models. The inversion parameters for 4 inversion runs are displayed in Table 5.2.

Table 5.2 – Inversion parameters of the horizontal slab model. Data uncertainty is $q = 0.15$ pTs/A and maximum step size $\delta\tau = 3.5$ msec. Number of data points is 231. Starting value of host conductivity is 30 mS/m (where applicable).

Starting-model	σ_{host} (mS/m) (start / final)	χ^2_{start}	Iter.	Time (min:sec)	# Active Parameters
'CDI'	30 / 45	2.3	15	4:15	165,600
'Zero' 3D-weights	50 / 50	4.7	67	5.52	180,000
'Zero' 1D-weights (a)	50 / 50	4.7	91	6 33	180,000
'Zero' 1D-weights (b)	30 / 46 7	4.1	49	4 36	180,000

All inversions attained a fit to the vertical dyke TEM moments and concluded successfully with a misfit of $\chi^2 \leq 1$. When compared with the result from the conductivity-depth imaging, the approximate 3D inversion produced a 'sharper' image of the geoelectrical subsurface structure. All recovered time constant models could indicate the position of the upper part of the vertical dyke prism. By design of the forward algorithm, each point conductor is parallel to the local primary field. For the vertical dyke example currents will predominantly flow in the plane of the dyke and taking into account conductivity gradients could be important. Conductivity gradients are part of future work (Appendix A).

CDI starting model The initial misfit of $\chi^2 = 2.3$ was relatively small since the CDI starting model already gave a fairly good fit. Inversion for the CDI starting model succeeded after 15 iterations. Variable background conductivity was 45 mS/m after inversion. Elevated values of the recovered time constant model are indicative of the location of the dyke. A broad conductive area is extending westwards as is also seen in the corresponding CDIs. Because CDIs are generated from total B-field amplitudes, it is expected that inversion of $|\mathbf{B}|$ TEM moments may produce a model which resembles the vertical dyke more closely. This is a subject of future work (Appendix A).

Zero starting model with conductivity weights The initial χ^2 -misfit of 4.7 for the zero starting model is the misfit between the 'observed' TEM moments and the strong 50 mS/m background response. The time constant model accurately depicts the upper part of the vertical dyke. Because small conductivity weights penalise conductive material eastside of the apparent conductive high, elevated values in the recovered time constant model are mostly confined to the volume of the dyke, though clustered in the upper third of the dyke. Recovered time constant values of up to ~ 330 msec approach the estimated time constant of the dyke ($\tau_{dyke} = 475$ msec).

Zero starting model with depth weights Recovered time constant models based on the depth weighting scheme give a satisfactory image of the vertical dyke model. Calculations have been conducted for a fixed and a variable background conductivity. In the case of the least-squares optimised background, resulting in a final half space conductivity of 46.7 mS/m, the recovered time-constant model values are somewhat more disseminated in order to compensate for the 'missing' host conductivity. The recovered time constant structure is partially located above the top of the vertical dyke and lower time constant values are truncated at $d_0 = 200$ m. The higher number of iterations, in case of the fixed background, is interpreted to be due to the fairly strong host response which effectively imposes a strong constraint so that the inversion requires a considerable number of iterations in order to achieve a fit to the data.

5.5 Concluding remarks

The algorithm for inversion of TEM data generates acceptable models as demonstrated for two distinct, synthetic examples. The inversion is fast and hence various different starting models can be examined in short time. The synthetic inversion examples illustrate how the non-unique nature of heterogeneous property inversion of TEM moments may be addressed by including a set of quantitative weights. The use of conductivity-based starting models and/or weights is very effective.

Depth information is restored by using CDI values either as initial time constant values or as weights. In particular, zero starting models with conductivity weights produced fast and accurate results. Because zero starting models omit initial calculation of the forward model response, the inversion is significantly faster than for CDI starting models. The CDIs for both models were already indicative of the true model and 3D inversion constrained by conductivity weights basically refined the CDI results.

Depth weighting penalises shallow solutions but is subjective to a certain degree. For inversion of TEM moments, the depth weights are guided by inspection of the CDIs, defined such that the weights decayed to about 0.5 at depths coinciding with the maximum apparent conductivity. Based on the depth weighting schemes, TEM moment inversion gave solutions in overall agreement with the synthetic models. The next chapter illustrates how incorporation of geological constraints, based on drill core samples, guides the inverse problem to a solution consistent with the available geological knowledge.

Chapter 6

Application of approximate 3D TEM inversion to field data.

Introduction This chapter illustrates application of the novel potential field-like 3D inversion approach to TEM field data with incorporated geological information as constraints. Fixed-loop **B**-field data were obtained along multiple survey lines employing a low-temperature SQUID sensor in conjunction with a SMARTTEM receiver. The TEM data were acquired across the Proterozoic metavolcanic-sedimentary succession which hosts the Gamsberg zinc deposit in South Africa. The time-domain EM field data are transformed to TEM moments (c.f. Chapter 2.8). Vertical component TEM moments which are linear with respect to time constants are subject to inversion for geoelectrical structure.

Geophysical information from magnetic and gravity surveys and geological information as well as petrophysical information from drill core samples are incorporated into a 3D geological model of the TEM survey site which is located in the Eastern portion of the Gamsberg prospect. This model expedites 3D integrated inversion of the TEM moments by guiding the inversion towards a solution that is consistent with the geological knowledge. The geological model consists of three formations: Nousees Mafic Gneiss, Gams Formation and Pella Quartzite. Only the Gams Formation carries significant mineralisation. The entire volume of the geological model consists of 738,224 cubic cells with side lengths of 20 m. The Gams Formation unit consists of 33,886 cells.

Due to the non-unique nature of the TEM moments inversion, the recovered time constant models may exhibit significant differences, depending on the starting models and constraints used (c.f. Chapter 5). A preferred solution may only be identified after exploring some of the range of acceptable models to develop an understanding of the variability of the results (Williams, 2008,

p.69). 3D inversion is therefore carried out with different starting models and constraints. Inversion solutions are deemed successful if the χ^2 -misfit of the modelled TEM moments are less than or equal to unity.

First, a minimum-structure starting model, initialised with zero cell time constants (i.e. cells that have zero time constants) and without any constraints, is subject to inversion. The minimum-structure model is defined as the entire volume of the supplied geological model and 3D inversion resolves the subsurface structure in terms of time constants within the boundaries of the supplied geological model. An unconstrained inversion without additional geological information has the largest degree of freedom and is expected to fit the data very well. The unconstrained solution is mathematical only and in general only poorly reflects the true geoelectrical subsurface.

Second, a minimum-structure starting model is generated from CDI pseudo-sections together with a positivity condition for the time constants. The CDI starting model yields a solution in close resemblance to the CDI conductivity structure. Inversion based on the CDI starting model was only successful when the inversion employs a 'bound cancelation' directive which deactivates any cell from inversion if its time constant attains a bound. Because cells are dynamically deactivated during inversion, bound cancelation imposes a gradually changing constraint which effectively reduces the number of active cells during inversion.

Third, a minimum-structure starting model initialised with zero cell time constants is subject to inversion. The inversion employs soft constraints which are defined either as (1D) depth weights or as (3D) conductivity weights. A positivity condition for the time constants was also employed. The starting model conditioned with conductivity weights is closely related to the CDI-starting model and penalises solutions inconsistent with conductivity-depth-imaging. The starting model conditioned with depth weights recovers smoothly varying time constants with depth. Inversion based on depth weights yielded solutions consistent with the information from drill holes, however inversion based on conductivity weights failed.

Fourth, a geologically constrained inversion is carried out in which the active geological unit is specified from the supplied geological model: only cells comprising the Gams Formation unit were able to change. A positivity condition for the time constants was employed. Based on the geologically constrained inversion, a recovered time constant model was obtained with sharp boundaries.

The time domain data can also be reasonably fitted to a conventional plate model. The inversion results for the Gamsberg data are consistent with the plate forward modelling and with the bore hole information. Inversion of the Gamsberg data set was considerably faster than interpretation based on interactive plate forward modelling. 3D inversion of the measured field data all completed in a relative short time. The longest run-time was ~ 30 minutes for inversion of the field data set for 738,224 cells, calculated on a Pentium 4 2.8 GHz processor from 2006. Shortest run-time was about 3 min for the geologically constrained inversion of the measured field data, involving only 33,886 cells.

6.1 Geological context

The Gamsberg zinc deposit lies within a Precambrian volcano-sedimentary succession, hosted by the Mesoproterozoic Bushmanland Group, South Africa. Gamsberg is one of five stratiform base metal deposits that are located in the Bushmanland Province and are collectively known as the Aggeneys-Gamsberg deposits (McClung et al., 2007). The other four deposits are Black Mountain, Broken Hill, Broken Hill Deeps and Big Syncline.

6.1.1 Exploration history

The Gamsberg deposit is located ~16 km to the east of the Broken Hill mine near Aggeneys in the Northern Cape Province of South Africa. The Gamsberg project is owned and managed by Anglo American plc (Base Metals Division). Exploration of Gamsberg commenced in 1972. Geological, geochemical and geophysical results, together with the discovery of significant gossan-capping in the north-western part of the prospect, merited detailed follow-up investigations. Rozendaal (1986) notes that geophysics played a particularly important part in the early assessment of the deposit by indicating the down-plunge continuation of the widest part of the gossan below outcropping quartzite. Unfortunately, the details of initial geophysical exploration have not been published. Surface drilling was commenced in 1972. By the end of 1973 a total of 47 boreholes had been drilled into the area of greatest development of gossan at Gamsberg West. By the end of 1978, a total of 42,130 m of surface diamond drilling and 16,317 m of percussion drilling as well as 22,026 m of underground diamond drilling had established a reserve of 150Mt averaging 7.10 per cent zinc and 0.55 per cent lead (Rozendaal, 1986).

6.1.2 Lithology and stratigraphy

Gamsberg is located in the Namaqualand District in the north-western part of the Northern Cape Province. The Gamsberg mountain, from which the deposit takes its name, is a steep-sided inselberg, about 7 km long and 5 km across, rising to an elevation of 1150 m above sea level and approximately 250 m above the general level of the surrounding plain. The flat top of the mountain has been partly eroded to form an internal basin. The base metal deposit is exposed as a prominent gossan along the western margin of this erosional basin.

Because of the complex structural pattern of the Aggeneys-Gamsberg district, different stratigraphic columns and stratigraphic names emerged in different areas. The stratigraphic nomenclature for the current thesis is based on the publication of Rozendaal (1986), which focuses solely on the Gamsberg zinc deposit. Bailie et al. (2007) includes a recent overview of various nomenclatures used for the Bushmanland Group.

The Gamsberg stratigraphy has been subjected to complex deformation, and mineralisation is understood to occur within a complex folded 'sheath' which extends for several kilometres (Figure 6.1b). The known deposit is located in the Gams Formation, where it crops out at the western end of the inselberg. The succession at Gamsberg consists of basal quartzo-feldspathic gneiss, identified as the Haramoep Gneiss formation. The Haramoep Gneiss is overlain by sillimanite-bearing pelitic schist, the Namiest Schist, which is ~ 70 m thick. The Namiest

Gamsberg	
<i>Formation</i>	<i>Lithology</i>
Nousees Mafic Gneiss	Quartz-feldspar-amphibole gneiss/fels, pyroxene-plagioclase-quartz fels and quartz-muscovite schist.
Gams Formation	<p>a Upper unit characterised by a concentration of pyroxenoid, garnet and magnetite with a stratigraphic thickness of 0–9m</p> <p>b Mineralised layer holding sulphides of zinc and lead with quartz-garnet- amphibole rocks and graphitic quartz-sillimanite-muscovite- feldspar containing major amounts of pyrite and pyrrhotite. The stratigraphic thickness of the zone varies from 0–80m</p> <p>c Basal banded garnet-clinopyroxene marble and banded quartz-garnet-feldspar-clyno- pyroxene rock with a maximum thickness of 10m</p>
Pella Quartzite	Massive recrystallised milky quartzite.
Namiest Schist	Quartz-biotite-muscovite-sillimanite schist.
Haramoep Gneiss	Pink granite-gneiss.

Table 6.1 – Litho-stratigraphy of the Bushmanland Group exposed at Gamsberg, after Rozendaal (1986).

Schist grades upwards into the Pella Quartzite, a thick succession of metaquartzite and interbedded lenses of aluminous schist which is about 250–375 m thick. The Pella Quartzite forms the exterior and interior cliffs as well as the flat top of Gamsberg.

The Gams Formation is in sharp contact with the Pella Quartzite and has a thickness of about 0–80 m. The ore bearing Gams Formation is a mineralogically complex unit which is exposed along the periphery of the Gamsberg erosional basin. The Gams Formation is further subdivided into three members **a**, **b** and **c** as described in Table 6.1. The Gams Formation is overlain by a thick succession consisting of quartz-muscovite schist, lenses of conglomerate, and bands of micaceous quartzite and amphibolite. These upper units are collectively identified as the Nousees Mafic Gneiss formation, and are about 400–500 m thick. Formations and typical lithologies are shown in Table 6.1.

6.2 Gamsberg-East geological model

Information from magnetic and gravity surveys as well as airborne EM and ground-loop EM, together with geological mapping and drill core logs were compiled into a digital geological 3D-model (T.Chalke, Mira Geoscience, pers. comm., 2008). Away from the drill holes the model is highly interpretative in nature. The 3D-model of Gamsberg-East was kindly supplied by Anglo American Exploration Division. The model had been constructed in Gocad by Mira Geoscience. The model, displayed in Figure 6.2, is a simplified representation of the local geology at the TEM survey site at Gamsberg-East. The 3D-model consists of three units, described earlier:

- (i) Nousees Gneiss (ii) Gams Formation (iii) Pella Quartzite

The basinal structure of the Gamsberg prospect means that Nousees Mafic Gneiss is effectively enclosed by the folded Gams Formation. Only the Gams Formation where ore mineralisation occurs is shown in Figure 6.2. Superimposed are drill markers in green which designate locations where mineralisation has been verified (members a, b and c in Table 6.1). The drill markers form the base of the ore mineral bearing Gams Formation. The depth of the mineral bearing locations range from ~200 m to ~1000 m.

The 3D-model of Gamsberg-East contains the TEM survey site. The transmitter loop, with dimensions 645×275 m, is included in Figure 6.1a. TEM data have been recorded along nine NNE-SSW survey lines traversing the transmitter loop. The survey lines are ~ 1.5 km long.

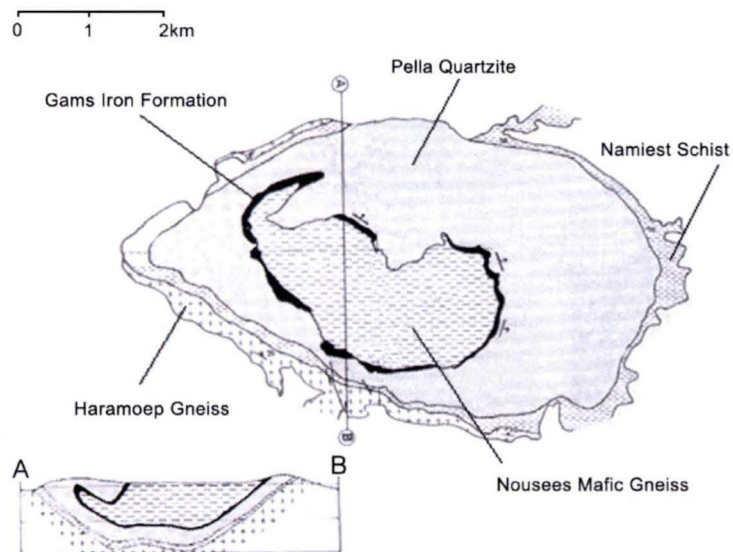
Downhole resistivity has not been measured in drill holes at the TEM survey site (pers. comm., O. Terblanche, Anglo American). However, about 3.5 km west from the transmitter centre at Gamsberg West, downhole resistivity logs were recorded in four boreholes (Trofimczyk, 2004). Within the ore horizon (Gams Formation), resistivity values are found to be of the order of tens of $\Omega\cdot\text{m}$, consistent with the Zn-rich nature of the mineralisation. High resistivity values, from ~ 1000 $\Omega\cdot\text{m}$ to greater than ~ 10,000 $\Omega\cdot\text{m}$, are observed within the country rock (Nousees Gneiss and Pella Quartzite).

The 3D-model has dimensions 1480 m East, 1720 m North and 2320 m depth extent. Subcell size is 20 m, so that the model consists of 738,224 cells with 74 cells in east direction, 86 cells in north direction and 116 cells along the vertical axis. The geological 3D-model was input for the employed litho-inversion scheme. The Gams Formation is ~ 80 m thick and the number of cells in the Gams Formation is 33,886 which amounts to ~ 4.6% of the total number of cells. The Gams Formation is truncated at the western and southern limits of the Voxet. Ground topography is assumed to be perfectly flat for modelling and inversion but varies between 20 m and 200 m in the southwest and northeast respectively. The UTM coordinates (Zone 34J) of the corners of the volume, shown in Figure 6.2, are

P1	(305927E,6762737N)
P2	(304467E,6762737N)
P3	(304467E,6764437N)
P4	(305927E,6764437N)



(a) Top view of Gamsberg from Google Maps. The exploration area is at the eastern end of Gamsberg. The red markers indicate the corners of the geological model. The corners of the fixed transmitter loop are marked by circles.



(b) Generalised geological map after Rozendaal (1986) shows the distribution of the local stratigraphic units constituting the Gamsberg prospect.

Figure 6.1 – Aerial view (top) and geological map (bottom) of the Gamsberg prospect.

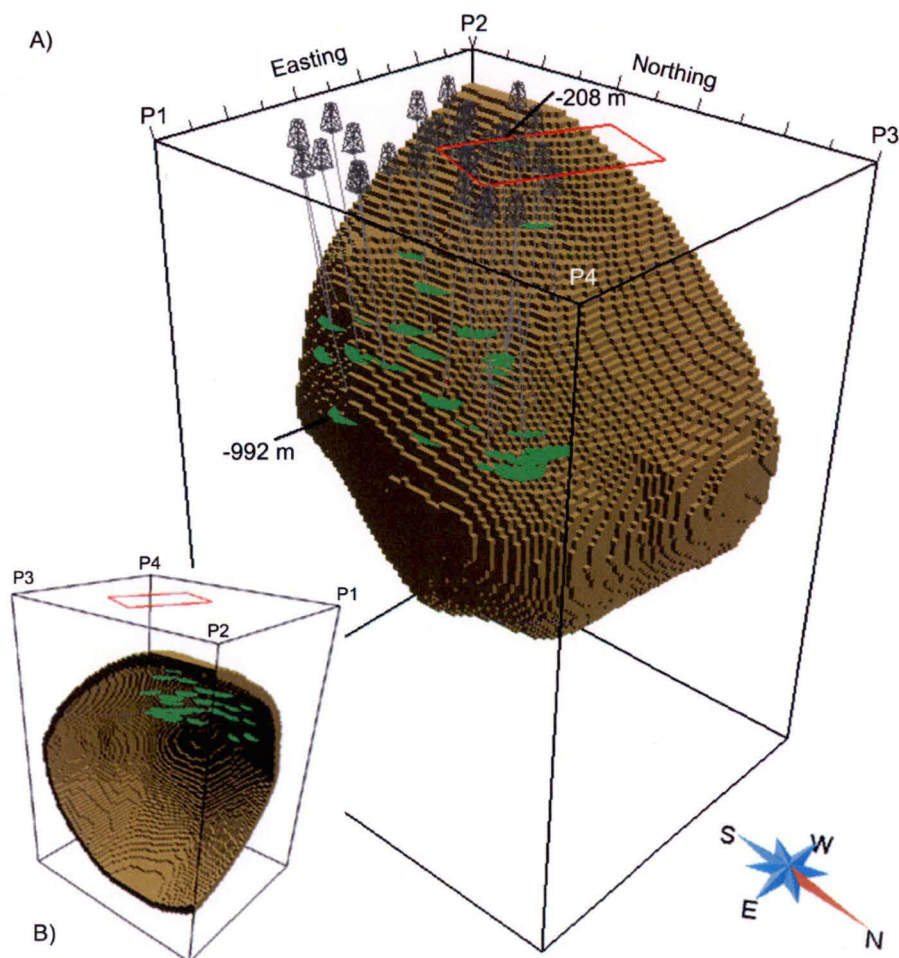


Figure 6.2 – 3D-model of Gamsberg-East. On display is the folded Gams Formation unit as viewed from the northeast (A). The inset shows the 'back' of the Gams Formation as viewed from the southwest (B). The coordinates of the corners P1, P2, P3 and P4 are given in the text. Model extents are 1480 m East, 1720 m North and 2320 Z. Superimposed, in green, are markers at drilled intersections of the Gams Formation. The markers designate locations where drill holes have intersected mineralisation which was recognised in the drill cores at depths ranging from ~200 m to ~1000 m. The transmitter loop is shown in red.

6.3 EM equipment and data acquisition

TEM field data were kindly provided by Anglo American Exploration Division, South Africa. The TEM survey was designed to test the possible extension of an already identified subsurface conductor (pers. comm., O. Terblanche, Anglo American). The transient EM data were measured in fixed-loop layout using a low-temperature Superconducting Quantum Interference Device (SQUID) sensor. Fixed-loop surveys are routinely conducted for detailed characterisation of deposits when there is already a good understanding of the prospective target.



(a) Cryostat and SQUID magnetometer.



(b) Dewar with liquid helium in field operations.

Figure 6.3 – Cryostat with SQUID magnetometer and liquid helium dewar for TEM measurements. In figure (a) the cryostat containing the SQUID is shown, being depressurised. In order to fill the cryostat with liquid helium, the chamber has to be evacuated, so that air-constituents do not freeze out during the filling process. Figure (b) depicts the dewar with liquid helium for a three week operation schedule. The dewar has a height of approximately two meters. These pictures were taken by the author during a similar TEM survey in 2008 at Saxby, Queensland, Australia.



(a) ZONGE GGT-30 transmitter



(b) SMART-EM-V receiver

Figure 6.4 – Transmitter and receiver during field operations. The transmitter, shown in figure (a), is powered by a mobile generator during field operations. The SMART-EM-V receiver is depicted in (b). These pictures were taken during a similar TEM survey in 2008 at Saxby, Queensland, Australia.

SQUIDS combine the physical phenomena of flux quantisation and Josephson tunnelling, providing sensitive detection of magnetic flux. A SQUID consists of a superconducting loop interrupted by two Josephson junctions connected in parallel on a superconducting loop. If the SQUID is biased with an appropriate current, the voltage across the SQUID is a function of the flux in the ring and therefore a function of the external magnetic field. When the flux in the loop is increased, the voltage oscillates with a certain period. By detecting a small change in the voltage, one is able to detect a change in flux (Kleiner et al., 2004). The low-temperature SQUID sensor is immersed in a liquid helium filled cryostat and cooled down below the superconducting temperature (4K). This system requires the refill of liquid helium periodically (Figure 6.3).

The main advantage of a SQUID system is the ability to measure very small signal amplitudes in the range of tens of femto-Tesla. The measured magnetic flux (B-field) does not decay as rapidly as traditional voltage (dB/dt) measurements, which ensures better resolution at later times and therefore a greater depth of investigation with enhanced signal-to-noise ratio. Hence, SQUIDS offer the capability to detect conductors well below the detector threshold for conventional coil detectors (Leslie et al., 2008). SQUID systems are now routinely used by mineral exploration teams (Hughes, 2006; Webb and Corscadden, 2009).

All three Cartesian components of the B-field at Gamsberg-East were recorded with a SMARTEM-V receiver in conjunction with a Zonge GGT-30 transmitter (Figure 6.4). The transmitter on and off times were 900 ms (0.2778 Hz fundamental, 18 Amp), with a turnoff ramp of 0.4 ms. The SMARTEM-V channel centre times for 41 channels ranged from 0.1 ms to 710.31 ms (Chapter 1, Table 1.2).

6.4 The field data

Figure 6.5 shows the survey layout. TEM data has been recorded along 9 survey lines at ~31 receiver stations per line (260 observation points in total). Receiver station spacing was 50 m, except when crossing the transmitter loop; line spacing was 100 m. The profiles are oriented 23 degrees east of grid north. Stacked profiles of the time-domain B-field are shown in Figure 6.6 and in 6.7 for the z-component and x-component. The x-component is defined as the component along the lines and the y-component is perpendicular. To avoid cluttering, the EM responses are shown for every third channel from the 4th to the 40-th channel on a linear-log scale. The stacked z-component profiles are contaminated with noise at early and late times, but channels from 10–30 (0.7 ms–52.9 ms) are mostly clean. At early times the z-component recordings are dominated by the strong transmitter loop response whereas at late times, higher frequency noise can be seen, the source of which is not known. The spike feature in the z-component of line 100E at distance 300 m may be due to an instrumentation problem or could be “cultural” noise, e.g. a metal object; these data were discarded. The x-component recordings are noise-contaminated for the entire time range. The y-component from all lines have small amplitudes and have been omitted due to anomalous high noise values (noise/signal ~ 0.8).

Crossovers seen for channels > 14 mark the edge of a large buried conductor. All profiles exhibit similar characteristics with sharp zero crossovers in the first third of the survey profiles starting at channel 14. These crossovers are marked with green arrows in Figure 6.6. The z-component crossovers migrate to the south as lines further east are considered, and thus are thought to reflect termination of the subsurface conductor in this direction. The cross-overs migrate NNE with time, suggesting a dip or plunge to NNE. The crossover locations are also indicated in Figure 6.5 by the oblique solid line. Additional crossovers, seen for a few channels < 14 at lines -200E, -100E and 0E, may indicate the presence of a more shallow, minor conductor. These crossovers are marked with a blue arrow.

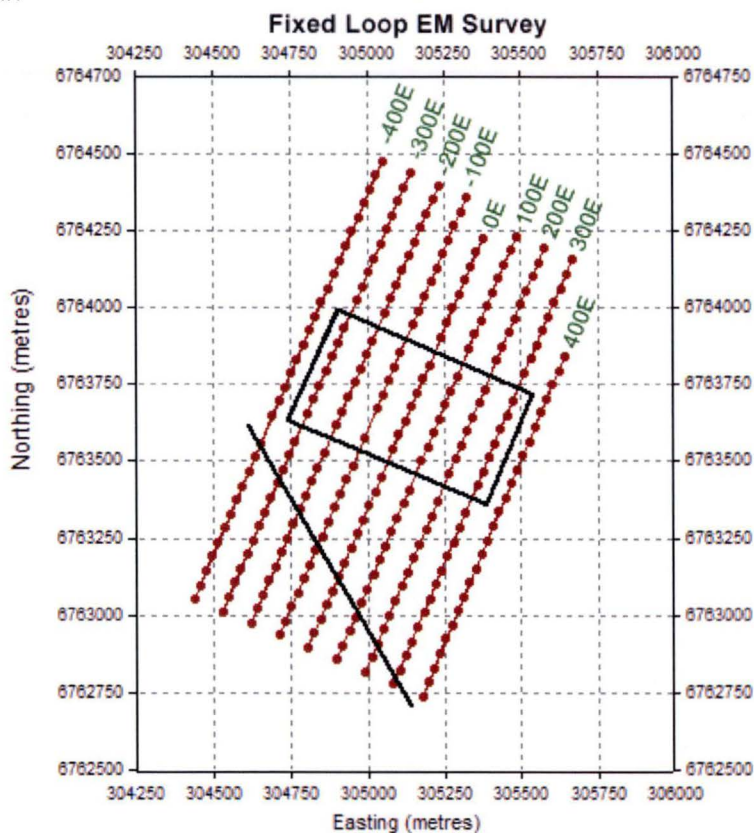


Figure 6.5 – Fixed-loop TEM survey layout at Gamsberg-East. TEM data has been recorded along 9 survey lines at ~ 31 receiver stations per line (260 observation points in total). The profiles are oriented 23 degrees east of grid north. For processing, the data have been converted into a local coordinate system with the transmitter loop centre as the origin and the local northings as the receiver plotting points. The transmitter loop had dimensions 645×275 m, with the long side of the loop oriented perpendicular to the survey lines. The loop was centred at (305138E, 6763677N). The zero-crossovers in the z-component are indicated by the oblique solid line crossing the survey lines.

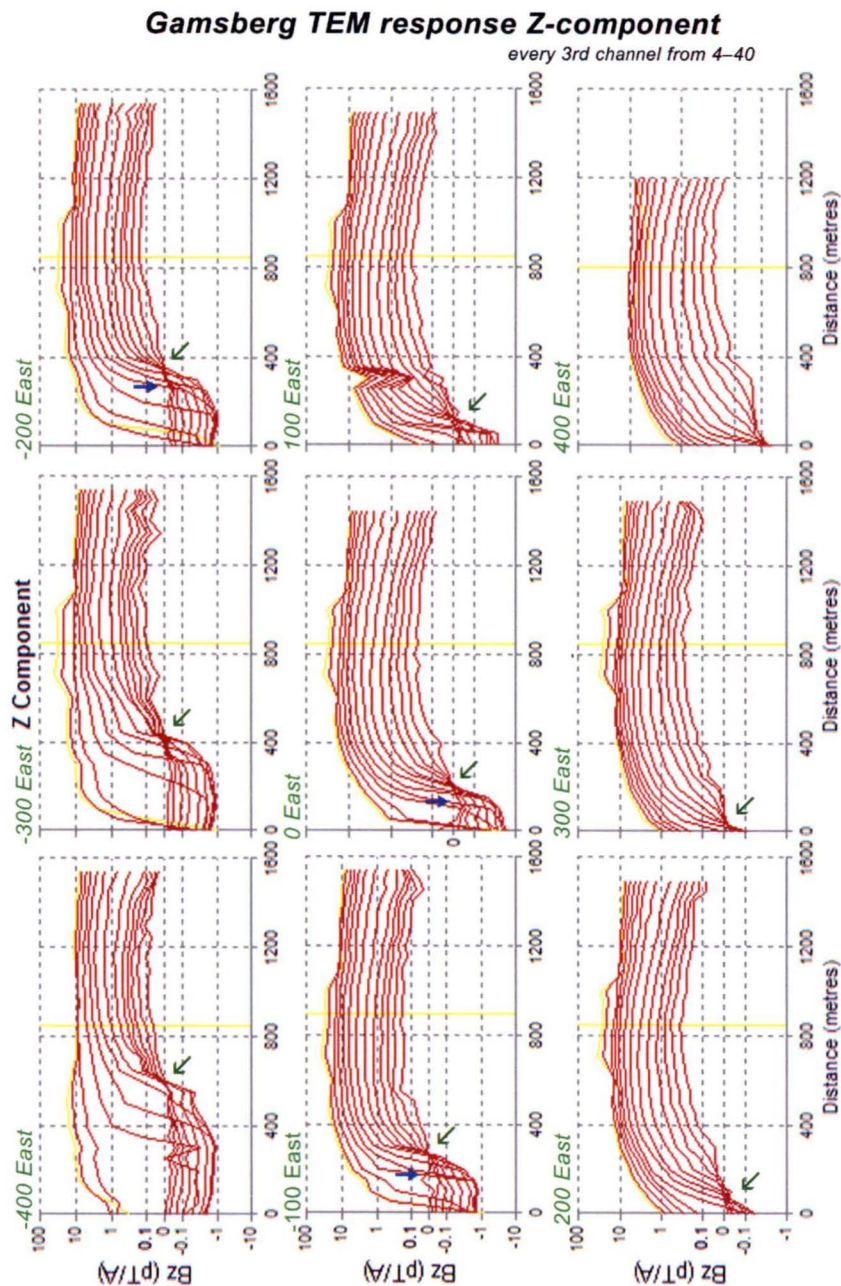


Figure 6.6 – Stacked B_z -profiles at Gamsberg-East. The TEM responses are shown for every third channel from the 4th to the 40th channel on a linear-log scale. Green arrows show sharp zero-crossovers for channels > 14. Blue arrows indicate sharp zero-crossovers for channels < 14 at lines -200E, -100E and 0E. The crossovers are interpreted to indicate termination of a deep conductor and a small conductive feature at more shallow depth, respectively. The yellow markers indicate the transmitter loop centre-line.

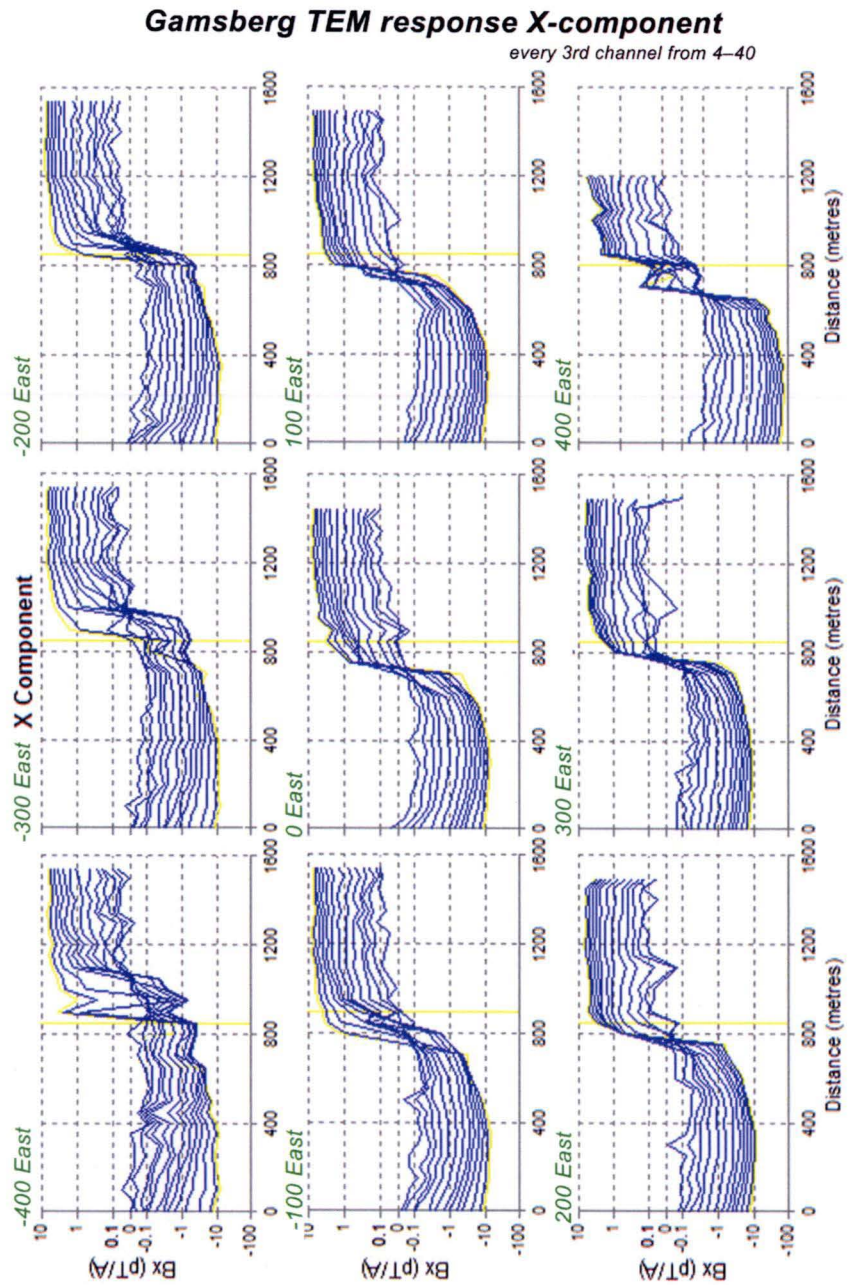


Figure 6.7 – Stacked Bx-profiles at Gamsberg-East. The TEM responses are shown for every third channel from the 4th to the 40th channel on a linear-log scale. The yellow markers indicate the transmitter loop centre-line.

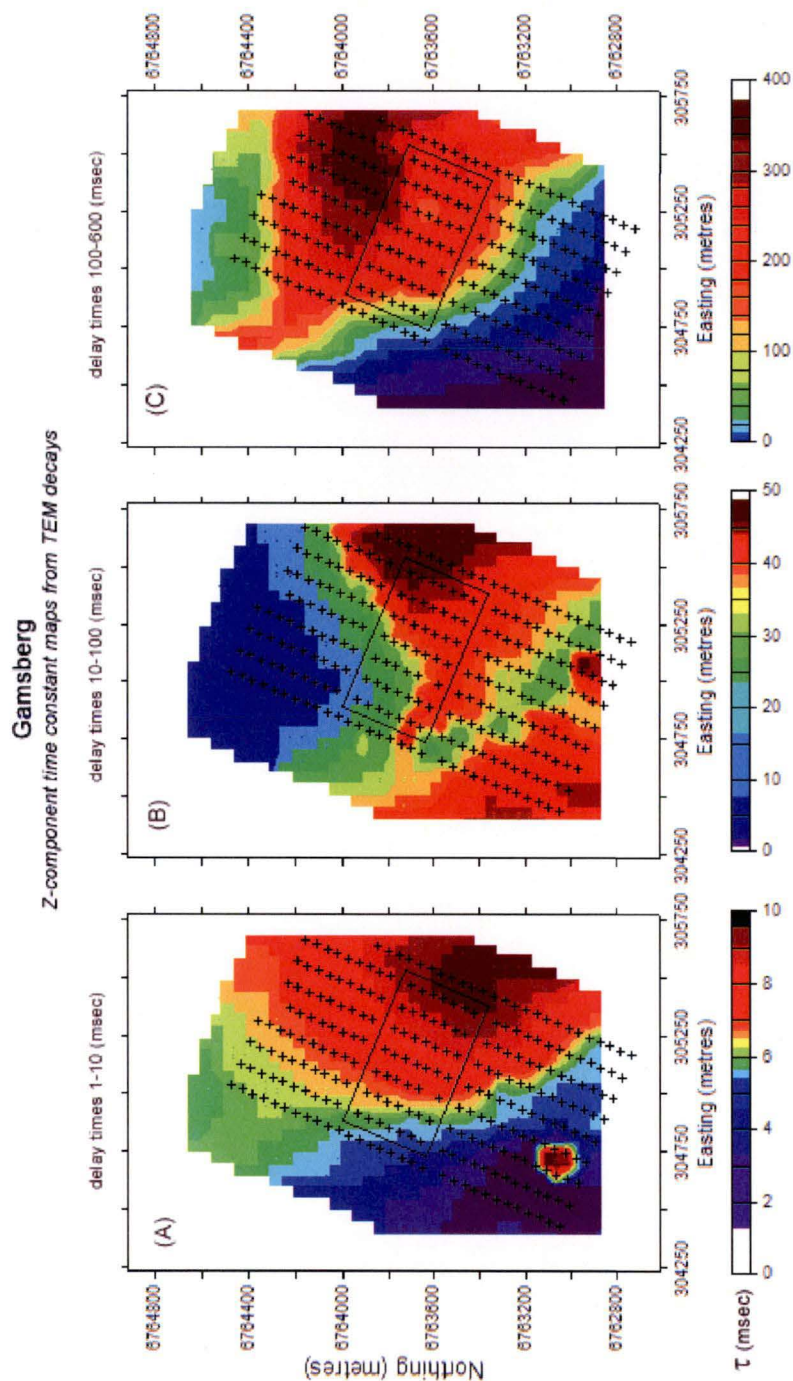


Figure 6.8 – Time constant maps from Gamsberg z-component TEM decays for three different time ranges. In Figure (A), the time constant map is calculated for delay times ~ 1 –10 msec (channels 11–22). Figure (B) shows the time constant map as calculated for delay times ~ 10 –100 msec (channels 22–33). Figure (C) shows the time constants as calculated for delay times ~ 100 –600 msec (channels 33–41).

6.5 Time constant analysis

A time constant (τ) analysis of the z-component decays for three different time ranges is shown in Figure 6.8. Such an analysis enables the isolation of any induced conductive responses progressively deeper or later in time (Terblanche, 2008). The analysis also gives an indication of the range of time constant values which can be expected after 3D inversion of the TEM data. The time constant decay analysis involves computing decay constant values (τ) along three logarithmic decades of the z-channel data from, respectively, delay times ~ 1 -10 msec, ~ 10 -100 msec and ~ 100 -600 msec. The time constants are automatically calculated by fitting an exponential to the decays in the specified time range for all profiles. The fit is accepted if it does not exceed an error of 2 % and if the absolute signal level is greater than 0.1 pTs/A. The time constants are displayed as 2D maps in Figure 6.8. The colour code indicates the value of the time constants. Panel (A) shows the time constant map for the first time range, panel (B) for the second and panel (C) for the third time range.

Panel (A) is dominated by transition from low τ in the west to high in the east where it shows a broad feature of elevated time constants. In the southwest of map (A) an isolated area of high time constants is visible. The isolated area approximately coincides with the zero crossovers for channels < 14 (blue arrows in Figure 6.6). It is interpreted to represent the response of a localised and minor, more shallow conductor. The broad feature of elevated time constants in map (A) represents the response of the large conductor at delay times ~ 1 -10 msec. The perimeter of the broad feature in the southwest of map (A) approximately coincides with the zero crossovers for channels > 14 (green arrows in Figure 6.6). In panel (B) the broad conductive area continues to the northeast. A conductive zone emerges in the southwest of panel (B) which is thought to be artificial, due to the anomaly crossovers at stations in the southwest. The broad feature of elevated time constants further migrates to the northeast in the third panel (C) and is indicative of deeper conductive or late time features in these areas.

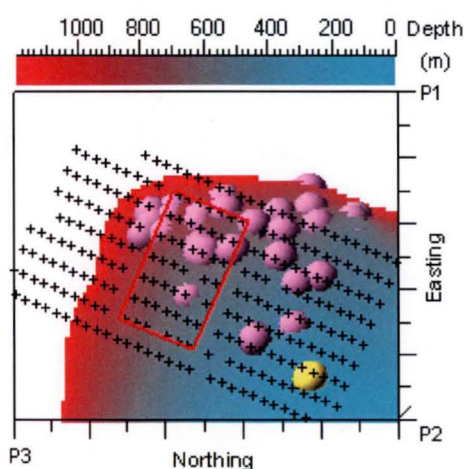


Figure 6.9 – Plan view of geological model with drill markers at increasing depth superimposed.

The migration of the broad conductive zone between map (A) and (C) suggests dip or plunge of the conductive zone to the NNE. Comparison with the geological model shows that the general trends of elevated time constants correlate reasonably well with the occurrence of mineralised drill sections. Figure 6.9 shows the geological model with the drill markers superimposed on the Gams Formation. The colour gradient indicates depth. The shallow drill marker (in yellow) coincides with the isolated conductive feature in panel (A) of the time constant map. Likewise, the drill markers at successively greater depths approximately coincide with position of the migrating conductive zones in panel (B) and (C) respectively.

6.6 Conductivity-depth imaging

CDIs have been calculated (c.f. Chapter 4) from total-field data using the z- and x-component. The CDI sections were used to devise conductivity weights which served as inversion constraints. Furthermore, a 3D conductivity model, interpolated from the CDI sections, served as a starting model for inversion as outlined in section 6.8.2. Apparent conductivity values were also employed for calculating the 'head' and 'tail' contributions of the TEM moment response, as described in Section 6.7.

To avoid the introduction of noise in the calculation of the apparent conductivities, the TEM profiles have been smoothed using a Savitzky-Golay (SG) filter prior to calculating CDI sections. The SG filter is a low-pass filter designed to smooth noisy data and can be thought of as a generalised moving average (Press et al., 2002). The main advantage of Savitzky-Golay filtering over moving average is the tendency to preserve features of the data such as relative maxima and minima. The simple moving average is obtained as the lowest-order version of the SG filter. The filter is applied along the lines so that apparent conductivities vary smoothly at successive stations along individual survey lines. The SG algorithm is based on performing a least squares linear regression fit of a polynomial of degree k over at least $k+1$ data points around each point. The chosen polynomial degree was 3 over 5 data points for the z-component and over 7 data points for the x-component. Figure 6.10 shows an example for three channels along line -400E at early, intermediate and late time.

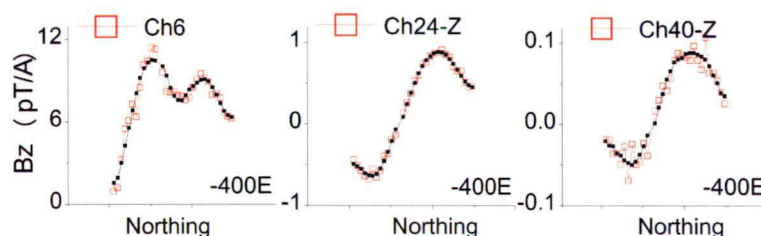


Figure 6.10 – Example of Savitzky-Golay filter for z-component along line -400E at early, intermediate and late time. Open squares mark data points. In black is the smoothed decay which preserves relative maxima and minima. Noise at early and late time is noticeable throughout the entire data set. Intermediate times are mostly clean with low noise levels.

Figure 6.11 (A) shows a conductivity-depth section through the 3D conductivity model interpolated from the CDI sections. A conductive high zone emerges at large depths, with the maximum conductivity at 1840 m. The conductive high coincides with the location of the postulated lower limb of the Gams Formation fold. Figure 6.11 (B) displays a plan at 1840 m, in which high conductivity values are clearly apparent. The mineralised regions in shallower depths as specified by the drill sections do not manifest in the CDIs. Because conductivity-depth-imaging is based on a half space model, it need not resemble the true conductivity structure, and there may be both, shallow and deep mineralisation.

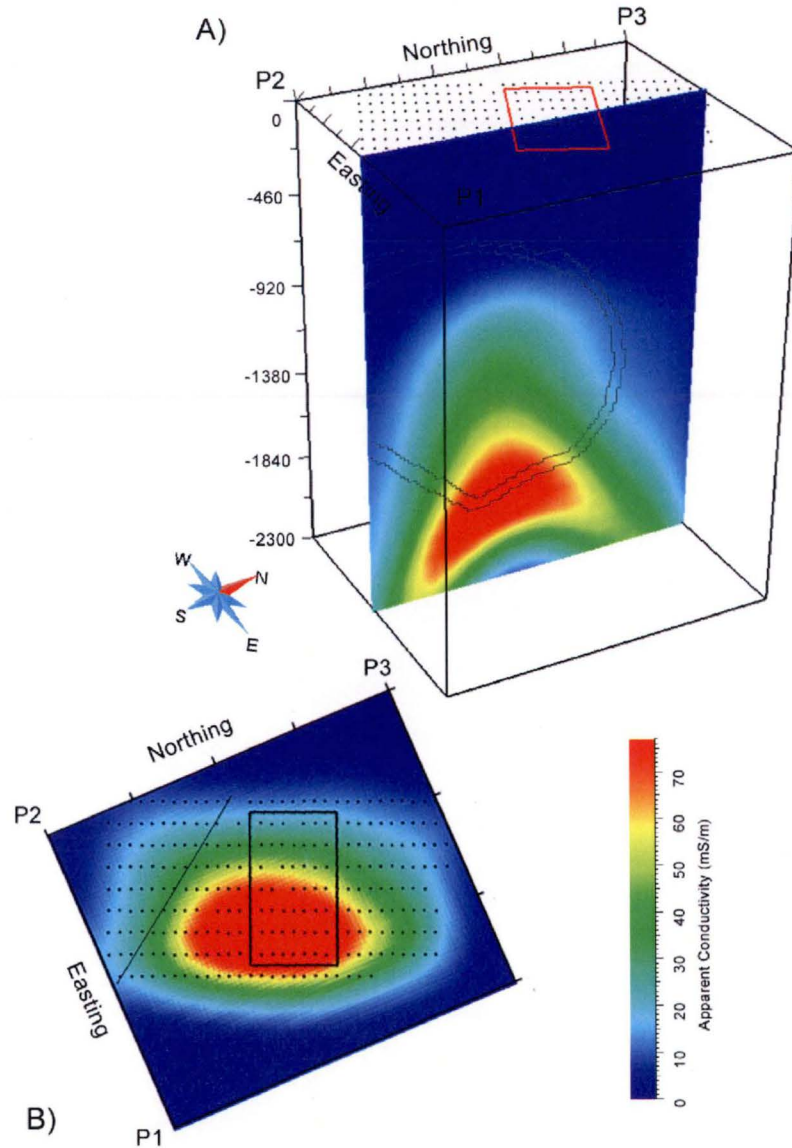


Figure 6.11 – CDIs of the Gamsberg data from total **B**-field amplitudes (based on z and x component only). Figure A) shows a South-North CDI section through the conductivity model; the interpolated intersection of the Gams Formation with this section is superimposed. Figure B) displays a horizontal CDI section at 1840 m where the maximum apparent conductivity occurs. The colour bar applies for both figures; the maximum value of apparent conductivity is ~ 100 mS/m. The zero-crossovers in the B_z -profiles suggest termination of a subsurface conductor; crossover positions are indicated by the oblique solid line in Figure B).

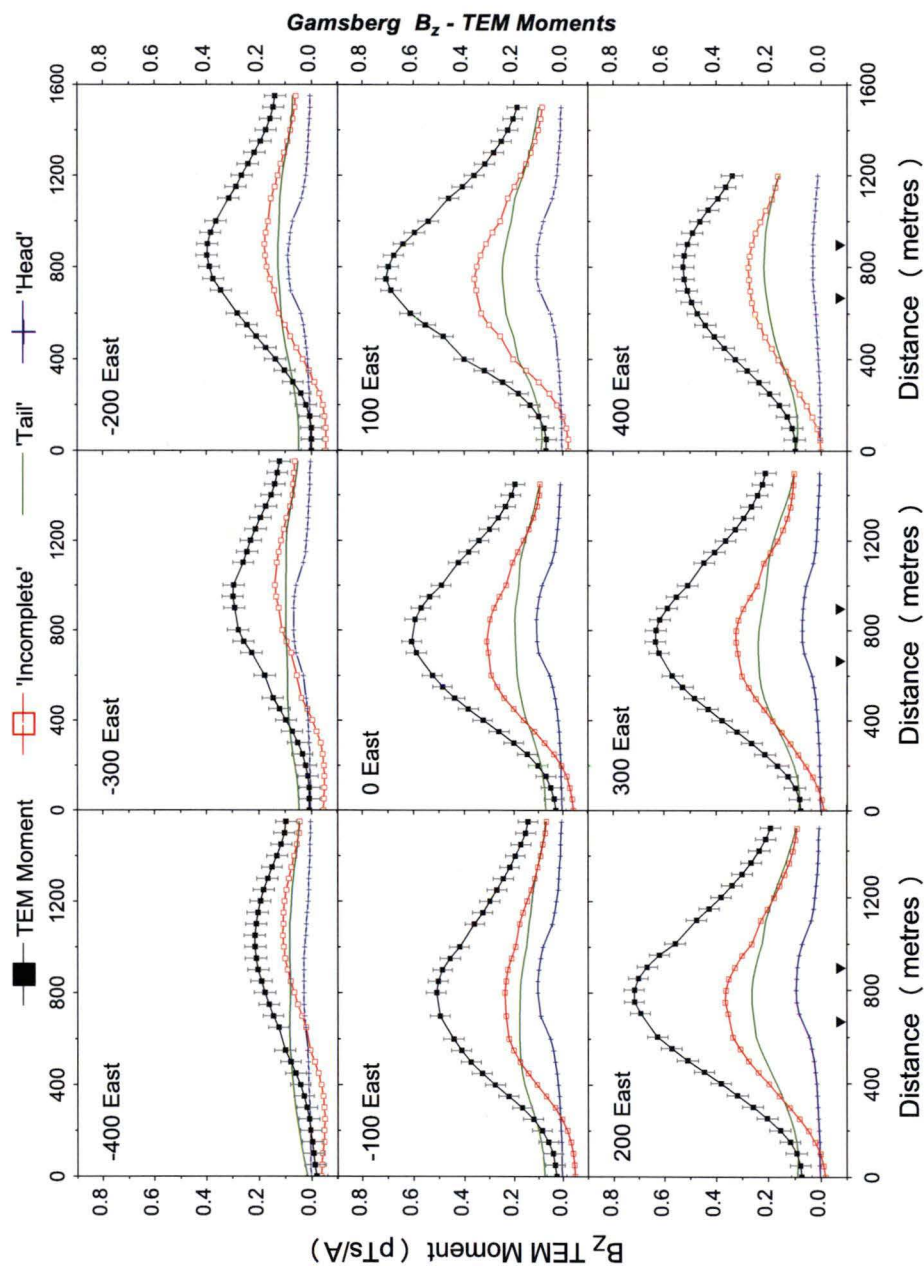


Figure 6.12 – 1st order TEM moments from B_z -decays at Gamsberg-East (solid squares). The transmitter position is indicated by the triangles on the bottom axes. The TEM moment is the sum of the incomplete TEM moment with the 'head' and 'tail' contribution. 'Head' and 'tail' are based on total-field apparent conductivities. Error bars specify the assumed data uncertainty of 0.04 pTs/A. Each receiver station is associated with a TEM moment response, giving a total of 259 TEM moments comprising the observed data vector.

6.7 Transformation of field data to TEM moments

Chapter 2 (Section 2.8) described the calculation of 'complete' TEM moments from measured field data. The complete TEM moment is the sum of the 'incomplete' TEM moment, which is defined as the TEM moment transform over the observed time range, and the 'head' and 'tail' contributions. 'Head' and 'tail' are calculated by extrapolating the magnetic field data at early and late times using estimated apparent conductivities. The extrapolated magnetic field data for 'head' and 'tail' are calculated from total-field apparent conductivities, σ_1 and σ_N , associated with the data, measured at the first and last channels, respectively. Inversion of the Gamsberg TEM moments was restricted to the vertical component only. The 1st order TEM moment for measured Bz-data, $\tilde{B}(t)$, is calculated according to Equation (2.112) :

$$M^{(1)} = \int_{t_1}^{t_N} \tilde{B}(t) dt + \int_0^{t_1} \underset{\text{'head'}}{B_{\sigma_1}(t)} dt + \int_{t_N}^{\infty} \underset{\text{'tail'}}{B_{\sigma_N}(t)} dt$$

where B_{σ_1} and B_{σ_N} are early and late time extrapolated magnetic field data at each receiver station. For transformation to the moment domain, the first three channels and the last channel have been omitted to avoid contamination of the TEM moments due to noise. Therefore, the effective measured time range is 0.195–572.15 msec. The data at station (305008E, 6763128N) of line 100E have been discarded.

As discussed earlier, the TEM decays have been smoothed along the survey lines so that apparent conductivities vary smoothly from station to station, which is critical to avoid the introduction of noise in the TEM moments when calculating 'head' and 'tail' contributions. The late time noise in the TEM decays varies from line to line but is on average about 5% in the latest channels of measured Bz. Late time noise is accentuated when transforming the TEM decays to TEM moments, therefore the first integral for $\tilde{B}(t)$ is evaluated using the smoothed TEM data (c.f. Chapter 2.8). The integrals for 'head' and 'tail' use the apparent conductivities from the smoothed TEM decays and are solved by applying the analytical formulae derived in Chapter 2, Equations (2.84) and (2.89).

Figure 6.12 displays the Gamsberg-East TEM moment profiles. The figure shows the complete TEM moments, together with the incomplete TEM moments and 'head' and 'tail' on the same vertical scale. Apparent conductivities are high at great depths, so that the tail contribution is substantial, however the shape of the complete TEM moment curves essentially conforms to the shape of the incomplete moment curves but with larger amplitudes. Negative values as seen in the incomplete moments, are not reflected in the 'head' moments because the extrapolation employs total-field apparent conductivities. The data uncertainty is set to a standard deviation of 0.04 pTs/A, which is about 5% of the maximum TEM moment amplitude.

6.8 Inversion of Gamsberg TEM moments

VPem3D inversion of the Gamsberg-East TEM moments produces a 3D distribution of time constants. VPem3D inversion was described in Chapter 5. Each receiver station is associated with a TEM moment response, giving a total of 259 TEM moments comprising the observed data vector. The inversion parameter vector is composed of the cell-time constants. For all inversion runs, the model Voxet is comprised of heterogeneous units with many more model parameters than observations, hence an under-determined inverse problem was solved. Inversion solutions are deemed successful if the χ^2 -misfit of the modelled TEM moments are less or equal unity. The plausibility of the inversion results was evaluated by comparing the information from drill hole intersections with the recovered conductivity structures. In addition, conventional trial-and-error forward modelling employing a plate-model was carried out and compared with the location of the recovered time constant models.

The host (Nousees Gneiss and Pella Quartzite) conductivity was held fixed at 1 mS/m during inversion. The value for the host conductivity was chosen according to apparent conductivity values at depths > 500 m, well above the conductive zone, as seen in Figure 6.11. The apparent conductivity values at the northern end of the survey line averages at ~ 1 –2 mS/m for depths of 400–500 m. The value of 1 mS/m is also reflected in the downhole resistivity logs at Gamsberg West, which intersected quartzites and schists.

3D inversion is carried out with different starting models and constraints. Depending on the starting models and constraints used, the recovered time constant models may exhibit significant differences due to the non-unique nature of the TEM moments inversion. Variability of the inversion solutions is examined by proceeding the inversion with different starting models as described in Chapter 5. Confidence in the results is gained if different starting models arrive at the same solution. All examples were computed on a Pentium 4 2.8 GHz processor from 2006. VPem3D inversion of the Gamsberg TEM moments was executed in different fashions, based on four different starting models as follows (c.f. Chapter 5):

1. **Unconstrained-starting model:**

The starting model was initialised with zero time constants in every cell. No constraints were employed during inversion; so that time constants were allowed to also have negative values. During unconstrained 3D inversion all cells were involved. The unconstrained inversion has the most degrees of freedom and is expected to fit the data very well. Solutions of the unconstrained inversion do not reflect the true subsurface conductivity structure. However, unconstrained inversion illustrates the effectiveness of the inversion algorithm and the importance of geological constraints.

2. **CDI-starting model.**

In order to neutralise the impact of the strong transmitter footprint at shallow depths, the CDI-starting model was categorised into two units: an inactive surficial layer and an active unit which encompasses the remainder of the model Voxet. Only the cells in the active unit took part in the inversion. The active unit was set up with a positivity bound for the time constants. No weighting scheme was applied. The starting model was

initialised with time constants, calculated from the conductivity-depth values (c.f. Chapter 5 1.3). The inversion was performed twice: first as a 'default' property inversion, where all cells of the active unit are retained during inversion, regardless whether they hit their bound. Second, the inversion was repeated with the option of 'bound cancelation'. Bound cancelation effectively imposes a dynamic constraint where cells are 'deactivated' during inversion if their time constant attains a bound which as described in Section 6.8.2. The CDI-starting model favours solutions exhibiting resemblance to the conductivity structure of the CDI sections.

3. Zero-starting model:

The starting model was initialised with zero time constants in every cell. A positivity condition was applied to the time constants. The inversion was performed twice: first including conductivity weights and second with depth weights. The zero-starting model in conjunction with conductivity weights is closely related to the CDI-starting model. The zero-starting model may be employed when there is only little knowledge of the exploration target, as for example in greenfields exploration.

4. Geological model:

The starting model was initialised with zero time constants in every cell, but changes were constrained to the Gams Formation unit. Only cells in the mineralised Gams Formation unit are involved, effectively imposing a strong geological constraint on the model solution. Model solutions are restricted by the volume of the Gams Formation unit. A positivity condition to the time constants was imposed.

6.8.1 Unconstrained inversion

Unconstrained 3D inversion exemplifies the impact of non-uniqueness and the influence of inversion constraints. The starting model is initialised with zero cell time constants. The entire model is active so that all cells are involved during inversion. The time constants are not bounded and are allowed to have negative values. The unconstrained inversion produces a mathematically valid solution which however may not be geologically acceptable as demonstrated on the synthetic example of the horizontal slab in Chapter 5.

The TEM moment profiles are shown in Figure 6.13. The recovered time constant model after inversion reproduces the Gamsberg TEM moments and achieves a fit of better than the data uncertainty of 0.04 pTs/A in a χ^2 -sense. Figure 6.14 shows the time constant model after inversion. Elevated values of recovered time constants are clustered at shallow depth around the loop perimeter and along the receiver stations. The time constants are mostly positive inside the transmitter loop whereas outside the loop, facing the long wires, the time constants are mostly negative. The time constant polarity reflects the orientation of the primary field of the transmitter and inside and outside the loop (c.f. Chapter 5.3.1).

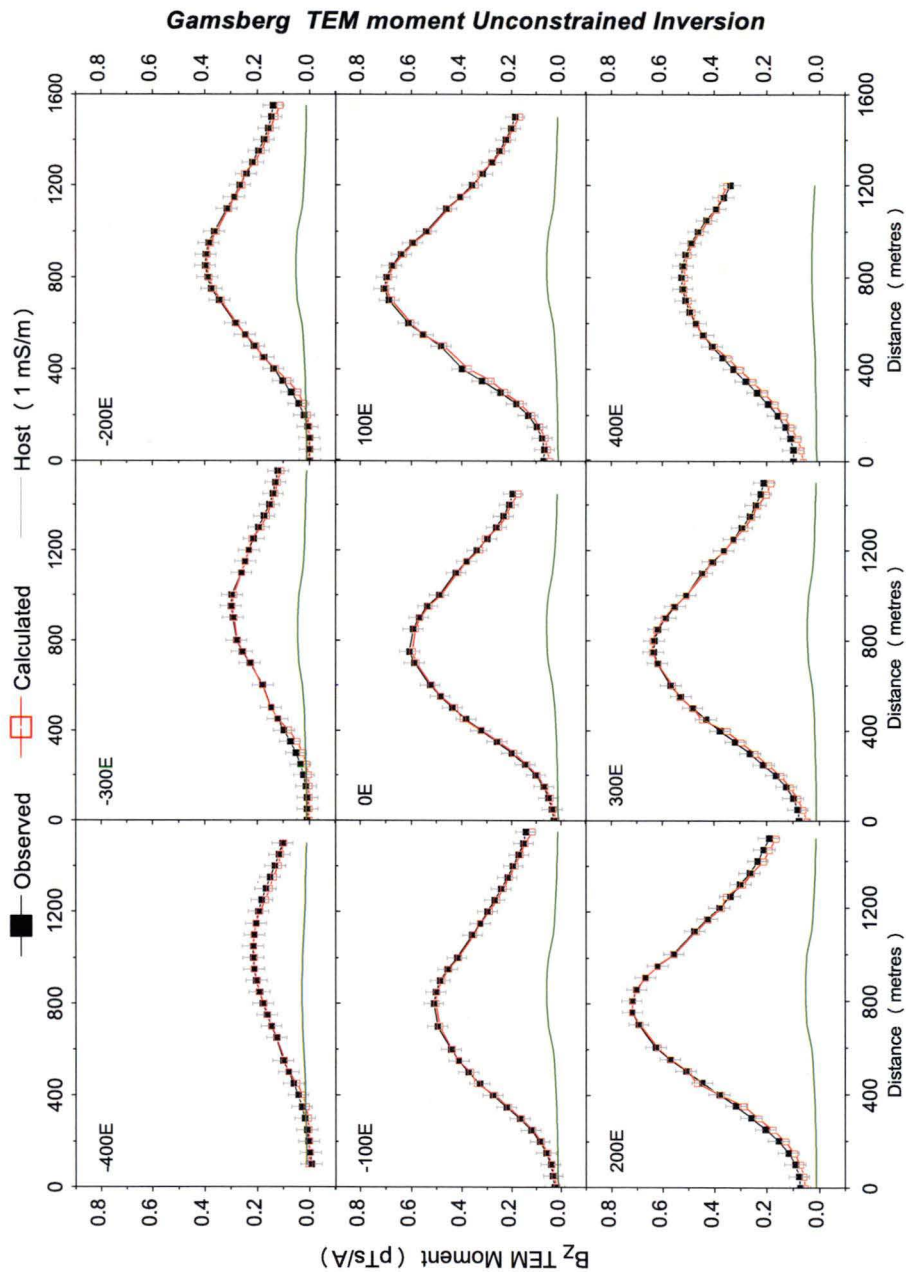


Figure 6.13 – TEM moments from recovered time constant model based on the unconstrained inversion. Solid squares mark the observed Gamsberg TEM moments. Open squares mark the calculated TEM moment response of the recovered time constant model. Inversion succeeded after 254 iterations and the calculated TEM moment response fits the data very well. Runtime was 44 minutes on a Pentium 4 2.8-GHz processor from 2006.

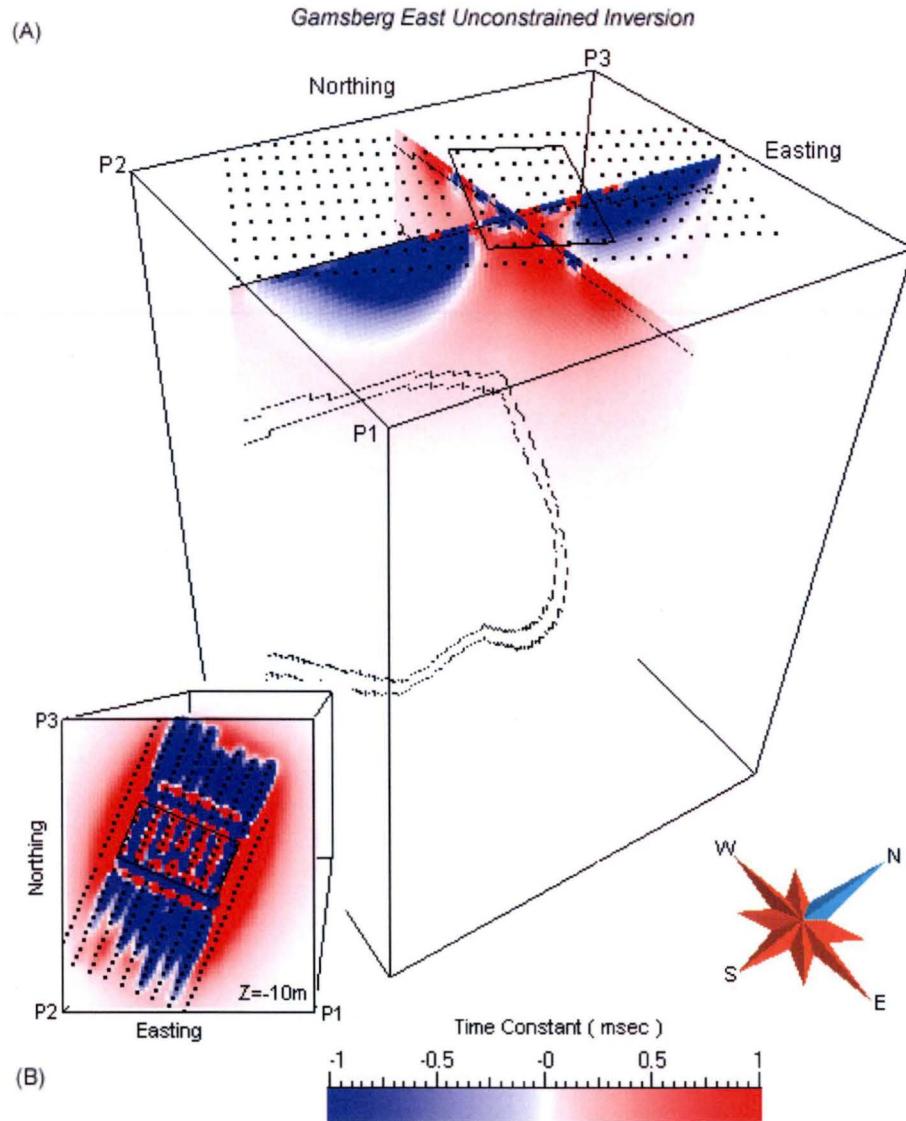


Figure 6.14 – Recovered time constant model after unconstrained inversion of the Gamsberg-East TEM data. The starting model was initialised with zero cell time constants. Panel (A) shows a north-south and east-west cross-section through the centre of the inverted model. The inset (B) displays a horizontal section at 10 m depth. The recovered cell time constants are clustered at the surface around the loop perimeter and immediately below the receivers. The polarity in time constants reflects the orientation of the primary field. The TEM moment model-response curves fit the measured TEM data to an accuracy of better than 0.04 pTs/A.

6.8.2 Inversion with CDI starting model

The cell time constants of the CDI starting model were initialised with values from the Gamsberg CDIs by re-scaling (re-scale factor was 7.5) the cell conductivities so as to fit the observed TEM moment response as close as possible (c.f. Chapter 5.1.3). Inversion based on CDI starting models tend to favour solutions which resemble the conductivity structure from the CDIs. Therefore, no depth weights are applied, which avoids overly stringent inversion conditions. Because the CDIs suggest possible conductive mineralisation at great depths, 3D inversion with a CDI starting model explores the possibility of deep conductive features.

The CDI starting model is comprised of an 'inert' surficial layer, designed to reduce the impact of high sensitivity in the vicinity of the transmitter. The active unit is defined as the remainder of the model. The layer thickness of 200 m was inferred from the supplied geological information since drill logs confirm mineralisation at depths greater than 200 m. The active unit consists of 674,584 cells and time constants are set up with a positivity bound.

'Default' property inversion, where all cells of the active unit are retained during inversion, regardless whether they hit their bound, did not succeed: for the specified uncertainty of 0.04 pTs/A, the inversion stalled after 32 iterations with a χ^2 -misfit of 3.2. The χ^2 -misfit of the starting-model was 5.5. Runtime was 26 min. Inversion failed due to the polarity of the primary field and the resulting attempts by the inversion to assign negative time constant values for a range of cells at shallow depth (c.f. Unconstrained Inversion). However, because the time constants are constrained by a lower bound of zero, the inversion cannot find a suitable distribution of time constants so as to fit the data. The recovered time constant model exhibits distinct resemblance to the CDI-starting model (Figure 6.15). The magnitude of the recovered time-constant values are of the same order as depicted in the time constant map of Figure 6.8 (C), which is based on time decays between channels 33–41.

In order to compensate for the effect of the primary field, the inversion was repeated employing a 'bound cancelation' directive which cancels any cell which hits its lower zero-bound during inversion. Bound cancelation can therefore reduce the number of active cells during inversion. The modality of the inversion changes when deploying the bound-cancelation option. Figure 6.16 (A) shows an eastwest cross-section through the model, straddling the Gams Formation. A region of elevated time constants emerges near, but above, the locations of the drill markers. Because cells are turned off when reaching their lower bound, a sharp contrast in time constants is observed in the eastern part of the model at 525 m depth. The conductive region at great depth (~ 1800 m) is interpreted as a residue of the CDI-starting model: due to non-uniqueness a valid solution was found without further adjustment of time constants at great depths. The Gams Formation as viewed from the southwest is displayed in Figure 6.16 (B). An isolated region of high time constant values is noticeable at ~ 320 m depth which approximately co-locates with the isolated region in the time constant map of Figure 6.8 (A).

During inversion with bound cancelation, the number of active cells decreased from 674,584 to 521,966 cells after inversion. The inversion with bound cancelation was successful after 24 iterations and the TEM moment response of the recovered model matched the data to an accuracy of better than 0.04 pTs/A. Runtime was 24 min. The TEM moments profiles for the recovered time constant models for both methods are shown in Figure 6.17.

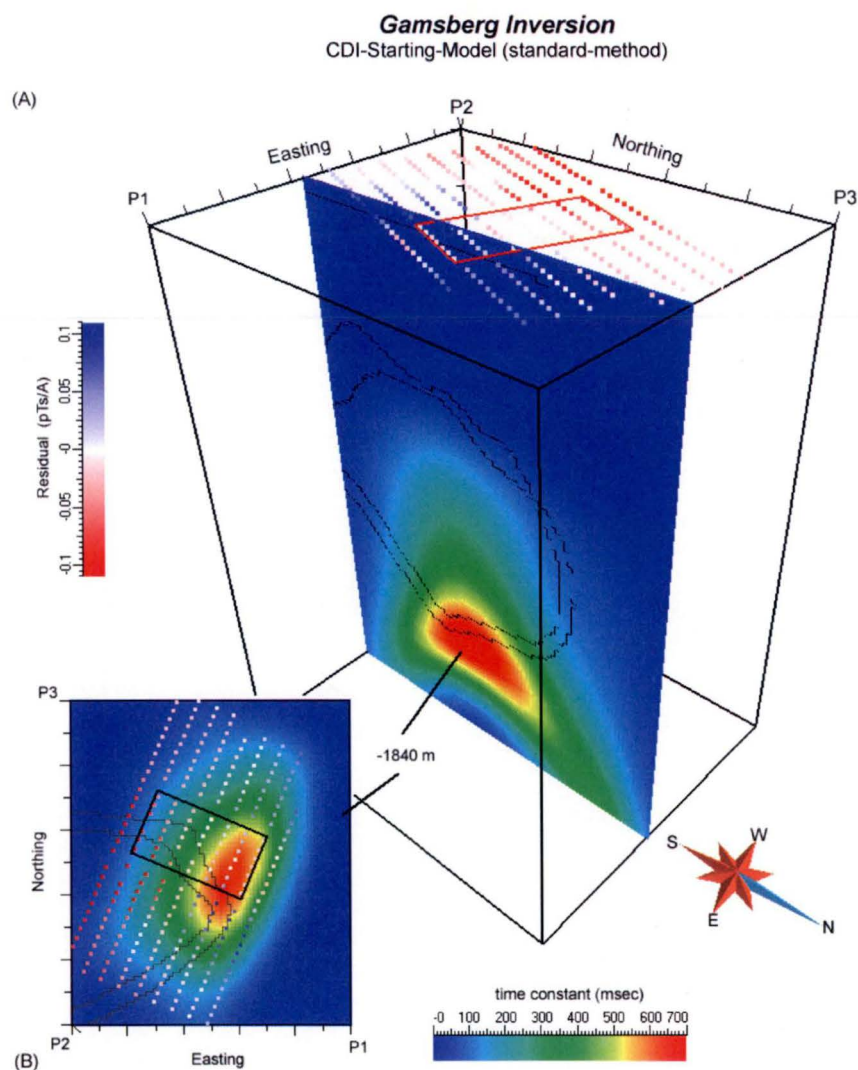


Figure 6.15 – Recovered time constant model after standard inversion based on a CDI-starting model. With the specified uncertainty of 0.04 pTs/A, the inversion did not achieve the desired χ^2 -misfit and stalled after 32 iterations. The recovered time constant model exhibits distinct resemblance to the CDI-starting model. A cross-section through the voxel in Figure (A) shows a conductive region at large depth of about 1840 m which straddles the Gams Formation unit which is superimposed. Inset (B) shows the region in plan view at 1840 m. The receiver stations are displayed as colour-coded residuals.

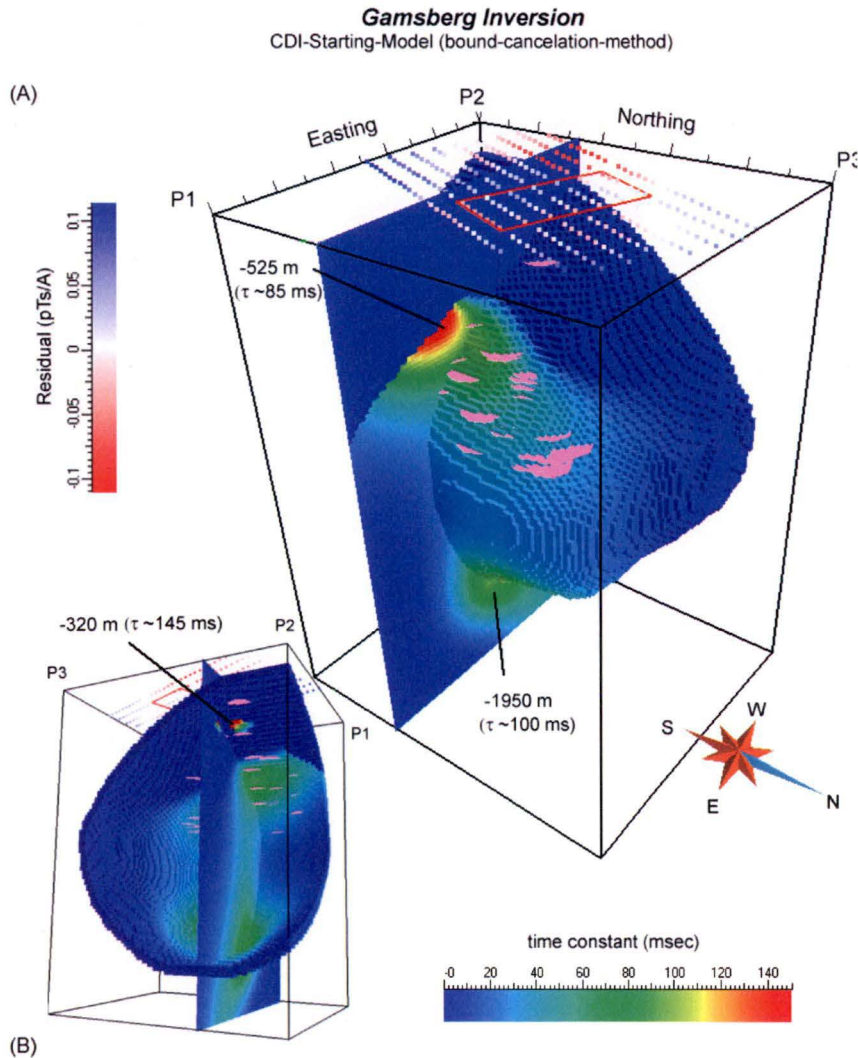


Figure 6.16 – Recovered time constant model after inversion with bound-cancellation, based on a CDI-starting model. With the specified uncertainty of 0.04 pTs/A, an acceptable fit was achieved after 24 iterations. Figure (A) shows an eastwest cross-section. Two regions of elevated time constants are seen at 525 m and at 1950 m depth. Inset (B) shows an isolated region of high time constant values in the neighbourhood of various drill markers. The receiver stations are displayed as colour-coded TEM moment residuals.

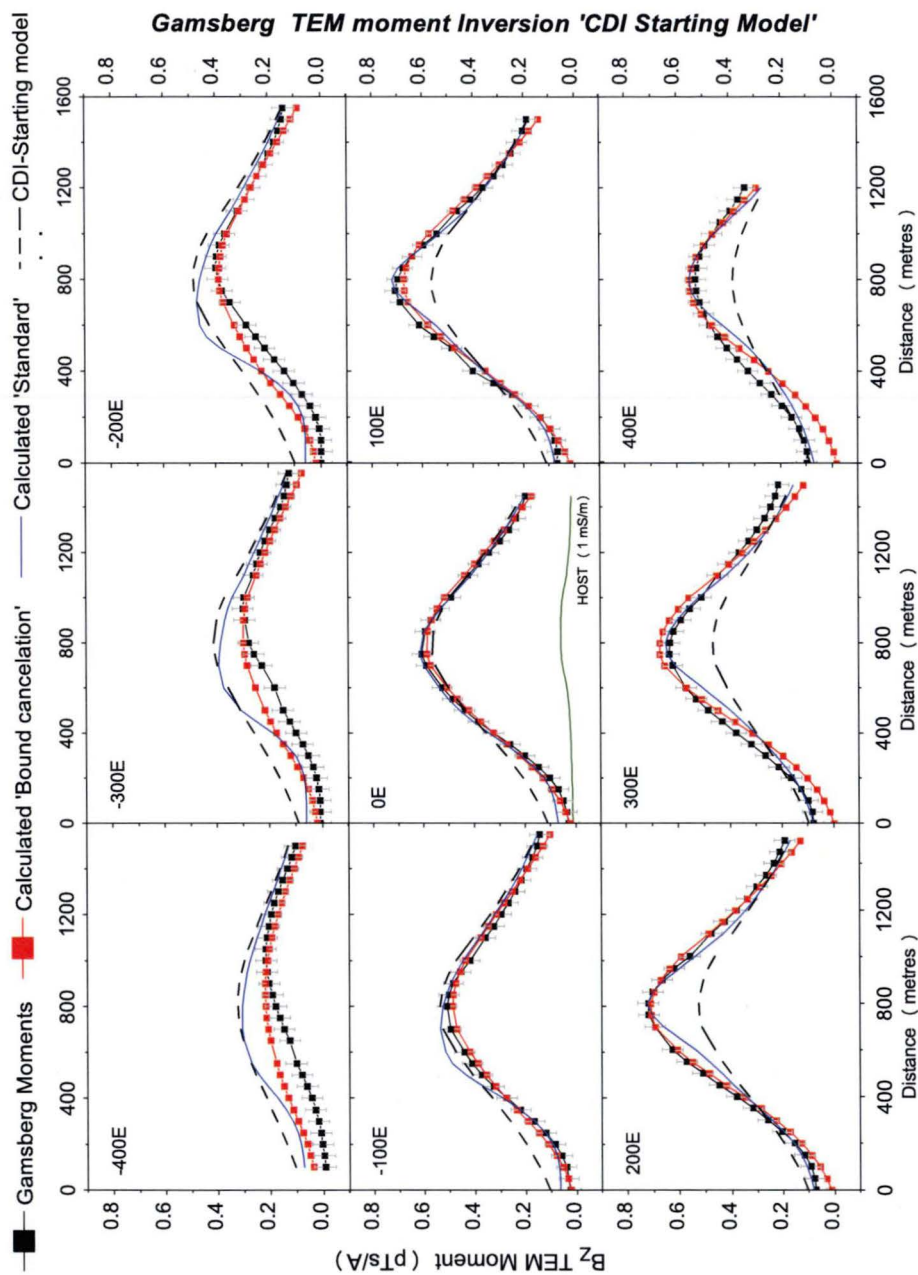


Figure 6.17 – TEM moment profiles for recovered time constant model after inversion based on a CDI-starting model. TEM moment responses are shown for the standard inversion method and for the 'bound cancelation' method. For reference, the background response is shown for the centre-line 0E, which is calculated as a 1mS/m half space response. The TEM moment response from the starting model is shown dashed. Only the TEM moment response from the bound-cancelation method gives a fit better than 0.04 pTs/A. The fit deteriorates along the southwestern edge of the model.

6.8.3 Inversion with Zero starting model

Unlike inversion based on the CDI starting model, which is biased according to CDI values, evolution of cell time constants during inversion for zero starting models is steered only by the model sensitivities and the supplied constraints, so that inversion with the zero starting model may further elucidate the Gamsberg-East mineralisation. The starting model was initialised with zero time constants in every cell. A positivity condition was applied to the time constants.

Inversion is first carried out with (3D) conductivity weights which were calculated from CDIs as described in Chapter 5.2.6. Conductivity weights penalise solutions deviating from the CDIs resulting in an output that incorporates some of the aspects of the CDI starting model. Parameter changes are favoured for cells associated with weights near unity which coincide with the location of the conductive high in the CDIs. Offside the conductive highs, the conductivity weights approach zero. Zero weights occur where the CDI values depict the background conductivity of 1 mS/m or smaller. The inversion with conductivity weights was ineffective, because cells associated with a zero weight were effectively turned off so that changes at shallow depths were prohibited. The inversion stalled after 43 iterations with a χ^2 -misfit of 3.7. Initial misfit was $\chi^2 \simeq 62$.

The inversion was repeated with less restrictive (1D) depth weights which recovers smoothly varying time constants with depth. The depth-weights were calculated via Equation 5.33 with a slope factor of $s_0 = 10^{-4}$, which produces slowly decaying weights, and a depth factor of $d_0 = 200$, which excludes changes in a surficial layer to neutralise the effect of the transmitter. The slowly decaying depth weights promote (but are not restricted to) solutions at a depth of ~ 1840 m where the conductive high in the CDIs emerges. Figure 6.18(A) shows a northsouth section through a highly conductive region of the recovered time constant model between ~ 500 m—800 m. The maximum time constant, ~ 60 ms, of the recovered model occurs at a depth of about 620 m. Due to the finite resolution of the method, the conductive region straddles the Gams Formation unit and the conductive zone extends in all three units of the geological model. The conductive structure broadly coincides with the localities of the mineralised intersections of the Gams Formation. The drill intercepts therefore corroborate the inversion result. The inset, Figure 6.18(B), displays the 'back' of the recovered time constant model as viewed from the southwest. In addition to the broad region of elevated time constants, an isolated localised region of elevated time constants is noticeable at a depth of ~ 280 m near several drill markers. Figure 6.19 shows the recovered time constant distribution as a 3D iso-surface of time constants > 40 msec which illustrates the gross 3D structure of the recovered time constants. The lateral position of the isolated region, as well as the broad conductive region correlates reasonably with features in the time constant maps, Figure 6.8 (A) and (B), respectively. The magnitudes of the recovered time constants of the inverted zero-model broadly agree with the time constant values as calculated from the TEM decays (Figure 6.8B).

With the specified uncertainty of 0.04 pTs/A, the inversion of the zero-model succeeded after 107 iterations and the final model is acceptable with $\chi^2 \leq 1$; runtime was 32 min. The TEM moment profiles of the recovered time constant model are shown in Figure 6.20. The fit of the lines traversing the loop is better than for lines outside the loop

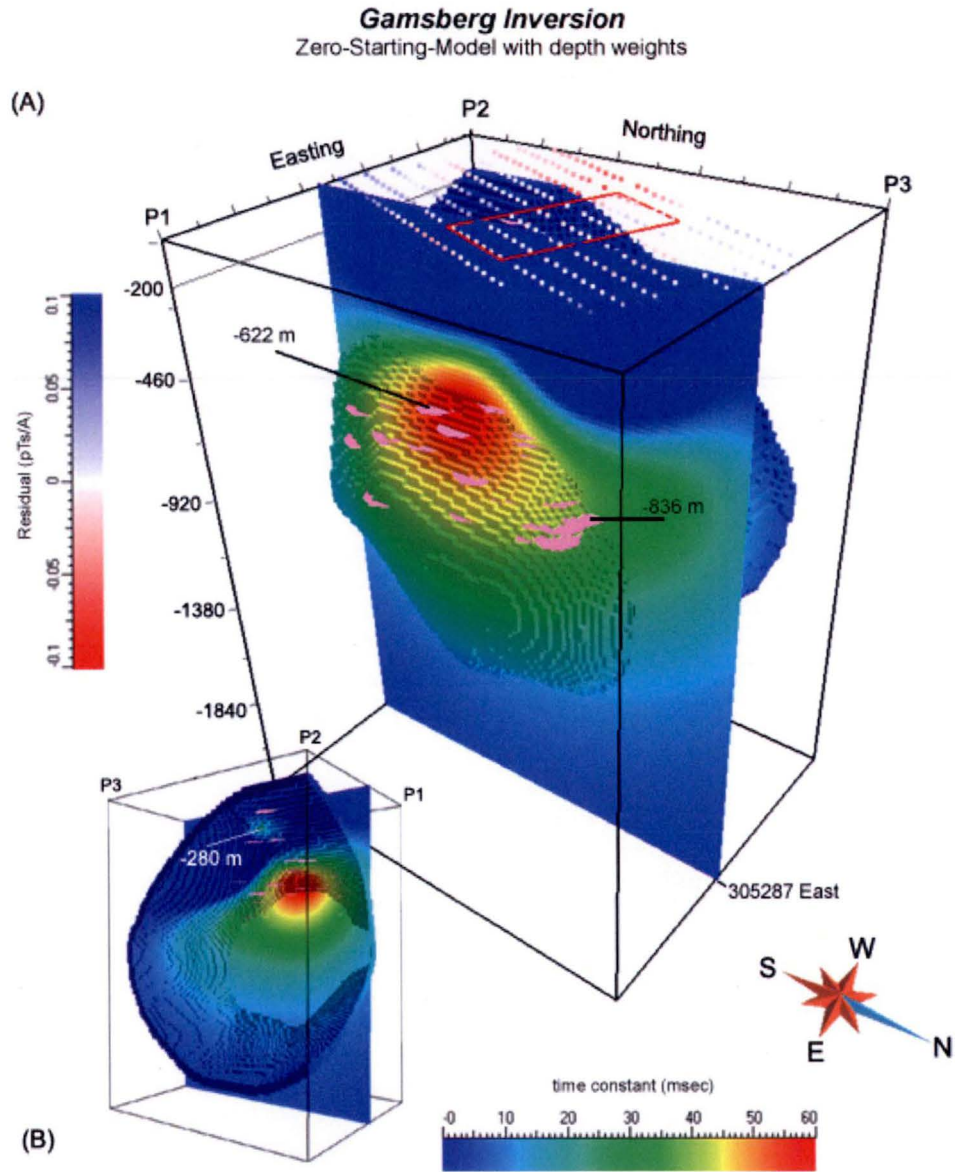


Figure 6.18 – 3D view of the recovered time constant model after inversion of the Gamsberg-East TEM data using a zero starting model, conditioned with depth weights. Panel (A) shows a north-south-section through the region of elevated time constants. The receiver locations are colour-coded according to the residual of the TEM moment after inversion. The recovered conductive region broadly coincides with the locations of the drill markers indicating mineralised Gams Formation. The inset (B) displays the same section as viewed from the southwest. An isolated region with time constants ~ 20 msec can be seen near 280 m depth. The maximum time constant, ~ 60 ms, of the recovered model occurs at a depth of about 620 m.

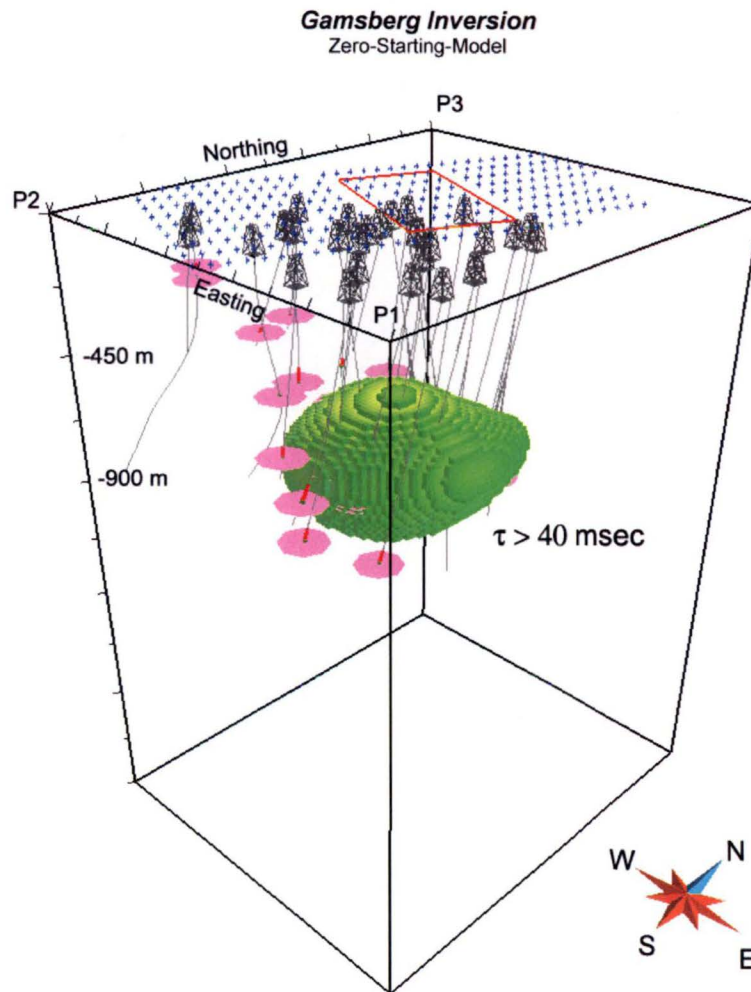


Figure 6.19 – 40 msec iso-surface of recovered time constant model after inversion of the Gamsberg-East TEM data using a zero starting model, as viewed from the southeast. (c.f. Figure 6.18). The isometric volume illustrates the gross 3D structure of the recovered time constants. The number of cells within the iso-surface is 15,929. The 3D iso-surface lies between 450 and 900 m depth. Drill collars and trajectories are shown with markers at the bottom of the Gams Formation.

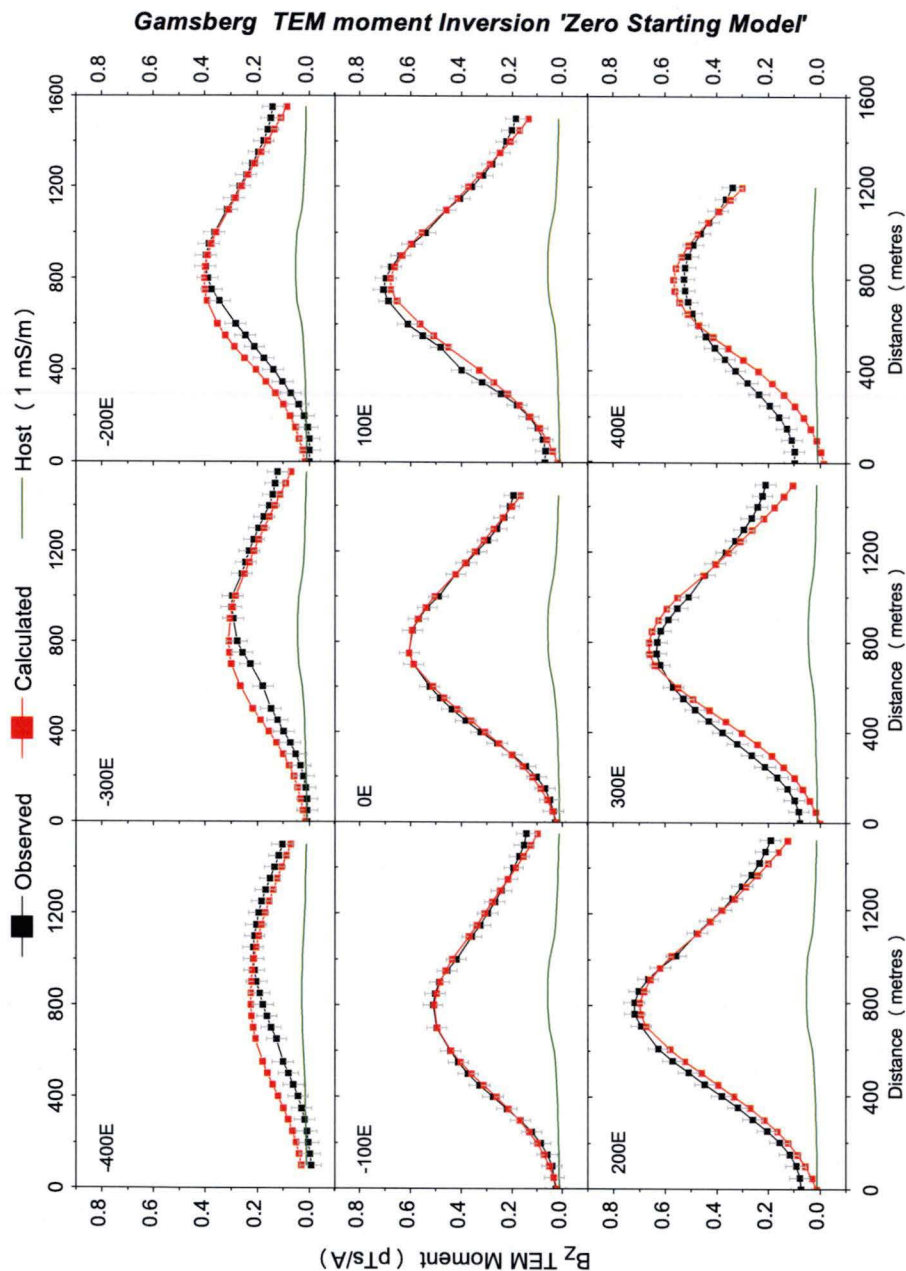


Figure 6.20 – TEM moment profiles for the recovered time constant model using a zero starting model conditioned with depth weights. The 'Observed' response denotes the TEM moments derived from Gamsberg-East field data. 'Calculated' denotes the TEM moment response of the recovered time constant model. The calculated TEM moments, fit the the Gamsberg-East data to better than 0.04 pTs/A in a χ^2 -sense. The fit deteriorates at stations in the southwest-corner, near the model boundaries.

6.8.4 Geologically constrained inversion

Geologically constrained inversion takes advantage of the pre-existing knowledge of Gamsberg-East, mainly in form of bore hole information, which were used to construct the geological model. In this case only cells which fall within the Gams Formation are inferred to contain significant mineralisation and were allowed to change their time constants, so that the solution provides combined geologic and physical property value information for the volume of interest. The time constants of the Gams Formation unit were initialised with zero time constants and a lower bound of zero was enforced. Standard property inversion was acceptable with $\chi^2 \leq 1$ after 164 iterations; χ^2 -misfit of the starting model was ~ 62 (data uncertainty 0.04 pTs/A). The inversion of 33,886 model parameters took less than three minutes on a Pentium4 2.8 GHz processor. Because all cells were retained during inversion, regardless whether they hit their bound, the number of iterations was relatively high. When invoking the 'bound cancelation' directive, the inversion succeeded after 96 iterations due to the deactivation of cells during inversion.

The recovered time constant distribution of the Gams Formation is depicted in the histograms of Figure 6.21. About 42% of all time constants in the Gams Formation are between 0 and ~ 40 msec and 0.1% of time constants lie in between ~ 1000 – 2000 msec. The location of the high time constant values are indicated in Figure 6.22.

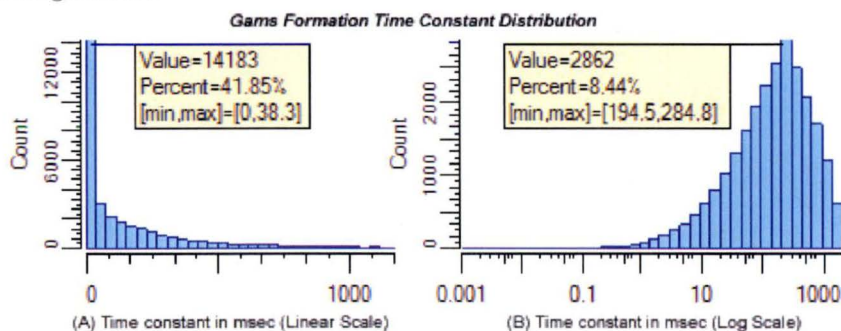


Figure 6.21 – Recovered time constant distribution of the Gams Formation unit on a linear (A) and logarithmic scale (B).

The inverted model for the 'standard' property inversion method is depicted in Figure 6.22. In comparison with the inversion result based on the zero-starting model, the cell time constants are substantially higher. In the zero-starting model case, elevated τ values are disseminated through a large volume of the model, extending across all three units of the geological model. In the geologically constrained case, τ values are confined to the Gams Formation, so the time constants are necessarily higher so as to reproduce the TEM moment response. Figure 6.22 shows a broad conductive region, generally coinciding with the drill markers. As was the case for the zero-starting model, an isolated, localised area of conductive cells is apparent near the southwest corner of the Voxet, which is also visible in the time constant map of Figure 6.8(A). The area is highlighted in the inset of Figure 6.22. Figure 6.23 shows the recovered time constant model as eastwest and northsouth sections and illustrates the imposed sharp contrast with the host-rock (Nousees Gneiss and Pella Quartzite).

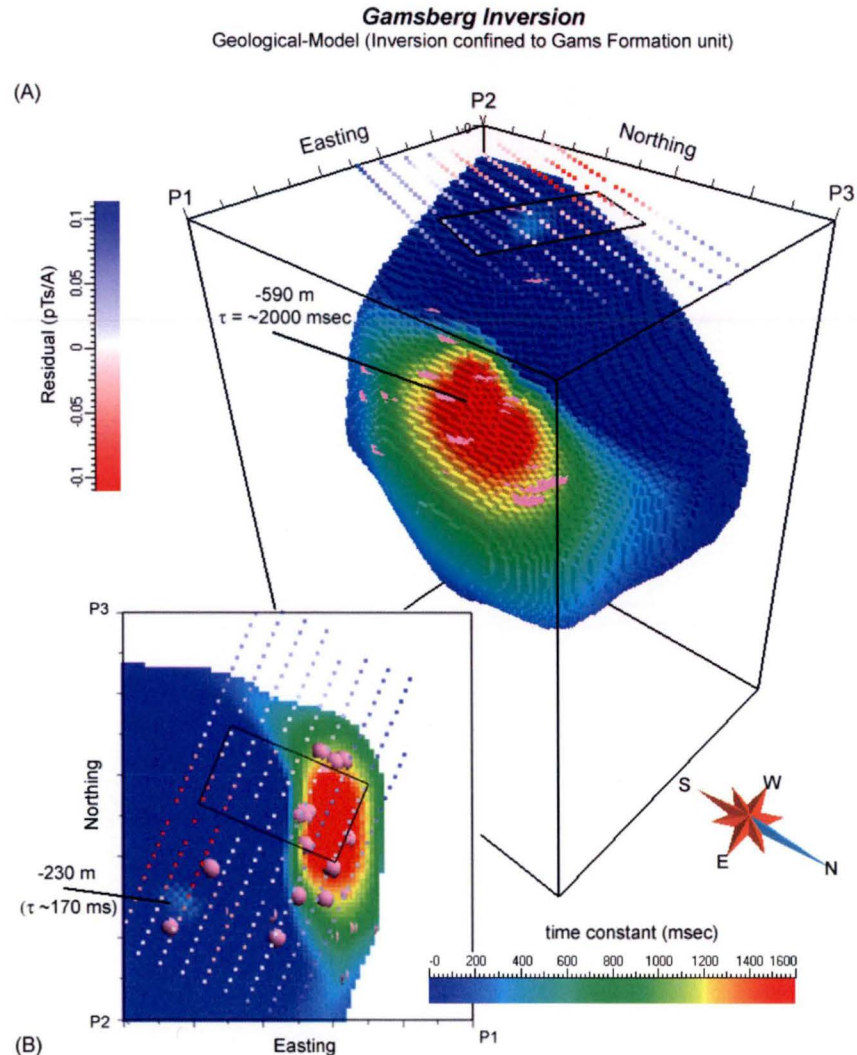


Figure 6.22 – 3D view of the recovered time constant model after geologically-constrained inversion. The figure illustrates the spatial distribution of cell time constants after inversion restricted to the Gams Formation. The receiver locations are colour-coded according to the residual of the TEM moment after inversion. The inset (B) highlights an isolated area of conductive cells near drill markers at 230 m depth. In order to emphasise the highly conductive region, the colour bar maximum value is 1600 msec, the maximum inverted time constant is ~ 2000 msec.

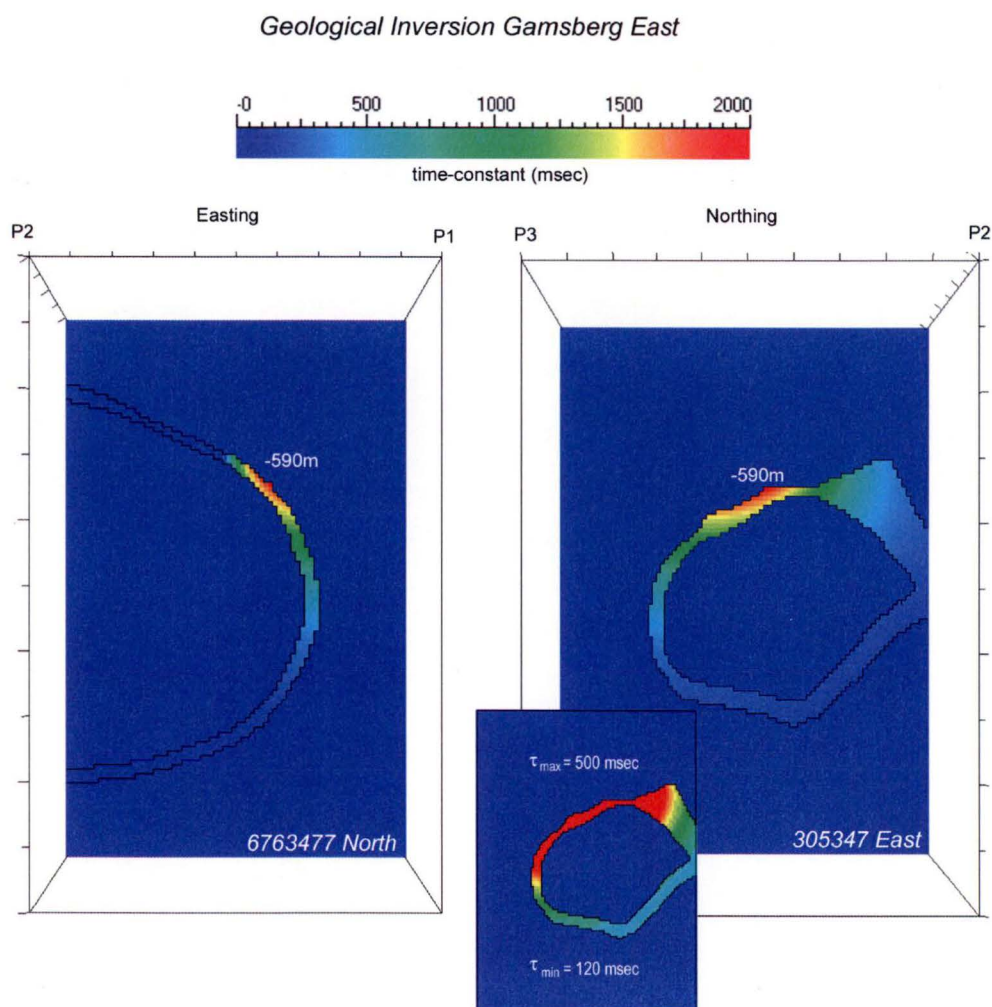


Figure 6.23 – Eastwest section (left) and northsouth section (right) of recovered time constant model after inversion of geological constrained model for Gamsberg-East. Highest recovered time constant of ~ 2000 msec is at ~ 590 m depth. Geological constraints ensure that the recovered time constant of the potentially mineralised Gams Formation is in sharp contrast with the host-rock (Nousees Gneiss and Pella Quartzite). The inferred boundary of the Gams Formation unit is superimposed. The inset on the right shows the northsouth section for a different colour scale with a maximum time constant of 500 msec in order to emphasize mineralisation at great depths where time constants in excess of 120 msec are observed.

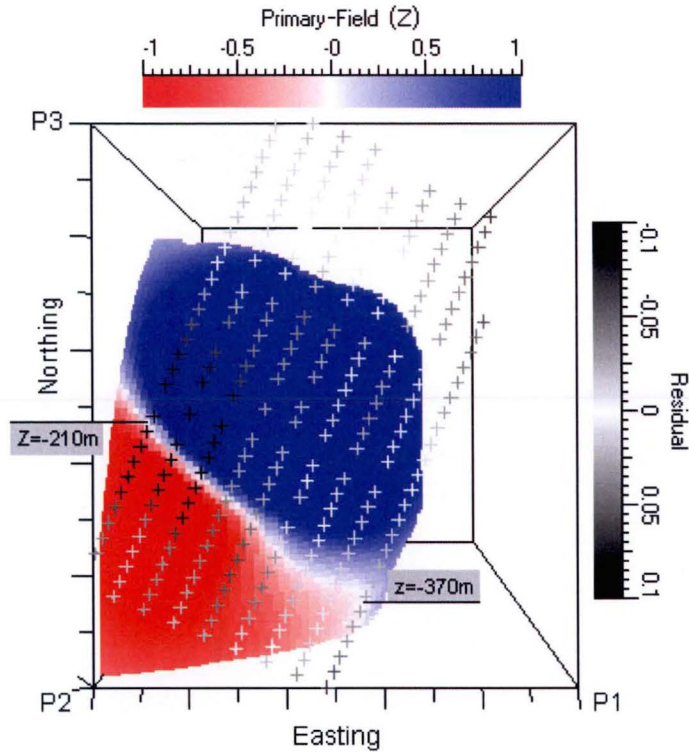


Figure 6.24 – Map of the amplitude of the normalised primary field (vertical component) intersecting the Gams Formation. Receiver stations are depicted as colour-coded residuals. Poor fits in the southwest corner of the model coincide with a sign-change in the vertical component of the primary field. The Gams Formation is nearly flat in the southwest corner at an elevation of ~ 210 m. The Gams Formation dips towards the southeast and is nearly vertical below the last survey line where dependence on the z-component primary field is less significant.

The TEM moment response of the recovered time constant model is depicted in Figure 6.25. A poor fit is noticeable at receiver stations between distances 200–800 m of survey lines -400E, -300E and -200E. Coincident with the locations of the poor fit is a sign-change in the vertical component of the primary field \mathbf{B}_0 where it intersects the Gams Formation at a relative shallow depth of ~ 210 m (Figure 6.24). In this area, the current flows preferentially in the almost horizontal plane of the Gams Formation. The observed TEM moment response is positive, so that a sign change in the z-component of \mathbf{B}_0 impedes the response of associated point-conductors which are bound to the orientation of the primary field, resulting in the relative poor fit. It is expected that this limitation of the algorithm will be resolved for inversion of total-field TEM moments, which is unaffected by sign changes (c.f. Appendix A)

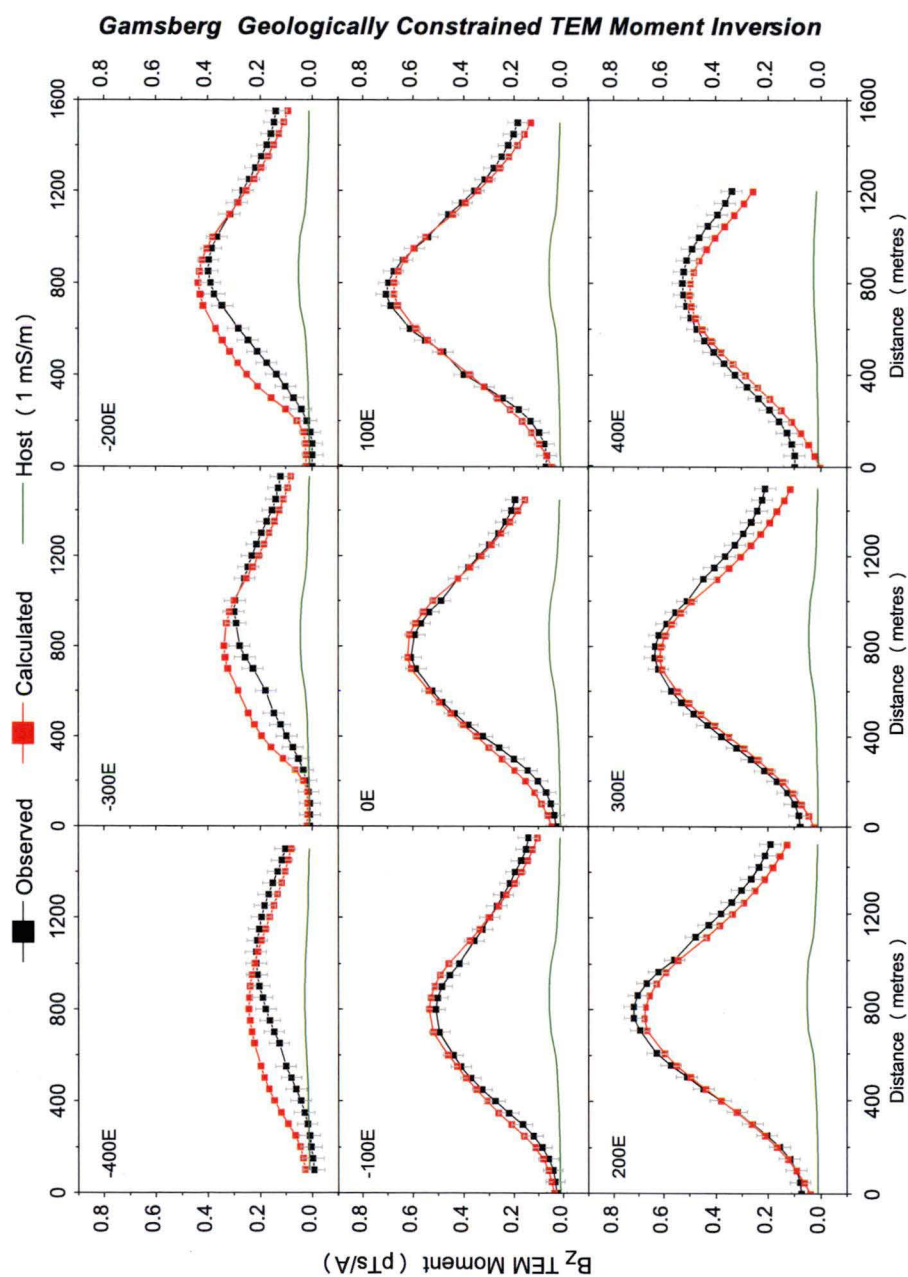


Figure 6.25 – TEM moment profiles for recovered time constant model after geologically constrained inversion. The 'Observed' response denotes the Gamsberg-East TEM moments. 'Calculated' denotes the TEM moment response of the recovered time constant model. The calculated TEM moments fit the the Gamsberg data set to better than 0.04 pTs/A in a χ^2 -sense. However, the fit deteriorates at stations between distances 200–800 m of survey lines -400E, -300E and -200E due to a sign-change in the vertical component primary field (c.f. Figure 6.24).

6.9 Conventional forward modelling employing plate conductors

Plate conductors are highly idealised representations of geological entities but are widely used for interpreting observed TEM data due to their speed and simplicity. However, despite the necessarily simplistic geometry, they can provide reasonable geometric representation of some geological features. Plate modelling in conjunction with conductivity-depth imaging was the only computationally feasible method for analysing 3D TEM data until recently. VPem3D inversion results of Gamsberg-East are compared with the results from interactive plate forward modelling in order to illustrate congruence to an established method and to gain confidence in the VPem3D inversion results.

The strong anomaly crossovers in the Z-component with elongated positive lobes over the transmitter loop suggest termination of a dipping plate conductor extending below the transmitter. The locus of the zero crossovers was indicated in Figure 6.11(B) trending southeast across the survey lines. The depth-to-top of the plate model may be approximately estimated by the width of the anomaly at two-thirds its maximum amplitude which evaluates as ~ -420 m (Gallagher et al., 1985). Guided by these preparatory observations of the TEM data, a plate forward model was computed and subjected to trial-and-error adjustments. The *Maxwell Plates* program was employed, which models plates in a free space. Given the resistive nature of the host rock environment, the free-space model is appropriate. The plate model is illustrated in Figure 6.26, and its parameters are defined in the figure's caption. A Gamsberg-East CDI section with the plate model superimposed is shown in Figure 6.27; and the plate model together with the result for the geologically constrained inversion in Figure 6.28.

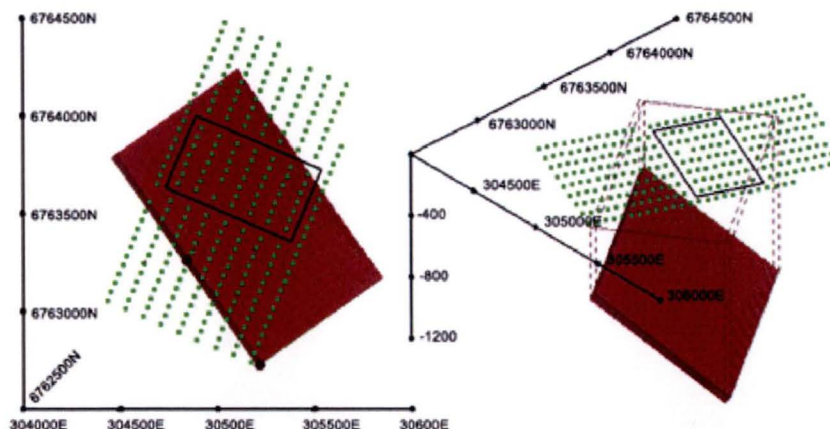


Figure 6.26 – 'Best fit' plate model model for the Gamsberg-East data set. The model is sensitive to geometry, size and conductivity. Top of the plate is centred at (304845E, 6763260N) at 450 m depth. Dip is 37° ; dip direction is 55° . Strike length is 1300 m; dip extent is 950 m. Thickness is 50 m and conductivity is 4 S/m. Number of ribbons and skew was set to 15 and 0.4 respectively.

The trial-and-error approach took considerably longer than the runtime of any of the inversions in order to achieve a satisfying degree of fit in anomaly profile shape and magnitude. Figure 6.29 shows the response for the z- and x-components. The decay rate of the observed TEM data is slower than the decay rate of the plate. If the plate conductivity is increased the response approaches the inductive limit, demonstrating the limitation of the plates approach. Based on Lamontagne's formula for a plate conductor (Equation 3.10) the time constant of the plate evaluates as $\tau_p \simeq 30$ msec.

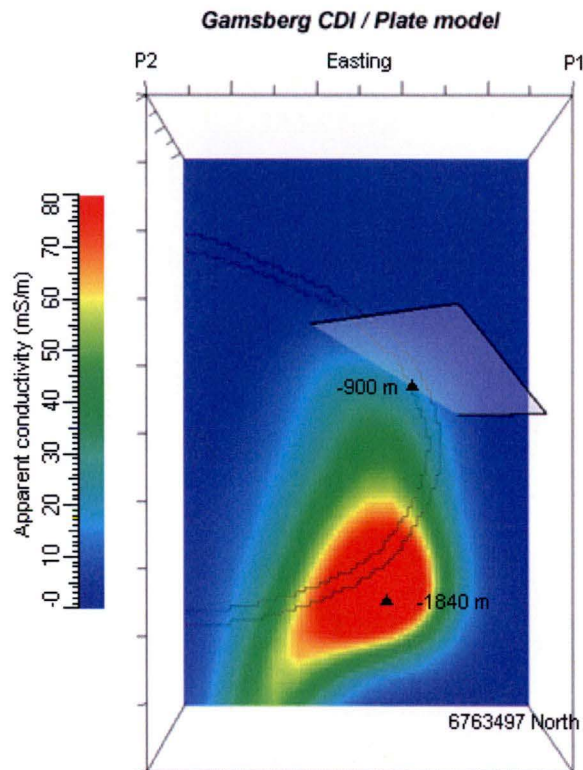


Figure 6.27 – Gamsberg-East CDI section with plate model superimposed. The plate location coincides with the shallow gradient of apparent conductivity values.

Comparison of the plate model with the Gamsberg-East CDIs in Figure 6.27, illustrates that the plate location coincides with the apparent conductivity gradient at the top of the anomalous zone in the CDI. The depth of a plate conductor often coincides with the conductivity gradient (Chapter 4.5.3). The conductive high at great depth in the Gamsberg CDI, therefore, may be a product of the conductivity-depth transformation. The plate model is compared with the result of the geologically constrained inversion in Figure 6.28, which demonstrates the overall consistency of the inversion result with the plate model in terms of location, however the effective orientation of the plate model and the elevated time constants of the geologically constrained inversion differ somewhat. In terms of conductivity (or time constant), however, the plate model is inadequate since the amplitudes cannot be fitted very well for any plate conductance.

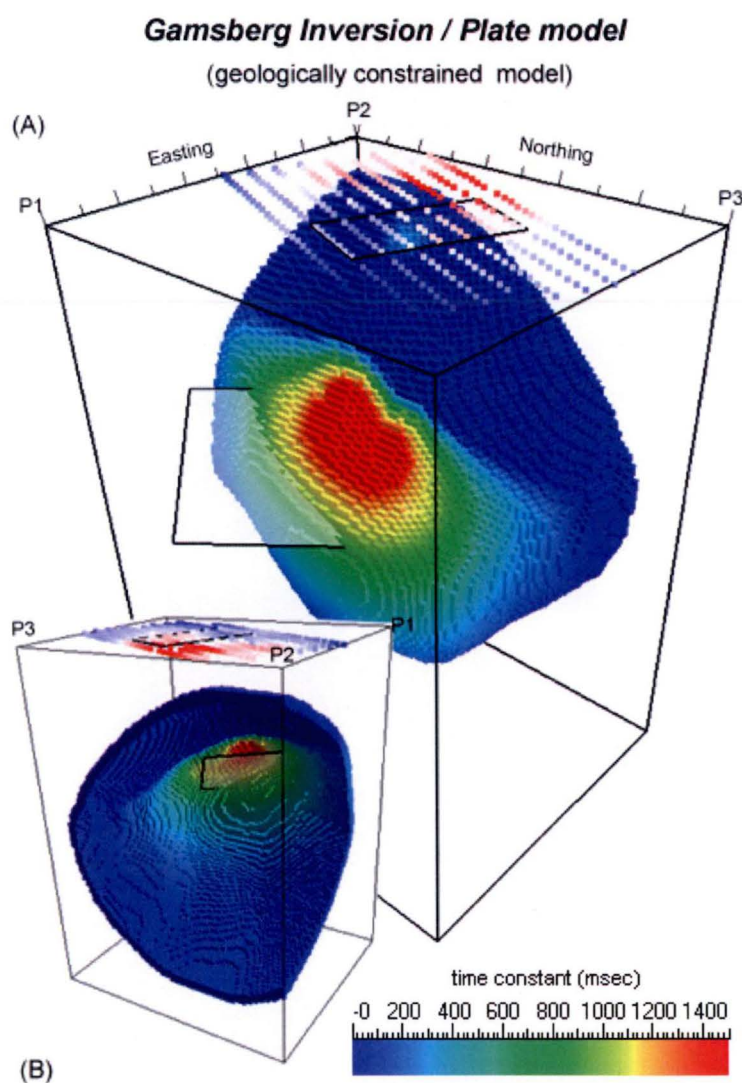


Figure 6.28 – Plate model and recovered time constant model for geologically constrained inversion. The plate model generally coincides with the highly conductive region of the recovered geologically constrained model. Inset (B) shows the 'back' of the model.

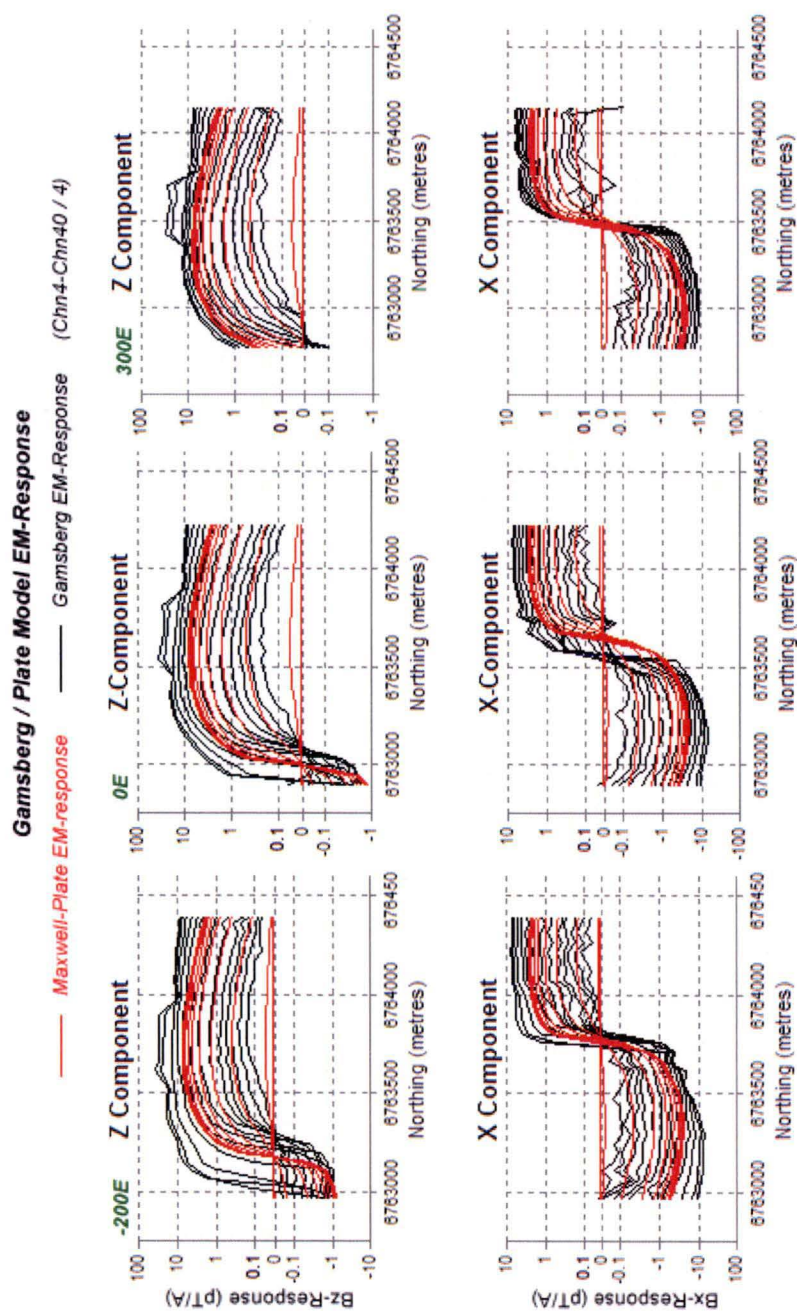


Figure 6.29 – Observed Gamsberg-East Bz and Bx TEM data and plate model responses for three survey lines. In terms of shape and anomaly cross-over, all lines provide a reasonable fit. The chi-squared misfit however is large with $\chi^2 \simeq 700$ due to the poor fit in amplitudes. Displayed are the responses for every fourth channel from channel 4 to channel 40 at lines -200E, 0E and 300E for the z- and x-component.

6.10 Discussion of inversion results

The applicability of the novel approximate 3D-TEM inversion scheme described in this thesis has been demonstrated for a ground-TEM field data set. The recovered time constant models of the successful inversions, initialised with different starting models and constraints, all exhibit similar features, providing some confidence in the results. The measured vertical component TEM decays were transformed to 1st order TEM moments employing total-field apparent conductivities for extrapolation at the earliest and latest valid channel to provide 'complete' TEM moments. 3D inversion of the vertical component TEM moments was carried out based on four different starting models: (i) unconstrained inversion, (ii) inversion with CDI starting model, (iii) inversion with zero starting model and (iv) geologically constrained inversion.

Successful inversions identified a broad conductive region that generally coincides with recognised mineralisation from drilled intersections. The location of the zones of elevated conductivity in the recovered time constant models are also broadly consistent with the result from interactive plate forward modelling, providing further confidence in the obtained inversion results. Furthermore, a localised, minor conductive feature at shallow depths from ~220–280 m in the southwest of the study area was identified in the inversion results as also supported by time-constant analysis of the TEM decays at early time between 1–10 msec. Both the broad conductive region as well as the isolated feature are visible in the vertical component TEM decays as anomaly crossovers.

For all inversions, a poor fit was noticeable at receiver stations between distances 200–800 m on survey lines -400E, -300E and -200E, thought to be mostly due to a sign-change in the vertical component of the primary field at the conductor location. Total-field inversion, which is subject of future research, should resolve this limitation of the algorithm as total-field data is theoretically unaffected by sign changes (c.f. Appendix A). Possible additional factors that may contribute to misfits in the TEM moment response may include a poor representation of ground topography (which was assumed to be perfectly flat) and proximity of receiver stations to model boundaries (where the Gams Formation was truncated in the southwest).

The unconstrained inversion gave a successful mathematical fit to the data, but it resulted in a geologically unreasonable time constant model with conductive zones aggregated near the surface close to receivers and also near the transmitter, due to high sensitivity in the vicinity of the transmitter. The result highlights the importance of encompassing constraints due to the non-unique nature of TEM moment inversion. Moreover, the unconstrained inversion illustrated the impact of the sign-reversal of the primary field on the recovered time constant model. The polarity of the primary field is reflected in the signs of the time constant values, which were unbounded during unconstrained inversion.

Inversion based on the CDI starting model did not adequately converge when retaining all cells during inversion, however it was successful with the option of 'bound cancelation' which deactivates cells which hit their lower bound. Depending on the primary field direction, time constants may trend to negative values, but will be deactivated because they hit their lower bound. Hence, the inversion is constrained to a dynamically smaller volume, therefore changing

the modality and outcome of the inversion. When retaining all cells however, the inversion did not achieve the desired fit because the algorithm constantly tries to adjust cells at shallow depths where sensitivities are largest, but fails to assign the calculated time constant when cells hit their lower bound. At the next iteration the process is repeated. The recovered time constant model when the inversion stalls, closely resembles the CDI sections. The recovered time constant model for the successful inversion shows conductive material at great depths as evinced by the CDI sections and also shows conductive material at shallow depths approximately corresponding to drill results and plate forward modelling. Because of non-uniqueness, conductive material at great depths cannot be unambiguously supported, however the TEM data do not preclude the occurrence of mineralisation at great depths as suggested by the CDIs which show a highly conductive, deep conductor.

In order to develop an understanding of the variability of the results, the inversion was repeated with a zero starting model with time constants constrained to non-negative values. When conditioning with conductivity weights defined from the CDIs, the inversion failed to adequately converge. The inversion failed since time constant changes at shallow depths were prohibited: conductivity weights restrict changes to areas with high conductivities and penalise solutions which deviates from the CDIs. The inversion succeeded when depth weights are employed which are less restrictive and which favour changes distributed with depth. High conductive zones in the recovered time constant model straddle the Gams Formation unit and broadly identifies conductive material as supported by recognised mineralisation from drilled intersections. A localised, minor feature was also identified at shallow depths. Conductive material at great depths is not inferred in this inversion result which may be a consequence of non-uniqueness.

Finally, geologically constrained inversion was performed where only cells which are member of the Gams Formation were allowed to change their time constants to non-negative values. Because of the restriction to the Gams Formation, inversion results produced a time constant model with sharp boundaries, consistent with pre-existing geological information. Elevated values of the recovered time constants are located in the fold nose of the Gams Formation, coinciding with recognised mineralisation from drilled intersections. An isolated conductive feature was also imaged at shallow depths, as was the case for the zero starting model with depth weights. However, deep mineralisation, as suggested by the CDIs, was not apparent in the resulting time constant model.

Run-times and some inversion execution parameters for the successful inversion runs are compiled in Table 6.2. The zero-starting model and the geologically constrained model were initialised with zero cell time constants, accordingly the result of the initial forward calculation was zero and hence this process can be bypassed which translates into faster run-times. By contrast, the forward calculation of the CDI-starting model takes ~8 min. Because the size of the geologically constrained inverse problem is much smaller, as compared with the zero- and CDI-starting model, 164 iterations completed in 3 minutes. The relatively small χ^2 value for the CDI-starting model results from the rescaling of cell conductivities so as to optimise the fit with respect to the observed TEM moment response.

	initial χ^2	iterations	run time	active cells
CDI-starting model (‘bound cancelation’)	5 53	24	24 min	674,584
Zero-starting model (depth weights)	61 9	107	32 min	738,224
Geologically constrained model	61.9	164	< 3 min	33,886

Table 6.2 – Inversion execution parameters for inversion of Gamsberg-East TEM moments. Data uncertainty was $q = 0.04$ pTs/A and maximum step size $\delta\tau = 2.5$ msec. Number of data points is 259. Background conductivity was held fixed to 1 mS/m. All models result in χ^2 values of 1 or less.

6.11 Concluding remarks

The rapid, approximate 3D inversion employing TEM moments of field data, acquired over complex geology, offers a complementary interpretation tool to conductivity-depth imaging and conventional plate modelling. The approximate 3D inversion identified mineralisation as a bulk conductive feature when employing a zero starting model with depth weights. Geologically constrained inversion produced a confined distribution of elevated time constants in sharp contrast with the host rock which reflects mineralisation from drilled intersections more realistically. Different starting models produced successful inversions which arrived at nearly the same solution. Mineralisation at great depths, as depicted in the CDIs, cannot unambiguously be substantiated with the 3D inversion results. Because of the non-unique nature of TEM moment inversion, a preferred time constant model may only be identified after exploring some of the range of acceptable models. It is advisable therefore to begin the inversion from a number of different starting models and assess the inversion results with other data.

Chapter 7

Conclusions

7.1 Summary and discussion of research

Motivated by the demand for a rapid and reliable 3D inversion method for TEM data, an approximate moment-based method has been developed, utilising geological constraints and potential field inversion devices. The present thesis provides a proof of concept for fast and practical, approximate 3D inversion of TEM moment data. The method has been illustrated in the context of fixed-loop ground-EM. Because the presented 3D inversion method is general and very fast, it is also suitable for AEM.

Fast, approximate EM modelling employs the TEM moment transform which is a weighted time-integration of the TEM earth response from 0 to ∞ . Measured TEM responses, defined for finite time-ranges, are extrapolated using apparent conductivities at the first and last valid channel. Extrapolation is required because the forward algorithm employs complete TEM moments defined for a time range from 0 to ∞ . Linearity with respect to the time constant is a property of complete TEM moments. Due to the weighted time-integration, the TEM moment transform compresses a multi-channel TEM decay to a single parameter. In the course of this thesis the 1st order TEM moment, equivalent to the resistive limit, has been exclusively utilised. The moment transform accentuates late-time features, so that EM interaction may tolerably be ignored.

The 3D inversion scheme relies on linear superposition of TEM moments associated with discretised sub-surface volumes and recovers the geoelectrical subsurface in terms of time constants via a steepest descent formulation. Computationally expensive matrix inversion is not required. Accumulation of TEM moment responses of point conductors defined in a continuous background has provided the basis for the approximate forward modelling approach. Linear superposition of a cubic network of point-conductors approximately reproduces the TEM moment response of a confined conductor if its time constant is assigned to each point-conductor. The predicted net TEM moment response of the ground is

compared with the measured TEM moment response and the inversion is deemed successful if the chi-squared misfit is unity or less.

Because depth-resolution is lost during the TEM moment transformation, CDIs serve as a device to restore depth information. The CDIs are based on total B-field amplitudes which facilitates derivation of unambiguous apparent conductivities for fixed-loop TEM. Conductivity models interpolated from CDIs serve as an initial estimate for a time constant starting model or can be employed to define a spatially defined weighting scheme. Conductivity weights penalise solutions which deviate from the conductivity model. Depth weights may be used alternatively to condition the depth and shape of causative bodies during inversion. Depth weights are subjective and penalise shallow solutions.

The weighting scheme is part of the integrated inversion approach which builds on the VPmg potential field modelling and inversion framework. In VPmg, each cell is linked to a rock type, therefore facilitating lithological inversion so that the recovered time-constant model is still recognisable as a geological model after inversion. Adoption of a categorical model structure does not limit options for property inversion which can be performed on a categorical model, with changes restricted to specific units or permitted throughout the entire subsurface. VPmg was modified so as to accommodate the TEM moments methodology; the new program is referred to as VPem3D.

The following three sections summarise the key-points of the conducted research and comments on achievements and limitations. Possible extensions and future work is described in Appendix A

7.1.1 Approximate forward modelling

Fast, approximate forward modelling has been accomplished by adding the analytical TEM moment response of a homogeneous half space to the analytical TEM moment response of a discretised target 3D-response while disregarding EM interaction. The discrete target is comprised of a cubic network of point conductors in free space. After excitation, each point conductor hosts a magnetic dipole with strength proportional to the product of local primary field, cell volume and time constant. The TEM moment response as modelled with point conductors is virtually scale invariant, i.e. independent of the cell size.

In the simplest form of the algorithm, each dipole inherits the orientation of the local primary field (a modified forward algorithm which adjusts the components of the primary field according to the conductivity gradient is in an experimental stage, c.f. Appendix A). Accordingly, 'smoke ring' current diffusion cannot be simulated because induced vortex currents are static. For this reason a continuous conducting half space was introduced. The half space response captures early-time and near-transmitter responses as well as the late time response of an extensive unbounded medium. The concept of the linear combination of target and host enables separation of the 'uninteresting' host response from the 'interesting' target response.

The inaccuracy associated with the approximate forward solution when neglecting EM-interaction has been qualitatively examined for the case of a sphere (5 S/m and 10 S/m) in a uniform host for a range of half space conductivities (1–100 mS/m). The analysis was based on an asymptotic semi-analytical formulation for a coincident loop configuration which decomposes the contribution from host, sphere and interaction, which includes contributions arising from inductive and galvanic coupling. The results show that the main contributions arise from the sphere and the half space. The TEM moment contribution from the interaction term depends mostly on the host conductivity and is small ($< 5\%$) for typical host conductivity ranges, and can be as high as $\sim 15\%$ for relatively high conductivities as found in weathered overburden.

In order to explore the suitability of the TEM moment modelling approach for application to measured field data, the approximate forward solution has been compared with fully 3D-TEM solutions, calculated by the integral equation solver MARCO. The examples are calculated for prisms buried in a continuous conducting half space. Two models which exemplify large ore deposits at great depths have been considered.

The first example is for a sizable horizontal slab of 1 S/m in a rather resistive background of 1 mS/m and buried directly under the fixed transmitter. The relatively small subcell dimension of 10 m chosen to demonstrate the rapid, approximate TEM moment computation for a large number of cells (192,000 cells) The VPem3D calculation completed in ~ 5 minutes. The computation for the fully 3D model by MARCO were calculated on a much coarser grid comprising a total of 1000 cells and completed in ~ 14 minutes. The time constant of each point conductor was assigned the time constant of the slab as estimated from the TEM decays. The TEM moments of the MARCO slab and the approximate VPem3D response agree, with RMS difference in the order of $\sim 1\%$ of the maximum amplitude.

The second example is for an extensive vertical dyke model of 50 S/m in a conductive host of 50 mS/m which gives rise to host-rock EM interactions. The fixed transmitter was centred at (0E,0N) with the eastern wire 450 m offset from the nearest edge of the dyke. For a subcell size of 10 m (giving a total of 140,000 cells) the computation in VPem3D completed in $\sim 2\frac{1}{2}$ minutes. The fully 3D response was computed by MARCO on a coarser grid for 1000 cells and completed in ~ 16 minutes. The TEM moment responses of MARCO and VPem3D agree, with RMS difference in the order of $\sim 2\%$ of the maximum amplitude. Comparison of the stripped TEM moment responses, i.e. with the half space response subtracted, illustrates that the VPem3D responses reasonably reproduce the shape of the MARCO responses. Deviations become apparent most clearly for lines traversing the centre of the dyke where the responses are the strongest. Because the vertical dyke will predominantly support eddy current flow in the plane of the plate, the calculations for VPem3D are imprecise since each point conductor inherits the orientation of the primary field.

7.1.2 Robust 1D imaging

Construction of a starting model for 3D inversion as well as calculation of the TEM moment data from measured TEM decays is supported by conductivity-depth-imaging. The transformation of measured TEM decays to TEM moments employs apparent conductivities: the incomplete TEM moment as obtained by integrating the measured decays between the first and last channel are augmented at early and late time using contributions from half space decays defined for the apparent conductivities at the first and last channel respectively. For TEM moment inversion, interpolated CDIs restore depth information in the starting model which has been lost due to the process of time-integration in the moment transform. CDIs may supply initial estimates of cell time constants or may serve as a set of spatially defined inversion weights which favour solutions close the conductivity distribution of the CDIs. It is desirable, therefore, that the calculated apparent conductivity values are reliable so as to avoid misleading CDI starting models.

Sensible portrayal of the subsurface conductivity in the CDIs is desirable in order to reliably condition the 3D inversion and to initiate the TEM moment data for inversion. Although well-defined for in-loop measurements, apparent conductivity is either dual-valued or undefined for vertical component ground-loop TEM measurements over a half space outside the transmitter-loop, both for step and impulse response data. In particular, if $B_z < 0$, for stations outside the loop, the apparent conductivity is extremely high at mid- to late-times. Artifacts may also arise from 3D geology. The ambiguity inherent in the calculation of apparent conductivity for fixed-loop TEM has been overcome by making use of multi-component **B**-field amplitudes. Apparent conductivity based on **B**-field amplitudes is unique because on a homogeneous ground, **B**-field amplitudes are a non-increasing function of time, except when the inductive limit is encountered. The technique's suitability was demonstrated on layered earth models. Apparent conductivities could be computed unambiguously and the recovered layered conductivity structure from conductivity-depth imaging resembles the true layered model without artifacts. Conductivity-depth imaging based on **B**-field amplitudes from synthetic 3D models has furthermore been shown to be less biased by 3D effects than conventional CDI interpretation which are based on the vertical component only. By interpolating total-field CDIs a smoothed representation of the 3D geoelectrical structure of the subsurface can be generated.

7.1.3 3D inversion of TEM moments

The inversion algorithm is sourced from VPmg. Parameter estimation was realised by iterative construction of a time constant model via linearised improvement of a starting model using a fast steepest descent formulation. A user-controlled step size avoids large jumps in the perturbation vector at each iteration. The

steepest descent method successively corrects a model estimate in direction of the negative gradient of the chi-squared misfit. At minimum, the recovered model defines a distribution of time-constants in the subsurface. For single component TEM moments, property inversion is linear and derivatives are independent of the model, therefore facilitating successive model corrections via the initially calculated derivatives only. The algorithm distinguishes background and target response. The background conductivity can be held fixed to an a priori estimate (for example from CDIs) or can be optimised employing a simple least-squares regression. The target response is subject to steepest descent inversion. The inversion may employ a 'bound cancelation' directive which deactivates any cell from inversion if its time constant attains a bound. Bound cancelation effectively reduces the number of active cells during inversion (thereby enhancing speed).

Each voxel in the model is associated with a property value and a lithological unit, so that the lithological significance is preserved throughout the inversion process. The mapping of the geological model onto the 3D grid facilitates geologically constrained inversion where only selected units participate in inversion which are expected to carry significant mineralisation. Inversion proceeds from a starting model. Together with selected inversion constraints, the starting model comprises the geological litho-model with initial time constant values assigned to each cell. The time constant model may be initialised with zero values or may be based on interpolated CDI sections. The starting model is then subject to successive corrections so as to find the optimal distribution of cell time constants which can explain a set of observed TEM moments.

Inversion constraints are needed owing to the inherent non-uniqueness associated with the potential-field-like inversion of TEM moments. For inversion, 3D-conductivity-weights or 1D-depth-weights have been employed. Bound constraints can furthermore be imposed to selected units. Also, the property of a cell in a heterogeneous unit can be held to a fixed value if petrophysical measurements are located within it. The conductivity-weights are calculated from apparent conductivity-depth pairs and penalise solutions which deviate markedly from conductivity-depth-imaging. Depth-weights are designed to suppress the impact of the transmitter and to penalise shallow variations in conductivity. The depth-weights are based on an empirical tanh-function and can be 'tuned' to suppress surficial layers and to emphasise conductive features at certain depths as seen in the CDIs.

3D-Inversion of synthetic examples

The vertical component TEM moments of the previously described synthetic models of the horizontal slab (768,000 inversion parameters) and vertical dyke (180,000 inversion parameters) were subjected to the 3D inversion scheme. For inversion, the TEM moments of both synthetic examples have been contaminated with 5% Gaussian random noise (231 data points). The calculations were conducted on a Pentium 4 2.8 Ghz processor from 2006. For both examples, the

synthetic TEM data is converted to an initial 3D conductivity model interpolated from CDIs based on total B-field amplitudes. In case of the horizontal slab model, apparent conductivity is disseminated throughout a large volume, extending far below the prism. Depth-to-top of the prism and the lateral model dimensions are adequately reflected in the CDIs. In case of the vertical dyke model the CDIs depict the depth-to-top and the depth-extent of the prism fairly accurately. However, a broad conductive region is pronounced west of the vertical dyke which extends far below the transmitter loop.

The purpose of 3D inversion of the two synthetic examples was to test whether the inversion can rapidly provide more accurate representations of the geoelectrical subsurface than the CDIs. In order to illustrate non-uniqueness, 3D inversion was performed with various distinct starting models: (i) a CDI starting model initialised with time constant values based on CDIs; (ii) a zero starting model with conductivity weights and (iii) a zero starting model with depth weights. A positivity constraint to the time constants was imposed to each starting model.

For the slab example, the inversion solution based on the CDI starting model, resembled the CDI conductivity structure; inversion succeeded after ~ 14 min (2 iterations). In case of the vertical dyke example, the recovered time constant model gave an improved representation of the true dyke model; inversion was successful after ~ 4 min (15 iterations). In order to suppress shallow conductivity structure, the CDI starting models were initialised with an inert surficial layer, resulting in a reduced number of parameters as compared with the zero starting models.

The recovered time constant models based on the zero starting model conditioned with conductivity weights were mostly confined by the volume of the original body. In case of the slab, inversion succeeded after ~ 9 min (4 iterations) and in case of the dyke, inversion was successful after ~ 6 min (67 iterations).

Dependent on the details of the used depth weighting scheme, different results were obtained from the zero starting model with depth weights as a result of non-uniqueness. The resulting time constant models calculated for different depth weights gave a good representation of the underlying true model. An acceptable fit was achieved after about 10 min for the horizontal slab (4 iterations) and after about 5 min for the vertical dyke (49 iterations).

Because the zero starting models do not need to calculate a forward model response, it is considerably faster than inversion based on the CDI starting models. Inversion based on the zero starting model with conductivity weights produced the most convincing results for both synthetic examples.

3D-Inversion of measured field data

The applicability of the approximate 3D inversion scheme was demonstrated on fixed-loop TEM field data from South Africa. Further objective was to build confidence in the existing interpretation or to see whether new conclusions could

be drawn based on the inversion results. Information from drilling, geological data and from geophysical measurements were incorporated into a simplified geological model which consists of three lithological units: quartzites, ore zone and mafic gneisses. The cell size was 20 m and the total number of cells in the geological model was 738,224; the number of cells in the ore zone unit was 33,886.

Different starting models were tried: a CDI starting model, a zero starting model conditioned with conductivity weights and a zero starting model with depth weights. Additionally a geologically constrained starting model was used where parameter changes were restricted to the ore zone unit and which was initialised with zero time constants. A positivity constraint was imposed during all inversions.

The various starting models were constructed to highlight various aspects of the data. For example inversion based on the zero starting model with conductivity weights penalised solutions inconsistent with the CDIs. On the other hand, the zero starting model with depth weights recovered smoothly varying time constants with depth. The geologically constrained starting model produced sharp boundaries where recovered time constants were confined to the ore zone unit.

The inversion based on the CDI starting model was successful if 'bound cancelation' was invoked (24 iterations in ~24 min). Elevated time constant values of the recovered time constant model broadly corresponded with occurrence of mineralisation from the drill holes. A broad conductive region of low time constants is furthermore apparent at great depths, which is interpreted as a residual of the CDI starting model.

Inversion based on the zero starting model conditioned with depth weights produced a model with a broad conductive region which generally coincides with the drilled ore zone and also with the result from plate forward modelling. Inversion was successful after 107 iterations in about ~32 min.

The result from the geologically constrained inversion produces a time constant model with sharp boundaries at depths coinciding with the drill intercepts and the result from plate forward modelling. Inversion for 33,886 active cells succeeded after 164 iterations in less than 3 minutes.

3D inversion of the synthetic examples and the measured field data all completed in a relative short time. The longest run-time was about ~30 min for inversion of the field data set which involved 738,224 parameters and 259 data points. Shortest run-time was about 3 min. for the geologically constrained inversion of the measured field data, involving only 33,886 cells. Inversion of the field data set was considerably faster than interpretation based on interactive plate forward modelling.

The recovered time constant models of the synthetic examples could all indicate the position of the true model, subject to selected constraints. As compared with the results from conductivity-depth-imaging, VPem3D provided much more accurate representations of the geoelectrical subsurface than the CDIs. The inversion result for the measured data is consistent with bore hole information and plate forward modelling.

Concluding remarks

The presented approximate 3D inversion scheme is supplemental to 1D interpretation and helps building confidence in the geological interpretation of the subsurface. The inversion scheme was successfully tested on synthetic fixed-loop TEM examples and on fixed-loop TEM field data from South Africa. The innovative key elements which were successfully completed during the current study were

- the development of an approximate, fast and practical 3D-TEM forward modelling program as a combination of a discrete target response and a continuous background response. The forward calculations are based on analytical parametrised TEM solutions in terms of TEM moment responses of point conductors added to the TEM moment response of a half space.
- the device for transforming measured TEM decays to complete TEM moments by extrapolating at the earliest and latest channels using a half space model based on apparent conductivities for the times in question.
- the development of a reliable and robust 1D-imaging scheme in the context of fixed-loop TEM, which is based on the calculation of unambiguous apparent conductivities derived from **B**-field amplitudes. Conductivity-depth imaging serves as a preparatory process for approximate 3D inversion and facilitates injection of depth information. It is also used to extrapolate 'measured' TEM moments.
- the development of a rapid 3D inversion scheme of TEM moments, which builds on the VPmg potential field framework, utilising geological constraints, primarily derived from boreholes, and potential field inversion devices such as depth weighting and property bounds.

Appendix A

Future work

Subsequent sections briefly describe future work which can be classified into three objectives:

- (i) **Enhanced speed**
This point involves technical aspects only. It is anticipated that the program execution can be accelerated by simple measures like recognising constrictions in the code. Primarily, however, enhanced speed will be realised by parallel programming due to the increased availability of multiprocessor computers. Because point conductor responses are each independent, a parallel scheme is thought to be promising.
- (ii) **Improved accuracy**
More appropriate forward modelling improves accuracy. For example, induced vortex currents are static in the current implementation of the target response due to the 'frozen' dipole direction of the point conductor. Implementation of the gradient scheme, described earlier in Chapter 3, will improve accuracy, since current flows preferentially orthogonal to conductivity gradients. Another example is the background response which is calculated as the response of a homogeneous conducting half space. While this facilitates fast and simple execution, it may often be a poor approximation to the host-rock geology. A better approximation, and therefore improved accuracy, may be a layered earth response as background.
- (iii) **Greater generality**
The current implementation of VPem3D is applicable for fixed-loop TEM. An example for greater generality includes implementation of moving loop and slingram systems. Inversion can be furthermore generalised to include higher order TEM moments and inversion of total-field TEM moments. Implementation of homogeneous body inversion and geometry inversion are further examples of greater generality.

Conductivity gradient method

In the forward algorithm, each point conductor inherits the orientation of the local primary field. As a consequence the magnetic dipole orientations associated with each point conductor are effectively frozen in the directions of the local primary field. However, a modified forward algorithm which adjusts the components of the primary field according to the conductivity gradient is in an experimental stage. The modified forward algorithm defines local 'next-neighbour' gradients which simply can be obtained from the difference in conductivity or time constants of adjacent cells.

The principle of the gradient methodology has been demonstrated at a 'thick' plate model. The TEM moment response of the subcelled volume has been compared with the TEM moment response of the plate-model as computed from the TEM decays of the approximate plate modelling software MAXWELL. Each VPem3D point conductor was assigned a rescaled time constant based on the analytical time constant of the plate. The VPem3D response curves match those of the plate when the primary exciting field consists only of the component orthogonal to the plane of the plate.

In the modified algorithm, the gradient scheme initially assigns a local gradient to each cell in the starting model. During inversion, after each iteration, the gradient is recalculated after update of cell time constants. In homogeneous conductive areas, the gradient evaluates as zero in which case the local primary field is adopted without modification. The gradient scheme is subject of active research and promises an interesting approach for computation with improved accuracy of TEM moments for arbitrarily shaped conductors.

Conductive overburden

The fully 3D synthetic examples in the current thesis concentrated on two different, extensive models buried at great depth in a homogeneously conducting host. Likewise, the field data example was a large conductor with complex geometry buried in a resistive host. All cases, synthetic and field data, were modelled via superposition of a discrete target TEM moment response and a homogeneous conducting half space response. The case of a conductive overburden, which commonly occurs in Australia, has not been investigated in the current study. The effect of overburden is to delay and smooth the target response, similar to the effect of a conducting host rock. At early times, the effect is known as 'overburden blanking' where only information from the overburden is present in the TEM decays. At later times the response from the target becomes visible if the blanking effect is not too strong. Superposition of overburden response and target response is a valid approximation at late times (Nabighian and Macnae, 1991, p.446).

The TEM moment transform will virtually 'smear' all contributions from the overburden response onto the entire time range of the decay, resulting thus in an increased TEM moment response. For the present inversion scheme, where the

background is a homogeneous conducting half space, the presence of a conductive overburden will manifest predominantly in a higher half space conductivity.

Improved accuracy may be achieved by a more direct approach by identifying conductive overburden from corresponding CDIs and include them explicitly as a conductive layer in the modelling and inversion scheme. The analytical formulation of the TEM moment response of a conductive layer of finite thickness for magnetic dipole excitation has been reported previously by Smith and Lee (2002c). The TEM moment of a layer of finite thickness has a very simple formulation and is linear with respect to conductivity, therefore facilitating simple-least squares optimisation which could be incorporated in the inversion scheme. The derivation of the TEM moment response of a layer with finite extent for rectangular loop excitation has yet to be realised, however .

Moving loop

The current study focused on fixed-loop ground-TEM but can readily be generalised to moving loop systems. Computationally, there is no difference in calculating the TEM moment response of an assembly of point conductors for moving loop or slingram. Because the modelling and inversion scheme is fast, it is suitable also for AEM. The TEM moment of a point conductor is related to the exciting EM system via direction and strength of the primary magnetic field at the point conductor's location. If the primary field vector is known at the point conductor's location, the same formulation as given in Equation (3.2) is employed for calculating the point conductor response. Algorithmically, the program has to account for a multiple transmitter system in case of moving-loop or slingram configurations.

Higher order moments

The implemented forward and inverse modelling scheme in VPem3D relies on the first order TEM moment which is equivalent to the resistive limit. Smith and Lee (2002b) use approximate moment orders from 0 to 9 for interpretation of measured data. The normalised higher order moments have larger amplitudes than the smaller order moments at the location of a known bedrock conductor. Smith and Lee (2002b) note that the higher order moments put greater emphasis on the late-time data. This can bring out conductive features that are deeper than other less conductive features, and normally only seen in the late-time data, however at the expense of simplicity, speed and sensitivity to noise. Nonetheless, generalisation to multitudinous TEM moments of varying order for the VPem3D inversion scheme may serve as a proxy for time channels in order to inject depth information in the inversion and to emphasise deep conductive features. (Smith et al., 2006, Fig.6) shows a synthetic imaging result obtained from TEM moment inversion for moment orders 0.5, 1.0 and 1.5.

Total field inversion

The property inversion scheme currently implemented in VPem3D inverts vertical component TEM moments. The advantage of vertical component inversion is that the inversion is linear. In linear inverse problems, sensitivities are model independent, which expedites successive model corrections via initially calculated sensitivities. Recalculating an updated forward model and sensitivities after each iteration is therefore not necessary. However, vertical component TEM moments which exhibit anomaly cross-overs caused by current migration in anomalous conductivity volumes cannot be replicated due to the 'frozen field' effect (Nabighian and Macnae, 1991, p.440).

Generalisation to inversion of total magnetic field moments can circumvent difficulties associated with anomaly cross-overs. The total magnetic field is always positive and not directly affected by current migration anomaly cross-overs. Moreover, the information content in total field amplitudes exceeds that of single component data, resulting in a more unambiguous inversion problem, therefore. Starting models are predominantly based on $|\mathbf{B}|$ -field amplitudes CDIs for these reasons. A disadvantage however, is that total field inversion is non-linear because sensitivities are now model-dependent, viz.:

$$\partial_{\tau}|\mathbf{M}| = \frac{1}{|\mathbf{M}|} \cdot \sum_{j=1}^3 M_j (\partial_{\tau} M_j) \quad j = 1, \dots, 3$$

where j denotes a component and \mathbf{M} is the moment response so that model dependence is encountered since the first order moment is linearly related to the time-constant. Most accurate results for successive model updates are obtained by re-calculating new sensitivities at each iteration so that the inversion process gets considerably slower. Alternatively, the model dependence of the sensitivities is ignored and the inversion scheme is regarded as 'quasi-linear' so that successive model updates are approximated with the initially calculated derivatives. $|\mathbf{B}|$ -field amplitudes inversion is expected to provide an additional useful tool to resolve ambiguity in TEM moments inversion.

Homogeneous body inversion

A geological unit is homogeneous if all cells in the unit share the same time constant. During inversion, the time constant of a unit may change without intra-unit variations. Single or multi-body parametrisation is used to model discrete changes in the time constants of the subsurface where each surface encloses a volume of the rock that has uniform time constants. The inverse problem is formulated to find a relatively small number of time constants which describe the homogeneous units. Because usually there will be far more data points than homogeneous units, the problem is over-determined. The advantage of generalisation to homogeneous body inversion is to easily and rapidly recover the bulk properties of target volumes so that the lithological significance remains

unchanged during inversion. Because only a few parameters are involved, the inversion is very fast. Moreover, homogeneous property inversion may serve as a first step in data inversion, followed by heterogeneous and geometry inversion. The homogeneous property inversion is described in Section 5.2.4 and is a standard VPmg option.

Geometry inversion

In geometry inversion, the geological contacts that define the boundaries of the litho-units of the geological model are subject to inversion. The geological surfaces are manipulated to achieve an improved fit between observed and calculated data. The geological significance of contacts is preserved so that the model is still recognisable as a geological model after inversion. During geometry inversion, the properties of all cells are fixed. If drill pierce points are available, geometry inversion can refine geological surfaces between holes. They are held fixed for geological credibility and to reduce the inherent ambiguity of geophysical interpretation. Geometry inversion is a standard option in VPmg.

In VPmg, modification of geological boundaries is achieved by moving the cell boundaries, with cell rock types invariant. The mesh deforms and arbitrarily small boundary adjustments are permitted. During geometry inversion, continuous vertical movement of the horizontal cell boundaries is permitted, but vertical prism boundaries are fixed. This type of 'adaptive mesh' is implemented in VPmg. The geological units can be heterogeneous or homogeneous and, as in heterogeneous property inversion, soft and hard constraints can be encompassed to the inversion Fullagar and Pears (2007); Fullagar et al. (2008). Generalisation to geometry inversion in VPem3D will be a major subject of ongoing active research in the near future.

Bibliography

- ABRAMOWITZ, M. AND STEGUN, I. 1965. *Handbook of Mathematical Functions*. Dover Publications.
- ANDERSON, W. L. 1983. Fourier cosine and sine transforms using lagged convolutions in double-precision. Tech. Rep. 83-320, USGS, Open-File Report.
- ANDERSON, W. L. 1984. Fast evaluation of Hr and Hz field soundings near a rectangular loop source on a layered earth. Tech. Rep. 84-275, USGS, Open-File Report.
- ANNAN, A. P. 1974. The equivalent source method for electromagnetic scattering analysis and its geophysical application. Ph.D. thesis, Memorial University of Newfoundland, Canada.
- ARFKEN, G. 1985. *Mathematical methods for physicists*, third ed. Academic Press, Inc.
- AUKEN, E., CHRISTIANSEN, A. V., JACOBSEN, B. H., FOGED, N., AND SORENSEN, K. I. 2005. Piecewise 1D laterally constrained inversion of resistivity data. *Geophysical Prospecting* 53, 497–506.
- AUKEN, E., CHRISTIANSEN, A. V., JACOBSEN, L., AND SORENSEN, K. I. 2004. Laterally Constrained 1D-Inversion of 3D TEM data. In *Electrical and Electromagnetic Methods*. EAGE. Extended abstract.
- AVDEEV, D. B. 2005. Three-Dimensional Electromagnetic Modelling And Inversion From Theory To Application. *Surveys in Geophysics* 26, 767–799.
- BACKUS, G. E. AND GILBERT, J. F. 1967. Numerical Applications of a Formalism for Geophysical Inverse Problems. *Geophysical Journal of the Royal Astronomical Society* 13, 247–276.
- BAILIE, R., ARMSTRONG, R., AND REID, D. 2007. The Bushmanland Group supracrustal succession, Aggeneys, Bushmanland, South Africa: Provenance, age of deposition and metamorphism. *South African Journal of Geology* 110, 59–86.

- BARNETT, C. T. 1984. Simple inversion of time-domain electromagnetic data. *Geophysics* 49, 07, 925–933.
- BHATTACHARYYA, B. K. 1980. A generalized multibody model for inversion of magnetic anomalies. *Geophysics* 45, 2, 255–270.
- BLAKELY, R. J. 1995. *Potential Theory in Gravity & Magnetic Applications*. Cambridge University Press.
- BOURGEOIS, B., SUGNARD, K., AND PERRUSSON, G. 2000. Electric and magnetic dipoles for geometric interpretation of three-component electromagnetic data in geophysics. *Inverse Problems* 5, 1225.
- BRODIE, R. AND MALCOLM, S. 2006. A holistic approach to inversion of frequency-domain airborne EM data. *Geophysics* 71, G301–G312.
- CHRISTENSEN, N. B. 1997. Electromagnetic Subsurface Imaging. A Case for an Adaptive Born Approximation. *Surveys in Geophysics* 18, 477–510.
- COMMER, M. 2003. Three-dimensional inversion of transient electromagnetic data: A comparative study. Ph.D. thesis, University of Cologne.
- COMMER, M. AND NEWMAN, G. 2004. A Parallel Finite-Difference Approach for Three-Dimensional Transient Electromagnetic Modeling With Galvanic Sources. *Geophysics* 69, 1192–1202.
- COMMER, M. AND NEWMAN, G. A. 2007. New advances in three-dimensional controlled-source electromagnetic inversion. *Geophysical Journal International* 172, 2, 513–535.
- CONSTABLE, S. C., PARKER, R. L., AND CONSTABLE, C. G. 1987. Occam's inversion: A practical algorithm for generating smooth models from electromagnetic sounding data. *Geophysics* 52, 289–300.
- COX, L. H. AND ZHDANOV, M. S. 2008. Advanced computational methods of rapid and rigorous 3-d inversion of airborne electromagnetic data. *Communications in Computational Physics* 3, 1, 160–179.
- DAVIS, P. J. AND RABINOWITZ, P. 1975. *Methods of numerical integration*. Academic Press, Inc.
- DEBYE, P. 1909. Der Lichtdruck auf Kugeln von beliebigem Material. *Annalen der Physik* 30, 57–136.
- DRUSKIN, V. AND KNIZHNERMAN, L. 1994. Spectral approach to solving three-dimensional Maxwell's diffusion equations in the time and frequency domain. *Radio Science* 29, 937–953.
- DUNCAN, A., AMANN, B., O'KEEFE, K., WILLIAMS, P., TULLY, T., AND WELLINGTON, A. 1998. Examples from a new EM and electrical methods receiver system. *Exploration Geophysics* 29, 347–354.

- DUNCAN, A. AND PERRY, A. 2008. *Maxwell Manual*. ElectroMagnetic Imaging Technology Pty Ltd, Midland, WA 6056, Australia.
- DUNCAN, A. C. 1987. Interpretation of down-hole transient EM data using current filaments. In *5th Geophysical Conference*, D. Pridmore, Ed. Vol. 18. Austr. Soc. Expl. Geophys., 36–39.
- DYCK, A. V. 1991. Drill-hole electromagnetic methods. In *Electromagnetic methods in applied geophysics*, M. N. Nabighian, Ed. Vol. 02. Soc. of Expl. Geophys., 881–930.
- DYCK, A. V., BLOORE, M., AND VALLEE, M. A. 1980. User manual for programs PLATE and SPHERE. Tech. rep., Geophysics Lab., Dept. of Physics, University of Toronto. Research in Applied Geophysics 14.
- EATON, P. A. 1989. 3D Electromagnetic Inversion Using Integral Equations. *Geophysical Prospecting* 37, 407–426.
- EATON, P. A. AND HOHMANN, G. W. 1989. A rapid inversion technique for transient electromagnetic sounding. *Physics of the Earth and Planetary Interiors* 53, 384–404.
- ELLIS, R. G. 1995. Airborne electromagnetic 3D modelling and inversion. *Exploration Geophysics* 26, 138–143.
- FARQUHARSON, C. G., DUCKWORTH, K., AND OLDENBURG, D. W. 2006. Comparison of integral equation and physical scale modeling of the electromagnetic responses of models with large conductivity contrasts. *Geophysics* 71, 04, G169–G177.
- FARQUHARSON, C. G. AND OLDENBURG, D. W. 1999. Approximate Sensitivities for the Multi-Dimensional Electromagnetic Inverse Problem. In *Three-Dimensional Electromagnetics*, M. L. Oristaglio and B. R. Spies, Eds. Number 7 in Geophysical Developments. Society of Exploration Geophysicists, Tulsa, Chapter III, 256–264.
- FARQUHARSON, C. G. AND OLDENBURG, D. W. 2002. An integral equation solution to the geophysical electromagnetic forward-modelling problem. In *Three-dimensional electromagnetics*, M. S. Zhdanov and P. E. Wannamaker, Eds. Elsevier, 3–19.
- FEDI, M., HANSEN, P. C., AND PAOLETTI, V. 2005. Analysis of depth resolution in potential-field inversion. *Geophysics* 70, A1.
- FULLAGAR, P. K. 1989. Generation of conductivity-depth pseudo-sections from coincident loop and in-loop TEM data. *Exploration Geophysics* 20, 43–45.
- FULLAGAR, P. K. 2002. *Emax transformation for B-field ground TEM data*. Fullagar Geophysics Pty. Ltd. Internal Memorandum

- FULLAGAR, P. K. 2007a. *Program VPmg Technical Documentation*. Fullagar Geophysics Pty. Ltd. Internal Memorandum.
- FULLAGAR, P. K. 2007b. *TEM moments and point conductors*. Fullagar Geophysics Pty. Ltd. Internal Memorandum.
- FULLAGAR, P. K. 2008a. *Conductivity Gradients in VPem3D*. Fullagar Geophysics Pty. Ltd. Internal Memorandum.
- FULLAGAR, P. K. 2008b. *Emax, User Guide*. Fullagar Geophysics Pty Ltd.
- FULLAGAR, P. K., HUGHES, N. A., AND PAINE, J. 2000. Drilling constrained 3-D gravity inversion. *Exploration Geophysics* 31, 17–23.
- FULLAGAR, P. K. AND OLDENBURG, D. W. 1984. Inversion of horizontal loop electromagnetic soundings. *Geophysics* 49, 150–164.
- FULLAGAR, P. K. AND PEARS, G. A. 2007. Towards geologically realistic inversion. In *Exploration 07, Exploration in the New Millennium*. Fifth Decennial International Conference on Mineral Exploration. Toronto.
- FULLAGAR, P. K., PEARS, G. A., HUTTON, D., AND THOMPSON, A. 2004. 3-D Gravity and Aeromagnetic Inversion for MVT Lead-Zinc Exploration at Pillara, Western Australia. *Exploration Geophysics* 35, 142–146.
- FULLAGAR, P. K., PEARS, G. A., AND MCMONNIES, B. 2008. Constrained inversion of geological surfaces - pushing the boundaries. *The Leading Edge* 27, 01, 98–105.
- FULLAGAR, P. K. AND REID, J. E. 1992. Conductivity-depth transformation of fixed loop TEM data. *Exploration Geophysics* 23, 515–520.
- GALLAGHER, P. R., WARD, S. H., AND HOHMANN, G. W. 1985. A model study of a thin plate in free space for the EM37 transient electromagnetic system. *Geophysics* 50, 1022–1019.
- GRANT, F. S. AND WEST, G. F. 1965. *Interpretation theory in applied geophysics*. New York, McGraw-Hill.
- GUILLEN, A., COURRIUX, G., CALCAGNO, P., LANE, R., LEES, T., AND MCINERNEY, P. 2004. Constrained gravity 3D litho-inversion applied to Broken Hill. *ASEG Extended Abstracts 2004*, -. ASEG 17th Geophysical Conference and Exhibition, Sydney 2004.
- GUPTASARMA, D. AND SINGH, B. 1997. New digital linear filters for Hankel J0 and J1 transforms. *Geophysical Prospecting* 45, 05, 745–762.
- HABASHY, T. M., GROOM, R. W., AND SPIES, B. R. 1993. Beyond the Born and Rytov Approximations: A Nonlinear Approach to Electromagnetic Scattering. *Journal of Geophysical Research* 98, 1759–1775.

- HABER, E., OLDENBURG, D. W., AND SHEKHTMAN, R. 2007. Inversion of time domain three-dimensional electromagnetic data. *Geophysical Journal International* 171, 550–564.
- HANNESON, J. E. 1992. The transient EM step response of a dipping plate in a conductive half-space. *Geophysics* 57, 09, 1116–1126.
- HANNESON, J. E. AND WEST, G. F. 1984. The horizontal loop electromagnetic response of a thin-plate in a conductive earth part I: Computational method. *Geophysics* 49, 04, 411–420.
- HOHMANN, G. W. 1975. Three-dimensional induced polarization and electromagnetic modeling. *Geophysics* 40, 309–324.
- HOHMANN, G. W. 1988. Numerical Modeling for Electromagnetic Methods of Geophysics. In *Electromagnetic methods in applied geophysics*, M. N. Nabighian, Ed. Vol. 01. Soc. of Expl. Geophys., 313–363.
- HUANG, H. AND PALACKY, G. J. 1991. Damped least-squares inversion of time-domain airborne EM data based on singular value decomposition. *Geophysical Prospecting* 39, 827–844.
- HUGHES, W. 2006. Case History: High Temperature SQUIDS in Raglan In *presented at Society of Exploration Geophysicists 76th Annual General Meeting. Workshop on SQUIDS in Exploration*
- HYDE, C. 2002. The electromagnetic response of a sphere in the moment domain: a building block for the construction of arbitrary 3D shapes. In *77th SEG Annual Meeting*. Expanded Abstract, Paper ER 1.5.
- HYDE, C. 2005. Imaging of airborne time-domain magnetic data via the moment transform. Unpublished PhD Thesis (Draft), University of British Columbia, Canada.
- JACKSON, D. D. 1972. Interpretation of inaccurate, insufficient and inconsistent data. *Geophysical Journal of the Royal Astronomical Society* 28, 97–109.
- JESSELL, M. 2001. Three-dimensional geological modelling of potential-field data. *Computers & Geosciences* 27, 4, 455–465.
- JUPP, D. L. B. AND VOZOFF, K. 1975. Stable Iterative Methods for the Inversion of Geophysical Data. *Geophysical Journal* 42, 957–976.
- KAUAIKUA, J. 1978. The electromagnetic fields about a horizontal electric wire source of arbitrary length. *Geophysics* 43, 1019–1022.
- KAUFMAN, A. 1978. Frequency and transient responses of electromagnetic fields created by currents in confined conductors. *Geophysics* 43, 05, 1002–1010.

- KAUFMAN, A. A. AND EATON, P. A. 2001. The theory of inductive prospecting. 33, XIII, 681. Rev. ed. of: Inductive mining prospecting. 1985 - Includes bibliographical references and index.
- KAUFMAN, A. A. AND KELLER, G. V. 1983. *Frequency and Transient Soundings*. Elsevier, Amsterdam.
- KAUFMAN, A. A. AND KELLER, G. V. 1985. *Inductive Mining Prospecting*. Vol. Part I, Theory. Elsevier Science Publ. Co., Inc.
- KING, A. 1997. Inversion of localized electromagnetic anomalies. Ph.D. thesis, Macquarie University, Australia.
- KING, A. AND MACNAE, J. C. 2001. Modeling of the EM inductive-limit surface currents. *Geophysics* 66, 02, 476–481.
- KLEINER, R., KOELLE, D., LUDWIG, F., AND CLARKE, J. 2004. Superconducting quantum interference devices: State of the art and applications. *Proceedings of the IEEE* 92, 10, 1534–1548.
- KNOX-ROBINSON, C. M. AND WYBORN, L. A. I. 1997. Towards a holistic exploration strategy: Using Geographic Information Systems as a tool to enhance exploration. *Australian Journal of Earth Sciences: An International Geoscience Journal of the Geological Society of Australia* 44, 4, 453–463.
- LAJOIE, J. J. AND WEST, G. F. 1976. The electromagnetic response of a conductive inhomogeneity in a layered earth. *Geophysics* 41, 6A, 1133–1156.
- LAMONTAGNE, Y. 1975. Applications of wide band, time domain EM measurements in mineral exploration. Ph.D. thesis, University of Toronto, Canada.
- LAMONTAGNE, Y., MACNAE, J., AND POLZER, B. 1988. Multiple conductor modeling using program multiloop. In *58th Ann. Internat. Mtg. Soc. of Expl. Geophys.*, Session:EM2.5.
- LAMONTAGNE, Y. AND WEST, G. F. 1971. EM response of a rectangular thin plate. *Geophysics* 36, 06, 1204–1222.
- LANE, R. AND GUILLEN, A. 2005. Geologically-inspired constraints for a potential field litho-inversion scheme. *Proceedings of IAMG '05: GIS and Spatial Analysis 1*, 181–186.
- LEE, K. H. AND XIE, G. O. 1993. A new approach to imaging with low-frequency electromagnetic fields. *Geophysics* 58, 780–796.
- LEE, T. 1974. Transient electromagnetic response of a sphere in a layered medium. Ph.D. thesis, Macquarie University, Australia.
- LEE, T. 1982. Asymptotic expansions for transient electromagnetic fields. *Geophysics* 47, 38.

- LEE, T. 1983. The Transient Electromagnetic Response Of A Conducting Sphere In An Imperfectly Conducting Half-Space. *Geophysical Prospecting* 31, 5, 766–781.
- LEE, T. AND THOMAS, L. 1988. A review of the application of analytical methods to the prediction of transient electromagnetic field responses. *Explor. Geophys.* 19, 3 (Jan.), 423–434.
- LEE, T. AND THOMAS, L. 1992. The Transient Electromagnetic Response of a polarizable Sphere in a Conducting Half Space. *Geophysical Prospecting* 40, 541–563.
- LEE, T. J. 1980. Transient electromagnetic response of a sphere in a layered medium. *Pure and Applied Geophysics* 119, 309–338.
- LEE, T. J., SMITH, R. S., AND HYDE, C. 2003. Using a non-integer moment of the impulse response to estimate the half-space conductivity. *Geophysical Prospecting* 51, 443–446.
- LESLIE, K. E., BINKS, R. A., LAM, S. K. H., SULLIVAN, P. A., TILBROOK, D. L., THORN, R. G., AND FOLEY, C. P. 2008. Application of high-temperature superconductor SQUIDS for ground-based TEM. *The Leading Edge* 27, 1 (Jan.), 70–74.
- LI, Y. AND OLDENBURG, D. W. 1996. 3-D inversion of magnetic data. *Geophysics* 61, 02, 394–408.
- LI, Y. AND OLDENBURG, D. W. 1998. 3-D inversion of gravity data. *Geophysics* 63, 01, 109–119.
- LINES, L. R. AND TREITEL, S. 1984. Tutorial: A review of least-squares inversion and its application to geophysical problems. *Geophysical Prospecting* 32, 159–186.
- LIU, G. AND ASTEN, M. W. 1993. Fast approximate solutions of transient EM response to a target buried beneath a conductive overburden. *Geophysics* 58, 810–817.
- LODHA, G. S. AND WEST, G. F. 1976. Practical airborne EM (AEM) interpretation using a sphere model. *Geophysics* 41, 6A, 1157–1169.
- LUKE, Y. L. 1962. *Integrals of Bessel Functions*. McGraw-Hill, New York.
- MACNAE, J., KING, A., STOLZ, N., AND KLINKERT, P. 1999. 3-D EM Inversion to the limit. In *Three-dimensional electromagnetics*, M. Oristaglio and B. Spies, Eds. Soc. of Expl. Geophys., 489–501.
- MACNAE, J. AND LAMONTAGNE, Y. 1987. Imaging quasi-layered conductive structures by simple processing of transient electromagnetic data. *Geophysics* 52, 04, 545–554.

- MALLET, J. L. 2002. *Geomodeling*. Oxford University Press, New York.
- MARCH, H. W. 1953. The field of a magnetic dipole in the presence of a conducting sphere. *Geophysics* 18, 03, 671–684.
- MCCLUNG, C. R., GUTZMER, J., BEUKES, N. J., MEZGER, K., STRAUSS, H., AND GERTLOFF, E. 2007. Geochemistry of bedded barite of the Mesoproterozoic Aggeneys-Gamsberg Broken Hill-type district, South Africa. *Mineralium Deposita* 42, 537–549.
- MCGAUGHEY, J. 2006. *GIS for the Earth Sciences*. Geological Association of Canada, Chapter The common earth model: a revolution in exploration data integration, 567–576.
- MCMONNIES, B. AND GERRIE, V. 2007. Ground and Borehole Geophysics - A Decade of Improvements. In *Exploration 07: Exploration in the new Millennium*. proceedings of the Fifth Decennial International Conference on Mineral Exploration. Decennial Mineral Exploration Conferences, Toronto, Canada.
- MCNEILL, J. D., EDWARDS, R. N., AND LEVY, G. M. 1984. Approximate calculations of the transient electromagnetic response from buried conductors in a conducting half-space. *Geophysics* 59, 918–924.
- MEJU, M. A. 1994. *Geophysical Data Analysis: Understanding Inverse Problem Theory and Practice*. Soc. of Expl. Geophys. Course Notes.
- NABIGHIAN, M. AND ASTEN, M. W. 2002. Metalliferous mining geophysics - State of the art in the last decade of the 20th century and the beginning of the new millenium. *Geophysics* 67, 3, 964–978.
- NABIGHIAN, M. N. 1970. Quasi-static transient response of a conducting permeable sphere in a dipolar field. *Geophysics* 35, 02, 303–309.
- NABIGHIAN, M. N. 1971. Quasi-static transient response of a conducting permeable two-layer sphere in a dipolar field. *Geophysics* 36, 01, 25–37.
- NABIGHIAN, M. N. 1979. Quasi-static transient response of a conducting half-space - An approximate representation. *Geophysics* 44, 10, 1700–1705.
- NABIGHIAN, M. N. AND MACNAE, J. C. 1991. Time domain electromagnetic prospecting methods. In *Electromagnetic methods in applied geophysics*, M. N. Nabighian, Ed. Vol. 02. Soc. of Expl. Geophys., 427–520.
- NABIGHIAN, M. N. AND MACNAE, J. C. 2005. Electrical and EM methods, 1980-2005. *The Leading Edge* 24, S42.
- NEWMAN, G. A. AND ALUMBAUGH, D. L. 1997. Remote Sensing - A Scientific Vision for Sustainable Development. In *Geoscience and Remote Sensing*. Vol. 2. IEEE International, Singapore, Chapter 3D electromagnetic modeling using staggered finite differences, 929–932.

- NEWMAN, G. A., ANDERSON, W. L., AND HOHMANN, G. W. 1987. Interpretation of transient electromagnetic soundings over three-dimensional structures for the central-loop configuration. *Geophysical Journal International* 89, 889–914.
- NEWMAN, G. A. AND HOHMANN, G. W. 1988. Transient electromagnetic responses of high-contrast prisms in a layered earth. *Geophysics* 53, 05, 691–706.
- OLDENBURG, D. W. AND LI, Y. 2005. Inversion for applied geophysics: A tutorial. In *Near-surface geophysics*, D. K. Butler, Ed. SEG, 89–150.
- OLDENBURG, D. W. AND PRATT, D. A. 2007. Geophysical inversion for mineral exploration - a decade of progress in theory and practice. In *Exploration 07, Exploration in the New Millennium*. Fifth Decennial International Conference on Mineral Exploration. Toronto.
- PALACKY, G. J. 1983. Tutorial: Research, application and publications in electrical and electromagnetic methods. *Geophysical Prospecting* 31, 861–872.
- PALACKY, G. J. 1988. Resistivity Characteristics of Geological Targets. In *Electromagnetic methods in applied geophysics*, M. N. Nabighian, Ed. Vol. 01. Soc. of Expl. Geophys., 53–129.
- PANOFSKY, W. K. H. AND PHILLIPS, M. 1962. *Classical Electricity and Magnetism*, second ed. Reading and London, Addison-Wesley.
- PATERSON, N. R. 2003. Geophysical developments and mine discoveries in the 20th century. *The Leading Edge* 22, 558–561.
- PODDAR, M. 1983. A rectangular loop source of current on multilayered earth. *Geophysics* 48, 01, 107–109.
- PORTNIAGUINE, O. AND ZHDANOV, M. 2002. 3-d magnetic inversion with data compression and image focusing. *Geophysics* 67, 5, 1532–1541.
- PRESS, W. H., TEUKOLSKY, S. A., VETTERLING, W. T., AND FLANNERY, B. P. 2002. *Numerical Recipes in Fortran in Fortran 90*, second ed. Vol. 2. Cambridge University Press.
- RAICHE, A., SUGENG, F., AND WILSON, G. 2007. Practical 3D EM inversion? the P223F software suite. In ASEG Extended Abstracts. *ASEG Extended Abstracts*.
- RAICHE, A. P. 1974. An integral equation approach to 3D modeling. *Geophysical Journal of the Royal Astronomical Society* 36, 363–376.
- RAICHE, A. P. 1987. Transient electromagnetic field computations for polygonal loops on layered earths. *Geophysics* 52, 06, 785–793.

- RAICHE, A. P. 1998. Modelling the time-domain response of AEM systems. *Exploration Geophysics* 29, 103–106.
- RAICHE, A. P. AND GALLAGHER, R. G. 1985. Apparent resistivity and diffusion velocity. *Geophysics* 50, 10, 1628–1633.
- RAICHE, A. P. AND SPIES, B. R. 1981. Coincident loop transient electromagnetic master curves for interpretation of two-layer earth's. *Geophysics* 46, 01, 53–64.
- REID, J. AND MACNAE, J. 2000. Current channelling in time-domain airborne electromagnetic data. *Exploration Geophysics* 31, 150–157.
- REID, J. E. 1994. Conductivity-Depth Transformation of Separated-Loop Transient Electromagnetic Data. Tech. rep., University of Sydney, Australia. January. Master Thesis.
- REID, J. E. AND FULLAGAR, P. K. 1998. Conductivity-depth transformation of slingram transient electromagnetic data. *Exploration Geophysics* 29, 570–576.
- REID, J. E. AND MACNAE, J. C. 2002. Resistive limit modeling of airborne electromagnetic data. *Geophysics* 67, 02, 492–500.
- ROZENDAAL, A. 1986. The Gamsberg Zinc Deposit, Namaqualand District. In *Mineral Deposits of Southern Africa*, C. R. Anhaeusser and S. Maske, Eds. Vol. 2. The Geological Society of South Africa, 1477–1488.
- SATTEL, D. AND REID, J. 2001. Automated anomaly modelling of AEM data with magnetic dipoles buried inside a layered earth. *ASEG Extended Abstracts 2001*, 1, –.
- SATTEL, D. AND REID, J. 2006. Modelling of airborne EM anomalies with magnetic and electric dipoles buried in a layered earth. *Exploration Geophysics* 37, 3, 254–260.
- SCHAA, R., REID, J. E., AND FULLAGAR, P. K. 2006. Unambiguous apparent conductivities for fixed-loop transient electromagnetic data. *Exploration Geophysics* 37, 348–354.
- SCHELKUNOFF, S. A. 1943. *Electromagnetic waves*. New York, Van Nostrand.
- SCHOLL, C. 2005. The influence of multidimensional structures on the interpretation of LOTEM data with one-dimensional models and the application to data from Israel. Ph.D. thesis, University of Cologne.
- SCHOLL, C., HELWIG, S. L., TEZKAN, B., GOLDMAN, M., AND KAFRI, U. 2009. 1-D multimodel joint inversion of TEM-data over multidimensional structures. *Geophysical Journal International* 176, 81–94.

- SILVA, J. B. C., MEDEIROS, W. E., AND BARBOSA, V. C. F. 2001. Potential-field inversion: Choosing the appropriate technique to solve a geologic problem *Geophysics* 66, 511–520.
- SINGH, S. K. 1973. Electromagnetic transient response of a conducting sphere embedded in a conductive medium. *Geophysics* 38, 05, 864–893.
- SMITH, R. S., EDWARDS, R. N., AND BUSELLI, G. 1994. An automatic technique for presentation of coincident-loop, impulse-response, transient electromagnetic data. *Geophysics* 59, 1542–1550.
- SMITH, R. S., HYDE, C., LEE, T. J., AND ALMOND, R. 2006. Impulsive moments at work. In *Three-Dimensional Electromagnetics III*, J. Macnae, Ed. Proceedings of the 3DEM-3 Symposium Adelaide February 2003.
- SMITH, R. S. AND LEE, T. J. 2002a. The impulse-response moments of a conductive sphere in a uniform field, a versatile and efficient electromagnetic model. *Exploration Geophysics* 32, 02, 113–118.
- SMITH, R. S. AND LEE, T. J. 2002b. The moments of the impulse response: A new paradigm for the interpretation of transient electromagnetic data. *Geophysics* 67, 04, 1095–1103.
- SMITH, R. S. AND LEE, T. J. 2002c. Using the moments of a thick layer to map conductance and conductivity from airborne electromagnetic data. *J. Appl. Geophys.* 49, 173–183.
- SMITH, R. S., LEE, T. J., ANNAN, A. P., AND O'CONNELL, M. D. 2005. Approximate apparent conductance (or conductivity) from the realizable moments of the impulse response. *Geophysics* 70, 01, G29–G32.
- SOLEIMANI, M. 2008. Computational aspects of low frequency electrical and electromagnetic tomography: A review study. *International Journal of Numerical Analysis and Modeling* 5, 3, 407–440.
- SPIES, B. R. AND EGGERS, D. E. 1986. The use and misuse of apparent resistivity in electromagnetic methods. *Geophysics* 51, 07, 1462–1471.
- SPIES, B. R. AND FRISCHKNECHT, F. C. 1991. Electromagnetic sounding. In *Electromagnetic methods in applied geophysics*, M. N. Nabighian, Ed. Vol. 02. Soc. of Expl. Geophys., 285–425.
- SPIES, B. R. AND PARKER, P. D. 1984. Limitations of large-loop transient electromagnetic surveys in conductive terrains. *Geophysics* 49, 902–912.
- STOLZ, E., MACNAE, J. C., AND RAICHE, A. P. 1995. Is full 3-D inversion necessary for interpreting EM data? *Exploration Geophysics* 26, 167–171.
- STOLZ, E. M. AND MACNAE, J. C. 1997. Fast approximate inversion of TEM data. *Exploration Geophysics* 28, 03, 317–322.

- STRATTON, J. A. 1941. *Electromagnetic Theory*. New York and London, McGraw-Hill.
- SUGENG, F., RAICHE, A., AND WILSON, G. 2006. An efficient compact finite-element modelling method for the practical 3D inversion of electromagnetic data from high contrast complex structures. In *IAGA WG 1.2 on Electromagnetic Induction in the Earth*. Extended Abstract 18th Workshop.
- TARANTOLA, A. 2005 *Inverse Problem Theory*. Philadelphia, Siam.
- TELFORD, W. M., GELDART, L. P., AND SHERIFF, R. E. 1985. *Applied Geophysics*, second ed. Elsevier Science Publ. Co., Inc.
- TERBLANCHE, O. 2008. Gamsberg East Fixed Loop2 Squid TEM data reprocessed using Time Constant decay analysis. Tech. rep., Anglo American plc.
- TORRES-VERDIN, C. AND HABASHY, T. M. 1994. Rapid 2.5-dimensional forward modeling and inversion via a new nonlinear scattering approximation *Radio Science* 79, 1051–1079.
- TREITEL, S. AND LINES, L. 2001. Past, present, and future of geophysical inversion - A new millenium analysis. *Geophysics* 66, 21–24.
- TROFIMCZYK, K. 2004. Physical Property Medians and Spreads Derived from Downhole Wireline Geophysical Logs for Lithologies Intersected in 4 Boreholes at Gamsberg. Tech. rep., Anglo American Corporation of South Africa Ltd., ATD Geosciences Resource Group. September. Technical Memorandum.
- TSENG, H. W., LEE, K. H., AND BECKER, A. 2003. 3D interpretation of electromagnetic data using a modified extended Born approximation *Geophysics* 68, 127–137.
- VAN ZON, T. AND ROY-CHOWDHURY, K. 2006. Structural inversion of gravity data using linear programming. *Geophysics* 71, J41.
- VIEZZOLI, A., AUKEN, E., AND MUNDAY, T. 2009. Spatially constrained inversion for quasi 3D modelling of airborne electromagnetic data - an application for environmental assessment in the Lower Murray Region of South Australia. *Exploration Geophysics* 40, 173–183.
- VIEZZOLI, A., CHRISTIANSEN, A. V., AUKEN, E., AND SORESENSEN, K. 2008. Quasi-3D modeling of airborne TEM data by spatially constrained inversion. *Geophysics* 73, 3, F105–F113.
- WAIT, J. R. 1951. A conducting sphere in a time varying magnetic field. *Geophysics* 16, 666–672.
- WAIT, J. R. 1953. A conducting permeable sphere in the presence of a coil carrying an oscillating current. *Canadian Journal of Physics* 31, 670–678.

- WAIT, J. R. 1960. On the electromagnetic response of a conducting sphere to a dipole field. *Geophysics* 25, 3, 649–658.
- WALKER, P. W. AND WEST, G. F. 1991. A robust integral equation solution for electromagnetic scattering by a thin plate in conductive media. *Geophysics* 56, 08, 1140–1152.
- WALKER, P. W. AND WEST, G. F. 1992. Parametric estimators for current excitation on a thin plate. *Geophysics* 57, 06, 766–773.
- WANG, T. AND HOHMANN, G. W. 1993. A finite-difference time-domain solution for three-dimensional electromagnetic modeling. *Geophysics* 58, 06, 797–809.
- WANG, T., ORISTAGLIO, M., TRIPP, A., AND HOHMANN, G. 1994. Inversion of diffusive transient electromagnetic data by a conjugate-gradient method. *Radio Science* 29, 1143–1156.
- WANG, X. AND HANSEN, R. 1990. Inversion for magnetic anomalies of arbitrary three-dimensional bodies. *Geophysics* 55, 1321–1326.
- WARD, S. H. AND HOHMANN, G. W. 1988. Electromagnetic theory for geophysical applications. In *Electromagnetic methods in applied geophysics*, M. N. Nabighian, Ed. Vol. 01. Soc. of Expl. Geophys., 131–312.
- WATSON, G. N. 1944. *A treatise on the theory of Bessel functions*. Cambridge University Press.
- WEBB, M. AND CORSCADDEN, B. 2009. A case study of deep electromagnetic exploration in conductive cover. *ASEG Extended Abstracts 2009*, 1 (Jan.), –.
- WEIDELT, P. 1975. Electromagnetic induction in three-dimensional structures. *Journal of Geophysics* 41, 85–109.
- WEIDELT, P. 1983. The harmonic and transient electromagnetic response of a thin dipping dike. *Geophysics* 48, 07, 934–952.
- WEST, G. F. AND MACNAE, J. C. 1991. Physics of the electromagnetic induction exploration method. In *Electromagnetic methods in applied geophysics*, M. N. Nabighian, Ed. Vol. 02. Soc. of Expl. Geophys., 5–45.
- WILLIAMS, N. C. 2008. Geologically-constrained UBC-GIF gravity and magnetic inversions with examples from the Agnew-Wiluna Greenstone Belt, Western Australia. Ph.D. thesis, University of British Columbia, Vancouver, Canada.
- WOLFGRAH, P., CHRISTENSEN, N. B., AND SATTEL, D. 2003. Approximate 2D inversion of AEM data. In 16th Conference and Exhibition, Adelaide,. *Australian Society of Exploration Geophysicists 16th Conference and Exhibition, Adelaide*,.

- XIONG, Z. AND TRIPP, A. C. 1995. A block iterative algorithm for 3-D electromagnetic modeling using integral equations with symmetrized substructures. *Geophysics* 60, 1, 291–295.
- ZEYEN, H. AND POUS, J. 1991. A new 3-D inversion algorithm for magnetic total field anomalies. *Geophysical Journal International* 104, 3, 583–591.
- ZHDANOV, M. S., DMITRIEV, V. I., AND GRIBENKO, A. V. 2007. Integral Electric Current Method in 3-D Electromagnetic Modeling for Large Conductivity Contrast. *IEEE Transactions on Geoscience and Remote Sensing* 45, 1282–1290.
- ZHDANOV, M. S. AND FANG, S. 1999. Three-Dimensional Quasi-Linear Electromagnetic Modeling and Inversion. In *Three-Dimensional Electromagnetics*, M. Oristaglio and B. Spies, Eds. Number 7 in Geophysical Developments. Society of Exploration Geophysicists, Tulsa, Chapter III, 233–255.
- ZHDANOV, M. S. AND HURSAN, S. F. G. 2000. Electromagnetic Inversion using Quasi-Linear Approximation. *Geophysics* 65, 1501–1513.
- ZHDANOV, M. S., LEE, S. K., AND YOSHIOKA, K. 2006. Integral equation method for 3D modeling of electromagnetic fields in complex structures with inhomogeneous background conductivity. *Geophysics* 71, G333+.
- ZHDANOV, M. S., PAVLOV, D. A., AND ELLIS, R. G. 2002. Localised S-inversion of time domain electromagnetic data. *Geophysics* 67, 1115–1125.
- ZHDANOV, M. S., TRAYNIN, P., AND BOOKER, J. R. 1996. Underground imaging by frequency-domain electromagnetic migration. *Geophysics* 61, 666–682.